

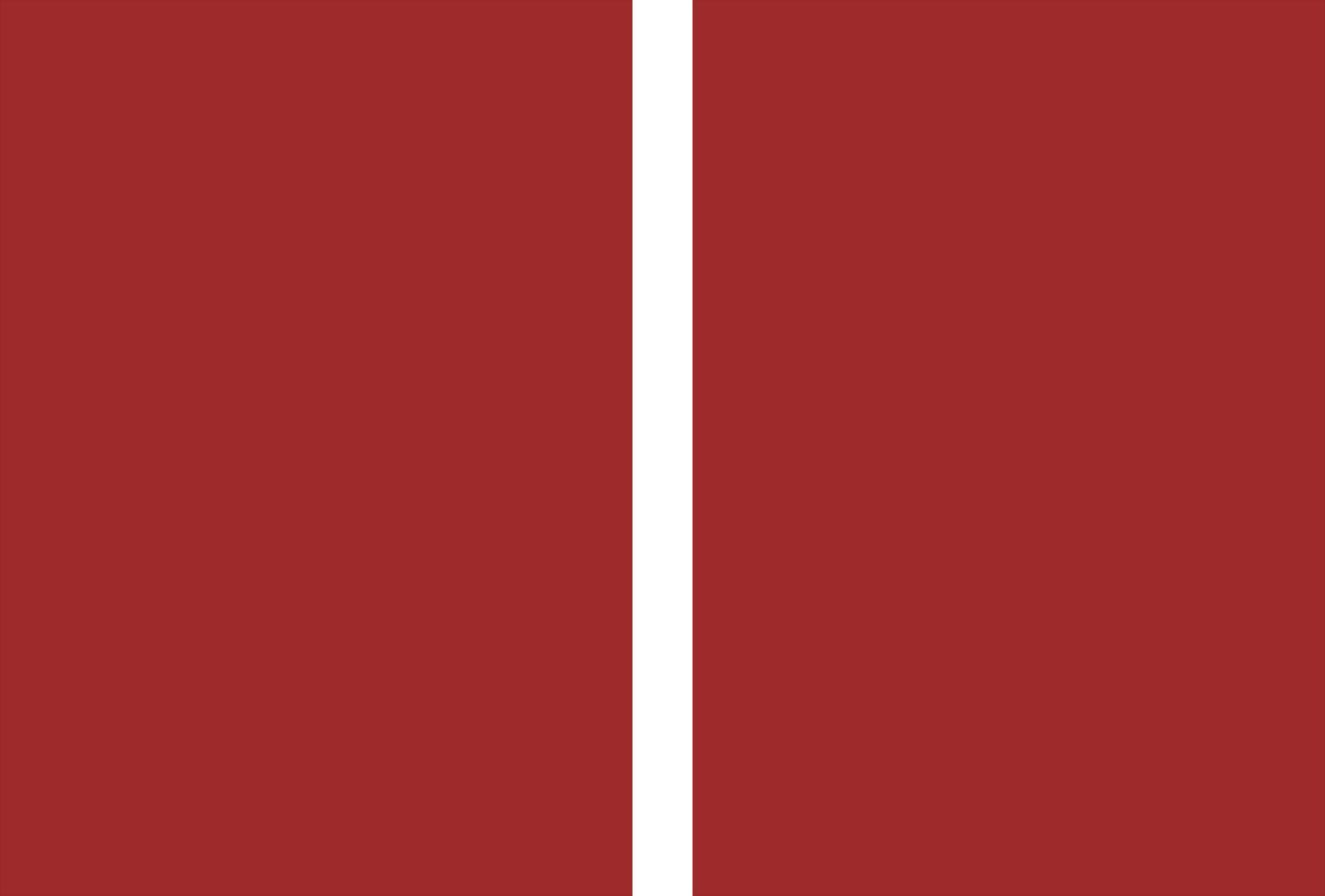


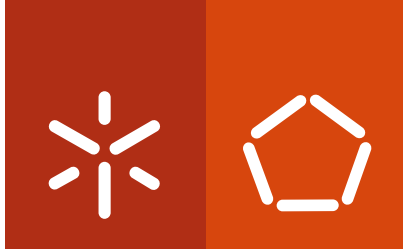
**Universidade do Minho**  
Escola de Engenharia

Luis Jorge Lima Ferrás **Theoretical and Numerical Studies of Slip Flows**

Luis Jorge Lima Ferrás

**Theoretical and Numerical Studies of Slip Flows**





**Universidade do Minho**  
Escola de Engenharia

Luis Jorge Lima Ferrás

## **Theoretical and Numerical Studies of Slip Flows**

Ph.D. Thesis in  
Polymers and Composites Engineering

Work accomplished under the orientation of  
**Professor João Miguel de Amorim Novais da  
Costa Nóbrega**  
**Professor Fernando Manuel Coutinho Tavares de Pinho**

August 2012

**Autor:** Luis Jorge Lima Ferrás **CC:** 12093453

**Email:** luis.ferras@dep.uminho.pt

**Título da tese:** Theoretical and Numerical Studies of Slip Flows

**Orientadores:**

Doutor João Miguel Amorim Novais da Costa Nóbrega

Doutor Fernando Manuel Coutinho Tavares de Pinho

**Ano de conclusão:** 2012

Doutoramento em Ciência e Engenharia de Polímeros e Compósitos

É AUTORIZADA A REPRODUÇÃO INTEGRAL DESTA  
TESE APENAS PARA EFEITOS DE INVESTIGAÇÃO, ME-  
DIANTE DECLARAÇÃO ESCRITA DO INTERESSADO,  
QUE A TAL SE COMPROMETE.

Universidade do Minho, 29 de Agosto de 2012

---

Luis Jorge Lima Ferrás

Dedicated to the loving memory of Maria Hilária Lima Rodrigues.

1953 – 2011



## ACKNOWLEDGMENTS

---

First of all I would like to acknowledge the funding provided by the Portuguese Foundation for Science and Technology (FCT) through the scholarship SFRH/BD/37586/2007, co-financed by the European Social Fund (ESF) under the Human Potential Operational Programme.

To my advisers, Professor Miguel Nóbrega and Professor Fernando Pinho, I express my truly gratitude for their patience, knowledge and ability to teach me the subject of Engineering. I must thank them for my hard times of unsuccessful search for theorems and proofs, that made me stronger and open-minded. I thank Professor Nóbrega for all the discussions we had and the ideas he brought to the table, for his kindness, support and knowledge, for the hours of sleep I took from him and for all the time he spent with me. I thank Professor Fernando for keeping simple what is complex, for sharing with me a tiny portion of his knowledge, and above all, his pedagogical and scientific skills. You are a true worker. For both advisers: I marked all your words, and without your guidance I would probably be lost. You were impeccable and truly professional.

I sincerely acknowledge Dr. Alexandre Afonso, a true worker and a brilliant mind. You gave me the power to improve this thesis. It is easy and a pleasure to work you. You are the true Jedi of computational fluid dynamics. May now the power be with you. I also acknowledge Professor Manuel Alves, always available to help and a true source of work and knowledge. I also believe that Dr. Alexandre, Professor Manuel, Professor Nóbrega and Professor Fernando have built a time travel machine. They somehow managed to work 48 hours per day. I also thank Professor Vera for taking care of Professor Nóbrega and Professor Olga for all the help.

I would like to thank all my colleagues at DEP, Paulo Teixeira and Célio Pinto (specially for their singing skills), Pedro Marques, Rui Novais, Vera Cruz, Filomena Costa, Nelson Gonçalves, Ângela Vergas Gonçalves, Mladen Motovilin (the Polymer Jedi), Simão Pereira, Sacha Mould and Gabriela Teixeira. Without you this thesis wouldn't be possible.

I would like to thank all my friends for their support and friendship along the years. I thank Mafaldinha for her constant smile and happiness. I thank Bruninha for all the support, patience and love. You are a true and unique human being that should live forever. Finally, I would like to express my gratitude to my mother for her endless support along 29 years. You were sweet, kind, and the best mother in the world!





## ABSTRACT

---

This thesis presents an intensive study on slip flows of Newtonian and Non-Newtonian fluids carried out both analytically and numerically. Industrial applications of these flows are found in classical industries such as in polymer processing (for instance in extrusion) and in more modern applications as in lab-on-chip devices.

Analytical solutions for flows under slip, are presented for both Newtonian, inelastic Newtonian and Non-Newtonian flows. These analytical solutions were missing in the literature and are helpful for both theoretical analysis and computer code validation.

Slip boundary conditions were implemented in a computational fluid dynamics code, based on the finite volume method framework. New techniques for their implementation were devised, allowing to obtain convergence for reasonable Weissenberg numbers, using an appropriate iterative procedure to couple velocity, pressure and stress.

The numerical code was then used to simulate benchmark problems, such as the 4:1 contraction, 1:4 expansion and slip-stick flows under slip, usually found in polymer processing..

The theoretical study of development length for Newtonian and viscoelastic fluids was performed for a channel flow under slip. New correlations for predicting the development length in micro and macro channels were devised.

Other part of these thesis was dedicated to the theoretical study of electro-osmotic flows of complex fluids, for which analytical solutions for simple flows under the influence of the linear and nonlinear Navier slip boundary conditions were devised.

### KEYWORDS:

Slip boundary conditions; finite volume method; contraction flow; expansion flow; development length; electro-osmotic flow



## RESUMO

---

Nesta tese é apresentado um estudo intensivo de escoamentos com escorregamento, envolvendo fluidos newtonianos e não-newtonianos. Este tipo de escoamentos pode ser encontrado na indústria, por exemplo no processo de extrusão e ainda em aplicações mais modernas, tais como aparelhos baseados no conceito “lab-on-chip”.

São apresentadas soluções analíticas com escorregamento para fluidos newtonianos, e diversos fluidos não-newtonianos, tanto inelásticos como viscoelásticos. Estas soluções analíticas não existiam na literatura e são úteis tanto em termos teóricos assim como para a validação de códigos numéricos.

As condições de fronteira de escorregamento foram implementadas num código numérico de mecânica dos fluidos computacional baseado no métodos dos volumes finitos. Foram desenvolvidas novas técnicas para a implementação destas condições de fronteira, permitindo obter convergência para valores razoáveis do número de Weissenberg, usando um processo iterativo para acoplar os campos de velocidades, pressões e tensões.

Este código numérico foi depois usado para simular problemas de referência, tais como os escoamentos numa contracção súbita 4:1, numa expansão 1:4 e o escoamento “slip-stick”, sob a influência do escorregamento na parede. Estas geometrias são frequentemente utilizadas em processamento de polímeros, o que substancia a utilidade prática destas simulações.

Foi feito um estudo numérico e teórico para descobrir o comprimento de desenvolvimento do escoamento num canal simples com escorregamento na parede, de fluidos newtonianos e viscoelásticos. Foram ainda propostas novas correlações para prever esse comprimento.

Outra parte do trabalho foi dedicada ao estudo de electro-osmose, onde novas soluções analíticas para escoamentos simples sob a influência do modelo de escorregamento linear de Navier, são apresentadas.

### PALAVRAS-CHAVE:

Condições fronteira de escorregamento; método dos volumes finitos; escoamento em contracções; escoamento em expansões; comprimento de desenvolvimento de um fluido; electro-osmose.



## PUBLICATIONS

---

Some ideas and figures have appeared previously in the following publications:

- L.L. Ferrás, J.M. Nóbrega, FT Pinho (2012), Analytical solutions for Newtonian and Inelastic non-Newtonian flows with wall slip, *Journal of Non-Newtonian Fluid Mechanics* **175-176** 76-88;
- L.L. Ferrás, J.M. Nóbrega, FT Pinho (2012), Analytical solutions for channel flows of Phan-Thien–Tanner and Giesekus fluids under slip, *Journal of Non-Newtonian Fluid Mechanics* **171-172** 97-105;
- L.L. Ferrás, J.M. Nóbrega, FT Pinho (2012), Implementation of Slip Boundary Conditions in the Finite Volume Method: New Techniques, accepted for publication in the *International Journal for Numerical Methods in Fluids*;
- L.L. Ferrás, A.M. Afonso, J.M. Nóbrega, M.A. Alves, F.T. Pinho (2012), A numerical and theoretical study on viscoelastic fluid slip-flows, to be submitted to *Theoretical and Computational Fluid Dynamics*;
- L.L. Ferrás, A.M. Afonso, J.M. Nóbrega, M.A. Alves, F.T. Pinho, Flow of Newtonian and Phan-Thien–Tanner fluids in a 4:1 planar contraction with slip boundary conditions, submitted to *Journal of Non-Newtonian Fluid Mechanics*;
- L.L. Ferrás, A.M. Afonso, J.M. Nóbrega, M.A. Alves, F.T. Pinho (2012), The Influence of Slip Velocity on the Newtonian and Viscoelastic Fluid Flow Through an Abrupt 1:4 Expansion, to be submitted to *Journal of Non-Newtonian Fluid Mechanics*;
- L.L. Ferrás, A.M. Afonso, J.M. Nóbrega, M.A. Alves, F.T. Pinho (2012), Development length in planar channel flows of Newtonian fluids under the influence of wall slip, accepted for publication in the *Journal of Fluids Engineering*;
- L.L. Ferrás, A.M. Afonso, J.M. Nóbrega, M.A. Alves, F.T. Pinho (2012), Numerical study of the Development Length Requirements for Fully Developed flow of Viscoelastic Fluids Under Slip, to be submitted to *Journal of Fluids Engineering*;
- A.M. Afonso, L.L. Ferrás, J.M. Nóbrega, M.A. Alves, F.T. Pinho (2012), Mixed electro-osmotic/pressure driven slip-flows of viscoelastic fluids in hydrophobic microchannels, to be submitted to *Journal of Non-Newtonian Fluid Mechanics*;

- A.M. Afonso, L.L. Ferrás, J.M. Nóbrega, M.A. Alves, F.T. Pinho (2012), Pressure-driven electrokinetic slip-flows of viscoelastic fluids in hydrophobic microchannels with assymmetric zeta potential, to be submitted to *Journal of Colloid and Interface Science*;

# CONTENTS

---

<b>I TO SLIP OR NOT TO SLIP: THAT IS THE QUESTION</b>	<b>1</b>
<b>1 INTRODUCTION</b>	<b>3</b>
1.1 Friction between solids	3
1.2 Friction between a solid and a liquid	5
1.2.1 Slip in Newtonian fluids	6
1.2.2 Slip in Non-Newtonian fluids	8
1.2.3 Objectives	11
1.2.4 Dissertation Outline	11
<b>II MATHEMATICAL MODELLING</b>	<b>15</b>
<b>2 MATHEMATICAL MODELLING</b>	<b>17</b>
2.1 Newtonian and Non-Newtonian fluids	17
2.1.1 What is a fluid?	17
2.1.2 Newtonian fluids	18
2.1.3 Non-Newtonian fluids (inelastic)	20
2.1.4 Non-Newtonian fluids (viscoelastic)	21
2.1.5 Electro-osmotic flow	25
2.2 Computational fluid dynamics	26
<b>III ANALYTICAL STUDIES OF FLOWS UNDER SLIP</b>	<b>33</b>
Introduction to Part III	35
<b>3 ANALYTICAL SOLUTIONS FOR NEWTONIAN AND INELASTIC FLOWS WITH WALL SLIP</b>	<b>37</b>
3.1 Introduction	37
3.2 Theory	39
3.2.1 Governing equations	39
3.2.2 Boundary conditions	40
3.2.3 Slip laws	41
3.3 Analytic and semi analytic solutions for Newtonian fluids	44
3.3.1 Couette flow	44
3.3.2 Couette-Poiseuille Flow	46
3.3.3 Discussion (Newtonian fluids)	50
3.4 Non-Newtonian Fluids (Poiseuille Flow)	54
3.4.1 Power law fluids	54
3.4.2 Sisko model-particular solutions for $n=0.5$ and $n=2$	57
3.4.3 Discussion (non-Newtonian fluids)	58
3.4.4 Yield Stress fluids - Herschel-Bulkley and Robertson-Stiff models	60
3.5 Conclusion	63

4	ANALYTICAL SOLUTIONS FOR CHANNEL SLIP FLOWS OF PTT AND GIESEKUS FLUIDS	71
4.1	Introduction	71
4.2	Governing equations	72
4.3	Analytical Solutions for the PTT fluid and Discussion	74
4.3.1	Couette flow - linear and exponential PTT models	76
4.3.2	Planar channel flow with the linear PTT model	78
4.3.3	Planar channel flow with the exponential PTT model	81
4.4	Analytical Solutions for the Giesekus fluid and Discussion	83
4.4.1	Couette flow	85
4.4.2	Planar Channel Flow	87
4.5	Conclusions	90
	<b>IV NUMERICAL STUDIES OF FLOWS UNDER SLIP</b>	<b>93</b>
	Introduction to Part IV	95
5	IMPLEMENTATION OF SLIP BC IN THE FVM: NEW TECHNIQUES	97
5.1	Introduction	97
5.2	Governing equations and numerical method	98
5.3	Numerical implementation of slip boundary conditions	102
5.3.1	Discretization	102
5.3.2	Explicit and Implicit implementations of the Navier slip law	104
5.3.3	Semi-Implicit implementation of slip laws (orthogonal meshes)	106
5.3.4	Semi-Implicit implementation of slip laws (orthogonal and nonorthogonal meshes)	107
5.4	Results and discussion	109
5.4.1	Newtonian fluids	109
5.4.2	Non-Newtonian fluids	114
5.5	Conclusions	117
6	a numerical and theoretical study on viscoelastic fluid slip-flows	125
6.1	Introduction	125
6.2	Governing Equations	126
6.3	Analytical Solutions	128
6.4	Numerical Method	129
6.5	Results and Discussion	135
6.5.1	Code Verification	135
6.5.2	Elasticity Effects	136
6.6	Conclusions	139



7	SLIP FLOWS OF NEWTONIAN AND PTT FLUIDS IN A 4:1 PLANAR CONTRACTION	147
7.1	Introduction	147
7.2	Governing equations	149
7.3	Numerical Method and Geometry	150
7.4	Results and discussion	153
7.4.1	Newtonian Fluids	153
7.4.2	Viscoelastic fluids	157
7.4.3	Effect of elasticity	161
7.5	Conclusions	162
8	THE INFLUENCE OF SLIP ON VISCOELASTIC FLUID FLOW THROUGH AN EXPANSION	167
8.1	Introduction	167
8.2	Governing equations	169
8.3	Numerical Procedure and Geometry	170
8.4	Results and discussion	175
8.4.1	Newtonian Fluids	175
8.4.2	Viscoelastic fluids	176
8.5	Conclusions	181
9	DEVELOPMENT LENGTH OF NEWTONIAN FLUIDS UNDER THE INFLUENCE OF WALL SLIP	189
9.1	Introduction	189
9.2	Equations, numerical analysis and geometry	190
9.3	Results and Discussion	192
9.4	Conclusions	197
10	DEVELOPMENT LENGTH OF UCM VISCOELASTIC FLUIDS UNDER SLIP	199
10.1	Introduction	199
10.2	Governing equations	201
10.3	Numerical Method	202
10.4	Results and Discussion	205
10.4.1	Slip and elasticity effects	205
10.4.2	Slip and inertia effects	209
10.5	Conclusions	211
V	ELECTRO OSMOTIC FLOW	213
	Introduction to Part V	215
11	MIXED EO/PD SLIP-FLOWS OF VISCOELASTIC FLUIDS	217
11.1	Introduction	217
11.2	Governing equations	220
11.2.1	Constitutive equations	221
11.2.2	Boundary conditions and slip-flow assumptions	222
11.3	Analytical solution	223
11.3.1	Analytical solution for the PTT model	223
11.3.2	Streaming potential solution	227
11.3.3	Analytical solutions for the FENE-P model	229

11.4	Results and Discussion	230
11.4.1	Newtonian fluid with mixed driving forcings with wall slip	231
11.4.2	Viscoelastic fluid driven bu electro-osmosis with wall slip	232
11.4.3	Viscoelastic fluid with mixed driving forcings with wall slip	233
11.5	Conclusions	235
12	EO/PD SLIP-FLOWS OF VISCOELASTIC FLUIDS IN HM WITH ASSYMETRIC ZP	239
12.1	Introduction	239
12.2	Governing equations	241
12.2.1	Slip boundary conditions	241
12.2.2	Constitutive equations	242
12.2.3	Poisson-Boltzmann equation and slip-dependent zeta potentials	243
12.3	Analytical solution	244
12.3.1	sPTT constitutive equation	244
12.3.2	FENE-P constitutive equation	245
12.3.3	Analytical solution for the sPTT model	245
12.3.4	Analytical solution for the FENE-P model	251
12.4	Results and discussion	251
12.4.1	Pure electro-kinetic case	251
12.4.2	Mixed driving forces	253
12.5	Conclusions	254
	<b>VI CONCLUSIONS AND OUTLOOK</b>	<b>259</b>
13	CONCLUSIONS	261
14	OUTLOOK	265
	<b>VII BIBLIOGRAPHY AND REFERENCES</b>	<b>267</b>
	BIBLIOGRAPHY	269

## ACRONYMS

---

**BC** Boundary Conditions  
**EO** Electro-Osmotic  
**FENE** Finitely-Extensible Nonlinear Elastic model  
**FDM** Finite Difference Method  
**FEM** Finite Element Method  
**FVM** Finite Volume Method  
**HM** Hydrophobic Microchannels  
**HWNP** High Weissenberg Number Problem  
**PTT** Phan-Thien Tanner  
**PD** Pressure Driven  
**UCM** Upper-Convected Maxwell  
**ZP** Zeta Potential



Part I

TO SLIP OR NOT TO SLIP: THAT IS THE  
QUESTION



## INTRODUCTION

[...] *Fluid dynamists were divided into: hydraulic engineers who observed things that could not be explained, and mathematicians who explained things that could not be observed [...]*

— Sir Cyril Norman Hinshelwood

We all grew up with the idea that everything is finite, and therefore we are limited. Even though we think of “time” as an endless (infinite) independent property, we can only see “time” locally (through our lifetime), which enhances again our limitation. All our actions and way of thinking were built upon these “fabricated” concepts, and most of the scientific problems that urged during the evolution of Mankind were unsolved for many years because of people’s beliefs and because of what people learned based on common sense. Our brain is capable of the most amazing things, but at the same time is influenced by external factors that deviate the scientific path. The main problem is the constant creation of dogmas for everything we do not know and do not completely understand.

The subject of friction/slip between a fluid and a solid is not completely understood. It suffered somehow from the same mind limitation over the years. The constant need for Gods or the need to believe in “something” superior, made us slaves of the ideas created in the past by great persons associated with fluid dynamics.

It is not easy to describe the flow between these two completely different materials, because there are no hard physical principles for friction/slip to be derived from (maybe our physical laws are a special case of a more general theory that we cannot understand), but the development of ever more sophisticated machines that are able to describe flows at smaller scales, made us question the truth of the ideas proposed before, and question the validity of the no-slip boundary condition.

## 1.1 FRICTION BETWEEN SOLIDS

From the early ages we have the proof of existence of friction between solids, such as the discovery of fire resulting from the friction between two rocks (or two pieces of wood), and the way we easily walk without sliding (we are in contact with the ground with a normal force pulling us against the center of the planet earth while a tangent force, friction, does not allow us to slide). Later we discovered that depending on the

*“The dogmas of the quiet past, are inadequate to the stormy present...”*  
Abraham Lincoln,  
annual message to Congress, December 1, 1862.

*Friction is a component of the science of tribology.*

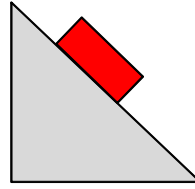


Figure 1.1: Inclined plane with friction between the two solids.

surface roughness between two bodies the “friction” could be different. For example, ice on steel has a low coefficient of friction, while rubber on pavement has a high coefficient of friction. There are two forms of friction, kinetic and static. If we try to slide two objects past each other, a small amount of force will result in no motion. In this case the force of friction is greater than the applied force. This is static friction. If we apply a little more force, the object “breaks free” and slides, although we still need to apply force to keep the object sliding. This is kinetic friction. We do not need to apply quite as much force to keep the object sliding as you needed to originally break free of static friction. An example of the static and dynamic friction is the inclined plane given in Fig. 1.1. Depending on the inclination of the plane the block will move or stay attached.

The empirical law that models friction between solids is given by

$$F_f \leq \mu F_n \quad (1.1)$$

where  $F_f$  is the force of friction exerted by each surface on the other. It is parallel to the surface, in a direction opposite to the net applied force. The constant  $\mu$ , is the coefficient of friction, which is an empirical property of the contacting materials and  $F_n$  is the normal force exerted by each surface on the other, directed perpendicular (normal) to the surface. The force of friction is always exerted in a direction that opposes movement (for kinetic friction) or potential movement (for static friction) between the two surfaces.

The friction between solids depends on several properties, but the most important is the surface roughness (Fig. 1.2) between the two ob-



Figure 1.2: Surface roughness.

jects and the possible existence of lubrication (lubrication is a technique employed to reduce wear of one or both surfaces in close proximity moving relative to each another by interposing a substance called a lubricant between the surfaces).

Friction can also have a negative effect. Although it is the principle behind the braking systems we find on our automobiles and that the

*The elementary properties of sliding (kinetic) friction were discovered by experiment in the 15th to 18th centuries and were expressed as three empirical laws:*  
**Amontons' First Law:** *The force of friction is directly proportional to the applied load.*  
**Amontons' Second Law:** *The force of friction is independent of the apparent area of contact.*  
**Coulomb's Law of Friction:** *Kinetic friction is independent of the sliding velocity.*



simple task of walking would not be possible without it, friction can also be our enemy. Friction inside a car engine and inside the wheel axes will slow a car down and wear out the engine parts. To prevent this we put oil or even grease on their surfaces (lubrication). This makes them more slippery and so reduces friction.

## 1.2 FRICTION BETWEEN A SOLID AND A LIQUID

For the interface between a solid and a liquid a powerful empirical law such as Eq. 1.1 is not available. Although for specific cases it is still possible to correctly model the slip velocity of certain fluids (Hatzikiriakos, 2012), a general function that works for all fluids is yet unavailable.

Along the years, we have witnessed an evolution of technology that is becoming more and more dependent on micro and nanostructures, in particular, on microscopic and nanoflows (an example is Microrheology (Crocker et al., 2000; Levine et al., 1975)). At the same time this technology allow us to see, and better understand, the interaction between a liquid and a solid (Neto et al., 2005), revealing that the validity of the no-slip boundary condition is compromised.

When speaking about slip velocity an important question pops to our heads:

*Do all the fluids show the same interaction with the wall?*

Although the phenomenon of slip velocity is not well understood, the answer to this question is “no”. We can think of an extreme case, a fluid with very high viscosity (almost solid) that slides (while being pushed) along a channel. Obviously, the interaction between this fluid and the wall is expected to be different from the interaction of water with the same wall.

For several decades the no-slip boundary condition has been successfully applied to model macroscopic experiments. This boundary condition states that the liquid molecules adjacent to the wall are stationary relative to the wall,

$$\mathbf{u} - \mathbf{u}_{wall} = \mathbf{0} \quad (1.2)$$

This boundary condition is empirical and as no supporting physical law (Lauga et al., 2005). The truth is that this model seems adequate for macroscopic flows of Newtonian fluids but fails for some non-Newtonian fluids (Brochard and De Gennes, 1992; De Gennes, 1979; Denn, 2001), electro-osmotic flow (Marry et al., 2003; Herr et al., 2000), flow in microfluidic devices (Gad-el Hak, 1999; Stone et al., 2004) and biological processes (Zhang et al., 2003; Beebe et al., 2002), and Gas flow (the assumption that gases may exhibit wall slip was first introduced by Maxwell (Maxwell, 1867b)). Even for Newtonian fluids new experiments gave results that question the validity of the no slip boundary condition (Pit et al., 2000; Craig et al., 2001).

*Microrheology is a technique to measure the rheological properties of a medium, such as viscosity in micron-sized systems, often involving the measurement of the trajectory of a flow tracer (a micrometre-size particle).*

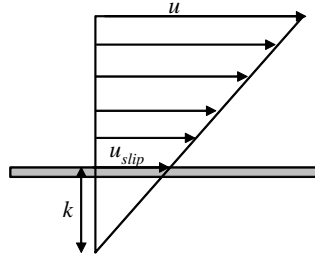


Figure 1.3: Slip length for the Navier slip law (Eq. 1.3).

### 1.2.1 Slip in Newtonian fluids

*How the no-slip boundary condition became an accepted truth (for most of us)?*

In the early experiments (Stokes, 1845), (Bernoulli, 1738), (Du Buat, 1786) and (Coulomb, 1801) all drew similar conclusions, that the fluid near the solid surface seems to have the same velocity as the surface.

In 1813, (Girard, 1813) proposed a model for the boundary condition; he believed in the formation of a thin layer of fluid attached to the wall, while the rest of the fluid would flow over this layer. If the fluid did not wet the solid surface, then the layer thickness would be zero, and the liquid would slip over the surface (such as mercury in glass tubes).

In 1822, Navier (Navier, 1822, 1823) brought to life the idea that a liquid may slip on a solid surface with the slip velocity ( $u_{slip}$ ) opposed by a frictional force proportional to the velocity gradient in the wall normal direction ( $n$ ),

$$u_{slip} = k \frac{\partial u}{\partial n} \quad (1.3)$$

the constant  $k$  was known as “slip length”, because it really represents a length (see Fig. 1.3) This simple slip boundary condition states that the velocity vector points in the tangent stress opposite direction.

This boundary condition is similar to the one given for solids (Eq. 1.1), but the Newtonian fluid has null normal stresses and therefore it is impossible to use the  $F_n$  force, instead we use the friction force as a way to allow the fluid to slip.

From this point until the 1900’s the idea that a fluid could slip along the walls was substituted by the no slip boundary condition. Poisson (Poisson, 1831, 1832) still proposed the use of the Navier slip boundary condition but in 1840 Stokes was asked to investigate the nature of boundary conditions and he adopted the theory of Bernoulli instead of the Navier slip boundary condition. In the next years there were some efforts to understand the existence of slip velocity, (Poiseuille, 1844), (Darcy, 1857), (Helmholtz, 1860). In the beginning of the 20th century (Maxwell, 1890), (Whetham, 1890), (Couette, 1890) and (Ladenburg, 1907) all agreed with the no-slip boundary condition. The experimental

work did not stop, and the results obtained agreed with the no-slip boundary condition. Technology could not deal with such small scales and consequently the slip boundary condition was becoming obsolete.

The fact that most of the books published on the subject of fluid dynamics present the no-slip boundary condition as a law, not providing the correct history and evolution of this assumption (that is still under debate), together with the knowledge gained with our common sense lead to the disappearance of any doubts regarding the validity of the no-slip boundary condition.

There are exceptions, though, such as the book by (Goldstein, 1965), where it is stated that:

*“At the present time it appears to be definitely settled that for practical purposes the fluid immediately in contact with a solid body may be taken as having no velocity relative to the solid, at any rate for nearly all fluids; but the exact conditions on a molecular scale remain still in doubt”,*

the classic book by (Lamb, 1932) where we can read:

*“It appears probable that in all ordinary cases there is no motion, relative to the solid, of the fluid immediately in contact with it. The contrary supposition would imply an infinitely greater resistance to the sliding of one portion of the fluid past another than to the sliding of the fluid over a solid.”*

or the book by (Batchelor, 2000) where the following two paragraphs are provided with a detailed discussion of the subject. Batchelor first states that:

*“...there being some doubt about whether molecular interactions at such an interface lead to momentum transfer of the same nature as that at a surface in the interior of a fluid...”*

which alerts for another possibility than the no-slip velocity, but then he says:

*“...but the absence of slip at a rigid wall is now amply confirmed by direct observations and by the correctness of its many consequences under normal conditions.”*

We can also say that  $u = 0$  is attractive to the eye and there is a wealth of studies regarding the wellposedness of differential equations using this Dirichlet boundary condition. Notice also that if we had to choose between  $u = 0$  and  $u = 0.000007861$  (a random number) we would prefer  $u = 0$  based on our common sense.

At the end of the 20th century we assist to the rapid growth of micro and nanofabrication. This provides the means for new experiments that revive once again the existence of slip velocity and its dependence on surface roughness, dissolved gas and bubbles, wetting, shear rate, electrical properties and pressure. The search for the correct boundary condition is a current topic of research. For a review on this subject the excellent papers by (Lauga et al., 2005) and (Neto et al., 2005) are advised.

**Nanotechnology** is a part of science and technology about the control of matter on the atomic and molecular scale - this means things that are about 100 nanometers or smaller. “Nano” means one-billionth of meter.

**Microfluidics** deals with the behavior, precise control and manipulation of fluids that are geometrically constrained to a small, typically sub-millimeter, scale, and emerged in the beginning of the 1980s.

### 1.2.2 Slip in Non-Newtonian fluids

As mentioned before, the behavior of Newtonian and non-Newtonian fluids is different on account of the different types of molecules involved with consequent modifications in the wall boundary conditions.

In the following discussion only polymer melts will be considered. For slip regarding other types of non-Newtonian fluids the work of (Archer, 2005) is advised.

#### 1.2.2.1 Extrusion Process

The extrusion process (see Fig. 1.4) basically consists of creating objects of a constant cross-sectional profile. The material is pushed or drawn through an extrusion die of the desired cross-section. The die assumes the shape of a block with depth, and its internal shape changes along its length, usually, from a circular to the a cross-section similar to the one of the profile to be produced (a part of this thesis is dedicated to study the influence of slip velocity inside the die geometry).

Commonly extruded materials include metals, polymers, ceramics, concrete and food stuffs.

**Extrusion:** the act or process of pushing or thrusting out.

In 1797, Joseph Bramah patented the first extrusion process for making lead pipe. It involved preheating the metal and then forcing it through a die via a hand driven plunger. In 1820, Thomas Burr constructed the first hydraulic powered press. In 1894, Alexander Dick expanded the extrusion process to copper and brass alloys.

The first thermoplastic extrusion was in 1935 by Paul Troester in Germany. Shortly after, Roberto Colombo developed the first twin screw extruders in Italy.

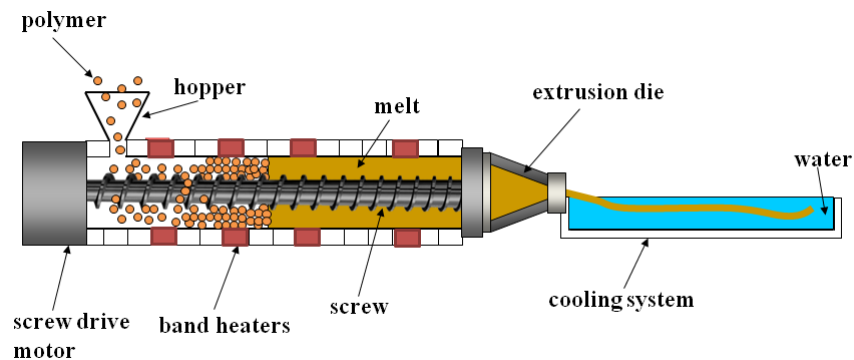


Figure 1.4: Extrusion process for polymer melts

For the polymer melts extrusion process (see Fig. 1.4), thermoplastic material in the form of small beads is gravity fed from a top mounted hopper into the barrel of the extruder. The rotation of the screw forces the material forward along the extruder and the presence of band heaters forces the material to melt. At the end a cooling system is used to ensure the final shape is not altered.

A real extrusion die used for the production of woodplastic composites, can be seen in Fig.1.5.

#### 1.2.2.2 Wall Slip in Polymer Melts

The presence of apparent wall slip in polymer melts was first given in 1961 by (Rielly and Price, 1961) and it consisted of an experiment with high density polyethylene (HDPE) and the use of colored wax

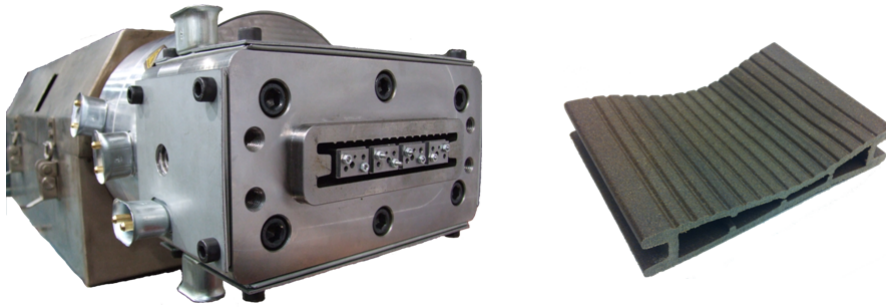


Figure 1.5: Extrusion die for the production of deck together with a sample of the extruded profile.

crayon marks in the interior face of the extruder channel. Benbow and Lamb, 1963 performed a variety of experimental works using different polymers and die materials, and, using again colored markers. They concluded that the unstable flow is connected to the existence of slip velocity along the die wall, slip velocity depends on the material from which the die is constructed, they also suggested the existence of a slip-tick regime and the dependence of slip velocity on some critical stress value.

Extrusion instabilities were first reported during World War II in 1945 (Denn, 2001) and in 1976, Petrie and Denn reviewed extensively these flow instabilities (Fig. 1.6).

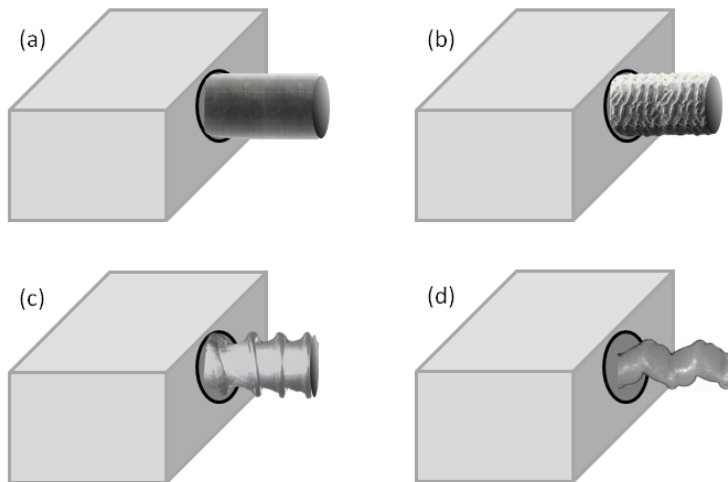


Figure 1.6: Extrusion instabilities. (a) stable (b) sharkskin (c) slip-stick (d) gross melt fracture.

These instabilities, or at least part of them, are assumed to be associated with the slip velocity ((Kalika and Denn, 1987)); also, the flow curve for an apparent shear rate versus the wall shear stress in a controlled-throughput experiment shows a discontinuity, usually attributed to the onset of wall slip (see Fig. 1.7). Polymer melts are known to show a sudden increase in flow rate above a critical pressure drop, in controlled stress capillary flow. These polymer melts also

*In Fig. 1.5 we see a sample of an extruded profile, and we notice that this profile is not perfect (it was the first attempt to produce that kind of profiles). This means that the extrusion process is still based on a tentative procedure, where a trial and error methodology is used before reaching the final product.*

show diameter dependence and slip-stick oscillations in controlled flow rate capillary flow (Joshi et al., 2000).

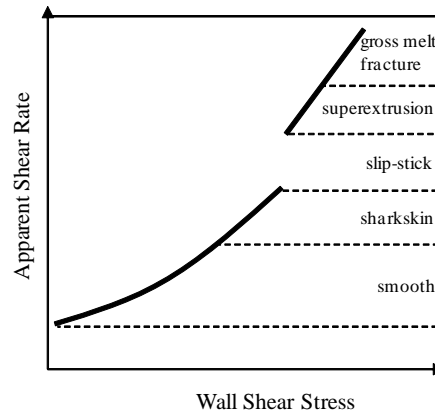


Figure 1.7: Typical flow curve of a linear polymer (obtained with a capillary rheometer).

From Fig. 1.7 we see that the surface of the extrudate initially is smooth and then becomes visibly rough at an higher value of the wall shear stress. This phenomenon is commonly referred as sharkskin (apparent periodicity in the small-amplitude distortion). At a higher level of stress the flow becomes slip-stick. At still higher stress levels, sometimes the extrudate surface is relatively smooth (“superextrusion” is not represented in Fig. 1.6) during the early part of this steady regime, with the appearance of gross melt fracture at higher stresses. This behavior is common for linear polymers (see (El Kissi and Paiu, 1990) ).

The association of sharkskin with the presence of slip velocity gained strength in 1986 with the remarkable experiment of Ramamurthy. He showed that the flow instabilities that occur during the extrusion of linear polymers can be suppressed if instead of chrome-plated stainless steel die an  $\alpha$ -brass die is used. Although the experiment was excellent, his conclusions were controversial. He believed that the  $\alpha$ -brass die was removing the ability of the fluid to slip while the results from other research groups suggested the opposite.

Until today, several other studies regarding the influence and origin of slip velocity have been made, but the conclusions are similar to the ones obtained earlier.

As for Newtonian fluids, the slip boundary condition for the non-Newtonian fluids also depends on several properties such as surface roughness, tangent stress, normal stress, temperature, energy, type of fluid, type of wall material. In order to model the slip velocity data obtained by experimental works, several models have been proposed. Most of the models are static, however there are experiments showing that the slip velocity may depend on the past states of the local tangent and normal stresses. For a review of this models the works of Archer

(Archer, 2005) (static) and Hatzikiriakos (Hatzikiriakos, 2012) (static and dynamic) should be consulted.

Static models are those that are going to be used in this thesis. They evolved from a simple Navier slip to the nonlinear Navier slip boundary condition, where the slip length also depends on the tangent stress. More sophisticated models for slip have been proposed during the years, that basically include the contribution from normal stresses, temperature and other properties.

### 1.2.3 Objectives

The aim of this thesis is the investigation of the effects of slip boundary conditions on a wide range of fluid flows, with application to the extrusion process, microfluidics and electro-osmotic flow. The objectives are the following:

- Derive analytical solutions for Newtonian and non-Newtonian fluids with slip boundary conditions. For the cases where an explicit formula is not possible, the existence and uniqueness of the solution must be proved;
- Derive analytical solutions for electro-osmotic flow under the influence of slip boundary conditions;
- Study the influence of the slip velocity on the development length of Newtonian and non-Newtonian fluids;

Other objectives are formulated as questions that will be answered along the thesis and at the conclusions Section.

- Is it possible to implement slip boundary conditions in the finite volume method framework and what are its limitations?
- Is it possible to use slip boundary conditions as a method to improve the limits of convergence associated with the High Weissenberg Number Problem (HWNP)?
- Is the presence of slip velocity always helpful during the extrusion process?

All this objectives/questions are pertinent and the answers are still missing in the literature. The main objective of this thesis is to obtain further improvements for the understanding of the slip physical phenomenon.

### 1.2.4 Dissertation Outline

The present study is a theoretical and numerical numerical study of slip flows. For the numerical implementation of the slip boundary

conditions a three-dimensional time dependent finite volume code (developed by (Oliveira et al., 1998), with improvements described later in (Oliveira and Pinho, 1999b) and (Alves et al., 2000)) was used.

This thesis is divided into six main parts and is built with published, submitted and “to be submitted” papers.

**PART I:** To slip or not to slip: that is the question

An introduction to the subject of slip velocity in Newtonian and non-Newtonian fluids is made.

**PART II:** Mathematical Modelling

The mathematical modelling of fluid flow is explained together with a brief description on the type of the numerical methods used to solve the system of partial differential equations.

**PART III:** Analytical studies of flows under slip

Two papers are presented with analytical solutions for Newtonian, inelastic non-Newtonian and viscoelastic non-Newtonian fluids under the influence of different types of slip boundary conditions. Four different slip models are used, most of them nonlinear. In the cases where a closed form solution is not possible the proof of existence and uniqueness of the simple analytical solution is provided (this way a basic numerical method can be used to find the solution in the provided range). These solutions are helpful for theoretical purposes and for the validation of numerical codes.

**PART IV:** Numerical studies of flows under slip

Six papers are presented. The first two, concern the implementation of slip boundary conditions in the finite volume method (FVM) and a study of the slip-stick flow through a geometry with a singular point. In the first paper the same slip models of Part III are used, and a detailed explanation of three different methods of implementation is presented. The second paper is based on two other slip models and investigates the effect of slip velocity on the singularity of a slip-stick geometry.

The third and fourth papers investigate flow development in channel flow and specifically look at the development length for Newtonian and non-Newtonian fluids under the influence of the Navier slip boundary condition. For the Newtonian fluids a correlation for the development length is presented as a function of the Reynolds number and the slip coefficient of the linear Navier slip model. This has a practical application in microfluidics. The other paper concerns viscoelastic fluids (the viscoelastic model used is the Upper Convected Maxwell, UCM) and has practical application in the extrusion process.

The last two papers of this part, present numerical simulations of flows through abrupt expansions and contractions under the influence



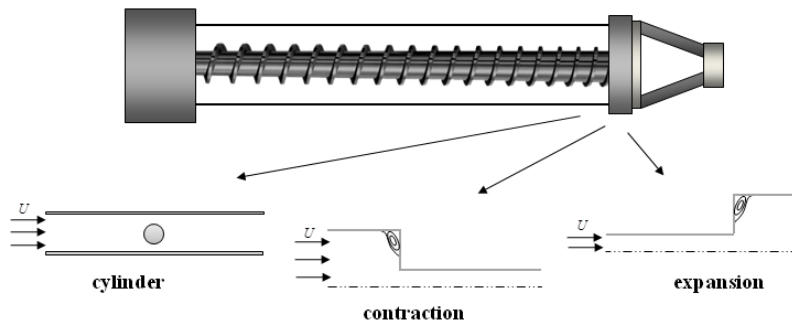


Figure 1.8: Type of geometries that can be found in the extrusion process.

of linear and nonlinear Navier slip boundary conditions. These geometries are easily found in flow channels employed in the extrusion process (c.f. Fig. 1.8) and the results are relevant to understand the fluid flow inside an extruder, and to study its influence upon the final shape of the extruded profile. From the results obtained we we noticed that the recirculation zone increases with the slip velocity for the 4:1 contraction flow, and decreases (or even vanishes) for the expansion flow.

#### PART V: Electro-Osmotic flow

Two papers analytically investigate electro-osmotic/pressure driven flows for viscoelastic fluids under the influence of slip boundary conditions. The first paper is about symmetric flow in a channel while the second paper concerns asymmetric wall conditions. This work is usefull because it gives the possibility of modeling the apparent slip velocity characteristic of the electro-osmotic flows, with the linear and nonlinear Navier slip laws.

#### PART VI: Conclusions and Outlook

In this last part of the thesis, the questions proposed as objectives are answered together with the possibilities of a future work.



Part II

MATHEMATICAL MODELLING



[...] *It would be better for the true physics,;  
if there were no mathematicians on earth. [...]*

— Daniel Bernoulli

There are two major steps when modelling physical phenomena. The first step is to find the mathematical model that reproduces (we hope) what we are trying to model, and the second step is to solve the mathematical equations (or else we will not know whether the model is correct). Usually these models are complex and difficult (if not impossible) to solve analytically, therefore a numerical procedure must be adopted. We can also try to find analytical solutions for specific fluids and geometries, but in this way the model will not be helpful predicting the behavior of the physical phenomena for different geometries and flows.

## 2.1 NEWTONIAN AND NON-NEWTONIAN FLUIDS

### 2.1.1 *What is a fluid?*

All the material in the universe (that follows the conservation laws of physics) can be classified as either, solid, liquid or gas. The key distinction between fluids and solids is their resistance to change shape. If a normal force is applied, both deform proportionally to the compressive force, but if a tangential force is applied, the fluid cannot sustain a finite deformation under the action of this shear force.

Suppose there is a small portion of fluid between two parallel plates (Fig. 2.1) and that a generic stress is applied to the upper plate (Couette flow). Then we expect the stress to be proportional to the constant velocity of the plate,  $U$ , and inversely proportional to  $H$  through a constant, designated dynamic viscosity,  $\mu$ , in such way that  $\tau = \mu \frac{U}{H}$ . If we think of two very thin and close layers of fluid with different directions than we would expect a tangent stress between the two surfaces of fluid given by,

$$\tau = \mu \frac{du}{dy} \quad (2.1)$$

where  $du$  is the difference of velocity while  $dy$  is the distance between the two layers. In a more general framework this equation is written

*Any continuous medium can be subject to two different types of forces, body (such as gravity) and surface forces (act on the surface of the medium). If we think of a force  $F$  acting on the surface (area of the surface= $S$ ) of an object, then the average stress,  $\tau$ , is given by  $\tau = \frac{F}{S}$ . The normal stress point in the normal vector direction and the tangent stress points in the tangent direction for a chosen point of the surface.*



Figure 2.1: Schematic of a Couette flow.



Figure 2.2: Shear stress variation.

as  $\boldsymbol{\tau} = \mu \left( \nabla \mathbf{u} + (\nabla \mathbf{u})^T \right) = 2\mu \mathbf{D}$ . The tensor  $\mathbf{D} = \frac{1}{2} \left( \nabla \mathbf{u} + (\nabla \mathbf{u})^T \right)$  is known as the deformation tensor.

Notice that at Fig. 2.1 the orange line represents a dye line that was injected in the flow. When the upper plate moves the line moves linearly with the flow. The friction between the several layers of fluid (viscosity) is constant.

Suppose now that we have a vessel filled with glycerin and that we carefully inject an orange line of dye, as shown in Fig. 2.2. If we place a block at the free surface of the glycerin and then move the block to the right, a nonlinear dye line is obtained. This happens because now we do not have a Couette flow anymore, the stress is not constant, and decreases as we move away from the free surface.

Viscosity is perhaps the most importante property of a fluid. It does not only describes the nature of the fluid (wether it is Newtonian or not), but predicts the behavior of the shear stress with respect to the rate of the angular deformation of the fluid. We know a great deal about the fluid if we know its viscosity.

### 2.1.2 Newtonian fluids

The Navier-Stokes equations were first proposed in 1822 by Navier. The equations of motion were independently rederived by Cauchy in 1828 and by Poisson in 1829, and in 1843 Barre de Saint-Venant published the derivation of the equations for both laminar and turbulent flows. It was George Gabriel Stokes, in 1845, that derived the equations in a manner that we still use today, and because of that he earned his place in the equation's name.

The system of differential equations that governs the fluid flow is given by,

$$\begin{aligned}\rho \frac{\partial \mathbf{u}}{\partial t} + \rho \nabla \cdot \mathbf{u} \mathbf{u} &= -\nabla p + \nabla \cdot \boldsymbol{\tau}, & \text{on } [0, T] \mathbb{R}^n \\ \frac{\partial \rho}{\partial t} + \nabla \cdot \rho \mathbf{u} &= 0, & \text{on } [0, T] \times \mathbb{R}^n \\ \mathbf{u}_{t=0} &= \mathbf{u}_0, & \text{on } [0, T] \times \mathbb{R}^n\end{aligned}\quad (2.2)$$

where  $\mathbf{u}$  is the velocity vector,  $p$  is the pressure,  $\rho$  is the density and  $\boldsymbol{\tau} = \mu \left( \nabla \mathbf{u} + (\nabla \mathbf{u})^T \right) + \left( \frac{2}{3} \nabla \cdot \mathbf{u} \right) \mathbf{I}$  is the deviatoric stress tensor ( $\mu$  is the viscosity). The first and second equations are the momentum (Cauchy equation of motion) and continuity equation, respectively. The substitution of the deviatoric stress tensor into the momentum equation gives the Navier-Stokes equations. Notice that this system of differential equations works for compressible fluids. For incompressible fluids, like the ones studied in this thesis,  $\nabla \cdot \mathbf{u} = 0$ .

These governing equations work well for Newtonian fluids such as water, glycerin, kerosene, milk, sugar solution, mineral oil, etc.

When thinking about a numerical procedure for solving this system of equations we notice that there is no evolution equation for the pressure,  $p$ . It seems we have four equations for the three velocity components, and there is no time derivative for the pressure. The idea is then to remove the pressure from the momentum equation by finding a relation between the velocity and pressure,  $p(\mathbf{u})$ , and transform the continuity equation in an evolution equation for  $p$ .

If we substitute  $\boldsymbol{\tau} = \mu \left( \nabla \mathbf{u} + (\nabla \mathbf{u})^T \right)$  in Eq. 2.2, the momentum equation can be rewritten as,

$$\rho \frac{\partial \mathbf{u}}{\partial t} + \rho \nabla \cdot \mathbf{u} \mathbf{u} = -\nabla p + \mu \Delta \mathbf{u} \quad (2.3)$$

If we compute the partial derivative  $\partial_{x_k}$  of the Navier-Stokes equations, we obtain the following componentwise equation,

$$\rho \left( \left( u_{x_k}^i \right)_t + u^j \left( u_{x_k}^i \right)_{x_j} + u_{x_k}^j u_{x_j}^i \right) = -p_{x_i x_k} + \mu \left( u_{x_k}^i \right)_{x_j x_j} \quad (2.4)$$

By introducing the notation  $\mathbf{U} \equiv (u_{x_k}^i)$  and  $\mathbf{P} \equiv (p_{x_i x_k})$  for the Hessian matrix of  $p$ , we obtain the following equation,

$$\frac{D\mathbf{U}}{Dt} + \mathbf{U}^2 = -\mathbf{P} + \mu \Delta \mathbf{U} \quad (2.5)$$

By taking the trace of this equation and based on the fact that  $tr[\mathbf{U}] = \nabla \cdot \mathbf{u} = 0$  we get,

$$\frac{D(\nabla \cdot \mathbf{u})}{Dt} + tr[\mathbf{U}^2] = -\Delta p + \mu \Delta(\nabla \cdot \mathbf{u}) \quad (2.6)$$

that results in a Poisson equation,

$$-\Delta p = tr[\nabla \mathbf{u}]^2 \quad (2.7)$$

*A Newtonian fluid (named after Isaac Newton) is a fluid whose stress versus strain rate curve is linear and passes through the origin. The constant of proportionality is known as the viscosity.*

**Lemma:** Let  $f \in \mathbb{R}^n$  be a smooth function vanishing when  $|x| \rightarrow \infty$  then the solution  $v$  to the Poisson equation  $\Delta v = f$  with  $\nabla v$  vanishing as  $|x| \rightarrow \infty$ , is given by  $v(x) = \int_{\mathbb{R}^n} N(x-y) f(y) dy$ , with  $N(x) = (2\pi)^{-1} \ln|x|$  if  $N = 2$  and  $N(x) = ((2-N)\omega)^{-1} |x|^{2-N}$  if  $N \geq 3$ .  $\omega$  is the surface area of a unit sphere in  $\mathbb{R}^n$ .

We now have more equations than variables.

Based on the Lemma on the right, Eq. 2.7 can be used to obtain  $p$  and then differentiating under the integral to obtain  $\nabla p$ ,

$$\nabla p(x, t) = C_N \int_{\mathbb{R}^n} \frac{x-y}{|x-y|^N} \text{tr} [\nabla \mathbf{u}(y, t)]^2 dy \quad (2.8)$$

The Navier-Stokes equation can now be written as,

$$\frac{D\mathbf{u}}{Dt} = -C_N \int_{\mathbb{R}^n} \frac{x-y}{|x-y|^N} \text{tr} [\nabla \mathbf{u}(y, t)]^2 dy + \mu \Delta \mathbf{u} \quad (2.9)$$

The most remarkable thing about Eq. 2.9 is that its solution already verifies the continuity equation (Majda and Bertozzi, 2001) and the pressure can be recovered from Eq. 2.7.

For the numerical solution of the Navier-Stokes equations a similar technique is used to obtain an equation for the pressure,  $p$ . An iterative procedure is then used between the discretized version Eqs. 2.3 and 2.7 until pressure and velocity verifies both equations (the restriction  $\nabla \cdot \mathbf{u} = 0$  is automatically verified).

### 2.1.3 Non-Newtonian fluids (inelastic)

Although the simulations of Newtonian fluids are of great interest, we are interested in a broader range of materials, as the ones where the shear viscosity is not constant, being dependent on shear rate, temperature and time.

Depending on how viscosity changes with time the flow behavior is characterized as thixotropic (time thinning, i.e. viscosity decreases with time) or rheopetic (time thickening, i.e. viscosity increases with time) Thixotropic fluids are quite common while rheopetic fluids are very rare (examples: thixotropic: yogurt, paint, rheopetic: gypsum paste).

Depending on how viscosity changes with shear rate the flow behavior is characterized as:

shear thinning - the viscosity decreases with increased shear rate.

shear thickening - the viscosity increases with increased shear rate.

plastic - exhibits a so-called yield stress value, i.e. a certain stress must be applied before flow occurs. Shear thinning fluids are also called pseudoplastic and shear thickening fluids are also called dilatant.

Examples of shear thinning fluids are, polymer melts, paints, shampoo and ketchup. Examples of shear thickening fluids are wet sand and suspensions. Examples of plastic fluids are tooth paste and hand cream.



The easiest way to implement this feature of the viscosity into the Navier-Stokes equation is to define the viscosity as a function of parameters such as temperature, shear rate and time.

For inelastic fluids remains valid a relation of the form  $\boldsymbol{\tau} = 2\mu\mathbf{D}$ , but, with a varying viscosity that must be a tensor of rank zero, a scalar. This is only possible if the viscosity is a function of the invariants of  $\mathbf{D}$ . For the case of simple shear flow only the second invariant,  $II_D = \frac{1}{2} \left[ (tr\mathbf{D})^2 - tr\mathbf{D}^2 \right]$  does not vanish, and the viscosity function can be written as  $\mu(II_D)$ . This explains why this model is only suitable for simple shear flows.

Two well known viscosity functions are the “power law” (created by Ostwald and de Waele) and the Carreau models.

The power law model is given by

$$\mu(\dot{\gamma}) = a\dot{\gamma}^{m-1} \quad (2.10)$$

with  $a$  and  $m$  ( $m = 1$ : Newtonian fluid,  $0 < m < 1$ : shear thinning,  $m > 1$ : shear thickening) empirical parameters. For  $0 < m < 1$ , if  $\dot{\gamma} \rightarrow \infty$  then  $\mu(\dot{\gamma}) \rightarrow 0$  (while in reality  $\mu(\dot{\gamma}) \rightarrow \mu_0$ ) and for  $m > 1$  if  $\dot{\gamma} \rightarrow 0$  then  $\mu(\dot{\gamma}) \rightarrow \infty$  (while in reality  $\mu(\dot{\gamma}) \rightarrow \mu_\infty$ ).  $\mu_0$  and  $\mu_\infty$  are the so-called zero-shear-rate viscosity and infinite shear rate viscosity, respectively.

The Carreau model is a more complex model that already accounts for these features of the Non-Newtonian fluids. It is given by,

$$\mu(\dot{\gamma}) = \mu_\infty + (\mu_0 - \mu_\infty) \left[ 1 - (\lambda\dot{\gamma})^2 \right]^{\frac{m-1}{2}} \quad (2.11)$$

Here,  $\mu_0$ ,  $\mu_\infty$ ,  $\lambda$  and  $m$  are constant parameters which are determined by experimental investigations and that characterize the fluid. For both models  $\dot{\gamma} = \sqrt{-4II_D}$

These fluids are known as “generalized Newtonian fluids”. Because they only describe well simple shear flows, they are not suitable for flows where the elastic effects are relevant (for example extensional flows), and new constitutive equations must be used.

#### 2.1.4 Non-Newtonian fluids (viscoelastic)

The different behavior observed in Newtonian and viscoelastic fluids can be illustrated with two well known examples: the die swell and the rod climbing phenomena (Fig. 2.3).

When a rotating rod is brought into a polymer melt or concentrated polymer solution, the meniscus climbs the rod. This is due to the normal stresses and is thus a purely non-Newtonian effect. Die swell is an instance where a non-Newtonian fluid stream is compressed by entrance into a die, and is followed by a partial recovery or “swell”

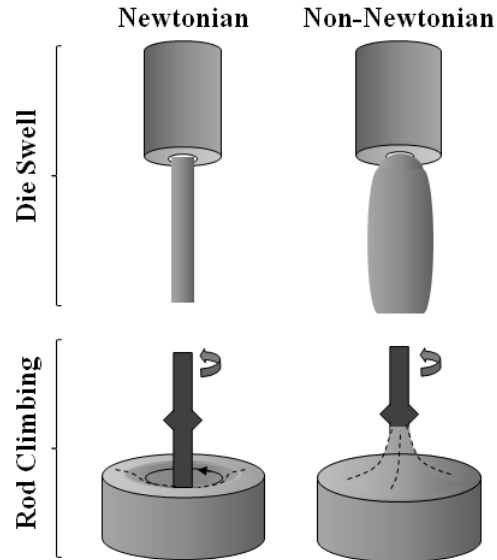


Figure 2.3: Die swell and rod climbing.

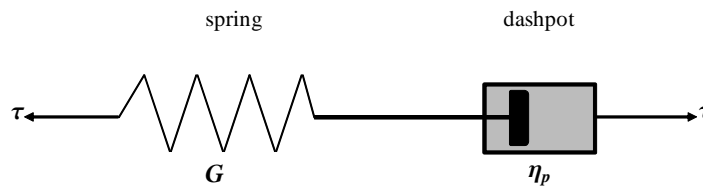


Figure 2.4: Mechanical model that represents the behavior of a Maxwell fluid.

back to the former shape and volume of the the fluid after exiting the die.

The key features of viscoelastic fluids, is the existence of relaxation and retardation times. When we apply a stress to a Newtonian fluid the response is instantaneous (the relaxation time is zero). On the other hand, if we have a viscoelastic fluid, the response will have a delay (the relaxation time is different from zero) (Gurtin, 1981; Majda and Bertozzi, 2001; Phan-Thien, 2002).

Maxwell proposed a viscoelastic model that couples two properties of the viscoelastic fluids, elasticity and viscosity. To represent the mechanical equivalent of this model we can assume a spring (elasticity) connected to a dashpot (viscosity), with both objects subject to the same stress (c.f. Fig. 2.4).

For quick deformations the fluid behaves as a Hookean elastic solid with modulus of elasticity  $G$ , for small deformations the fluid behaves as a Newtonian fluid. For solids, the stress is given by a constant ( $G$ ) times the deformation (strain)  $\tau = G\gamma_e$ , while for a liquid, the deformation can be infinite so the measure “deformation” is of no use, the rate of deformation ( $\dot{\gamma}_v$ ) is used instead,  $\tau = \eta_p \dot{\gamma}_v$ . The total rate of deformation is given by  $\dot{\gamma} = \dot{\gamma}_e + \dot{\gamma}_v$  meaning that,

$$\frac{1}{G} \frac{d\tau}{dt} + \frac{\tau}{\eta_p} = \dot{\gamma} \quad (2.12)$$

Integration (simple integration and then integration by parts) of this equation leads to,

$$\tau(t) = \int_{-\infty}^t \frac{\eta_p}{\lambda^2} \exp\left(-\left(\frac{t-s}{\lambda}\right)\right) \gamma(s) ds \quad (2.13)$$

This equations shows that the stress at a certain moment depends on the strain history. The function that controls this dependence is the memory function  $\frac{\eta_p}{\lambda^2} \exp\left(-\left(\frac{t-s}{\lambda}\right)\right)$ , with  $\lambda = \frac{\eta_p}{G}$  being called the relaxation time. It tells us that the further we move back in time, the less the strain contributes to the actual stress.

A parameter which is used to measure the influence of the relaxation time is the Deborah number ( $De$ ). It is defined as the ratio between the characteristic relaxation of the fluid and the time length of the observed phenomenon (*time*),

$$De = \frac{\lambda}{time} \quad (2.14)$$

Eq. 2.12 can be rewritten using a general framework based on tensors as ,

$$\boldsymbol{\tau} + \lambda \frac{d\boldsymbol{\tau}}{dt} = \eta_p \dot{\boldsymbol{\gamma}} \quad (2.15)$$

This model was proposed by (Maxwell, 1867a) to study the possible viscoelasticity of gases.

This model does not respect the conditions proposed by (Oldroyd, 1950), therefore, Oldroyd proposed a correction, the substitution of  $\frac{d\boldsymbol{\tau}}{dt}$  by the upper convected derivative,

$$\overset{\nabla}{\boldsymbol{\tau}} \equiv \frac{d\boldsymbol{\tau}}{dt} + \nabla \cdot \mathbf{u} \boldsymbol{\tau} - \boldsymbol{\tau} \cdot \nabla \mathbf{u} - (\nabla \mathbf{u})^T \cdot \boldsymbol{\tau} \quad (2.16)$$

giving an equation of the form,

$$\boldsymbol{\tau} + \lambda \overset{\nabla}{\boldsymbol{\tau}} = \eta_p \dot{\boldsymbol{\gamma}} \quad (2.17)$$

named Upper Convected Maxwell (UCM) model.

Later, Oldroyd proposed a similar model, based on the Jeffreys (1924) model. Jeffrey's "added another dashpot" to the UCM model, as seen in Fig. 2.5 . The constitutive equation can be written as,

$$\boldsymbol{\tau} + \lambda \frac{d\boldsymbol{\tau}}{dt} = \eta_p \left( \dot{\boldsymbol{\gamma}} + \lambda_r \frac{d\dot{\boldsymbol{\gamma}}}{dt} \right) \quad (2.18)$$

where  $\boldsymbol{\tau} = \boldsymbol{\tau}_p + \boldsymbol{\tau}_s$  ,  $\eta_0 = \eta_s + \eta_p$  and  $\lambda_r = \lambda \frac{\eta_s}{\eta_0}$ .

Again, this model does not respect the conditions proposed by (Oldroyd, 1950), and Oldroyd, proposed the Oldroyd-B model,

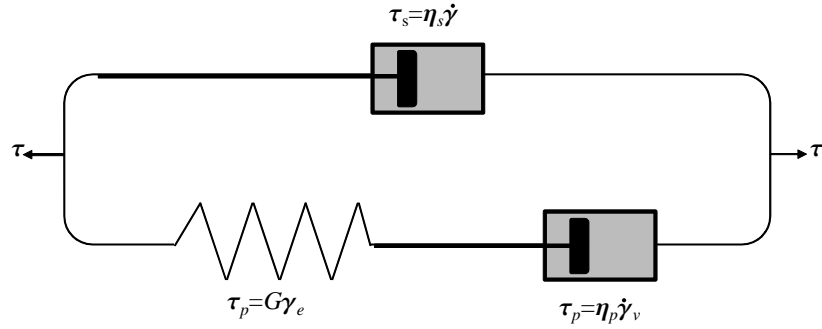


Figure 2.5: Mechanical model that represents the behavior of a Jeffrey fluid.

$$\boldsymbol{\tau} + \lambda \overset{\nabla}{\boldsymbol{\tau}} = \eta_p \left( \dot{\boldsymbol{\gamma}} + \lambda_r \overset{\nabla}{\dot{\boldsymbol{\gamma}}} \right) \quad (2.19)$$

Both UCM and Oldroyd-B models predict a zero second normal stress difference.

The normal stress differences are given by: first normal stress difference  $N_1 = \tau_{yy} - \tau_{xx}$  and second normal stress difference  $N_2 = \tau_{zz} - \tau_{yy}$ .

Constitutive equations can also be derived from molecular theory. In order to improve the modelling and the prediction of normal stress differences, the PTT model, proposed by (Phan-Thien and Tanner, 1977), was based on molecular networks and predicts a negative second normal stress difference, in agreement with experimental results. The model depends on the first invariant of the stress tensor (the trace of the tensor) and is given by,

$$\begin{aligned} \boldsymbol{\tau} &= \boldsymbol{\tau}_p + \boldsymbol{\tau}_s \\ \boldsymbol{\tau} &= \eta_s \left( \nabla \mathbf{u} + (\nabla \mathbf{u})^T \right) \\ f(\text{tr} \boldsymbol{\tau}_p) \boldsymbol{\tau}_p + \lambda \overset{\nabla}{\boldsymbol{\tau}}_p + \frac{\zeta}{2} \lambda (\dot{\boldsymbol{\gamma}} \cdot \boldsymbol{\tau}_p + \boldsymbol{\tau}_p \cdot \dot{\boldsymbol{\gamma}}) &= \eta_p \dot{\boldsymbol{\gamma}} \end{aligned} \quad (2.20)$$

with

$$f(\text{tr} \boldsymbol{\tau}_p) = 1 + \frac{\lambda \varepsilon}{\eta_p} \text{tr} \boldsymbol{\tau}_p \quad (2.21)$$

as given in the original version, or

$$f(\text{tr} \boldsymbol{\tau}_p) = \exp \left( \frac{\lambda \varepsilon}{\eta_p} \text{tr} \boldsymbol{\tau}_p \right) \quad (2.22)$$

proposed later by (Phan-Thien, 1978).

The model has five parameters,  $\lambda$ ,  $\eta_s$  and  $\eta_p$ , which are the relaxation time, solvent viscosity and polymer viscosity,  $\varepsilon$  is a parameter that eliminates the singularity in the extensional viscosity and  $\zeta$  is related to the fluidity of the molecular network.

Several other models have been proposed along the years to model accurately specific fluids. In spite of all these developments, there is still no general model which is able to predict the behavior of all types

of fluid. For more information on constitutive equations the works by (Larson, 1999; Phan-Thien, 2002) are advised.

### 2.1.5 Electro-osmotic flow

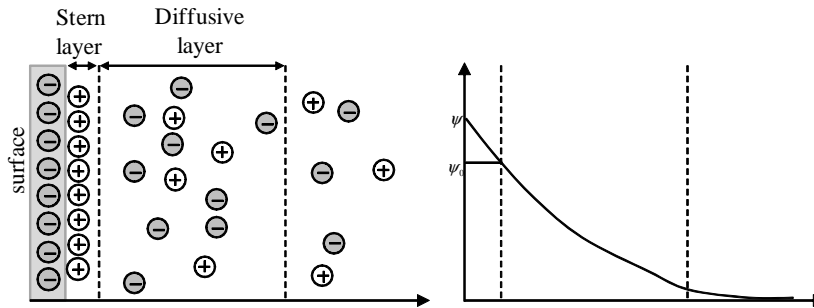


Figure 2.6: (a) Schematic of the ions distribution near a charged wall. (b) Variation of the potential,  $\psi$ , with the distance from the wall.

Electroosmotic flow is the motion of liquid induced by an applied potential across a porous material, capillary tube, membrane, microchannel, or any other fluid conduit. It was first reported in 1809 by F.F. Reuss in the Proceedings of the Imperial Society of Naturalists of Moscow. He showed that water could be made to flow through a plug of clay by applying an electric voltage. Clay is composed of closely packed particles of sand and other minerals, and water flows through the narrow spaces between particles just as it would through a narrow glass tube.

One of the most significant effects of the charged surface (Fig. 2.6) is the attraction of ions with opposite sign of the charge (counter-ions) and the repulsion of the ions with the same sign (co-ions). Near the charged wall we can distinguish two different types of layers. The first layer is called Stern layer and is composed of counter-ions. At zero absolute temperature the counter-ions would screen the charged wall, but due to thermal fluctuations the screening is only partial. The second layer is called diffusive layer where the ions have the ability to move around freely. The different concentrations of counter-ions and co-ions leads to the creation of a varying potential field  $\psi$  (see Fig. 2.6).

These two layers near the wall form what is called the Electrical Double Layer (EDL). If we assume a flow between parallel plates with charged walls and the existence of a current potential difference between two electrodes at the inlet and outlet, then an electric field is generated that exerts a body force on the counter-ions of the EDL, which move along the channel dragging the neutral liquid core.

The governing equations for this type of flow are given by,

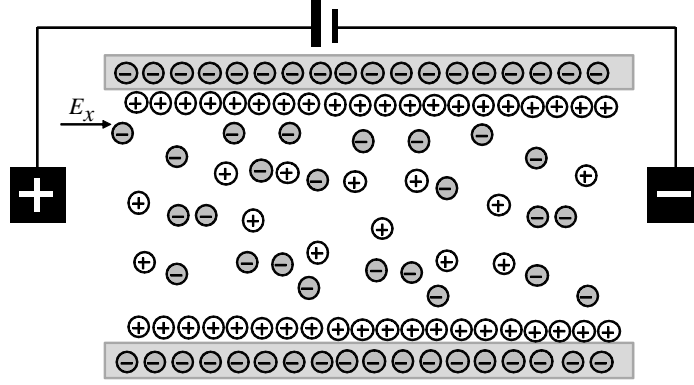


Figure 2.7: Schematic representation of electro-osmotic flow in a microchannel.

$$\begin{aligned}
 -\nabla p + \nabla \cdot \boldsymbol{\tau} + \rho_e \mathbf{E} &= \mathbf{0}, & \text{on } [0, T] \mathbb{R}^n \\
 \nabla \cdot \mathbf{u} &= 0, & \text{on } [0, T] \times \mathbb{R}^n \\
 \mathbf{u}_{t=0} &= \mathbf{u}_0, & \text{on } [0, T] \times \mathbb{R}^n
 \end{aligned} \tag{2.23}$$

where  $\boldsymbol{\tau}$  is the polymeric extra stress tensor and  $\rho_e \mathbf{E}$  represents a body force per unit volume, where  $\mathbf{E}$  is the applied external electric field and  $\rho_e$  is the net electric charge density in the fluid.

In this thesis we propose the use of slip boundary conditions to model the slip zone between the ions that can move freely and those attached to the charged surface.

## 2.2 COMPUTATIONAL FLUID DYNAMICS

Predicting the future has always been in everyone's mind. Even ancient civilizations presented us the idea of predicting the course of actions.

There are two possible ways for predicting the future, either you have special powers, or the future repeats itself over and over again, in such a way that you start finding patterns.

Computational fluid dynamics is the prediction of the future of a fluid flow. Because no special powers seem to solve the problem, the idea of finding patterns seems reasonable. These patterns were translated to mathematical language some years ago, when the Navier-Stokes equations were written. It is remarkable how so many information was compacted in such a small system of equations. Because of this compactness another tool must be created to unlock the Navier-Stokes information when desired. This tool is nowadays known as "numerical solution of partial differential equations" and involves techniques such as, finite difference methods (FDM), finite element methods (FEM), finite volume methods (FVM), spectral methods, boundary element methods, vorticity based methods, lattice gas/lattice Boltzmann, etc. Each method has its own advantages and disadvantages.

Anyway, the recent commercial codes for the prediction of fluid flow are mostly based on the FVM.

The finite volume method (FVM) is a numerical method well suited for various types of conservation laws. It is used in fluid mechanics, meteorology, electromagnetics, semi-conductor device simulation, models of biological processes and many other engineering areas governed by conservative systems that can be written in integral control volume form.

The method is attractive because while variables may not be continuously differentiable across shocks and other discontinuities, mass, momentum and energy are always conserved. In the FVM, conservativeness is explicitly enforced, in sharp contrast to Finite Difference Methods (FDM) and Finite Element Methods. The late 1970's early 1980's, saw the development of body-fitted grids (Wesseling, 2010) while in the 1990's, unstructured grid methods have appeared. A disadvantage of this methods is the appearance of false diffusion when low order numerical methods are used.

The method consists of dividing the domain into control volumes, integrate the differential equation over the control volume and apply the divergence theorem. The derivative terms are evaluated with discrete values at the center of the control volume and this results in a set of linear algebraic equations: one for each control volume. At the end we can solve the system of equations iteratively (the most used procedure in computational fluid dynamics) or simultaneously.

Historically, the finite difference method (FDM) is the oldest of the three. The technique was first presented by L. F. Richardson in 1910 at the Royal Society of London, for the stress analysis of a masonry dam. In 1922, Richardson developed the first numerical weather prediction system. His own attempt to calculate weather for a single eight-hour period took six weeks and ended in failure. In 1928, Courant, Fredrichson and Lewy (Courant et al., 1967) derived stability criteria for explicit time stepping (known as CFL condition).

The first numerical solution with the FDM was given by (Thom, 1933) for the flow over a circular cylinder and (Kawaguti, 1953) obtained a solution for flow around a cylinder, by using a mechanical desk calculator, working 20 hours per week for 18 months.

The FDM is very easy to implement but is restricted to simple grids and does not conserve momentum, energy, and mass. The domain is discretized into a series of grid points. The governing equations are discretized and approximated by truncated Taylor series expansions. The resulting set of linear algebraic equations is then solved either iteratively or simultaneously. For more on the FDM see (Roache, 1972).

The FEM earliest use was by Courant (1943) for solving a torsion problem (see (Courant, 1994)), and in 1956, Turner, Clough, Martin and Topp published in the Aeronautical Science Journal an FEM study of an aircraft stress analysis ((Turner et al., 1956)). The method was

refined greatly in the 60's and 70's, mostly for analyzing structural mechanics problem and in the mid 70's for fluid flow.

For more on the FEM with fluid flow applications, see (Zienkiewicz, 1991);

In order to understand the difference between these three methods, consider the two-point boundary value problem,

$$\begin{aligned} -\frac{d^2u}{dx^2} &= f \text{ in } (0,1) \\ u(0) &= 0, \quad u'(1) = 0 \end{aligned} \tag{2.24}$$

FEM:

Let  $u$  be the solution to the differential equation and  $v$  be any regular function with the restriction  $v(0) = 0$ . Multiplying both side of the equation by  $v$  and integrating over the range  $(0,1)$  leads to,

$$\int_0^1 f(x) v(x) dx = \int_0^1 -\frac{d^2u}{dx^2} v(x) dx = \int_0^1 \frac{du}{dx} \frac{dv}{dx} dx \tag{2.25}$$

For the second equality integration by parts was used.

The weak or variational formulation of the problem can be stated as,

$$\begin{aligned} \text{find } u \in V \text{ such that } \int_0^1 \frac{du}{dx} \frac{dv}{dx} dx &= \int_0^1 f(x) v(x) dx \quad \forall v \in V \\ V &= \left\{ v \in L^2(0,1) : \int_0^1 \frac{dv}{dx} \frac{dv}{dx} dx < \infty \text{ and } v(0) = 0 \right\} \end{aligned} \tag{2.26}$$

**Theorem:** Suppose  $f \in C^0([0,1])$  and  $u \in C^2([0,1])$  satisfy Eq. 2.26. Then  $u$  solves Eq. 2.24.

Based on the theorem given on the left we see that the solution for the problem can be achieved with the weak formulation. The weak formulation is less restrictive because only the first derivative for  $u$  is needed.

The "discretization" of the problem can be easily introduced with the Ritz-Galerkin approximation. Let  $S \subset V$  be any (finite dimensional) subspace. If we rewrite the weak formulation of Eq. 2.24 in terms of  $S$ , then,

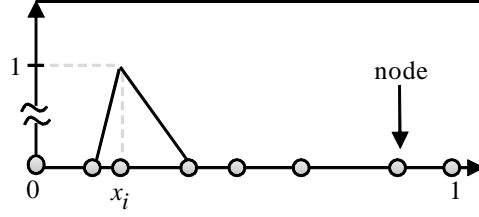
$$\text{find } u_S \text{ such that } \int_0^1 \frac{du_S}{dx} \frac{dv}{dx} dx = \int_0^1 f(x) v(x) dx \quad \forall v \in S \tag{2.27}$$

**Theorem:** Given  $f \in L^2(0,1)$  then 2.27 has a unique solution. (see (Brenner and Scott, 2008)).

Let  $\{\phi_i : 1 \leq i \leq n\}$  be a basis of  $S$ ;  $u_S$  can be written in terms of the basis elements by  $u_S = \sum_{j=1}^n U_j \phi_j$ . Let  $K_{ij} = \int_0^1 \frac{d\phi_i}{dx} \frac{d\phi_j}{dx} dx$  and  $F_i = \int_0^1 f(x) \phi_i dx$  for  $i, j = 1, \dots, n$ . Then the problem 2.27 is equivalent to solve the system of equations (see Livro Susanne),

$$[K_{ij}] [U_j] = [F_i] \tag{2.28}$$




 Figure 2.8: Linear basis function  $\phi_i$ 

Let  $0 = x_0 < x_1 < \dots < x_n = 1$  be a partition of  $[0, 1]$ . Suppose we chose  $S$  as the piecewise polynomial space, constituted by linear space functions  $v$  such that  $v \in C^0([0, 1])$ ,  $v|_{[x_{i-1}, x_i]}$  is a linear polynomial ( $i = 1, \dots, n$ ) and  $v(0) = 0$ . For the proof of  $S \subset V$  see (Brenner and Scott, 2008). Define  $\phi_i$  with the requirement that  $\phi_i(x_j) = \delta_{ij}$  (Kronecker delta) as in Fig. 2.8., then  $\{\phi_i : 1 \leq i \leq n\}$  is a basis for  $S$  (nodal basis).

**Definition:** Given  $v \in C^0([0, 1])$ , the interpolant  $v_{Int} \in S$  of  $v$  is determined by  $v_{Int} = \sum_{i=1}^n v(x_i) \phi_i$ . Note that  $v \in S \Rightarrow v = v_{Int}$ .

The following theorem finalizes the exposition on the finite element method, giving an approximation result for the interpolant.

**Theorem:** Let  $h = \max_{1 \leq i \leq n} (x_i - x_{i-1})$  then  $\|u - u_{Int}\|_E \leq ch \left\| \frac{d^2 u}{dx^2} \right\|$  for all  $u \in V$  ( $c$  is independent of  $h$  and  $u$ ).

We now have all the elements to compute the numerical solution of the Eq. 2.24 by using the system of equations 2.28.

FDM:

Making use of the same example given for the FEM we can derive the FDM formulation. Let  $h_i = x_i - x_{i-1}$ , then the matrix  $[K_{ij}]$  can be written as

$$\begin{bmatrix} k_{11} & k_{12} & 0 & 0 & 0 \\ k_{21} & k_{22} & k_{23} & 0 & 0 \\ 0 & k_{32} & k_{33} & \cdots & 0 \\ 0 & 0 & \vdots & \ddots & k_{(n-1)n} \\ 0 & 0 & 0 & k_{n(n-1)} & k_{nn} \end{bmatrix} \quad (2.29)$$

with  $K_{ii} = \frac{1}{h_i} + \frac{1}{h_{i+1}}$ ,  $K_{i,i+1} = K_{i+1,i} = -\frac{1}{h_{i+1}}$  and  $K_{nn} = \frac{1}{h_n}$  (this also works for the FEM). Remember that  $F_i = \int_0^1 f(x) \phi_i dx$  and it can be approximated by  $\frac{1}{2} (h_i + h_{i+1}) (f(x_i) + \mathcal{O}(h))$  with  $h = \max h_i$  (this follows from the fact that the integral of  $\phi_i$  is  $\frac{1}{2} (h_i + h_{i+1})$  and from Taylor's theorem). Assuming a uniform mesh, the  $i$ -th equation of  $[K_{ij}] [U_j] = [F_i]$  can be written as,

$$-\frac{U_j - 2U_j + U_j}{h^2} = f(x_i) + \mathcal{O}(h^2) \quad (2.30)$$

which is a familiar difference equation. Basically in the FDM the derivatives are approximated by finite differences.

#### FVM

The FVM makes use of an integral formulation of the equations. For the sake of simplicity assume the variables are equally spaced (except at the boundary) as shown in Fig. 2.9. and assume that  $f$  is constant.

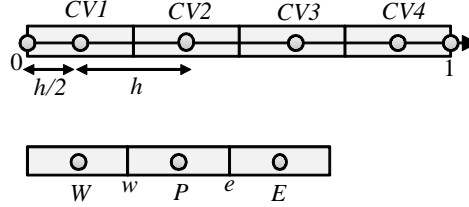


Figure 2.9: Finite volume grid for a one dimensional case.

In this example we have four variables, four control volumes, and also a Dirichlet and a Newman boundary condition. The integral version of the two-point boundary value problem is given by

$$\begin{aligned} \int -\frac{d^2u}{dx^2} &= \int f \text{ in } (0,1) \\ u(0) &= 0, \quad u'(1) = 0 \end{aligned} \quad (2.31)$$

The existence of control volumes, forces the approximation of our integral equation into four integrals.

For a control volume without boundary conditions, the integration  $-\int_w^e \frac{d^2u}{dx^2} dx = \int_w^e f dx$  yields  $\left(\frac{du}{dx}\right)_e - \left(\frac{du}{dx}\right)_w + fh = 0$  (this equation represents the diffusive flux conservation in a control volume) where the one dimensional divergence theorem was used on the left side of the equal sign and the mid-point rule was used to approximate the right hand side integral. Assuming a simple central difference to approximate the derivatives,

$$\left(\frac{du}{dx}\right)_e \simeq \frac{u_E - u_P}{h}, \quad \left(\frac{du}{dx}\right)_w \simeq \frac{u_P - u_W}{h} \quad (2.32)$$

the following equation is obtained,

$$\begin{aligned} a_P u_P &= a_W u_W + a_E u_E + fh \\ a_W &= a_E = \frac{1}{h}; \quad a_P = a_W + a_E \end{aligned} \quad (2.33)$$

This equation applies for control volumes 2 and 3.

For the control volume number 1, if a one-sided first order approximation is used,  $\left(\frac{du}{dx}\right)_w \simeq \frac{u_P - u_w}{h/2}$ , then we have (notice that  $u_w = u(0)$ ),

$$\begin{aligned} a_P u_P &= a_W u_W + a_E u_E + fh + \frac{2u(0)}{h} \\ a_W &= 0; \quad a_E = \frac{1}{h}; \quad a_P = a_E + \frac{2}{h} \end{aligned} \quad (2.34)$$

If a similar procedure is used for the control volume number 4, with  $\left(\frac{du}{dx}\right)_e = \frac{du(1)}{dx} = 0$  then,

$$\begin{aligned} a_P u_P &= a_W u_W + a_E u_E + fh \\ a_W &= \frac{1}{h}; a_E = 0; a_P = a_W + a_E \end{aligned} \quad (2.35)$$

Combining all the discretized equations, the following algebraic system of equations is obtained,

$$\begin{bmatrix} \frac{3}{h} & -\frac{1}{h} & 0 & 0 \\ -\frac{1}{h} & \frac{2}{h} & -\frac{1}{h} & 0 \\ 0 & -\frac{1}{h} & \frac{2}{h} & -\frac{1}{h} \\ 0 & 0 & -\frac{1}{h} & \frac{1}{h} \end{bmatrix} \begin{bmatrix} u_1 \\ u_2 \\ u_3 \\ u_4 \end{bmatrix} = \begin{bmatrix} fh + \frac{2u(0)}{h} \\ fh \\ fh \\ fh \end{bmatrix} \quad (2.36)$$

Notice the similarity between the coefficients matrix and the matrix  $[K_{ij}]$  from the FEM.

The FVM is a powerful method with a very intuitive and physical interpretation. Therefore this is the adopted method for this thesis. For a more detailed description of the FVM in the field of fluid dynamics the books of ((Patankar, 1980; Wesseling, 2010)) are advised.



Part III

ANALYTICAL STUDIES OF FLOWS UNDER  
SLIP



## INTRODUCTION TO PART III

In this Part, the following papers based on analytical solutions for both Newtonian and Non-Newtonian fluids, are presented:

▷L.L. Ferrás, J.M. Nóbrega, FT Pinho (2012), Analytical solutions for Newtonian and Inelastic non-Newtonian flows with wall slip, *Journal of Non-Newtonian Fluid Mechanics* **175-176** 76-88;

▷L.L. Ferrás, J.M. Nóbrega, FT Pinho (2012), Analytical solutions for channel flows of Phan-Thien–Tanner and Giesekus fluids under slip, *Journal of Non-Newtonian Fluid Mechanics* **171-172** 97-105;





## ANALYTICAL SOLUTIONS FOR NEWTONIAN AND INELASTIC FLOWS WITH WALL SLIP

---

### Abstract<sup>1</sup>

*This work presents analytical solutions for both Newtonian and inelastic non-Newtonian fluids with slip boundary conditions in Couette and Poiseuille flows using the Navier linear and non-linear slip laws and the empirical asymptotic and Hatzikiriakos slip laws. The non-Newtonian constitutive equation used is the generalized Newtonian fluid model with the viscosity described by the power law, Bingham, Hershel-Bulkley, Sisko and Robertson-Stiff models. While for the linear slip model it was always possible to obtain closed form analytical solutions, for the remaining non-linear models it is always necessary to obtain the numerical solution of a transcendental equation. Solutions are included with different slip laws or different slip coefficients at different walls.*

### 3.1 INTRODUCTION

Wall slip occurs in many industrial applications, such as in polymer extrusion processes, thus affecting the throughput and the quality of the final product (Denn, 2001). Therefore, analytical solutions of slip in shear flows are important to solve relevant industrial problems and better understand them, but also for the assessment of computational codes used in fluid flow simulations. There are many exact solutions for fluid flow in the literature (Berker, 1963; Bird et al., 2002) some of which are very simple, and others that use complex rheological models (Bird et al., 2002). Even though the simple exact solutions seem trivial, they are the building blocks to the understanding of more complex solutions. They usually rely on the Dirichlet type (no-slip) boundary condition ( where stands for the velocity at the wall). However, there is experimental evidence suggesting that some fluids do not obey this condition at the wall (Lauga et al., 2005), and show instead slip along the wall. For a review on wall slip with non-Newtonian fluids, slip laws and techniques to measure this property, the works of (Denn, 2001), (Lauga et al., 2005) and (Hatzikiriakos, 2012) are strongly advised.

Meijer and Verbraak, 1988 and (Potente et al., 2002, 2006) present analytical solutions for Poiseuille flow in extrusion using wall slip for Newtonian and power law fluids. Chatzimina et al. (2009) solves for non-linear slip in annular flows and analyses its stability. Ellahi et al.

---

<sup>1</sup> L.L. Ferrás, J.M. Nóbrega, F.T. Pinho (2012). Analytical solutions for Newtonian and Inelastic non-Newtonian flows with wall slip, *Journal of Non-Newtonian Fluid Mechanics Volumes 175–176*, May 2012, 76–88.

(2010) presents an analytical solution for viscoelastic fluids described by the 8-constant Oldroyd constitutive equation with non-linear wall slip. Wu et al. (2008) investigated analytically the pressure driven transient flow of Newtonian fluids in microtubes with Navier slip, whereas (Matthews and Hill, 2007) presented analytical solutions for pipe, annular and channel flows with the slip boundary conditions given by (Thompson and Troian, 1997). Yang and Zhu (2006), and the references cited therein, report analytical solutions and theoretical studies of squeeze flow with the Navier slip boundary condition. It is also worth mentioning the works on the well-posedness of the Stokes equations with leak, slip and threshold boundary conditions (Fujita, 2002; Roux and Tani, 2007), which also included their numerical implementation.

In spite of the wealth of solutions in the literature, there is a wide range of slip conditions, which have not been addressed analytically. With the exception of the simple linear Navier slip, for most other slip laws in the literature the analytical solutions for the so-called indirect problem are missing. Here, the results are dependent on the imposed flow rate. For the direct problem the literature is rich on the solutions but lack the corresponding reverse case, and this is not just a matter of inverting the final expressions given the non-linearity of the slip models and of the constitutive equations. In fact, the inverse problem is invariably more difficult to obtain than the solution of the direct problem. The main purpose of this paper is precisely to address these issues and report some new analytical solutions in particular for the inverse problem.

The remainder of this paper is organized as follows: subsection 2 presents the governing equations and the employed slip models. The study of Newtonian fluid flows with slip is presented first in subsection 3, starting with the simple Couette flow for the sake of understanding and this is followed by the Poiseuille flow using linear and non-linear slip boundary conditions and different slip coefficients at the upper and bottom walls (the existing relevant literature is only concerned with the direct problem for melt flow in extrusion screws). Subsection 3 ends with a study of Newtonian Poiseuille flow with the Hatzikiriakos and asymptotic slip laws and is followed by subsection 4 which describes solutions for the generalized Newtonian model with the viscosity function given by Power law, (Sisko, 1958), (Herschel and Bulkley, 1926) (Bingham) and Robertson-Stiff (Robertson and Stiff, 1976) models, both for linear and non-linear slip models. The text ends with the conclusions, in section 5.

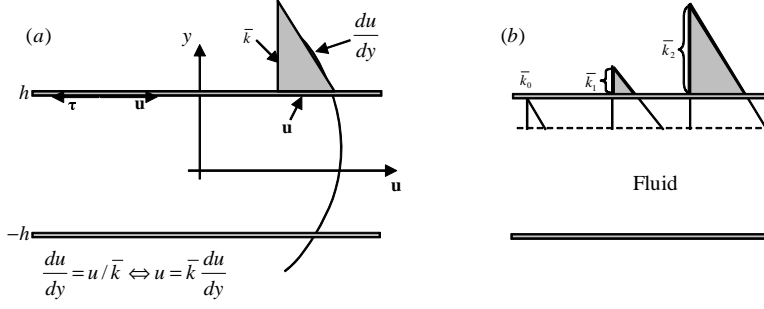


Figure 3.1: (a) Velocity profile across the flow channel assuming Couette-Poiseuille flow and slip at the wall (b) Different slip lengths  $0 = \bar{k}_0 < \bar{k}_1 < \bar{k}_2$  (zoom of the channel near the wall).

## 3.2 THEORY

### 3.2.1 Governing equations

This work concerns incompressible fluids which are governed by the continuity equation

$$\nabla \cdot \mathbf{u} = 0 \quad (3.1)$$

and the momentum equation,

$$\frac{\partial \rho \mathbf{u}}{\partial t} + \rho \nabla \cdot \mathbf{u} \mathbf{u} = -\nabla p + \nabla \cdot \boldsymbol{\tau} \quad (3.2)$$

In Eq. 2  $\mathbf{u}$  is the velocity vector,  $p$  is the pressure,  $\boldsymbol{\tau}$  is the deviatoric stress tensor and the gravity contribution is incorporated in the pressure. All equations are written in a coordinate free form. The stress tensor obeys the following law for generalized Newtonian fluids,

$$\boldsymbol{\tau} = 2\eta(\dot{\gamma}) \mathbf{D} \quad (3.3)$$

with the rate of strain tensor  $\mathbf{D}$  given by,

$$\mathbf{D} = \frac{1}{2} \left( [\nabla \mathbf{u}] + [\nabla \mathbf{u}]^T \right) \quad (3.4)$$

and  $\eta(\dot{\gamma})$  representing the fluid viscosity function.

Considering steady, incompressible, laminar flow (in the streamwise direction) between two infinite parallel horizontal plates, with no movement in the direction (Fig. 3.1), the momentum equation (Eq. 3.2) written in a Cartesian coordinate system reduces to,

$$\frac{d}{dy} \left( \eta(\dot{\gamma}) \frac{du}{dy} \right) = p_x \quad (3.5)$$

where  $p_x = dp/dx$ . This equation is valid for both planar Couette and Poiseuille flow.

For fluids described by the Generalized Newtonian model, the empirical viscosity function  $\eta(\dot{\gamma})$  can be given by any of the models in Eqs. 3.6 to 3.9. These are the power law model

$$\eta(\dot{\gamma}) = a |\dot{\gamma}|^{n-1} \quad (3.6)$$

and the Sisko model

$$\eta(\dot{\gamma}) = \mu_\infty + a |\dot{\gamma}|^{n-1} \quad (3.7)$$

where  $\dot{\gamma}$  is the shear rate obtained from the following definition involving the second invariant of the rate of deformation tensor ( $|\dot{\gamma}| = \sqrt{D_{ij}D_{ij}/2}$ ) and  $a, n$  are the consistency and power law indices with  $n \geq 0$ , and  $\mu_\infty$  is the viscosity at a very large shear rates. Analytical solutions are also presented for yield stress fluids described by the following two models,

Herschel Bulkley:

$$\begin{cases} \tau = \left( \mu_0 |\dot{\gamma}|^{n-1} + \frac{\tau_0}{|\dot{\gamma}|} \right) \dot{\gamma} & \text{if } |\tau| > \tau_0 \\ \dot{\gamma} = 0 & \text{if } |\tau| < \tau_0 \end{cases} \quad (3.8)$$

Robertson-Stiff:

$$\begin{cases} \tau = \left( \mu_0^{1/n} |\dot{\gamma}|^{(n-1)/n} + \left( \frac{\tau_0}{|\dot{\gamma}|} \right)^{1/n} \right)^n \dot{\gamma} & \text{if } |\tau| > \tau_0 \\ \dot{\gamma} = 0 & \text{if } |\tau| < \tau_0 \end{cases} \quad (3.9)$$

where  $\tau_0$  is the yield stress and  $\mu_0 > 0$ . For  $n = 1$  the Herschel-Bulkley model reduces to the Bingham model. For the yield stress models  $|\tau|$  is the second invariant of the deviatoric stress tensor  $|\tau| = \sqrt{\tau_{ij}\tau_{ij}/2}$ .

### 3.2.2 Boundary conditions

The specification of boundary conditions is mandatory to guarantee the wellposedness of the problem. As mentioned before, most solutions in the literature are for the Dirichlet type no-slip wall boundary condition,

$$\mathbf{u} = \mathbf{0} \quad (3.10)$$

This imposes that the fluid adheres to the wall, together with the impermeability condition.

However, this boundary condition cannot be derived from first principles (Lauga et al., 2005). Lamb (1932), (Batchelor, 2000) and (Goldstein, 1965) mention that slip may be wrong and that the use of no-slip stems from the need to agree predictions with experiments

(some of the experiments referred to were not carried out carefully and consequently their results are contradictory). Several authors try to explain the existence of slip and its dependence on parameters like surface roughness, dissolved gas and bubbles attached to the wall, wetting characteristics, shear rate, electrical properties and pressure, and this list keeps increasing with time.

In any case it is now an established fact that for macro geometries the interaction between small fluid molecules and walls is equivalent to a no-slip condition for most fluid-wall pairs. However, as the Knudsen number (the ratio between the mean free path and the characteristic flow size) increases, slip effects become more important (see (Lauga et al., 2005) and references cited therein). Regarding long molecules, such as the ones found in polymer melts, slip effects can actually be found also at the macro scale leading to some flow instabilities reviewed by (Denn, 2001), such as sharkskin, stick-slip and gross melt fracture. Other investigations concerning slip at the liquid-solid interface for polymers are Potente et al. (Potente et al., 2002) and Mitsoulis et al. (Mitsoulis et al., 2005).

### 3.2.3 Slip laws

Friction between a fluid in contact with a wall generates a tangent stress vector  $\tau$  (Fig. 3.1) that may be sufficient to eliminate slip of the fluid. Therefore, a way to promote slip is to reduce that friction, leading to the appearance of a nonzero velocity along the wall. The tangent stress vector depends on the velocity gradient of the fluid at the wall, with both variables related in such a way that the tangent velocity and tangent stress vectors are pointing in opposite directions (Fig. 3.1). Since all the analytical solutions in this work concern flow between parallel plates aligned with the axis  $x$  direction, there is no need to continue using vector notation, so, all the slip laws will be presented in their streamwise component.

Navier (1822) argued that in the presence of slip the liquid motion must be opposed by a force proportional to the relative velocity between the first liquid layer and the solid wall. Fig. 3.1 illustrates an interpretation of slip with Fig. 3.1(a) showing the velocity profile across the channel and the relation between the velocity and its derivative at the wall. This derivative at the wall is the same as the slope given by  $u/\bar{k}$ . Thus, the following relation that involves the slip velocity can be obtained,

$$\frac{u_{ws}}{\bar{k}} = \left. \frac{du}{dy} \right|_{wall} \quad (3.11)$$

Solving for  $u_{ws}$ , the relationship between the slip velocity and the wall velocity gradient is,

$$u_{ws} = \bar{k} \left. \frac{du}{dy} \right|_{wall} \quad (3.12)$$

where the coefficient  $\bar{k}$  is named slip length or friction coefficient. As illustrated in Fig. 3.1(b) the slip length can take any positive value ( $\bar{k} \geq 0$ ), with no-slip at wall for  $\bar{k} = 0$ , and increasingly large slip velocity as  $\bar{k}$  increases to infinity in which case the velocity profile becomes a plug with zero velocity gradient. Eq. 3.12 must be combined with the rheological constitutive equation. Considering the Generalized Newtonian Fluid model for inelastic fluids, near the wall the tangent stress is given by,

$$\tau_{xy} = \eta(\dot{\gamma}) \frac{du}{dy} \quad (3.13)$$

Eq. 3.12 can now be rewritten for a Generalized Newtonian fluid as,

$$u_{ws} = \text{sign}(du/dy) k \tau_{xy} \quad (3.14)$$

with  $k = \bar{k}/\eta(\dot{\gamma}) \geq 0$ . Based on the fact that the velocity points to the stress opposite direction and because scalar variables are employed, different signs will be used in Eq. 3.14 depending on the sign of the shear rate  $\text{sign}(du/dy)$ . For the “top wall”, the equation makes use of the minus sign and for the “bottom wall” the plus sign, since the tangent velocity is positive in both walls but the  $\text{sign}(du/dy)$  in the top and bottom walls is negative and positive, respectively. This notation will stand for the other slip laws.

This linear relationship between slip velocity at the wall and shear stress at the wall is called the **linear Navier Slip law** (Navier, 1822) or simply the **Navier slip law**. It has been used extensively to represent experimental data, for both Couette and Poiseuille flows.

Slip laws are models to bridge the gap between theory and experimental data, and to fit experimental observations a variety of slip models were created, such as those stating the dependence of the friction coefficient on wall shear rate or stress and models derived from molecular kinetic theory (Schowalter, 1988; Hatzikiriakos, 1993).

The **nonlinear Navier Slip law** (Schowalter, 1988) assumes that the friction coefficient is a function of the shear stress, thus providing a non-linear power function,

$$u_{ws} = \text{sign}(du/dy) k |\tau_{xy}|^{m-1} \tau_{xy} \quad (3.15)$$

where  $m > 0$  ( $m \in \mathbb{R}$ ). For  $m = 1$  the Navier slip law is recovered.

This non-linear model has been used to represent experimental data in Couette and Poiseuille flows by (Thompson and Troian, 1997; Schowalter, 1988). It provides a good approximation for several conditions, but it fails to describe the slip velocity in the neighborhood of the critical stress at which the slip starts. To eliminate this discrepancy,

Hatzikiriakos proposed an alternative slip law based on the Eyring theory of liquid viscosity in order to provide a smooth transition from no-slip to slip flow at the critical shear stress (Hatzikiriakos, 1993). The argument goes as follows:

Let  $\tau_c$  be the positive critical stress at which slip starts and  $k_1, k_2 \geq 0$ . Then, the **Hatzikiriakos slip law** is given by,

$$u_{ws} = \begin{cases} k_1 \sinh(k_2 \text{sign}(du/dy) \tau_{xy} - \tau_c) & \text{if } \tau_{xy} \geq \tau_c \\ 0 & \text{if } \tau_{xy} < \tau_c \end{cases} \quad (3.16)$$

The **asymptotic slip law** is given by

$$\tau = (-1/k_2) [1 - \exp(u/k_1)] \quad (3.17)$$

for one dimensional flow, and can also be written as an explicit function for the slip velocity,

$$u_{ws} = k_1 \ln(1 + k_2 \text{sign}(du/dy) \tau_{xy}) \quad (3.18)$$

For both the Hatzikiriakos and the asymptotic slip models, the coefficients  $k_1$  and  $k_2$  allow controlling the amount of slip and the shape of the curve  $\tau$  vs  $u_{ws}$  that is obtained by experimental measurements. Schowalter (1988) used the Hatzikiriakos slip law model to model wall slip in Couette and Poiseuille flows, respectively.

For the Poiseuille and Couette flows of Figs. 3.1 and 3.2 the boundary conditions for these slip laws can be written in a general form for both the “top” (+h) and “bottom” (-h) walls.

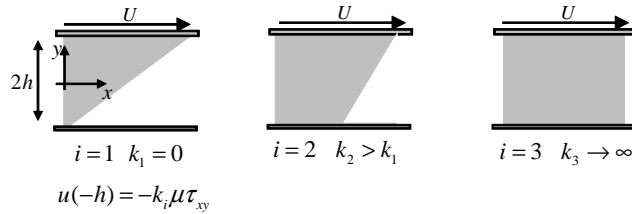


Figure 3.2: Couette flow velocity profiles for different slip lengths  $\bar{k}_1 < \bar{k}_2 < \bar{k}_3$ .

Integrating the momentum equation (Eq. 3.5)  $\tau_{xy}$  is given by,

$$\tau_{xy} = p_x y + c \quad (3.19)$$

Combining Eq. 3.19 with Eqs. 3.15, 3.16 and 3.18 for all the investigated slip laws gives the general form of the boundary conditions at the upper and bottom walls.

For the non-linear Navier slip law ( $m = 1$  for the linear Navier slip law):

$$u(h) = k_{nl1} (-p_x h - c)^m \quad (3.20)$$

$$u(-h) = k_{n2} (-p_x h + c)^m \quad (3.21)$$

For the Hatzikiriakoc slip law:

$$u(h) = k_{H1} \sinh(k_{H2} (-p_x h - c)) \quad (3.22)$$

$$u(-h) = k_{H3} \sinh(k_{H4} (-p_x h + c)) \quad (3.23)$$

For the asymptotic slip law:

$$u(h) = k_{A1} \ln(1 + k_{A2} (-p_x h - c)) \quad (3.24)$$

$$u(-h) = k_{A3} \ln(1 + k_{A4} (-p_x h + c)) \quad (3.25)$$

For symmetrical boundary conditions  $c_1 = 0$ , thus the top and bottom slip velocities become identical, as expected.

### 3.3 ANALYTIC AND SEMI ANALYTIC SOLUTIONS FOR NEWTONIAN FLUIDS

Newtonian fluids have a constant viscosity so  $\eta(\dot{\gamma}) = \mu$  in Eq. 3.13.

#### 3.3.1 Couette flow

In pure Couette flow (Fig. 3.2) the pressure gradient is null and Eq. 3.5 reduces to:

$$u(y) = c_1 y + c_2 \quad (3.26)$$

with  $c_1$  the shear rate  $\dot{\gamma} = du/dy$ .

##### 3.3.1.1 Navier slip at the bottom wall and no slip at the upper wall

Assume the upper wall is moving with velocity  $U$  and that a Navier slip boundary condition applies to the bottom wall (cf. Fig. 3.2) so that

$$u(h) = U \text{ and } u(-h) = k\mu \left( \frac{du}{dy} \right)_{y=-h} = k\mu c_1 \quad (3.27)$$

Using the boundary condition of Eq. 3.27 the coefficients  $c_1$  and  $c_2$  are given by,

$$c_2 = U - c_1 h \quad (3.28)$$

$$c_1 = \frac{U}{2h + k\mu} \quad (3.29)$$

The final solution for the velocity profile across the channel is then,



$$u(y) = \frac{U(y-h)}{2h+k\mu} + U \quad (3.30)$$

Let  $f(k)$  be defined by,

$$f(k) = \frac{U(y-h)}{2h+k\mu} + U, \quad k \geq 0 \quad (3.31)$$

For  $k = 0$ ,  $f(0) = (U/2h)(y+h)$  which is the original solution with Dirichlet boundary condition  $u = 0$ . As  $k$  increases the solution approaches plug flow conditions, i.e.,

$$\lim_{k \rightarrow \infty} f(k) = \lim_{k \rightarrow \infty} \frac{U(y-h)}{2h+k\mu} + U = U \quad (3.32)$$

This equation states that it is impossible to obtain a slip velocity larger than  $U$ , which is in agreement with the physical constraints of the problem. Fig. 3.2 illustrates the evolution of the flow with the slip length.

If  $U = 0$  the flow profile is given by the trivial solution  $u(y) = 0$  for  $0 \leq y \leq h$ . The main problem with this slip boundary condition (Eq. 3.27) is that both the bulk and wall velocities depend on the velocity gradient, so that a nonzero gradient will develop only if some velocity is given at the boundary. Therefore, it can be said that the Navier slip boundary condition is somewhat weaker than the Dirichlet boundary condition, so that in the absence of a pressure gradient and of an imposed velocity the fluid will not move. Note that for  $U = 0$  and imposing slip at both walls leads again to the trivial solution  $u(y) = 0$ .

### 3.3.1.2 Nonlinear slip laws at the bottom wall and no slip at the upper wall

Assume the upper wall is moving with velocity  $u(h) = U$  and a nonlinear slip boundary condition is imposed at the bottom wall. Following a procedure similar to that of the previous section the following boundary conditions are obtained: for the non-linear Navier slip law we have  $u(-h) = k_{nl2}(\mu c_1)^m$ , for the Hatzikiriakos slip law  $u(-h) = k_{H3} \sinh(k_{H4} \mu c_1)$  and for the asymptotic slip law the boundary condition is given by  $u(-h) = k_{A3} \ln(1 + k_{A4} \mu c_1)$ . To determine the integration constant, the following equations must be solved for the non-linear Navier slip law, Hatzikiriakos and asymptotic slip laws, respectively,

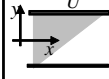
$$(c_1)^m + (2h/k\mu^m) c_1 - (U/k\mu^m) = 0 \quad (3.33)$$

$$k_{H3} \sinh(k_{H4} \mu c_1) + 2hc_1 - U = 0 \quad (3.34)$$

$$k_{A3} \ln(1 + k_{A4} \mu c_1) + 2hc_1 - U = 0 \quad (3.35)$$

Table 3.1: Analytical solutions for Couette flow with linear and nonlinear Navier slip laws and slip only at the bottom wall. The top row shows the general system of equations to be solved and the next four rows show the solution for different values of the slip exponent  $m = 0.5, 1, 2, 3$ .

Couette Flow [linear ( $m=1$ ) and nonlinear Navier Slip ( $m \neq 1$ )]	$\begin{cases} u(y) = c_1(y-h) + U \\ (c_1)^m + (2h/k\mu^m)c_1 - (U/k\mu^m) = 0 \end{cases}$
$m = 0.5$	$u(y) = \left[ \frac{(k\mu^{0.5})^2}{8h^2} \left( 1 - \sqrt{1 + \frac{8hU}{(k\mu^{0.5})^2}} \right) + \frac{U}{2h} \right] (y-h) + U$
$m = 1$	$u(y) = \frac{U(y-h)}{2h+k\mu} + U$
$m = 2$	$u(y) = \frac{-2h + \sqrt{4(h^2 + k\mu^m U)}}{2k\mu^m} (y-h) + U$
$m = 3$	$u(y) = \left\{ \sqrt[3]{(U/k\mu^m)/2 + \sqrt{((U/k\mu^m)/2)^2 + ((2h/k\mu^m)/3)^3}} + \sqrt[3]{(U/k\mu^m)/2 - \sqrt{((U/k\mu^m)/2)^2 + ((2h/k\mu^m)/3)^3}} \right\} (y-h) + U$



For the special cases  $m = 0.5, 2, 3$  of the analytical solutions are possible for the nonlinear Navier slip law, the results of which are presented in Table 3.1 and Appendix A. For the other solutions and equations we prove the existence of a unique solution in Appendix A.

### 3.3.2 Couette-Poiseuille Flow

Integrating twice the momentum equation (Eq. 3.5) for a constant viscosity fluid, the result is,

$$u(y) = \frac{p_x}{2\mu} y^2 + c_1 y + c_2 \quad (3.36)$$

with  $c_1 = c/\mu$ ,  $c_2 \in \mathbb{R}$  two real constant numbers,  $\mu \geq 0$  and  $0 - h \leq y \leq h$ . Applying boundary conditions  $u(-h)$  and  $u(h)$  to the velocity profile in Eq. 3.36 the constants of integration  $c_1$  and  $c_2$  can be determined and the following final form of the velocity profile is obtained

$$u(y) = \frac{p_x}{2\mu} (y^2 - h^2) + \left( \frac{u(h) - u(-h)}{2h} \right) y + \frac{u(-h) + u(h)}{2} \quad (3.37)$$

For the particular case of pure Poiseuille flow, symmetry leads to  $c_1 = 0$  and  $c_2 = u(h) - (p_x/2\eta(\dot{\gamma})) h^2$ .

For the inverse problem of Couette-Poiseuille flow with an imposed flow rate  $Q = \bar{U} \cdot 2h$  where  $\bar{U}$  is the mean velocity obtained by integration of the velocity profile across the channel, we obtain the relation of

Eq. 3.38 between the imposed mean velocity and the ensuing pressure gradient,

$$\bar{U} = \frac{1}{2h} \int_{-h}^h \left( \frac{p_x}{2\mu} y^2 + c_1 y + c_2 \right) dy \Leftrightarrow -\frac{p_x}{3\mu} h^2 + \frac{u(-h) + u(h)}{2} - \bar{U} = 0 \quad (3.38)$$

Notice that  $u(-h)$  and  $u(h)$  are themselves functions of the pressure gradient, and nonlinear equations may arise.

### 3.3.2.1 Linear and nonlinear slip laws - pure Poiseuille flow

For the linear and non-linear slip models and from the boundary conditions of Eqs. 3.20, 3.22 and 3.24 the flow velocity profile for the direct problem becomes,

$$u(y) = \frac{p_x}{2\mu} (y^2 - h^2) + u(h) \quad (3.39)$$

whereas for the inverse problem the pressure gradient is obtained from the following transcendent equation for a given bulk velocity  $\bar{U}$ ,

$$-\frac{p_x}{3\mu} h^2 + u(h) - \bar{U} = 0 \quad (3.40)$$

Generally speaking the solution of the previous equation must be obtained numerically, but for the particular cases of the non-linear Navier slip law with  $m = 0.5$ ,  $m = 1$  (linear),  $m = 2$  and  $m = 3$  full analytical solutions can be obtained and are given in Table 3.2. For the Hatzikiriakos and asymptotic slip laws, the corresponding solutions are presented in Table 3.3. Details on these solutions are given in Appendix B, where the existence of a unique solution for all the boundary conditions is also proved.

Note that the solution of Hatzikiriakos and Mitsoulis (Hatzikiriakos and Mitsoulis, 2009) is more general since they investigated a power law fluid with non-linear Navier slip boundary conditions, but they restricted their solutions to the particular case  $m = 1/n$ , where  $n$  is the power law exponent, meaning that for the Newtonian case they only explore the linear Navier slip.

### 3.3.2.2 Different slip in the upper and bottom walls for Couette-Poiseuille flow

When compared to the pure Poiseuille flow we see that for the Couette-Poiseuille flow the symmetry condition ( $c_1 = 0$ ) can no longer be used, meaning that, a system of nonlinear equations will be obtained for the constant of integration and the pressure gradient (Eq. 3.41).

Table 3.2: Analytical solutions for Poiseuille flow with identical slip at both walls for the linear and nonlinear Navier slip laws. In the top row the general system of equations to be solved and the next four rows show the solution for different values of the slip exponent  $m = 0.5, 1, 2, 3$ .

Poiseuille Flow [linear (m=1) and nonlinear Navier Slip (m ≠ 1)]	$\begin{cases} u(y) = \frac{p_x}{2\mu}(y^2 - h^2) + kh^m(-p_x)^m \\ -\frac{p_x}{3\mu}h^2 + kh^m(-p_x)^m - \bar{U} = 0 \end{cases}$
	$m = 0.5 \quad p_x = -\frac{9\mu^2}{4h^4} \left( 2k^2h + \frac{4h^2\bar{U}}{3\mu} - 2kh^{0.5} \sqrt{k^2h + \frac{4h^2\bar{U}}{3\mu}} \right)$
	$m = 1 \quad p_x = \bar{U}(-h^2/3\mu - kh)^{-1}$
	$m = 2 \quad p_x = \frac{h^2/3\mu \pm \sqrt{(h^2/3\mu)^2 + 4kh^2\bar{U}}}{2kh^2}$
	$m = 3 \quad p_x = \left( \sqrt[3]{(\bar{U}/2kh^3)} + \sqrt{(\bar{U}/2kh^3)^2 + (9kh\mu)^{-2}} + \sqrt[3]{(\bar{U}/2kh^3) - \sqrt{(\bar{U}/2kh^3)^2 + (9kh\mu)^{-2}} \right)$

Table 3.3: Semi-analytical solutions for the Poiseuille flow of a Newtonian fluid with Hatzikiriakos and asymptotic slip laws.

Poiseuille Flow [Hatzikiriakos and asymptotic]	$\begin{cases} u(y) = \frac{p_x}{2\mu}(y^2 - h^2) + u(h) \\ -\frac{p_x}{3\mu}h^2 + u(h) - \bar{U} = 0 \end{cases}$
---	--

$$\begin{cases} -2hc_1 + u(h) - u(-h) = 0 \\ -\frac{p_x}{3\mu}h^2 - c_1h + u(h) - \bar{U} = 0 \end{cases} \quad (3.41)$$

For linear Navier slip law at both walls (with slip coefficients  $k_{l1}$  at the bottom and  $k_{l2}$  at the top), the analytical solution is still possible and is given by Eq. 3.42,

$$u(y) = \frac{p_x}{2\mu}y^2 + c_1y + p_x \left( -k_{l1}h - \frac{h^2}{2\mu} \right) + c_1(-k_{l1}\mu - h) \quad (3.42)$$

with

$$p_x = -\frac{(3/2)(2 + k_{l1}(\mu\bar{U}/h) + k_{l2}(\mu\bar{U}/h))}{\left[ 3k_{l1}k_{l2}(\mu\bar{U}/h)^2 + 2k_{l1}(\mu\bar{U}/h) + 2k_{l2}(\mu\bar{U}/h) + 1 \right] (\mu\bar{U}/h^2)} \quad (3.43)$$

$$c_1 = \frac{(3/2)(\mu\bar{U}^2/h)(k_{l1} - k_{l2})}{\left[ 3k_{l1}k_{l2}(\mu\bar{U}/h)^2 + 2k_{l1}(\mu\bar{U}/h) + 2k_{l2}(\mu\bar{U}/h) + 1 \right] h} \quad (3.44)$$

For this case, the boundary conditions are given by Eq. 3.20 and 3.21 with  $m = 1$ . The term  $(k_{l1} - k_{l2})$  will determine the sign of  $c_1$ . If  $k_{l1} > k_{l2}$  the maximum velocity value is on the positive half of the channel  $0 \leq y \leq h$  whereas for  $k_{l1} < k_{l2}$  it is on the lower half  $-h \leq y \leq 0$ .

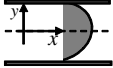
For the **nonlinear Navier slip law**, full analytical solutions can also be found, when the linear Navier slip law is valid in one wall, and on the other the non-linear Navier slip law applies with  $m$  equal to 2 or 3. These solutions can be very helpful to test numerical codes with different slip boundary conditions in the same domain, and can be found in Appendix C.

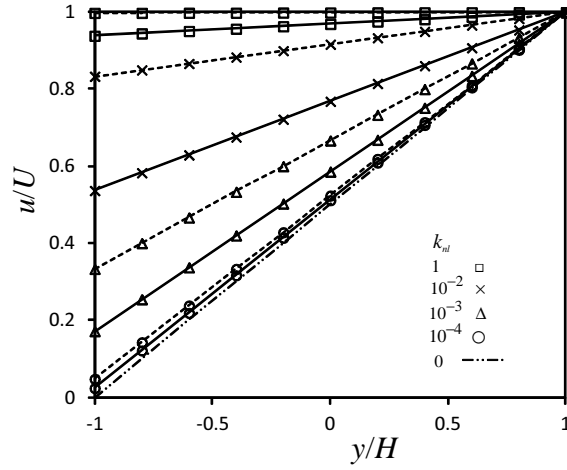
For the remaining values of the exponent and for the other two slip models (asymptotic and Hatzikiriakos), semi-analytical solutions are obtained. Their restrictions  $du/dy < 0$ , in the upper wall,  $du/dy > 0$  in the bottom wall and a favorable pressure gradient ( $p_x < 0$ ), are helpful to narrow down the possible solutions, especially when the use of a numerical method is required.

$$\begin{aligned} p_x < 0 \text{ and } -p_x h - \mu c_1 > 0 \text{ and } -p_x h + \mu c_1 > 0 \\ \Leftrightarrow p_x < 0 \text{ and } c_1 \in \left] \frac{p_x}{\mu} h; -\frac{p_x}{\mu} h \right[ \end{aligned} \quad (3.45)$$

See Table 3.4 for a summary of these solutions.

Table 3.4: Semi-analytical solutions for the Poiseuille flow of a Newtonian fluid with Hatzikiriakos and asymptotic slip laws.

Poiseuille Flow [different slip at top and bottom walls]	$u(y) = \frac{p_x}{2\mu} y^2 + c_1 y + p_x \left( -k_1 h - \frac{h^2}{2\mu} \right) + c_1 (-k_1 \mu - h)$	
	$p_x = -\frac{1.5(2 + k_1(\mu\bar{U}/h) + k_2(\mu\bar{U}/h))}{[3k_1(\mu\bar{U}/h)k_2(\mu\bar{U}/h) + 2k_1(\mu\bar{U}/h) + 2k_2(\mu\bar{U}/h) + 1]} (\mu\bar{U}/h^2)$	
	$c_1 = \frac{1.5U(\mu\bar{U}/h)(k_1 - k_2)}{[3k_1(\mu\bar{U}/h)k_2(\mu\bar{U}/h) + 2k_1(\mu\bar{U}/h) + 2k_2(\mu\bar{U}/h) + 1]h}$ Linear Navier slip	
	$\begin{cases} -2hc_1 + u(h) - u(-h) = 0 \\ -\frac{p_x}{3\mu} h^2 - c_1 h + u(h) - U = 0 \end{cases}$	
	Nonlinear Navier slip $u(h) = k_1 (-p_x h - \mu c_1)^m$ $u(-h) = k_2 (-p_x h + \mu c_1)^m$	Hatzikiriakos $u(h) = k_3 \sinh(k_4 (-p_x h - \mu c_1))$ $u(-h) = k_3 \sinh(k_4 (-p_x h + \mu c_1))$
	asymptotic $u(h) = k_5 \ln(1 + k_6 (-p_x h - \mu c_1))$ $u(-h) = k_5 \ln(1 + k_6 (-p_x h + \mu c_1))$	

Figure 3.3: Velocity profiles for the Couette flow with the non-linear Navier slip model (full line  $m = 2$ , dashed line  $m = 1$ ) at the fixed wall.

### 3.3.3 Discussion (Newtonian fluids)

All the solutions obtained for the Newtonian fluids are summarized in Tables 3.1 to 3.4, which will be used for the subsequent discussion. In Poiseuille flow the following dimensionless variables will be used. The slip friction coefficients are given by  $k'_{nl} = k_{nl} \bar{U}^{m-1} (\mu/h)^m$  for the Navier nonlinear slip model,  $k'_1 = k_1 \bar{U}$  and  $k'_2 = k_2 (\mu \bar{U}/h)$ , for the first and second coefficients in the asymptotic and Hatzikiriakos slip laws. The velocity is given by  $u' = u/\bar{U}$  and the pressure gradient by  $p'_x = p_x / (\eta \bar{U}/h^2)$ .

#### 3.3.3.1 Couette flow

For the Couette flow several flow conditions were studied. Fig. 3.3 shows the influence of the non-linear Navier slip model exponent ( $m$ )

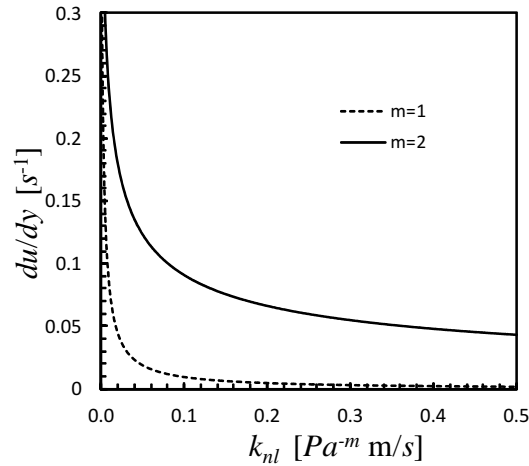


Figure 3.4: Integral constant  $c_1$  versus the friction coefficient for the Couette flow with non-linear Navier slip model at the fixed wall

on the velocity profile, for different values of the friction coefficient ( $k'_{nl}$ ). The slip velocity decreases inversely to exponent, so it becomes increasingly difficult to attain the plug flow conditions when increases.

This behavior can be also verified by variation of the shear rate  $c_1 = du/dy$  with the slip coefficient, seen in Fig. 4. As shown for the case with exponent  $m = 2$ ,  $du/dy$  is larger than for the  $m = 1$  case. Notice that  $du/dy$  will multiply a negative number (see Table 3.1), thus reducing the slip velocity for higher slip exponents.

### 3.3.3.2 Poiseuille flow (symmetrical conditions)

In Fig. 3.5(a) the difference in slip velocity between the asymptotic and Hatzikiriakos slip laws is illustrated. For different values of the slip coefficient  $k'_2$  the sensitivity of the models is different. Notice that the Hatzikiriakos slip law is built with the inverse function of the asymptotic law, and therefore its growth is exponential. For small values of  $k'_2$  both functions tend to a linear “local” behavior for some specific range of the pressure gradient, and for these values they locally have a similar behavior as can be seen in Fig. 3.5.

The Hatzikiriakos slip law is much more sensitive to the  $k'_2$  coefficient than the asymptotic slip law, as can be seen in Fig. 3.5(b). This fact can be a problem when implementing this law in numerical codes, mainly due to convergence difficulties, since along the iterative procedure large variations in the slip velocity can occur and cause divergence (overflow) or even round off errors on the final data.

The other slip parameter  $k'_1$  increases or decreases the slip velocity establishing a linear relationship between the slip velocity and the hyperbolic sine or logarithmic functions. In Fig 3.5(b) we can also see the agreement between the Hatzikiriakos and asymptotic slip laws for lower values of the shear stress. Notice the almost linear

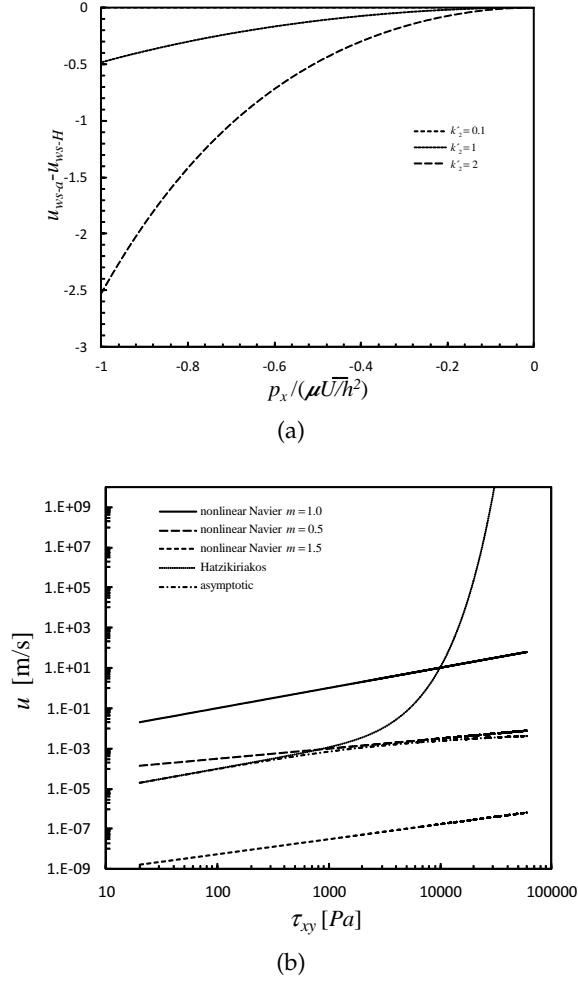


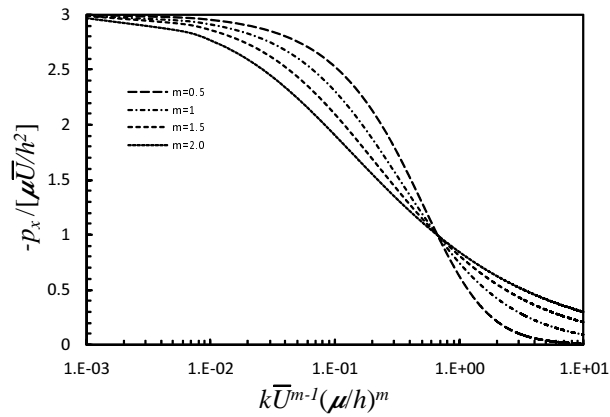
Figure 3.5: (a) Difference between the asymptotic (A) and the Hatzikiriakos (H) slip velocities for different values of the slip coefficient  $k'_2$ . It is assumed that  $k'_1 = 1$ . (b) Representation of the four slip boundary conditions (slip velocity versus shear stress) for equal and constant friction coefficients.

growth of the slip velocity for the nonlinear Navier slip laws, while the Hatzikiriakos slip law has a sigmoid shape with an inflection point where the curvature changes (in Fig. 3.5(b) the complete sigmoid shape cannot be seen because we use null critical stress).

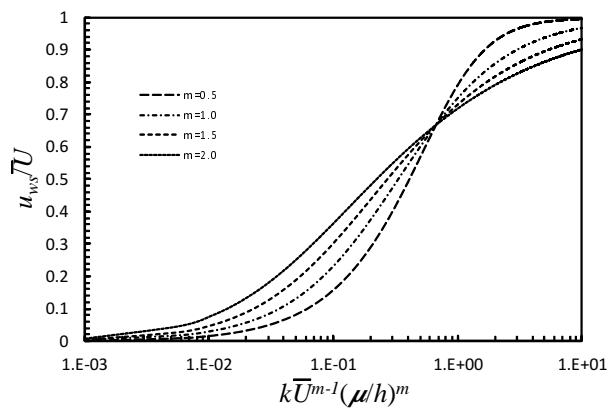
The slip intensity influences the pressure gradient, which promotes the fluid flow. As the resistance of the walls decrease a smaller pressure gradient is enough to ensure motion as shown in Fig. 3.6(a), where the variation of the pressure gradient with the slip coefficient is represented. These effects can also be analyzed in terms of the dimensionless slip velocity, shown in Fig. 3.6(b), where similar trends to those obtained for pressure gradient are depicted.

It should be noticed that with dimensional variables the slip coefficient  $k'_{nl}$  depends on the slip exponent which may influence the results, since the coefficient is different for each flow exponent ( $m$ ).





(a)



(b)

Figure 3.6: Variation of the normalized pressure gradient (a) and slip velocity (b) with the dimensionless slip coefficient  $k'_{nl}$  for different values of the slip exponent  $m$  for Poiseuille flow in a channel.

However, plotting the data in nondimensional form shows the same qualitative behavior.

For the Hatzikiriakos and asymptotic slip models, the behavior is slightly different when compared with the Navier slip model as shown Fig. 3.7. For the slip constant  $k'_1 = 1$ , both models exhibit the same qualitative behavior as is also the case for the Navier Slip model. However, as the coefficient  $k'_1$  decreases, their behavior departs from each other and from the Navier slip.

The asymptotic model is greatly influenced by the slip coefficient  $k'_1$  showing a nearly constant pressure gradient which slowly decreases with slip whereas the slip velocity increases strongly with the slip coefficient  $k'_2$ .

The Hatzikiriakos model results in smaller pressure gradient and higher slip velocities than the asymptotic, for the same numerical value. As seen in Fig. 3.7, the trend in the slip velocity for the  $k'_1 = 10^{-3}$  (Hatzikiriakos) is quite different from the other slip trend lines. At some point this model seems to be very sensitive to the friction coefficients and the slip velocity increases drastically, thus creating numerical instabilities.

### 3.3.3.3 Different slip in both walls

For the analysis of the different slip coefficients at both walls, the linear Navier slip boundary condition was chosen. The variation of the pressure gradient with  $k'_1$  is shown in Fig. 3.8(a) for a case with no slip at one boundary, showing that the normalized pressure gradient varies from  $-3$  for  $k'_1 = 0$  to a maximum value of  $-0.75$  for  $k'_1 \rightarrow \infty$ . Different slip conditions distort the velocity profile as plotted in Fig. 3.8(b). As the slip velocity increases the velocity peak tends to the wall where there is slip ( $y/h = -1$ ). Still in this particular case, it is easily proven that the velocity profile for the limiting condition of infinite friction coefficient is given by the following quadratic expression.

$$\frac{u}{U} = 0.375 \left[ \left( \frac{y}{h} \right)^2 - 1 \right] + \left( \frac{y}{h} - 1 \right) \quad (3.46)$$

## 3.4 NON-NEWTONIAN FLUIDS (POISEUILLE FLOW)

### 3.4.1 Power law fluids

Analytical and semi-analytical solutions are derived for non-Newtonian fluids obeying the “power law” viscosity model. The solution for imposed pressure gradient flow (direct problem) in the extrusion barrel geometry given by Newtonian slip law has been reported elsewhere (Meijer and Verbraak, 1988; Potente et al., 2006) and we look now at the inverse solution.

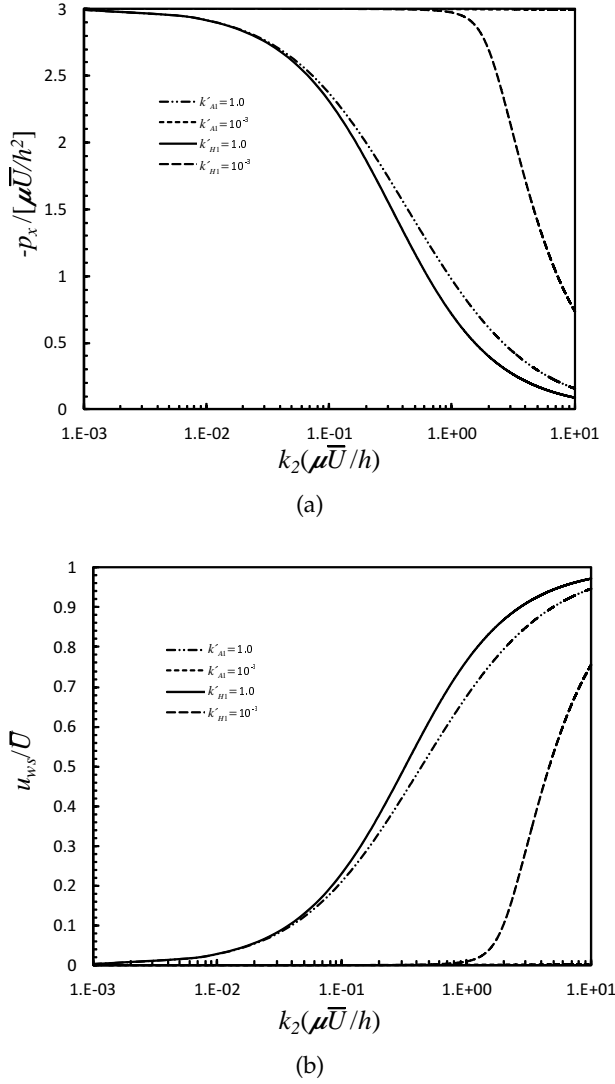


Figure 3.7: Comparison between the asymptotic and Hatzikiriakos slip laws for Poiseuille flow in a channel. (a) Variation of the normalized pressure drop for different values of the slip coefficient  $k'_2$  and two different values of  $k'_1$ . (b) Variation of the normalized slip velocity with the pressure drop.

Consider the momentum equation (Eq. 3.2), with the variable viscosity of Eq. 3.6. For symmetric boundary conditions consider only the lower half channel, where the velocity gradient is positive.

$$\eta(\dot{\gamma}) = a \left( \frac{du}{dy} \right)^{n-1} \tag{3.47}$$

For wall slip  $u(-h)$  the velocity profile is given by (cf. (Bird et al., 2002) for the pipe flow case),

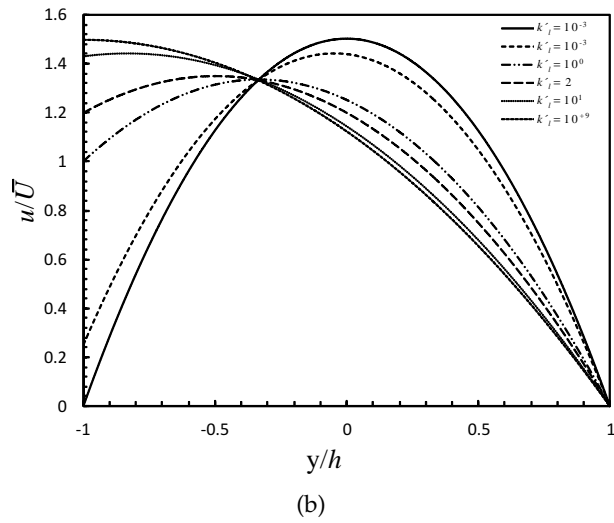
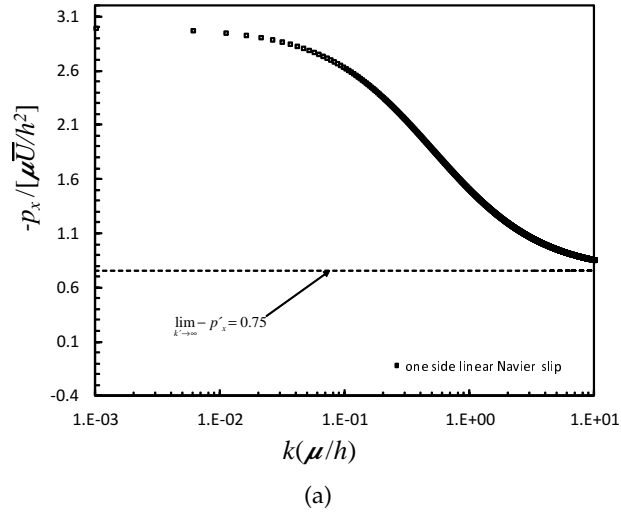


Figure 3.8: Study of the linear Navier slip boundary condition applied to the bottom wall of a channel flow: (a) Variation of the pressure gradient with the friction coefficient. (b) Velocity profile with no slip velocity at the top wall ( $y = 1$ ) and different slip coefficients at bottom ( $y = -1$ ).

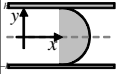
$$u(y) = \left(\frac{-p_x}{a}\right)^{1/n} \left(\frac{h^{1/n+1} - (-y)^{1/n+1}}{1/n+1}\right) + u(-h) \quad (3.48)$$

The solution for the “inverse problem” with an imposed mean velocity  $\bar{U}$  is given by solving Eq. 3.49,

$$\left(\frac{-p_x}{a}\right)^{1/n} \left(\frac{h^{1/n+1}}{1/n+2}\right) + u(-h) - \bar{U} = 0 \quad (3.49)$$

Hatzikiriakos and Mitsoulis (Hatzikiriakos and Mitsoulis, 2009) studied these flows with Navier non-linear slip law for special cases

Table 3.5: Analytical solutions for Poiseuille flow of a power law fluid for different sets of power law ( $n$ ) and slip ( $m$ ) coefficients.

Poiseuille Flow: Power-law fluid [linear ( $m=1$ ) and nonlinear Navier Slip ( $m \neq 1$ )] 	$n = 0.5$ $m = 1$	$p_x = \frac{k_n h^m - (k_n h^m + 4\bar{U}[a^{-2}h^{(1/n)+1}(1/n+2)^{-1}])^{0.5}}{2[a^{-2}h^{(1/n)+1}(1/n+2)^{-1}]}$
	$n = 0.5$ $m = 2$	$p_x = -\left(\bar{U}/[h^{(1/n)+1}((1/n+2)a^2)^{-1}] + k_n h^m\right)^{0.5}$
	$n = 0.5$ $m = 3$	Method given in Appendix C
	$n = 1/3$ $m = 1$	$p_x = \sqrt[3]{-q/2 + \sqrt{(q/2)^2 + (p/3)^2}} + \sqrt[3]{-q/2 - \sqrt{(q/2)^2 + (p/3)^2}}$ $p = \frac{k_n h}{[a^{-3}h^{(1/n)+1}(1/n+2)^{-1}]} \quad q = \frac{\bar{U}}{[a^{-3}h^{(1/n)+1}(1/n+2)^{-1}]}$
	$n = 1/3$ $m = 2$	Method given in appendix C
	$n = 1/3$ $m = 3$	$p_x = -\left(\bar{U}/[h^{(1/n)+1}((1/n+2)a^3)^{-1}] + k_n h^m\right)^{1/3}$
	$n = 2$ $m = 1$	$p_x = -\left(\frac{-L + (L^2 + 4\bar{U}L)^{0.5}}{2L}\right)^2 \quad L = [a^{-0.5}h^{(1/n)+1}(1/n+2)^{-1}]$

of the slip exponents  $1/n = m$  and making use of lubrication theory in tapered dies. They only presented full analytical solutions for the direct problem, whereas for the inverse problem the solutions are approximate because there is an unsolved integral in the equations. However, there is a closed form solution for their special case “Power-law ( $n = 1/2$ ) with linear slip” which we give at the end of Appendix D. For our geometry (Poiseuille flow in a channel), the analytical solutions for the special cases  $n = 1/2$  with  $m = 1, 2, 3$ ,  $n = 1/3$  with  $m = 1, 2, 3$ , and  $n = 2$  with  $m = 1$  are also in closed form and given in Table 3.5. For other values of the slip exponents and other slip laws Appendix D includes the proof of existence of a unique solution.

### 3.4.2 Sisko model-particular solutions for $n=0.5$ and $n=2$

When the fluid viscosity obeys the Sisko model (Eq. 3.7), integration of the momentum equation gives,

$$\mu_\infty \frac{du}{dy} + a \left(\frac{du}{dy}\right)^n - p_x y = 0 \tag{3.50}$$

The solution of Eq. 3.50 is complex and is only given below (in closed form for the direct problem) for the cases  $n = 0.5, 2$  (see Appendix E for the details).

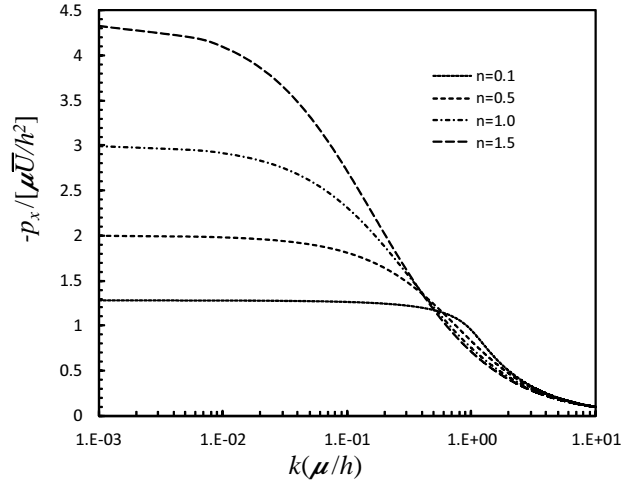
For  $n = 0.5$ :

$$u(y) = -\frac{\mu_\infty}{2a}(y+h) + \frac{[(\mu_\infty)^2 + 4ap_x y]^{3/2} - [(\mu_\infty)^2 + 4ap_x h]^{3/2}}{12a^2 p_x} + u(-h) = 0 \tag{3.51}$$

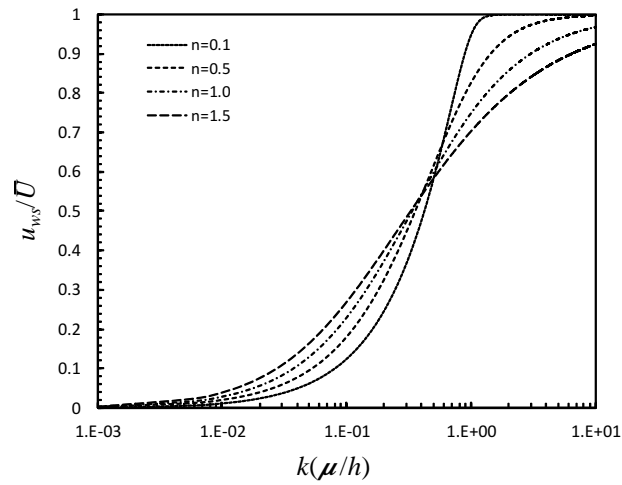
For  $n = 2$ :

$$u(y) = \frac{a^2(y+h)}{2\mu_\infty^2} + \frac{p_x(y^2-h^2)}{2\mu_\infty} + \frac{a\left([a^2-4\mu_\infty p_x h]^{3/2} - [a^2+4\mu_\infty p_x y]^{3/2}\right)}{12\mu_\infty^3 p_x} + u(-h) = 0 \quad (3.52)$$

### 3.4.3 Discussion (non-Newtonian fluids)



(a)



(b)

Figure 3.9: Power law fluid with Navier slip boundary condition: (a) Normalized pressure drop versus slip coefficient (b) Normalized slip velocity versus slip coefficient.

Figs. 3.9(a) and (b) show the variations of pressure gradient and the slip velocity with the slip coefficient for both shear-thinning ( $n < 1$ ) and shear-thickening ( $n > 1$ ) fluids. Increasing the slip coefficient decreases the magnitude of the favorable pressure gradient, with shear-thickening fluids leading to higher frictional loss than shear-thinning fluids. Similar variations are observed for the slip velocity in Fig.

3.9(b), except that for slip coefficients in excess of about  $5 \times 10^{-1}$  where shear-thinning fluids have higher velocities than shear-thickening fluids. For the non-linear Navier slip law, the viscosity power-law exponent has the major influence on the pressure gradient as seen in Fig. 3.10(a), something that is confirmed also by Fig. 3.10(b), for the Hatzikiriakos and asymptotic slip models. Fig. 3.10(b) also shows that the asymptotic model is much less sensitive to the friction coefficient than the Hatzikiriakos model.

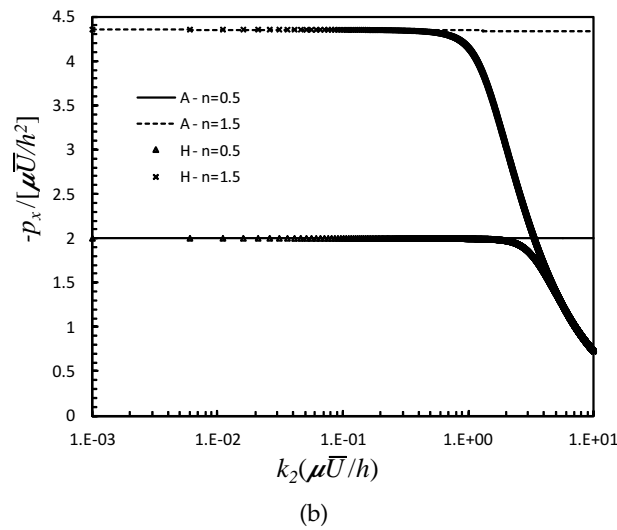
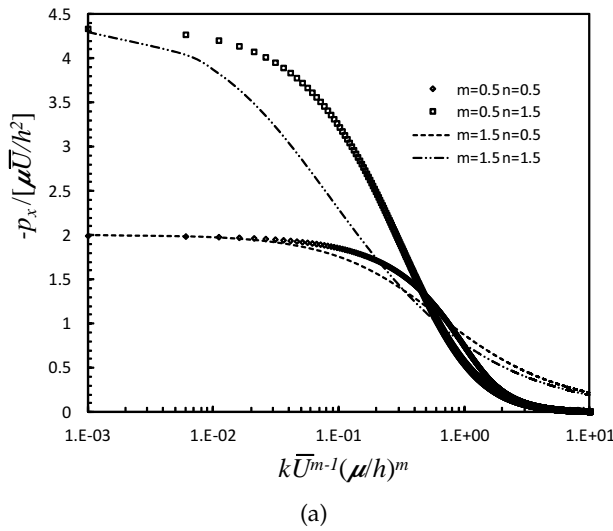


Figure 3.10: (a) Pressure drop versus friction coefficient for different slip and power law exponents. (b) Pressure drop versus friction coefficient for the asymptotic and Hatzikiriakos slip models with  $k'_1 = k_1 / U = 1E - 3$ ,  $k'_2 = k_2 \eta U / h$ .

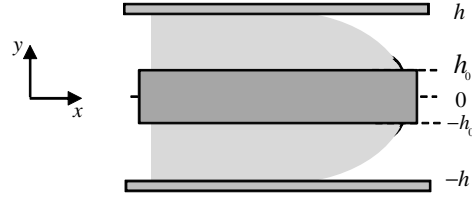


Figure 3.11: Geometry for the yield stress fluids. The plug zone goes from  $-y_0$  to  $y_0$ . The channel width is  $2h$ .

#### 3.4.4 Yield Stress fluids - Herschel-Bulkley and Robertson-Stiff models

The Poiseuille flow of a yield stress fluid is characterized by a “plug region” everywhere the yield stress  $\tau_0$  is not exceeded and where the rate of strain tensor is identically zero. The motion of the plug region, is determined by the following form of the momentum equation (Frigaard et al., 1994),

$$\oint_{\partial\Omega} (\boldsymbol{\sigma} \cdot \mathbf{n}) ds = \int_{\Omega} \rho \frac{d\mathbf{u}}{dt} d\Omega \quad (3.53)$$

with,  $\boldsymbol{\sigma} = -p\boldsymbol{\delta} + \boldsymbol{\tau}$ ,  $p$ - pressure,  $\boldsymbol{\delta}$ - unity tensor,  $\boldsymbol{\tau}$ - deviatoric stress tensor and  $\mathbf{n}$  the normal vector to the surface  $\partial\Omega$ .

Considering the geometry in Fig. 3.11, integration of the momentum equation gives the shear stress distribution,

$$\tau_{xy} = -p_x y \quad (3.54)$$

For fully developed flow the momentum equation applied to the geometry of Fig. 3.11 states that,

$$\underbrace{\int_a^b \tau_{xy} dx}_{\text{upper wall}} - \underbrace{\int_a^b -\tau_{xy} dx}_{\text{bottom wall}} + \underbrace{\int_{-y}^y \tau_{xya} - p_a dx}_{\text{left side}} - \underbrace{\int_{-y}^y \tau_{xyb} - p_b dx}_{\text{right side}} = 0 \quad (3.55)$$

The stress profile is linear across the channel and based on equation 3.54 the yield surface distances are given by,

$$\pm h_0 = \tau_0 / p_x = \tau_0 h / \tau_w \quad (3.56)$$

$$p_x = \tau_w / h \quad (3.57)$$

$$\pm h_0 = \tau_0 h / \tau_w \quad (3.58)$$

where  $\tau_w$  with  $\tau_w > 0$  is the stress at the walls ( $y = \pm h$ ) and  $\tau_0$  is the yield stress.

To obtain the solution for the Herschel-Bulkley and the Robertson-Stiff models, we followed the procedure of (Fordham et al., 1991),



except that here the slip velocity is included. The two rheological models can be written depending on the stress invariant,

$$\left\{ \begin{array}{l} \dot{\gamma} = \left(\frac{\tau_0}{\mu_0}\right)^{1/n} \left(\frac{|\tau|}{\tau_0} - 1\right)^{1/n} \\ \dot{\gamma} = \left(\frac{\tau_0}{\mu_0}\right)^{1/n} \left(\left(\frac{|\tau|}{\tau_0}\right)^{1/n} - 1\right) \end{array} \right. \text{ if } |\tau| > \tau_0 \text{ and } (\dot{\mathbf{f}} = 0 \text{ if } |\tau| \leq \tau_0) \quad (3.59)$$

The flow rate dependence on the pressure gradient (direct problem) results from integration of the velocity profile over the domain (half of the domain because of symmetry) and lead to the following velocity profiles (subscripts HB and RS stand for the Herschel-Bulkley and Robertson-Stiff models, respectively).

$$\left\{ \begin{array}{l} u(y)_{HB} \\ u = \frac{n\left(\frac{p_x}{\mu_0}\right)^{1/n}}{1+n} \left[ (h-h_0)^{(1+n)/n} - (y-h_0)^{(1+n)/n} \right] + u(h), \quad h_0 \leq |y| \leq h \\ u_{plug} = \frac{n\left(\frac{p_x}{\mu_0}\right)^{1/n}}{1+n} \left[ (h-h_0)^{(1+n)/n} \right] + u(h), \quad 0 \leq |y| \leq h_0 \end{array} \right. \quad (3.60)$$

$$\left\{ \begin{array}{l} u(y)_{RS} \\ u = \left(\frac{\tau_0}{\mu_0}\right)^{1/n} (y-h) - \frac{n\left(\frac{p_x}{\mu_0}\right)^{1/n}}{1+n} \left[ (y)^{(1+n)/n} - (h)^{(1+n)/n} \right] + u(h), \quad h_0 \leq |y| \leq h \\ u_{plug} = \left(\frac{\tau_0}{\mu_0}\right)^{1/n} (y-h) - \frac{n\left(\frac{p_x}{\mu_0}\right)^{1/n}}{1+n} \left[ (h_0)^{(1+n)/n} - (h)^{(1+n)/n} \right] + u(h), \quad 0 \leq |y| \leq h_0 \end{array} \right. \quad (3.61)$$

To determine the inverse problem solution we impose a flow rate  $Q = \bar{U}h$  and integrate over half of the channel width leading to the following solutions for the Herschel-Bulkley model,

$$\frac{n\left(\frac{p_x}{\mu_0}\right)^{1/n}}{1+n} \left[ h(h-h_0)^{(1+n)/n} - \frac{n(h-h_0)^{(1+2n)/n}}{1+2n} \right] + hu(h) - Q = 0 \quad (3.62)$$

and the Robertson-Stiff model,

$$\frac{n\left(\frac{\tau_0}{\mu_0}\right)^{1/n}(h_0)^{-1/n}}{1+2n} \left(h^{1/n+2} - (h_0)^{1/n+2}\right) - \frac{1}{2} \left(\frac{\tau_0}{\mu_0}\right)^{1/n} \left(h^2 - (h_0)^2\right) + hu(h) - Q = 0 \quad (3.63)$$

respectively. In both cases  $h_0 = \tau_0/p_x$  and the non-linear equations must be solved numerically.

Bingham fluids:

For the special case of Bingham fluids (Herschel-Bulkley model with  $n = 1$ ) with Navier slip boundary condition, the full analytical solution is possible and is given by Eq. 3.64 for the direct problem,

$$u(y)_{HB} = \begin{cases} u_{fluid} = \frac{B}{2x} \left[ (1-x)^2 - (|y'| - x)^2 \right] + k_B, & x \leq |y| \leq 1 \\ u_{plug} = \frac{B}{2x} (1-x)^2 + k_B, & 0 \leq |y| \leq x \end{cases} \quad (3.64)$$

and by Eq. 3.65 for the inverse problem,

$$\underbrace{\frac{\tau_0^3 (B/6)}{6\mu_0}}_a x^3 - \underbrace{(B/2 + 1)}_b x + \underbrace{B/3 + k_B}_c = 0 \quad (3.65)$$

where  $B$  is the Bingham number  $B = \tau_0 h / \mu_0 \bar{U}_0$ ,  $x = \tau_0 / \tau_w$ ,  $k_B = k \tau_0 / \bar{U}_0$ . The algebraic solution of this cubic equation is given as Eq. 3.66 with  $p = b/a$  and  $q = c/a$ .

$$x = \sqrt[3]{-q/2 + \sqrt{(q/2)^2 + (p/3)^2}} + \sqrt[3]{-q/2 - \sqrt{(q/2)^2 + (p/3)^2}} \quad (3.66)$$

Note that this solution is presented in the literature (Frigaard et al., 1994) in the absence of slip. Analytical solutions for Bingham fluids with Navier Slip boundary conditions could be found for the special case of squeeze flow between parallel disks for the regularized bi-viscosity model with imposed pressure gradient (Yang and Zhu, 2006); a similar study is also given by (Estellé and Lanos, 2007).

#### 3.4.4.1 Discussion (non-Newtonian fluids with yield stress):

For the yield stress fluids, the Bingham fluid was chosen. The studies were made varying the parameters  $B$  and  $k_B$ . Fig. 3.12 shows the dramatic increase of stress ratio  $\tau_0 / \tau_w$  with the slip coefficient, which means that the pressure gradient decreases and the plug size increases. The stress ratio  $\tau_0 / \tau_w$  also decreases with the increase of the Bingham number. As the slip coefficient increases the plug grows in size towards the wall and it is not always possible to have a solution (un-yielded fluid). In fact the yield stress cannot exceed the wall stress. Table 3.6

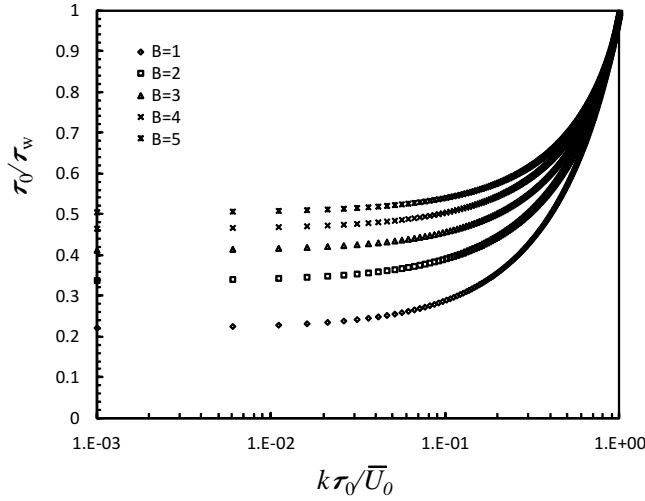


Figure 3.12: Variation of  $y_0 = \tau_0/\tau_w$  with the (dimensionless) slip coefficient  $k_B = k\tau_0/\bar{U}_0$ .

Table 3.6: Different values of  $y_0 = \tau_0/\tau_w$  for different slip coefficients  $k_B = k\tau_0/\bar{U}_0$ .

$k_B$	$B=1$	$B=2$	$B=3$	$B=4$	$B=5$
0	0.22414	0.34041	0.41466	0.46748	0.50762
0	0.23025	0.34519	0.41868	0.47100	0.51078
0	0.29165	0.39349	0.45939	0.50669	0.54285
1	1.00000	1.00000	1.00000	1.00000	1.00000
10	4.70831	3.79807	3.38972	3.14680	2.98233

shows that for some values of  $k_B$  this condition is violated and this can bring problems to numerical simulation.

### 3.5 CONCLUSION

Analytical and semi-analytical solutions were presented for the direct and inverse flow problems of Couette-Poiseuille flows of Newtonian and non-Newtonian fluids. As for the non-Newtonian fluids only inelastic models were considered namely the Power law, Sisko and two yield stress fluid models (Herschel-Bulkley and Robertson-Stiff). Four different slip models were considered, namely the Navier linear and non-linear slip laws, the asymptotic law and the Hatzikiriakos slip law. For some fluids, only particular solutions were presented, as for the Sisko fluid, whereas for cases where the solution could not be found analytically, the existence of the solution was proven, and the interval where the solution lies was given.

The proposed analytical solutions are valid for any values of the employed models' parameters, thus they cover all the slip velocity data given in the literature both for Newtonian and non-Newtonian fluids.

## ACKNOWLEDGEMENTS

The authors would like to acknowledge the financial support provided by Fundação para a Ciência e Tecnologia (FCT) under the project SFRH / BD / 37586 / 2007, and FEDER via FCT, under the POCI 2010 and Pluriannual programs.

## APPENDIX A: COUETTE FLOW OF NEWTONIAN FLUIDS WITH THE NONLINEAR NAVIER SLIP BOUNDARY CONDITION AT THE BOTTOM WALL AND NO-SLIP AT THE TOP WALL

In the nonlinear Navier slip law the boundary conditions are given by,

$$u(-h) = k(\mu c_1)^m \quad (3.67)$$

$$u(h) = U \quad (3.68)$$

This implies that the constant  $c_1 = \frac{U - k(\mu c_1)^m}{2h} \Leftrightarrow (c_1)^m + (2h/k\mu^m) c_1 - U/k\mu^m = 0$

For  $m = 0.5$  this nonlinear equation can be solved with the help of a variable change  $c_1^{0.5} = x \Rightarrow x^2 = c_1$ ,  $x > 0$  leading to the equation,

$$(2h/k\mu^m) x^2 + x - U/k\mu^m = 0 \quad (3.69)$$

which needs to be solved for the positive solution.

For  $m = 2$  the solution is trivial and for  $m = 3$  the Cardan-Tartaglia formula is used.

**Remark.** The solution  $c_1$  is always positive. Let  $f(c_1)$  be a function of the constant  $c_1$  and given by  $f(c_1) = (c_1)^m + (2h/k\mu^m) c_1 - U/k\mu^m$ . The derivative of  $f(c_1)$  is  $f'(c_1) = m(c_1)^{m-1} + (2h/k\mu^m)$ . It can also be seen that  $f'(c_1) > 0, \forall c_1 \geq 0$ ,  $f(0) < 0$  and that  $f\left([U/k\mu^m]^{1/m}\right) > 0$ . We can now conclude by Bolzano and Rolle theorems that there is a unique solution  $c_1$  to equation  $f(c_1) = 0$ , in the range,  $\left[0; [U/k\mu^m]^{1/m}\right]$ .

## APPENDIX B: POISEUILLE FLOW OF A NEWTONIAN FLUID WITH NON-LINEAR SLIP LAWS

For  $m = 0.5, 1, 2$  and  $3$ , a full analytical solution can be obtained and is given in table 3.2.

The existence of a unique solution can be proved provided  $m > 0$ . The derivative of Eq. 3.38 is given by,

$$-\frac{h^2}{3\mu} - mkh^m (-p_x)^{m-1} < 0, \forall p_x < 0 \quad (3.70)$$

Let

$$f(p_x) = -\frac{p_x}{3\mu}h^2 + kh^m(-p_x)^m - \bar{U} \quad (3.71)$$

Then  $f(0) = -\bar{U}$  and  $f(-3\bar{U}\mu/h^2) = kh^m(3\bar{U}\mu/h^2)^m > 0$ , together with  $f(-\bar{U}^{1/m}/kh^m) = \bar{U}^{1/m}h^2/(3\mu kh^m) > 0$ . By Bolzano and Rolle theorems there is a unique solution in the range  $]0; A[$  with  $A = \min\{-3\bar{U}\mu/h^2; -\bar{U}^{1/m}/kh^m\}$ .

#### APPENDIX C: DERIVATION OF EQUATIONS FOR DIFFERENT SLIP COEFFICIENTS AT TOP AND BOTTOM WALLS

Assume for the top wall the Navier slip boundary condition of Eq. 3.72 and at the bottom wall the non-linear Navier slip law of Eq. 3.73 with  $m = 2, 3$ .

$$u(h) = k_1(-p_x h - \mu c_1) \quad (3.72)$$

$$u(-h) = k_2(-p_x h + \mu c_1)^m \quad (3.73)$$

The system of equations to be solved is,

$$\begin{cases} -2hc_1 + u(h) - u(-h) = 0 \\ -\frac{p_x}{3\mu}h^2 - c_1h + u(h) - \bar{U} = 0 \end{cases} \quad (3.74)$$

where the second equation of the system is independent of the slip exponent and can be solved for the pressure gradient,

$$p_x = \frac{c_1h + k_1\mu c_1 + U}{-k_1h - \frac{h^2}{3\mu}} \quad (3.75)$$

By substitution of Eq. 3.75 into 3.74 a quadratic and a cubic equation are obtained for  $c_1$  for  $m = 2$  and 3, respectively.

The solution for  $m = 2$  is given by Eq. 3.74 with constants (Eqs.) 3.75 and 3.76,

$$c_1 = \left(16k_2\mu^2(1.5k_1\mu + h)^2\right)^{-1} \left(\sqrt{24}[(3k_1\mu + h)^2(1.5k_1^2\mu^4k_2U + 2.5k_2\mu^3k_1Uh + h^2\mu^2[k_2U + (1/6)k_1^2] + (1/6)h^3k_1\mu + (1/24)h^4)]^{0.5} - 18k_2\mu^3k_1U + (-6k_1^2 - 12k_2U)h\mu^2 - 5h^2k_1\mu - h^3\right) \quad (3.76)$$

For  $m = 3$  one has to solve the equation,

$$c_1^3 + bc_1^2 + cc_1 + d = 0 \quad (3.77)$$

with coefficients,

$$\begin{aligned}
b &= \frac{B}{A}, \quad c = \frac{C}{A}, \quad d = \frac{D}{A} \\
A &= 288k_2\mu^4h^2 + 432k_2\mu^5hk_1^2 + 64k_2\mu^3h^3 + 216k_2\mu^6k_1^3 \\
B &= 432k_2\mu^4hk_1U + 144k_2\mu^3h^2U + 324k_2\mu^5k_2U \\
C &= 16h^3k_1\mu + 42h^2k_1^2\mu^2 + 36hk_1^3\mu^3 + 108k_2\mu^3hU^2 + 162k_2\mu^4k_1U^2 + 2h^4 \\
D &= -3k_1\mu Uh^2 - 18k_1^2\mu^2Uh + 27k_2\mu^3U^3 - 27k_1^3\mu^3U
\end{aligned} \tag{3.78}$$

Making the substitution  $c_1 = x - b/3$  the equation transforms to  $x^3 + ex + f = 0$ , and the so called Vieta substitution  $x = y - e/3y$ , leads to a quadratic equation for  $y^3$ .

$$(y^3)^2 + f(y^3) - e^3/27 = 0 \tag{3.79}$$

This equation gives six solutions that reduce to three after back substitution.

#### APPENDIX D: PROOF OF EXISTENCE OF A UNIQUE SOLUTION FOR POISEUILLE FLOWS OF POWER LAW FLUIDS WITH SLIP

Let  $f(p_x)$  be given by Eq. D1 and  $u(h)$  be given by Eqs.3.20, 3.22 and 3.24.

$$f(p_x) = \left(\frac{-p_x}{a}\right)^{1/n} \left(\frac{h^{1/n+1}}{1/n+2}\right) + u(h) - \bar{U} \tag{3.80}$$

Let  $f'(p_x)$  represent the derivative of the function  $f(p_x)$ ,

$$f'(p_x) = \left(\frac{h^{1/n+1}}{(1/n+2)an}\right) \left(\frac{-p_x}{a}\right)^{1/n-1} + \frac{du(h)}{dp_x} < 0 \quad \forall p_x < 0 \tag{3.81}$$

$\frac{du(h)}{dp_x}$  is given by,

$$-m kh^m (-p_x)^{m-1} < 0 \tag{3.82}$$

$$-k_1 k_2 h \cosh(-k_2 p_x h) < 0 \tag{3.83}$$

$$\frac{-k_1 k_2 h}{1 - k_2 p_x h} < 0 \tag{3.84}$$

for the non-linear Navier, asymptotic and Hatzikiriakos slip models, respectively.

$$\begin{aligned}
\text{For all cases } f(0) &= -\bar{U} \text{ and } f\left(-a \left[\frac{\bar{U}(1/n+2)}{h^{1/n+1}}\right]^n\right) > 0, \\
f\left(-\bar{U}^{1/m}/kh^m\right) &= \bar{U}^{1/m} h^2 / 3\mu kh^m > 0.
\end{aligned}$$

Regarding now the application of the slip condition, we have the following three models:

Non-linear Navier slip law:

$f\left(-\bar{U}^{1/m}/kh^m\right) = \bar{U}^{1/m}h^2/3\mu kh^m > 0$ . By Bolzano and Rolle theorems there is a unique solution in the range  $]0; A[$ , with:

$$A = \min \left\{ -a \left[ \frac{\bar{U}(1/n+2)}{h^{1/n+1}} \right]^n ; -\bar{U}^{1/m}/kh^m \right\}.$$

Hatzikiriakos slip law:

$f\left(-\operatorname{arcsinh}(\bar{U}/k_1)\right)/hk_2 > 0$ . There is unique solution in the range  $]0; A[$  with:

$$A = \min \left\{ -a \left[ \frac{\bar{U}(1/n+2)}{h^{1/n+1}} \right]^n ; -\operatorname{arcsinh}(\bar{U}/k_1)/hk_2 \right\}.$$

Asymptotic slip law:

$f\left(-(\exp(\bar{U}/k_1) - 1)/hk_2\right) > 0$ . There is unique solution in the range  $]0; A[$  with:

$$A = \min \left\{ -a \left[ \frac{\bar{U}(1/n+2)}{h^{1/n+1}} \right]^n ; -(\exp(\bar{U}/k_1) - 1)/hk_2 \right\}.$$

**Power-law Case ( $n = 1/2$ ) with Linear Slip** from Hatzikiriakos and Mitsoulis (Hatzikiriakos and Mitsoulis, 2009).

Their Eq. 11 is now simplified and given by,

$$\Delta p = \frac{B}{2A} \left[ \frac{1}{R_L} - \frac{1}{R_0} \right] - \left( \frac{R_0(B^2R_0+4QA)\sqrt{\frac{B^2R_0+4QA}{A^2R_0^5}}}{12QA} + \frac{R_1(B^2R_1+4QA)\sqrt{\frac{B^2R_1+4QA}{A^2R_1^5}}}{12QA} \right) \quad (3.85)$$

#### APPENDIX E: DERIVATION OF ANALYTICAL SOLUTION FOR SSKO MODEL

The Sisko model is given by Eq. 3.7 and its substitution into the integrated form of the momentum equation (Eq. 3.5) gives

$$\mu_\infty \frac{du}{dy} + a \left( \frac{du}{dy} \right) - p_x y = 0 \quad (3.86)$$

It is difficult to obtain the solution of this equation, because of its non-linear nature associated with the exponent, unless some particular values are explored such as  $n = 0.5, 1, 2$ .

For  $n = 0.1$  Eq. 3.86 is quadratic in  $du/dy$ . Let  $x = (du/dy)^{0.5}$  leading to,

$$\mu_\infty x^2 + ax - p_x y = 0 \quad (3.87)$$

The solutions for this equation is given by,

$$x = -\frac{a}{2\mu_\infty} \pm \frac{1}{2\mu_\infty} \sqrt{a^2 + 4\mu_\infty p_x y} \quad (3.88)$$

In order to pick the physically solution acceptable, it should be noticed that  $du/dy > 0$  at  $y = -h$ . Notice that  $4\mu_\infty p_x y \geq 0$  for  $y \in$

$[-h; 0]$ (favorable pressure gradient is negative) and  $\sqrt{a^2 + 4\mu_\infty p_x y} > a^2$  leading to,

$$\frac{du}{dy} = \frac{a^2}{2\mu_\infty^2} - \frac{a\sqrt{a^2 + 4\mu_\infty p_x y}}{2\mu_\infty^2} + \frac{p_x y}{2\mu_\infty} \quad (3.89)$$

After integration

$$u(y) = \frac{a^2}{2\mu_\infty^2} y + \frac{p_x y^2}{2\mu_\infty} - \frac{a}{12\mu_\infty^3 p_x} [a^2 + 4\mu_\infty p_x y]^{3/2} + c \quad (3.90)$$

and applying the slip boundary condition  $u(-h)$ , the constant  $c$  is revealed and the final solution, depending on the pressure gradient, is given by

$$u(y) = \frac{a^2(y+h)}{2\mu_\infty^2} + \frac{p_x(y^2-h^2)}{2\mu_\infty} + \frac{a([a^2-4\mu_\infty p_x h]^{3/2} - [a^2+4\mu_\infty p_x y]^{3/2})}{12\mu_\infty^3 p_x} + u(-h) \quad (3.91)$$

The solution to the inverse problem is given by solving the following equation with  $p_x$  as a variable,

$$\frac{\frac{a^2 h}{4\mu_\infty^2} - \frac{p_x h^2}{3\mu_\infty} + \frac{a[a^2-4\mu_\infty p_x h]^{3/2}}{8\mu_\infty^3 p_x}}{\frac{a([a^2-4\mu_\infty p_x h]^{5/2} - a^5)}{120h\mu_\infty^4 p_x^2}} + u(-h) - \bar{U} = 0 \quad (3.92)$$

For  $n = 1$  the solution is exactly the same as the one obtained for the Poiseuille flow and Newtonian fluid, but  $\eta_0 + a$  should be used instead of  $\mu$ .

For  $n = 2$  the integrated momentum equation is again quadratic,

$$a \left( \frac{du}{dy} \right)^2 + \mu_\infty \frac{du}{dy} - p_x y = 0 \quad (3.93)$$

and its solution is given by,

$$\frac{du}{dy} = -\frac{\mu_\infty}{2a} \pm \frac{1}{2a} \sqrt{\mu_\infty^2 + 4ap_x y} \quad (3.94)$$

Proceeding as for the case  $n = 0.5$  one has that,

$$u(y) = -\frac{\mu_\infty}{2a} y + \frac{2(\mu_\infty^2 + 4ap_x y)^{3/2}}{24a^2 p_x} + c \quad (3.95)$$

Applying the boundary condition  $u(-h)$ , we find the final solution depending on the pressure gradient,

$$u(y) = -\frac{\mu_\infty}{2a} (y+h) + \frac{(\mu_\infty^2 + 4ap_x y)^{3/2} - (\mu_\infty^2 - 4ap_x h)^{3/2}}{12a^2 p_x} + u(-h) \quad (3.96)$$



The solution to the inverse problem is given by the following equation with  $p_x$  as a variable,

$$-\frac{\mu_\infty h}{2a} - \frac{(\mu_\infty^2 - 4ap_x h)^{3/2}}{12a^2 p_x} + \frac{(\mu_\infty^5 - (\mu_\infty^2 - 4ap_x h)^{3/2})^{3/2}}{120ha^2 p_x} + u(-h) - \bar{U} = 0 \quad (3.97)$$



## ANALYTICAL SOLUTIONS FOR CHANNEL SLIP FLOWS OF PTT AND GIESEKUS FLUIDS

---

### Abstract<sup>1</sup>

*Analytical and semi-analytical solutions are presented for the cases of channel and pipe flows with wall slip for viscoelastic fluids described by the simplified PTT (using both the exponential and the linearized kernel) and the Giesekus models. The slip laws used are the linear and nonlinear Navier, the Hatzikiriakos and the asymptotic models. For the nonlinear Navier slip only natural numbers can be used for the exponent of the tangent stress in order to obtain analytical solutions. For other values of the exponent and other nonlinear laws a numerical scheme is required, and thus, the solution is semi-analytical. For these cases the intervals containing the solution and the corresponding proof for the existence and uniqueness are also presented. For the Giesekus model the influence of the wall slip on the restrictions of the slip models are also investigated.*

### 4.1 INTRODUCTION

Analytical solutions are a valuable tool to understand the complexity of fluid dynamics. The Cauchy equation together with a rheological constitutive equation, allow the determination of the flow characteristics of non-Newtonian fluids. However, these are complex equations for which analytical solutions can only be obtained for basic flows in simple geometries. Adding slip boundary conditions to this system of equations increases the complexity to obtain analytical solutions. Understanding the influence of slip on the flow behaviour is crucial to comprehend some characteristics of industrial flows (Denn, 2001), relevant for the polymer processing industry. The mathematical study of Navier slip boundary conditions for Stokes fluids was carried out by (Fujita, 2002), who was only concerned with the wellposedness of the system of equations. Mitsoulis and Hatzikiriakos (2009) have studied the application of these slip boundary conditions to polymer extrusion using generalized Newtonian fluids. Later they presented some analytical solutions for lubrication flows in convergent channels and compared them with the corresponding numerical results (Hatzikiriakos and Mitsoulis, 2009). In this way they could identify the conditions for validity of the analytical solution obtained using the lubrication theory, for different degrees of contraction.

---

<sup>1</sup> L.L. Ferrás, J.M. Nóbrega, FT Pinho (2012), Analytical solutions for channel flows of Phan-Thien–Tanner and Giesekus fluids under slip, *Journal of Non-Newtonian Fluid Mechanics* **171-172** 97-105;

For viscoelastic materials described by a differential stress constitutive equation, published work using slip boundary conditions is scarce. Here, (Pereira, 2009) studied microfluidic flows under slip of Newtonian, generalized Newtonian and viscoelastic fluids governed by the linearized White-Metzner model using the Navier slip boundary condition.

For the simplified Phan-Thien—Tanner (PTT) and Giesekus models no analytical solutions with slip boundary conditions have been reported in the literature, but there are several analytical solutions in the absence of wall slip. For the PTT fluid we single out the solutions for Couette flow (Azaiez et al., 1996; Carew et al., 1993; Alves et al., 2001a), and for channel and pipe flows (Oliveira and Pinho, 1999a). For the Giesekus model solutions exist for no slip channel and pipe flows with the inclusion of a solvent contribution (Yoo and Choi, 1989) as well as without solvent (Schleiniger and Weinacht, 1991). There are also analytical solutions for no slip planar Couette-Poiseuille flow (Raisi et al., 2008), concentric annular flow (Mostafaiyan et al., 2004; Mohseni and Rashidi, 2010) and Taylor-Couette flow with inner cylinder rotation (Ravanchi et al., 2007).

The aim of this work is then, to fill the gap of analytical solutions for Couette and Poiseuille flows of viscoelastic fluids described by the simplified PTT and Giesekus constitutive equations considering slip velocity at the wall.

The paper is organized as follows: first, in subsection 2, the governing equations are presented for both constitutive models and the various slip models used are also presented and simplified for the simple case of flow between parallel plates. These slip laws are the linear and the nonlinear Navier, the Hatzikiriakos and the asymptotic slip models. In subsection 3 analytical solutions are given for the Couette and the Poiseuille flows of a PTT fluid under various conditions for the selected slip laws. For some cases like the Navier slip law, it is possible to present an analytical solution for the inverse problem (where the pressure gradient is computed as a function of the average velocity), but for the remaining cases the numerical solution of an equation is required (semi-analytical solution). In subsection 4, the Giesekus model (Giesekus, 1982) is considered and again the Couette and Poiseuille flows are studied for the various slip laws. Subsection 5 concludes/summarizes the main findings of this work.

## 4.2 GOVERNING EQUATIONS

It is assumed that the fluid is incompressible and governed by the continuity (Eq. 4.1) and momentum (Eq. 4.2) equations,

$$\nabla \cdot \mathbf{u} = 0 \quad (4.1)$$

$$\frac{\partial \rho \mathbf{u}}{\partial t} + \rho \nabla \cdot \mathbf{u} \mathbf{u} = -\nabla p + \nabla \cdot \boldsymbol{\tau} \quad (4.2)$$

together with a constitutive equation for the stress  $\boldsymbol{\tau}$ . In Eqs. 4.1 and 4.2,  $\mathbf{u}$  is the velocity vector,  $p$  is the pressure and  $\boldsymbol{\tau}$  is the deviatoric stress tensor.

The simplified PTT constitutive model is given by Eq. 4.3,

$$f(tr\boldsymbol{\tau}) \boldsymbol{\tau} + \lambda \left( \overset{\nabla}{\boldsymbol{\tau}} \right) = \eta \left( \nabla \mathbf{u} + (\nabla \mathbf{u})^T \right) \quad (4.3)$$

where  $f(tr\boldsymbol{\tau})$  is a function depending on the trace of the stress tensor,  $\lambda$  is the relaxation time,  $\eta$  is the viscosity coefficient and  $\overset{\nabla}{\boldsymbol{\tau}}$  stands for Oldroyd's upper convective derivative (Eq. 4.4),

$$\overset{\nabla}{\boldsymbol{\tau}} = \frac{\partial \boldsymbol{\tau}}{\partial t} + \mathbf{u} \cdot \nabla \boldsymbol{\tau} - \left[ (\nabla \mathbf{u})^T \cdot \boldsymbol{\tau} + \boldsymbol{\tau} \cdot \nabla \mathbf{u} \right] \quad (4.4)$$

The function  $f(tr\boldsymbol{\tau})$  can take the form of the exponential equation (Phan-Thien, 1978),

$$f(tr\boldsymbol{\tau}) = \exp \left( \frac{\varepsilon \lambda}{\eta} (tr\boldsymbol{\tau}) \right) \quad (4.5)$$

as well as the linearized function (Eq. 4.6), presented by (Phan-Thien and Tanner, 1977),

$$f(tr\boldsymbol{\tau}) = 1 + \frac{\varepsilon \lambda}{\eta} (tr\boldsymbol{\tau}) \quad (4.6)$$

Parameter  $\varepsilon$  is inversely proportional to the extensional viscosity of the fluid and the linearized function only approaches well the exponential form at low deformations.

The Giesekus constitutive model is given by,

$$\boldsymbol{\tau} + \frac{\alpha \lambda}{\eta} (\boldsymbol{\tau} \cdot \boldsymbol{\tau}) + \lambda \overset{\nabla}{\boldsymbol{\tau}} = \eta \left( \nabla \mathbf{u} + (\nabla \mathbf{u})^T \right) \quad (4.7)$$

where  $\alpha$  is the so-called mobility parameter. This model is based on molecular concepts and it reproduces well many of the characteristics of polymeric fluids (Giesekus, 1982).

Considering a Cartesian coordinate system  $x, y, z$  with in the stream-wise, transverse and spanwise directions, respectively, and since the flows studied in this work are the fully developed Couette and Poiseuille flows (cf. Fig. 4.1), the governing equations can be simplified because,

$$\partial/\partial x = 0 \text{ (except for pressure)}, \partial v/\partial y = 0, \partial p/\partial y = 0 \quad (4.8)$$

This implies the automatic satisfaction of the continuity equation, whereas the momentum equation simplifies and can be integrated to become,

$$\tau_{xy} = p_x y + c_1 \quad (4.9)$$

where  $p_x$  stands for the pressure gradient in the  $x$  direction,  $\tau_{xy}$  is the shear stress and  $c_1$  is a stress constant. Eq. 4.9 is valid regardless of the rheological constitutive equation.

The simplified forms of the constitutive equations for the fully developed flow conditions are somewhat different and they will be presented later, at the beginning of the corresponding results section.

The slip boundary conditions investigated here are the linear and nonlinear Navier, the Hatzikiriakos and the asymptotic slip laws. For the **nonlinear Navier slip law** (Schowalter, 1988) the nonlinear power function relating wall shear stress and wall slip is given by Eq. 4.10,

$$u_{ws} = k_{nl} (\mp \tau_{xy,w})^m \quad (4.10)$$

where  $m > 0$  ( $m \in \mathbb{R}$ ). When  $m = 1$  the Navier linear slip law (Navier, 1822) is recovered. The signs  $\mp$  stand for the upper  $-$  and bottom  $+$  walls, assuming there is flow between the parallel plates and the coordinate system is given in Fig. 4.1.

Hatzikiriakos (Hatzikiriakos, 1993) proposed a slip model based on Eyring's theory of liquid viscosity that provides a smooth transition from no-slip to slip flow at the critical shear stress  $\tau_c$  (positive constant). The one dimensional **Hatzikiriakos slip law** is given by,

$$u_{ws} = \begin{cases} k_{H1} \sinh(k_{H2} (\mp \tau_{xy,w}) - \tau_c) & \text{if } \tau_{xy} \geq \tau_c \\ 0 & \text{if } \tau_{xy} < \tau_c \end{cases} \quad (4.11)$$

where  $k_{H1}, k_{H2} \in [0; +\infty[$  are the friction coefficients. In this work we have considered only a null critical stress ( $\tau_c = 0$ ).

The last slip model investigated here is the **asymptotic slip law**, given for one dimensional flow by,

$$u_{ws} = k_{A1} \ln(1 + k_{A2} (\mp \tau_{xy,w})) \quad (4.12)$$

with  $k_{A1}, k_{A2} \in [0; +\infty[$ .

### 4.3 ANALYTICAL SOLUTIONS FOR THE PTT FLUID AND DISCUSSION

For the fully developed Couette and Poiseuille flows (cf. Fig. 4.1), the system of rheological constitutive equations for the simplified PTT model is given by,

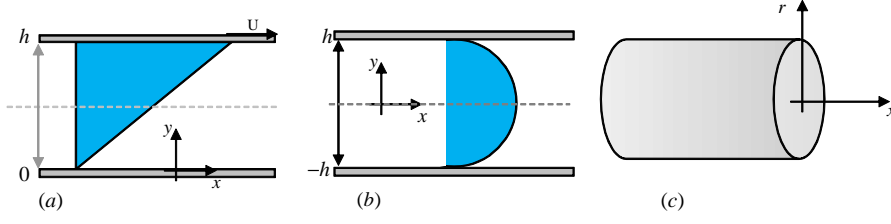


Figure 4.1: (a) Velocity profile across the flow channel assuming Couette-Poiseuille flow and slip at the wall (b) Different slip lengths  $0 = \bar{k}_0 < \bar{k}_1 < \bar{k}_2$  (zoom of the channel near the wall).

$$f(\tau_{xx} + \tau_{yy}) \tau_{xx} = 2\lambda \tau_{xy} (\partial u / \partial y) \quad (a)$$

$$f(\tau_{xx} + \tau_{yy}) \tau_{yy} = 0 \quad (b) \quad (4.13)$$

$$f(\tau_{xx} + \tau_{yy}) \tau_{xy} = \eta (\partial u / \partial y) + \lambda \tau_{yy} (\partial u / \partial y) \quad (c)$$

From Eq. 4.13(b) one can see that  $f(\tau_{xx} + \tau_{yy}) = 0 \vee \tau_{yy} = 0$ , but if  $f(\tau_{xx} + \tau_{yy}) = 0$ , unrealistic results would be obtained hence, the only possible solution is  $\tau_{yy} = 0$ .

Dividing Eq. 4.13(a) by Eq. 4.13(c), the former becomes  $\tau_{xx} = 2\lambda / \eta (\tau_{xy})^2$ . If Eqs. 4.13(a), (b), (c) are combined with the momentum equation, the following system is obtained,

$$\tau_{xy} = p_x y + c_1 \quad (a)$$

$$\tau_{xx} = 2\lambda / \eta (\tau_{xy})^2 \quad (b) \quad (4.14)$$

$$\tau_{yy} = 0 \quad (c)$$

$$f(\tau_{xx} + \tau_{yy}) \tau_{xy} = \eta (\partial u / \partial y) \quad (d)$$

Length, velocity and stresses are scaled with  $h$ ,  $U$  and  $\eta U / h$ , respectively ( $U$  is the mean streamwise velocity), leading to the dimensionless system of equations in Eq. 6.44, with  $y' = y/h$ ,  $u'(y') = u(y') / U$ ,  $c'_1 = c_1 / (\eta U / h)$  and  $\tau'_{xy} = \tau_{xy} / (\eta U / h)$

$$\tau'_{xy} = p'_x y' + c'_1 \quad (a)$$

$$\tau'_{xx} = 2Wi (p'_x y' + c'_1)^2 \quad (b) \quad (4.15)$$

$$\tau'_{yy} = 0 \quad (c)$$

$$(\partial u' / \partial y') = f[\tau'_{xx}] (p'_x y' + c'_1) \quad (d)$$

together with  $f[\tau'_{xx}] = 1 + 2\epsilon Wi^2 (p'_x y' + c'_1)^2$  for the linear PTT and the function  $f[\tau'_{xx}] = \exp(2\epsilon Wi^2 (p'_x y' + c'_1)^2)$  for the exponential PTT. In the previous expressions  $Wi = \lambda U / h$  is the Weissenberg number.

The boundary conditions are written in a dimensionless form for Couette flow in Eqs. 4.16, 4.17, 4.18 for the nonlinear Navier, the Hatzikiriakos and the asymptotic slip laws, respectively,

$$u'_{ws}(0) = k'_{nl} (c'_1)^m \quad (4.16)$$

$$u'_{ws}(0) = k'_{H1} \sinh(k'_{H2} c'_1) \quad (4.17)$$

$$u'_{ws}(0) = k'_{A1} \ln(1 + k'_{A2} c'_1) \quad (4.18)$$

and correspondingly by Eqs. 4.19, 4.20, 4.21 for Poiseuille flow,

$$u'_{ws}(\pm 1) = k'_{nl} (p'_x)^m \quad (4.19)$$

$$u'_{ws}(\pm 1) = k'_{H1} \sinh(k'_{H2} p'_x) \quad (4.20)$$

$$u'_{ws}(\pm 1) = k'_{A1} \ln(1 + k'_{A2} p'_x) \quad (4.21)$$

where  $k'_{nl} = kU^{m-1}(\eta/h)^m$ ,  $k'_{H1} = k_{H1}/U$ ,  $k'_{H2} = k_{H2}\eta U/h$ ,  $k'_{A1} = k_{A1}/U$ ,  $k'_{A2} = k_{A2}\eta U/h \in \mathbb{R}_0^+$ ,  $m \in \mathbb{R}^+$

#### 4.3.1 Couette flow - linear and exponential PTT models

For the Couette flow (Fig. 4.1(a)) with slip velocity at the moving wall, the only admissible solution for the velocity profile is the trivial solution  $u'(y') = 0$  (Ferrás et al., 2012c), regardless of the boundary condition at the immobile wall.

For the Couette flow with slip velocity at the immobile wall and no slip at the moving wall and since the pressure gradient is null (by Eq. 4.13(a) the shear stress is constant  $c'_1$ ) the system of equations simplifies to Eq. 19,

$$\begin{aligned} \tau'_{xy} &= c'_1 & (a) \\ \tau'_{xx} &= 2Wi (c'_1)^2 & (b) \\ \tau'_{yy} &= 0 & (c) \\ (\partial u' / \partial y') &= f[c'_1] (p'_x y' + c'_1) & (d) \end{aligned} \quad (4.22)$$

with  $f[c'_1] = 1 + 2\epsilon Wi^2 (c'_1)^2$  for the linear PTT and the function  $f[c'_1] = \exp(2\epsilon Wi^2 (c'_1)^2)$  for the exponential PTT.

Integrating equation 4.22(d) and applying the Dirichlet boundary condition at the upper wall,



$$u'_{ws}(1) = 1 \quad (4.23)$$

together with one of the slip boundary conditions (Eqs. 4.16, 4.17, 4.18) at the lower wall, the velocity profile  $u'(y')$  and  $c'_1$  are given by Eqs. 4.24 and 4.25 for the linear PTT model

$$u'(y') = \left[ c'_1 + 2\varepsilon Wi^2 (c'_1)^3 \right] y' + u'_{ws}(0) \quad (4.24)$$

$$c'_1 + 2\varepsilon Wi^2 (c'_1)^3 + u'_{ws}(0) - 1 = 0 \quad (4.25)$$

and by Eqs. 4.26 and 4.27 for the exponential PTT model

$$u'(y') = \exp\left(2\varepsilon Wi^2 (c'_1)^2\right) c'_1 y' + u'_{ws}(0) \quad (4.26)$$

$$\exp\left(2\varepsilon Wi^2 (c'_1)^2\right) c'_1 + u'_{ws}(0) - 1 = 0 \quad (4.27)$$

Due to nonlinearities, the full analytical solutions are obtained only for the following few cases: the linear PTT model with Navier slip law and exponents  $m = 1, 2, 3$ , and the exponential PTT with no slip velocity.

For the linear PTT with  $m = 1$ , we have that,

$$c'_1 = \left( (4\varepsilon Wi^2)^{-1} + \sqrt{(4\varepsilon Wi^2)^{-2} + \left(\frac{1+k'_{nl}}{6\varepsilon Wi^2}\right)^3} \right)^{1/3} + \left( (4\varepsilon Wi^2)^{-1} - \sqrt{(4\varepsilon Wi^2)^{-2} + \left(\frac{1+k'_{nl}}{6\varepsilon Wi^2}\right)^3} \right)^{1/3} \quad (4.28)$$

whereas for exponential PTT with  $k'_{nl} = 0$ ,  $c'_1$  is given by,

$$c'_1 = \left( 2 (\varepsilon Wi^2 / \mathbf{W} (4\varepsilon Wi^2))^{0.5} \right)^{-1} \quad (4.29)$$

Substitution of Eqs. 4.28 and 4.29 on the expressions for the velocity profile Eqs. 4.24 and 4.26 (for the linear and exponential PTT, respectively) gives the final solution. Note that the latter solution depends on the Lambert function, that can be expressed as the solution of Eq. 31.

$$\mathbf{W}(x) \exp(\mathbf{W}(x)) = x \quad (4.30)$$

These results show that the stress will be influenced by the presence of slip.

The analytical solutions for the nonlinear Navier slip model with  $m = 2, 3$  can be found in Appendix A, which includes the proof for

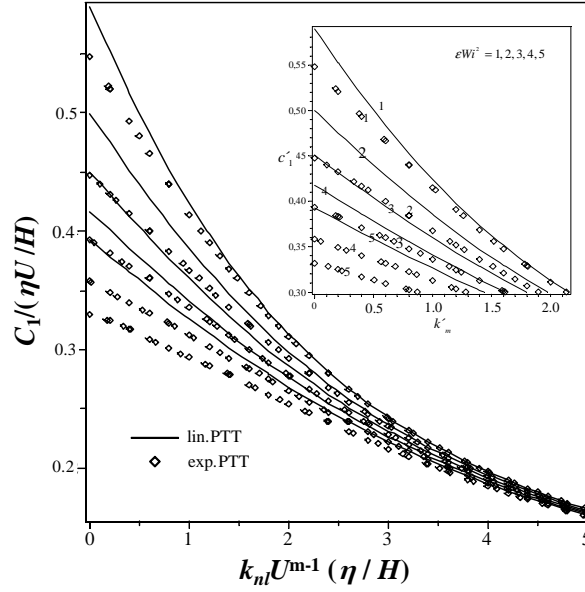


Figure 4.2: Variation of  $c'_1$  as a function of  $k'_{nl}$  and  $\epsilon Wi^2$  for Couette flow with slip at the fixed wall and no-slip at the moving wall. The  $\epsilon Wi^2$  numbers are given next to each graph in the zoomed view.

the existence and uniqueness of solutions for other values of  $m$  and for the Hatzikiriakos and asymptotic slip models, together with the corresponding interval where the solutions are located.

The relationship between slip velocity, stress and  $\epsilon Wi^2$  was studied for both PTT models with linear Navier slip law, and are plotted in Fig. 4.2.

As the slip velocity increases to total slip, the dimensionless shear stress decreases to zero, regardless of the slip model and Weissenberg number (for full slip conditions, the velocity profile is a plug flow since there is no shear and the normal stresses are null).

Lower shear stresses are obtained for the exponential PTT when compared with the linear PTT especially as the no-slip condition is approached. As slip increases the shear rates are smaller and under these conditions the linear stress function (first two terms of a Taylor expansion) approaches well the exponential stress function. It is also shown that the shear stress decreases with the increase of  $Wi$  on account of shear thinning behavior.

#### 4.3.2 Planar channel flow with the linear PTT model

For the Poiseuille flow (Fig. 4.1(b)) it is assumed that the same boundary condition is applied at the top and bottom walls leading to a symmetric flow, hence from Eq. 6.44(a) .

From Eq. 6.44(d) one obtains,

$$\begin{aligned}
\tau'_{xy} &= p'_x y' + c'_1 & (a) \\
\tau'_{xx} &= 2Wi \left( p'_x y' + c'_1 \right)^2 & (b) \\
\tau'_{yy} &= 0 & (c) \\
(\partial u' / \partial y') &= f \left[ \tau'_{xx} \right] \left( p'_x y' + c'_1 \right) & (d)
\end{aligned} \tag{4.31}$$

together with  $f \left[ \tau'_{xx} \right] = 1 + 2\epsilon Wi^2 \left( p'_x y' + c'_1 \right)^2$  for the linear PTT and the function  $f \left[ \tau'_{xx} \right] = \exp \left( 2\epsilon Wi^2 \left( p'_x y' + c'_1 \right)^2 \right)$  for the exponential PTT. In the previous expressions  $Wi = \lambda U/h$  is the Weissenberg number.

$$(\partial u' / \partial y') = p'_x y' + 2\epsilon Wi^2 \left( p'_x y' \right)^3 \tag{4.32}$$

that after integration gives,

$$u' \left( y' \right) = 0.5 p'_x y'^2 + 0.5 \epsilon Wi^2 \left( p'_x \right)^3 y'^4 + c, \quad c \in \mathbb{R} \tag{4.33}$$

where there are two unknowns, the pressure gradient  $p'_x$  and  $c$ . In order to obtain a unique solution and determine  $c$ , a boundary condition given by any of the Eqs. 4.19, 4.20, 4.21 must be provided, here represented by  $u'_{ws}(1)$ . The velocity profile is then given by Eq. 4.34,

$$u' \left( y' \right) = 0.5 p'_x \left( y'^2 - 1 \right) + 0.5 \epsilon Wi^2 \left( p'_x \right)^3 \left( y'^4 - 1 \right) + u'_{ws}(1) \tag{4.34}$$

By applying a constant flow rate  $Q = Uh$  (with the imposed average velocity) and integrating Eq. 4.34 over half of the channel width, the following equation is achieved for the pressure gradient,

$$\int_0^1 u' \left( y' \right) dy' = 1 \Rightarrow -\frac{2}{5} \epsilon Wi^2 \left( p'_x \right)^3 - \frac{p'_x}{3} - 1 + u'_{ws}(1) = 0 \tag{4.35}$$

The nonlinearity of Eq. 4.35 ( $u'_{ws}(1)$  depends on  $p'_x$ , cf. Eqs. 4.19, 4.20, 4.21) reduces the existence of full analytical solutions to just a few cases  $m = 1, 2, 3$ .

Assuming  $m = 1$  in Eq. 4.19(a), Eq. 4.35 can be rewritten after some algebra as,

$$\left( p'_x \right)^3 + \underbrace{p'_x \frac{1/3 + k'_{nl}}{2/5 \epsilon Wi^2}}_R + \underbrace{\left( (2/5) \epsilon Wi^2 \right)^{-1}}_Q = 0 \tag{4.36}$$

According to the Cardano-Tartaglia formula (Guilbeau, 1930) this cubic equation has the following real solution for the pressure gradient as a function of the imposed flow rate,

$$p'_x = \left( -Q/2 + \left[ (Q/2)^2 + (R/3)^3 \right]^{1/2} \right)^{1/3} + \left( -Q/2 - \left[ (Q/2)^2 + (R/3)^3 \right]^{1/2} \right)^{1/3} \quad (4.37)$$

with  $R$  and  $Q$  defined in Eq. 4.36.

With this explicit formula, the velocity profile (Eq. 4.34) will no longer depend on the pressure gradient, and it can be written (Eq. 4.38) as a function of the  $y'$  coordinate (assuming all the parameters are known),

$$u'(y') = ((a+b)^{1/3} + (a-b)^{1/3}) \left[ 0.5(y'^2 - 1) - k'_{nl} \right] + ((a+b)^{1/3} + (a-b)^{1/3}) 0.5\epsilon Wi^2 (y'^4 - 1) \quad (4.38)$$

where  $(a \pm b)^{1/3}$  is given by:

$$\left( - \left( \frac{4\epsilon Wi^2}{5} \right)^{-1} \pm \left[ \left( \frac{4\epsilon Wi^2}{5} \right)^{-2} + \left( \frac{1/3 + k'_{nl}}{(6/5)\epsilon Wi^2} \right)^3 \right]^{1/2} \right)^{1/3}$$

For  $m = 2$  Eq. 4.35 can be rearranged and rewritten as Eq. 4.39,

$$(p'_x)^3 + \frac{k'_{nl}}{(-2/5)\epsilon Wi^2} (p'_x)^2 + \frac{1/3}{(62/5)\epsilon Wi^2} p'_x + ((2/5)\epsilon Wi^2)^{-1} = 0 \quad (4.39)$$

The solution of the Cardano-Tartaglia formula shows that the real roots of this cubic equation are different. For  $m = 3$ , the cubic Eq. (4.40) for the pressure gradient is similar to Eq. (4.36) and its real solution is also given by Eq. (4.37), with the new definitions of  $R$  and  $Q$ .

$$(p'_x)^3 + p'_x \underbrace{\frac{1/3}{(2/5 + k'_{nl})\epsilon Wi^2}}_R + \underbrace{\left( (2/5 + k'_{nl})\epsilon Wi^2 \right)^{-1}}_Q = 0 \quad (4.40)$$

Hence, the velocity profile can be computed by Eq. 4.41,

$$u'(y') = ((a+b)^{1/3} + (a-b)^{1/3}) \left[ 0.5(y'^2 - 1) \right] + ((a+b)^{1/3} + (a-b)^{1/3}) 0.5\epsilon Wi^2 (y'^4 - 1 - k'_{nl}) \quad (4.41)$$

where  $(a \pm b)^{1/3}$  is given by:

$$\left( - (X)^{-1} \pm \left[ (X)^{-2} + \left( \frac{1/3}{(6/5 + 3k'_{nl})\epsilon Wi^2} \right)^3 \right]^{1/2} \right)^{1/3}$$

with  $X = \left(\frac{4}{5} + k'_{nl}\right) \varepsilon Wi^2$ .

For the Hatzikiriakos and asymptotic models and for other non-linear slip exponents, the solution is semi-analytical and requires a procedure like the one adopted in Appendix A. Incidentally, for  $m = 4$  it is still possible to obtain a closed form analytical solution. In the supplementary material appended to this work we give the solution for the pressure gradient equation (Eq. 4.35) for the four different slip boundary conditions and for different values of  $\varepsilon Wi^2$ ,  $k'_{nl}$ ,  $k'_{H1}$ ,  $k'_{H2}$ ,  $k'_{A1}$  and  $k'_{A2}$ .

#### 4.3.3 Planar channel flow with the exponential PTT model

Eq. 6.44(d) for the exponential PTT model (Eq. 4.5) and considering symmetry on the centreplane leads to .

$$\left(\partial u' / \partial y'\right) = \exp\left(2\varepsilon Wi^2 \left(p'_x y'\right)^2\right) p'_x y' \quad (4.42)$$

After integration and application of the boundary condition  $u'_{ws}(1)$  the velocity profile is

$$u' \left(y'\right) = \left[4\varepsilon Wi^2 \left(p'_x\right)\right]^{-1} \exp\left(2\varepsilon Wi^2 \left(p'_x y'\right)^2\right) - \exp\left(2\varepsilon Wi^2 \left(p'_x\right)^2\right) + u'_{ws}(1) \quad (4.43)$$

where  $u'_{ws}(1)$  is the boundary condition given by any of the Eqs. 4.19, 4.20, 4.21.

The solution of the inverse problem is achieved as for the linear PTT model, i.e. integrating the velocity profile of Eq. 4.43 now leading to,

$$\int_0^1 \exp\left(2\varepsilon Wi^2 \left(p'_x y'\right)^2\right) dy' = \exp\left(2\varepsilon Wi^2 \left(p'_x\right)^2\right) + 4\varepsilon Wi^2 \left(p'_x\right) - 4\varepsilon Wi^2 \left(p'_x\right) u'_{ws}(1) = 0 \quad (4.44)$$

and then solving in order to the pressure gradient. To evaluate the left hand side (lhs) of Eq. 4.44 use is made of the definition of the error function (*erf*), giving

$$-\frac{i\sqrt{\pi}}{2\sqrt{G}} \operatorname{erf}\left(i\sqrt{2\varepsilon Wi^2 \left(p'_x\right)^2}\right) = \exp\left(2\varepsilon Wi^2 \left(p'_x\right)^2\right) + 4\varepsilon Wi^2 \left(p'_x\right) - 4\varepsilon Wi^2 \left(p'_x\right) u'_{ws}(1) = 0 \quad (4.45)$$

Eq. 4.45 can be further simplified and written as,

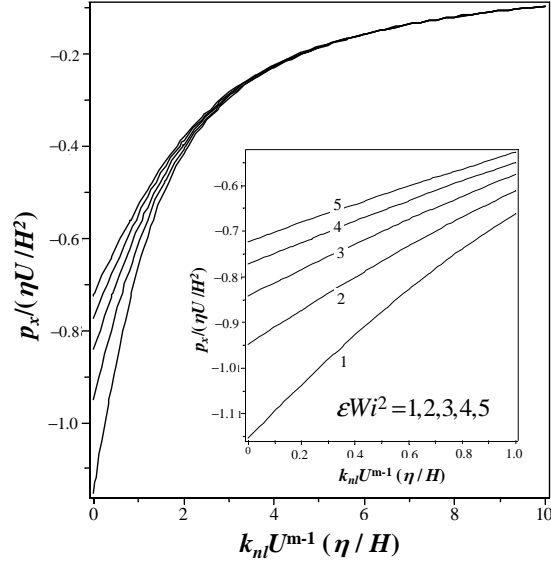


Figure 4.3: Variation of  $p'_x$  as a function of  $k'_{nl}$  and  $\epsilon Wi^2$  for a Poiseuille planar channel flow with the linear PTT model and linear Navier slip. The  $\epsilon Wi^2$  numbers are given next to each graph in the zoomed view.

$$\sum_{k=0}^{\infty} \frac{(2\epsilon Wi^2 (p'_x)^2)^k}{(2k+1)k!} = \exp\left(2\epsilon Wi^2 (p'_x)^2\right) + 4\epsilon Wi^2 (p'_x) - \quad (4.46)$$

$$4\epsilon Wi^2 (p'_x) u'_{ws}(1) = 0$$

This series is convergent and since it calculates the area under a known function, it can be shown that the lhs of Eq. 4.46 is a monotonic function in the range  $p'_x \in ]-\infty, 0]$ . To obtain the pressure gradient the range containing the solution must be known and the bisection method is then applied. Care must be taken because of the sharp changes occurring while changing the slip friction coefficient.

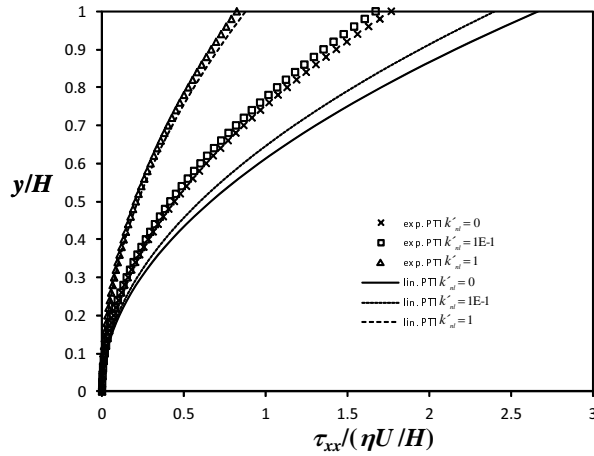
Tables are given as supplementary material containing the solution for the pressure gradient equation (Eq. 4.46) for the four different slip boundary conditions and for different values of  $\epsilon Wi^2$ ,  $k'_{nl}$ ,  $k'_{H1}$ ,  $k'_{H2}$ ,  $k'_{A1}$  and  $k'_{A2}$ .

The results for the Poiseuille flow with the linear and exponential PTT models can be summarized as follows. For the linear PTT model with linear Navier slip, the absolute value of the pressure drop decreases (tends to zero) with the increase of both slip and  $\epsilon Wi^2$ , as observed in Fig. 4.3. So, the effect of slip on  $p'_x$  is as in Couette flow. An increase in  $\epsilon Wi^2$  increases the shear rate, while imparting shear-thinning behaviour to the fluid so that ultimately it reduces significantly its shear viscosity as shown in Fig. 4.4(a) in terms of the shear stress  $\tau'_{xy}$ . The corresponding normal stress  $\tau'_{xx}$  variation is shown in Fig. 4.4(b) and is similar to that of the shear stress given that

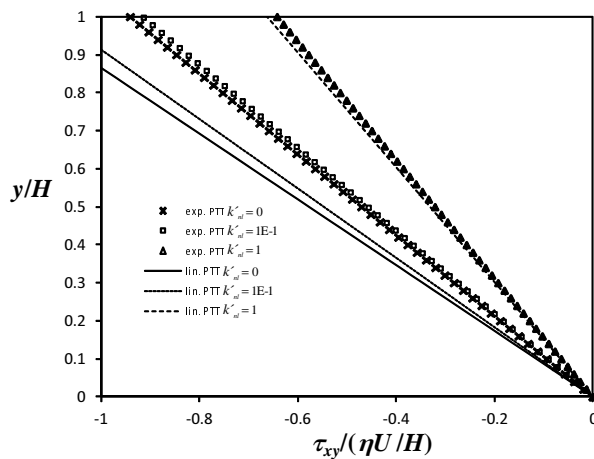
they are proportional. In the absence of slip the results match those of (Oliveira and Pinho, 1999a).

As in the Couette flow, and for the same reasons, the exponential PTT model exhibits lower stresses than the corresponding linear PTT model.

The solution for the Poiseuille pipe flow of a PTT fluid (linear and exponential) is given in Appendix B.



(a)



(b)

Figure 4.4: Variation of  $\tau'_{xx}$  (a) and  $\tau'_{xy}$  (b) along the channel half width  $y'$  for a Poiseuille flow of a PTT model with different values of  $k'_{nl}$  and constant  $\varepsilon Wi^2 = 1$ .

#### 4.4 ANALYTICAL SOLUTIONS FOR THE GIESEKUS FLUID AND DISCUSSION

The derivation of the equations is well explained by (Yoo and Choi, 1989), and here we follow the same sequence as in subsection 3 for the PTT model.

Based on the simplifications for fully developed flow in the geometries of Fig. 4.1, the dimensionless momentum and constitutive equations become ( $h$ ,  $U$  and  $\eta U/h$  are the length, velocity and stress scales, respectively),

$$\begin{aligned} \frac{\partial \tau'_{xy}}{\partial y'} &= p'_x & (a) \\ 2Wi\tau'_{xy} \left( \frac{\partial u'}{\partial y'} \right) &= \tau'_{xx} + \alpha Wi \left( \tau'^2_{xx} + \tau'^2_{yy} \right) & (b) \\ \left( 1 + Wi\tau'_{yy} \right) \left( \frac{\partial u'}{\partial y'} \right) &= \tau'_{xy} + \alpha Wi\tau'_{xy} \left( \tau'_{xx} + \tau'_{yy} \right) & (c) \\ \alpha Wi \left( \tau'^2_{xy} + \tau'^2_{yy} \right) + \tau'_{yy} &= 0 & (d) \end{aligned} \quad (4.47)$$

where  $Wi = \lambda U/h$  is the Weissenberg number.

Redefining dimensionless quantities as  $u^* = Wi u'$ ,  $\tau^*_{xx} = Wi\tau'_{xx}$ ,  $\tau^*_{yy} = Wi\tau'_{yy}$  and  $\tau^*_{xy} = Wi\tau'_{xy}$  the previous system of equations (Eq. 4.47) can be integrated and presented as in Eq. 44,

$$\begin{aligned} \tau^*_{xy} &= Wi \left( p'_x y' + c'_2 \right) & (a) \\ \frac{\partial u^*}{\partial y'} &= 2\alpha \tau^*_{xy} \frac{\left( 1 \pm (2\alpha - 1) \sqrt{1 - 4\alpha^2 (\tau^*_{xy})^2} \right)}{\left( 2\alpha - 1 \pm \sqrt{1 - 4\alpha^2 (\tau^*_{xy})^2} \right)^2} & (b) \\ \tau^*_{xx} &= \frac{\left[ (1 - \alpha) \left( 1 \mp \sqrt{1 - 4\alpha^2 (\tau^*_{xy})^2} \right) + 2\alpha^2 (\tau^*_{xy})^2 \right]}{\alpha \left( 2\alpha - 1 \pm \sqrt{1 - 4\alpha^2 (\tau^*_{xy})^2} \right)} & (c) \\ \tau^*_{yy} &= \frac{\left( -1 \pm \sqrt{1 - 4\alpha^2 (\tau^*_{xy})^2} \right)}{2\alpha} & (d) \end{aligned} \quad (4.48)$$

Eqs. 4.48(b) and (c) require  $1 - 4\alpha^2 (\tau^*_{xy})^2 > 0$  and in addition, thermodynamic considerations require a positive first normal stress difference ( $\tau^*_{xx} - \tau^*_{yy} \geq 0$ ). This inequality can be further simplified leading to  $2\alpha - 1 \pm \sqrt{1 - 4\alpha^2 (\tau^*_{xy})^2} > 0$ . These restrictions on the system of equations bring two sets of solutions, the so-called upper branch solution, where ,

$$\begin{cases} \tau^*_{xy} < \sqrt{1/\alpha - 1} & \alpha \in ]0; 1/2] \\ \tau^*_{xy} < 1/2\alpha & \alpha \in ]1/2; 1] \end{cases} \quad (4.49)$$

and the lower branch solution for which .

$$\sqrt{1/\alpha - 1} < \tau^*_{xy} \leq 1/2\alpha \text{ for } \alpha \in ]1/2; 1] \quad (4.50)$$

These restrictions imply that for some values of the Weissenberg number the solutions for Couette and Poiseuille flows with no slip may not exist as already shown by (Yoo and Choi, 1989). Next we analyse the cases with slip but since the lower branch solution presents



physically unrealistic solutions only the upper branch solution needs to be considered.

#### 4.4.1 Couette flow

Following (Yoo and Choi, 1989) let  $\Psi = 2\alpha\tau_{xy}^*$ ,  $p_x^* = 0$  in Couette flow, so  $\Psi$  can be written as  $\Psi = 2\alpha Wic'_2$  (with the help of Eq. 4.48(a)) and integrate Eq. 4.48(b) to obtain the following velocity profile .

$$u^*(y') = \frac{\Psi \left(1 \pm (2\alpha - 1) \sqrt{1 - \Psi^2}\right)}{(2\alpha - 1 \pm \sqrt{1 - \Psi^2})^2} y' + c \quad (4.51)$$

where  $c$  is the constant of integration determined by the lower wall slip boundary conditions with the proper normalization (Eqs. 4.16, 4.17, 4.18) multiplied by  $Wi$ ). These are given by,

$$u_{ws}^*(0) = Wik'_{nl} \left(\frac{\Psi}{2\alpha Wi}\right)^m \quad (4.52)$$

for the (non)linear Navier slip law,

$$u_{ws}^*(0) = Wik'_{H1} \sinh\left(k'_{H2} \frac{\Psi}{2\alpha Wi}\right)^m \quad (4.53)$$

for the Hatzikiriakos slip law, and

$$u_{ws}^*(0) = Wik'_{A1} \ln\left(1 - k'_{A2} \frac{\Psi}{2\alpha Wi}\right)^m \quad (4.54)$$

for the asymptotic slip law. At the upper wall there is no slip (cf. Section 3.1 for the justification) and the Dirichlet boundary condition is

$$u_{ws}^*(1) = Wi \quad (4.55)$$

and this condition together with Eq. 4.51 provides the following implicit equation relating the Weissenberg number and  $c'_2$  (note that  $\Psi = 2\alpha Wic'_2$ )

$$2\alpha Wic'_2 \frac{\left(1 \pm (2\alpha - 1) \sqrt{1 - (2\alpha Wic'_2)^2}\right)}{\left(2\alpha - 1 \pm \sqrt{1 - (2\alpha Wic'_2)^2}\right)^2} + u_{ws}^*(0) - Wi = 0 \quad (4.56)$$

This equation must be solved numerically with the following restriction on  $Wi$ ,

$$Wic'_2 \leq \frac{1}{2\alpha} \quad (4.57)$$

For the special case of the linear Navier slip law it is possible to analytically find the limiting admissible values for  $Wi$  and  $c'_2$ . Based on the definition of  $\Psi$ , the upper branch solution (Eq. 4.49) can be rewritten as,

$$\begin{cases} \Psi < 2\alpha\sqrt{1/\alpha - 1} & \alpha \in ]0; 1/2] \\ \Psi < 1 & \alpha \in ]1/2; 1] \end{cases} \quad (4.58)$$

Eq. 4.56 with the Navier slip boundary condition can be rewritten as,

$$Wi(\Psi) = \Psi \frac{(1 \pm (2\alpha - 1)\sqrt{1 - \Psi^2})}{(2\alpha - 1 \pm \sqrt{1 - \Psi^2})^2} + \frac{\Psi k'_{nl}}{2\alpha} \quad (4.59)$$

$$Wi(\Psi) = \frac{\partial u^*}{\partial y'} + \frac{\Psi k'_{nl}}{2\alpha} \quad (4.60)$$

Physical reasons require the solution to verify  $\partial(\partial u^*/\partial y')/\partial\tau_{xy}^* = 2\alpha\partial(\partial u^*/\partial y')/\partial\Psi > 0$ , i.e., shear rate increases with shear stress and this is verified by the upper branch solution. Since  $\partial(\partial u^*/\partial y')/\partial\Psi > 0$  and  $\partial(\partial\Psi k'_{nl}/2\alpha)/\partial\Psi > 0$ , by Eq. 4.60  $\partial(Wi(\Psi))/\partial\Psi > 0$  meaning that  $Wi(\Psi)$  is a monotonically increasing function of  $\Psi$ . Thus, for  $\alpha \in ]1/2; 1]$  and considering Eq. 4.59, the restrictions are given by,

$$\lim_{\Psi \rightarrow 1} Wi(\Psi) = \frac{1}{(2\alpha - 1)^2} + \frac{k'_{nl}}{2\alpha} \quad (4.61)$$

for the Weissenberg number and by .

$$\left( \frac{2\alpha}{(2\alpha - 1)^2} + k'_{nl} \right)^{-1} \leq c'_2 < 1 \quad (4.62)$$

for the stress coefficient  $c'_2$  (obtained combining Eqs. 4.59, 4.60 and 4.61). Note that  $c'_2 < 1$  because the fluid is shear thinning. For the range  $\alpha \in ]0; 1/2]$  there are no restrictions.

As shown by Eqs. 4.61 and 4.62, increasing the slip velocity smoothes the restriction on  $Wi$  and  $c'_2$ . For the other slip laws, it is more difficult to determine these restrictions on the Weissenberg and stress constants. Although those slip laws can be written using  $\Psi$ , they always depend on  $Wi$  or  $c'_2$ , so the same approach cannot be used to identify those restrictions.

It was shown that limiting values of  $Wi$  and  $c'_2$  depend on slip. Increasing the slip coefficient, a higher limiting value for  $Wi$  is obtained and the range of admissible solutions for the stress coefficient  $c'_2$  also increases, because the admissible values of  $Wi$  and  $c'_2$  are inversely

Table 4.1: Minimum and maximum admissible values for  $c'_2$  and  $k'_{nl}$  as a function of  $\alpha$  and  $k'_{nl}$  for Couette flow of Giesekus model with the linear Navier slip law.

$\alpha \backslash k'_{nl}$	$c'_{2min}$	$Wi_{max}$	$c'_{2min}$	$Wi_{max}$	$c'_{2min}$	$Wi_{max}$	$c'_{2min}$	$Wi_{max}$	$c'_{2min}$	$Wi_{max}$	$c'_{2min}$	$Wi_{max}$
	0		1		2		3		4		5	
0.6	0.033	25.000	0.032	25.833	0.031	26.667	0.030	27.500	0.032	26.200	0.029	29.167
0.7	0.114	6.250	0.103	6.964	0.103	6.950	0.098	7.300	0.093	7.650	0.089	8.000
0.8	0.225	2.778	0.184	3.403	0.175	3.578	0.157	3.978	0.143	4.378	0.131	4.778
0.9	0.356	1.563	0.262	2.118	0.226	2.463	0.191	2.913	0.165	3.363	0.146	3.813
1	0.500	1.000	0.333	1.500	0.250	2.000	0.200	2.500	0.167	3.000	0.143	3.500

proportional to each other. Table 4.1 presents a set of limiting values for  $Wi$  and  $c'_2$  as a function of  $\alpha$  and the slip coefficient.

Although the existence of slip seems to smooth the problem of nonexistence of analytical solutions, such limitation continues to exist, at least for specific cases. In fact, as the Weissenberg number is increased a larger slip velocity is required to guarantee the existence of solution. From Eq. 4.59 with  $Wi = 1$ ,  $\alpha = 1$ ,  $k'_{nl} = 0.1$  (linear Navier slip) and some manipulation, the result is  $(1/2)c'_2 - 1/20 = 1/\left(1 + \sqrt{1 - 4(c'_2)^2}\right)$ , an equation without a real number solution, i.e., although slip widens the range of conditions for a solution to exist with the Giesekus model, by itself it does not guarantee its existence.

#### 4.4.2 Planar Channel Flow

The symmetry condition of planar Poiseuille flow (see Fig. 4.1(b)), defines the shear stress distribution given by  $\tau_{xy}^* = Wi(p'_x y')$  (see Eq. 4.48(a)). Using  $\phi = -2\alpha Wi(-p'_x)$  the differential equation for the velocity derivative (Eq. 4.48(b)) becomes (see (Yoo and Choi, 1989) for more details),

$$\frac{\partial u^*(y')}{\partial y'} = -\frac{\phi y' \left(1 \pm (2\alpha - 1) \sqrt{1 - (\phi y')^2}\right)}{\left(2\alpha - 1 \pm \sqrt{1 - (\phi y')^2}\right)^2} \quad (4.63)$$

The solution of the direct problem with wall slip is,

$$u^*(y') = \frac{a(\phi)}{\phi} + u_{ws}^*(1) \quad (4.64)$$

with:

Table 4.2: Variation of  $p'_x$  with different values of  $\alpha$ ,  $k'_{nl}$  and constant  $Wi = 1$  for a Poiseuille flow with the Giesekus model with the linear Navier slip law.

$\alpha \backslash k'_{nl}$	1	2	3
0.6	0.666951	0.420398	0.298136
0.7	0.653780	0.419802	0.298037
0.8	X	0.419456	0.298005
0.9	X	0.419394	0.298044
1	X	0.419677	0.298163

$$a(\phi) = (1 - 2b^2) \ln \left[ \frac{b + \sqrt{1 - (\phi y')^2}}{b + \sqrt{1 - (\phi)^2}} \right] + b \left( \sqrt{1 - (\phi y')^2} - \sqrt{1 - (\phi)^2} \right) + b(1 - b^2) \left[ \frac{1}{b + \sqrt{1 - (\phi y')^2}} - \frac{1}{b + \sqrt{1 - (\phi)^2}} \right] \text{ and } b = 2\alpha - 1.$$

The solution for the inverse problem is obtained as for the PTT fluid, integrating the velocity profile, here with the modified dimensionless velocity .

$$\int_0^1 u^*(y') dy' = Wi \quad (4.65)$$

Once again the only physically acceptable solution is the upper branch here is given as,

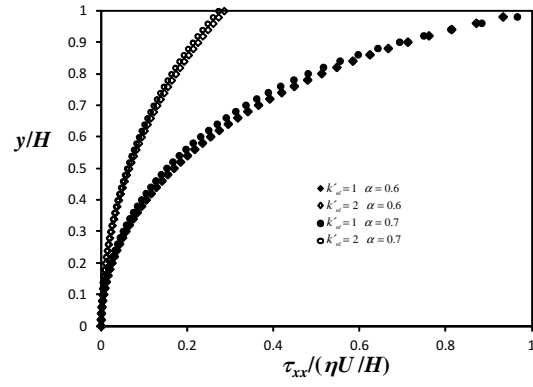
$$\begin{cases} |\phi y'| < 2\alpha \sqrt{1/\alpha - 1} & \alpha \in ]0; 1/2] \\ |\phi y'| < 1 & \alpha \in ]1/2; 1] \end{cases} \quad (4.66)$$

for a fixed  $y'$ . As expected, restrictions on the admissible Weissenberg number  $Wi$  and pressure gradient  $p'_x$  arise.

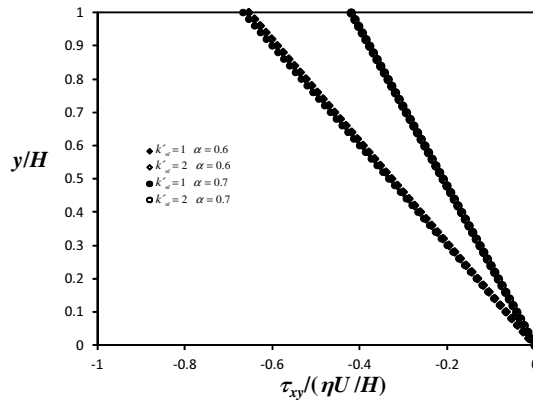
For Poiseuille flow, slip also relaxes the Weissenberg number restriction and in order to obtain the pressure gradient the nonlinear Eq. 4.65 must be solved numerically.

Assuming that  $Wi = 1$  (Yoo and Choi, 1989) showed that there should be no solution for Eq. 4.65, but its existence can be proved for some cases with slip even though it has to be determined numerically. For this particular case, Table 4.2 lists the pressure gradient for different values of  $\alpha$  and  $k'_{nl}$ , no solution exists for  $\alpha = 0.8, 0.9, 1.0$  and  $k'_{nl} = 1$  and the pressure gradient decreases when  $\alpha$  increases.

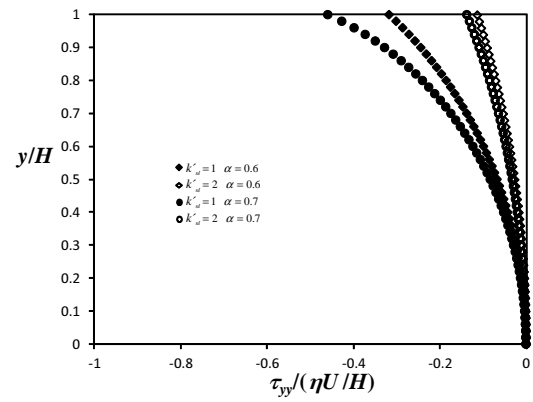
The variation of the shear stress  $\tau_{xy}^*$  (and of the other stress components) with slip, shown in Fig. 4.5, is qualitatively similar to that for the PTT models. For the normal stress  $\tau_{xx}^*$  the Giesekus model exhibits lower values than the corresponding PTT models, everything else being the same. Even though the effect of  $\alpha$  on both  $\tau_{xy}^*$  and  $\tau_{xx}^*$  is very small, it leads to a non-zero second normal stress difference



(a)



(b)



(c)

Figure 4.5: Variation of  $\tau'_{xx}$  (a),  $\tau'_{xy}$  (b), and  $\tau'_{yy}$  (c) along the channel half width  $y'$  for a Poiseuille flow of a Giesekus model with different values of  $\alpha$ ,  $k'_{nl}$  and for a constant  $Wi = 1$ .

(here  $N_2 = -\tau'_{yy}$ ) that decreases with slip as shown in the plots of  $\tau'_{yy}$  of Fig. 4.5(c) ( $\tau'_{yy} = 0$  for any of the simplified PTT models).

The solution for the Poiseuille pipe flow of a Giesekus fluid is given in Appendix B.

#### 4.5 CONCLUSIONS

Analytical and semi analytical solutions (for the direct and inverse problems) are presented for the Couette and Poiseuille flows of linear and exponential simplified PTT fluids, together with an analysis of the existence of solutions for the one mode Giesekus model. For the sPTT fluids it could be proved that for the four slip models presented there is always a unique solution for the flow between parallel plates, but full analytical solutions could only be found for special values of the exponent in the nonlinear Navier slip law. For the Giesekus fluid, the procedure to obtain the solution is very similar as the one employed for the sPTT. The proof of existence of solutions (that could not exist without slip velocity) is made analytically for the Couette flow and is studied numerically for the Poiseuille flow. For both flows this study is carried out for the Navier slip law, although, for the other nonlinear laws the results are qualitatively similar.

#### ACKNOWLEDGEMENTS

The authors would like to acknowledge the financial support provided by Fundação para a Ciência e Tecnologia (FCT) under the project SFRH / BD / 37586 / 2007.

#### APPENDIX A: SOLUTIONS FOR THE COUETTE FLOW AND NONLINEAR NAVIER SLIP WITH THE PTT MODELS

The nonlinear Navier slip law is given by,

$$u'_{ws}(0) = k'_{nl} (c'_1)^m \quad (4.67)$$

where  $k'_{nl} = k_{nl} U^{m-1} (\eta/h)^m$ . The velocity profile is obtained by solving the following two systems of equations. For the linear PTT model they are,

$$u'(y') = \left[ c'_1 + 2\varepsilon Wi^2 (c'_1)^3 \right] y' + k'_{nl} (c'_1)^m \quad (4.68)$$

$$2\varepsilon Wi^2 (c'_1)^3 + c'_1 + k'_{nl} (c'_1)^m - 1 = 0 \quad (4.69)$$

Let  $g(c'_1) = 2\varepsilon Wi^2 (c'_1)^3 + c'_1 + k'_{nl} (c'_1)^m - 1$ , then, the derivative of  $g(c'_1)$  is positive and given by,

$$\frac{dg(c'_1)}{dc'_1} = 6\varepsilon Wi^2 (c'_1)^2 + mk'_{nl} (c'_1)^{m-1} + 1 > 0 \quad (4.70)$$

Since  $g(0) = -1$  and  $g(1) = 2\varepsilon Wi^2 + k'_{nl} > 0$ , Bolzano and Rolle theorems imply a unique solution in the range  $[0, 1]$ .

For the special case of  $m = 3$ , the solution is given next and was obtained with the help of the Cardan-Tartaglia formula,

$$c'_1 = \left( - \left( -2\varepsilon Wi^2 - k'_{nl} \right)^{-1} / 2 + \sqrt{Y} \right)^{1/3} + \left( - \left( -2\varepsilon Wi^2 - k'_{nl} \right)^{-1} / 2 - \sqrt{Y} \right)^{1/3} \quad (4.71)$$

$$\text{with } Y = \left( \left( -2\varepsilon Wi^2 - k'_{nl} \right)^{-1} / 2 \right)^2 + \left( \left( 2\varepsilon Wi^2 + k'_{nl} \right)^{-1} / 3 \right)^3$$

For the special case of  $m = 2$ , the analytical solution is obtained as a general solution of a cubic equation.

The system of equations for the exponential PTT is,

$$u'(y') = \exp \left( 2\varepsilon Wi^2 (c'_1)^2 \right) c'_1 y' + k'_{nl} (c'_1)^m \quad (4.72)$$

$$\exp \left( 2\varepsilon Wi^2 (c'_1)^2 \right) c'_1 + k'_{nl} (c'_1)^m - 1 = 0 \quad (4.73)$$

Let  $g(c'_1) = \exp \left( 2\varepsilon Wi^2 (c'_1)^2 \right) c'_1 + k'_{nl} (c'_1)^m - 1$ , the derivative of  $g(c'_1)$  is positive and given by equation, .

$$\frac{dg(c'_1)}{dc'_1} = \exp \left( 2\varepsilon Wi^2 (c'_1)^2 \right) \left( 1 + 4\varepsilon Wi^2 (c'_1)^2 \right) + mk'_{nl} (c'_1)^{m-1} > 0 \quad (4.74)$$

Since:

$$g(0) = -1 \text{ and } g(k'^{-1/m}_{nl}) = \exp \left( 2\varepsilon Wi^2 (k'_{nl})^{-2/m} \right) k'^{-1/m}_{nl} > 0,$$

we have, once again by Bolzano and Rolle theorems, a unique solution in the interval  $\left[ 0, k'^{-1/m}_{nl} \right]$ .

For the other two slip boundary conditions given by Eqs. 4.17 and 4.18 we have similar results. For the linear PTT let  $g(c'_1) = 2\varepsilon Wi^2 (c'_1)^3 + c'_1 + u'_{ws}(0) - 1$ , then the following positive derivative is obtained,

$$\frac{dg(c'_1)}{dc'_1} = 6\varepsilon Wi^2 (c'_1)^2 + \frac{du'_{ws}(0)}{dc'_1} + 1 > 0 \quad (4.75)$$

For the exponential PTT let:

$$g(c'_1) = \exp \left( 2\varepsilon Wi^2 (c'_1)^2 \right) c'_1 + u'_{ws}(0) - 1, \text{ then,}$$

$$\frac{dg(c'_1)}{dc'_1} = \exp\left(2\epsilon Wi^2 (c'_1)^2\right) \left(1 + 4\epsilon Wi^2 (c'_1)^2\right) + \frac{du'_{ws}(0)}{dc'_1} > 0 \quad (4.76)$$

Since  $g(0) < 0$  and  $g(1) > 0$  for both linear and exponential PTT once again is proved the existence of a unique solution in the range  $[0, 1]$ .

#### APPENDIX B: PIPE FLOW FOR THE SPTT AND GIESEKUS MODELS

##### sPTT:

The solutions for the pipe flow (Fig. 4.1(c)) are very similar to those of channel flow. A practical way to obtain the simplified governing equations is to substitute  $y$  by  $r/2$  in Eq. 6.44 leading to,

$$\begin{aligned} \tau'_{xr} &= p'_x r' / 2 & (a) \\ \tau'_{xx} &= 2Wi \left(p'_x r' / 2\right)^2 & (b) \\ \tau'_{rr} &= 0 & (c) \\ (\partial u' / \partial r') &= f \left( (2\lambda / \eta) \left(p'_x r' / 2\right)^2 \right) p'_x \left(r' / 2\eta\right) & (d) \end{aligned} \quad (4.77)$$

The solution for the direct problem is given by the following two equations for the linear and the exponential models, respectively.

$$u' (r') = 0.125 p'_x (r'^2 - 1) + 0.0625 \epsilon Wi^2 (p'_x)^3 (r'^4 - 1) + u'_{ws} (1) \quad (4.78)$$

$$u' (r') = \left(2\epsilon Wi^2 (p'_x)\right)^{-1} \left(\exp(Zr'^2) - \exp(Z)\right) + u'_{ws} (1) \quad (4.79)$$

with  $Z = 0.5\epsilon Wi^2 (p'_x)^2$ .

The term  $u'_{ws}(1)$  is once again given by any of the Eqs 4.19, 4.20, 4.21. The solution for the inverse problem is very similar to the channel flow.

##### Giesekus:

For the pipe flow, the solution is very similar to that in the pressure-driven channel flow. The main difference is that  $y$  is replaced by  $r$ , and  $\phi$  gives place to  $\Psi_1 = aWi (-p'_x)$ .

$$u^* (r') = \frac{a\Psi_1}{\Psi_1} + u^*_{ws} (1) \quad (4.80)$$



Part IV

NUMERICAL STUDIES OF FLOWS UNDER  
SLIP



## INTRODUCTION TO PART IV

Part IV can be divided into three distinct sets of papers. The first two papers that are presented, are related to the implementation of different slip boundary conditions into a computer code based on the finite volume method:

▷L.L. Ferrás, J.M. Nóbrega, F.T. Pinho (2012), Implementation of Slip Boundary Conditions in the Finite Volume Method: New Techniques, accepted for publication in the *International Journal for Numerical Methods in Fluids*;

▷L.L. Ferrás, A.M. Afonso, J.M. Nóbrega, M.A. Alves, F.T. Pinho (2012), A numerical and theoretical study on viscoelastic fluid slip-flows, to be submitted to *Theoretical and Computational Fluid Dynamics*;

In the second set of papers, a study concerning the influence of the slip velocity on Newtonian and viscoelastic fluid flow through contractions and expansions, is presented:

▷L.L. Ferrás, A.M. Afonso, J.M. Nóbrega, M.A. Alves, F.T. Pinho, 4:1 Contraction flow of Non-Newtonian fluids with slip boundary conditions, submitted to *Journal of Non-Newtonian Fluid Mechanics*;

▷L.L. Ferrás, A.M. Afonso, J.M. Nóbrega, M.A. Alves, F.T. Pinho (2012), The Influence of Slip Velocity on the Newtonian and Viscoelastic Fluid Flow Through an Abrupt 1:4 Expansion, to be submitted to *Journal of Non-Newtonian Fluid Mechanics*;

In the third set of papers, a study concerning the development length requirements for fully developed fluid flows under the influence of slip velocity, is presented:

▷L.L. Ferrás, A.M. Afonso, J.M. Nóbrega, M.A. Alves, F.T. Pinho (2012), Development length in planar channel flows of Newtonian fluids under the influence of wall slip, accepted for publication in the *Journal of Fluids Engineering*;

▷L.L. Ferrás, A.M. Afonso, J.M. Nóbrega, M.A. Alves, F.T. Pinho (2012), Numerical study of the Development Length Requirements for Fully Developed flow of Viscoelastic Fluids Under Slip, to be submitted to *Journal of Fluids Engineering*;



## IMPLEMENTATION OF SLIP BC IN THE FVM: NEW TECHNIQUES

---

### Abstract<sup>1</sup>

*Two different techniques for the implementation of the linear and the non-linear slip boundary conditions into a finite volume method based numerical code are presented. For the linear Navier slip boundary condition an implicit implementation in the system of equations is carried out for which there is no need for any relaxation, especially when handling high slip coefficients. For three different nonlinear slip boundary conditions, two different methods are devised, one based on solving a transcendental equation for the boundary and the other based on the linearization of the slip law. For assessment purposes comparison is made between these new methods and the usual iterative process. With these new methods the convergence difficulties, typical of the iterative procedure, are eliminated and for some of the test cases the convergence rate even increased with the slip velocity. The details of these implementations are given first for a simple geometry using orthogonal meshes and Cartesian coordinates followed by their generalization to non-Cartesian coordinates and nonorthogonal meshes. The developed code was tested in the benchmark slip-stick and 4:1 contraction flows, evidencing the robustness of the proposed procedures.*

### 5.1 INTRODUCTION

Most of the literature related to the computation of the Navier-Stokes equations with slip boundary conditions is based on the finite element method (FEM). Some works present the variational and FEM studies of the Stokes and the Navier-Stokes equations with free slip boundary conditions (see (Liakos, 2001; Verfürth, 1986) and the literature cited therein), others give friction an important role, and investigate the effects of slip and leak boundary conditions (John, 2002; Stokes and Carey, 2008).

This paper concerns friction slip models. Even though a number of difficulties have been reported in the FEM literature on handling friction slip models (John, 2002), some recent techniques, such as the penalty approach (Stokes and Carey, 2008), seem to work well, at least when applied to Stokes flow. However, other contributions using linear and nonlinear slip models in the context of FEM (Sunarso et al.,

---

<sup>1</sup> L.L. Ferrás, J.M. Nóbrega, FT Pinho (2012), Implementation of Slip Boundary Conditions in the Finite Volume Method: New Techniques, accepted for publication in the *International Journal for Numerical Methods in Fluids*;

2006, 2007; Wesson and Papanastasiou, 1988) frequently refer the need to use relaxation in order to obtain convergence.

To our best knowledge numerical codes based on the finite volume method (FVM) comprising slip boundary conditions are scarce and a comparison between FEM and FVM shows that the solver for the Navier-Stokes equations is often quite different: whereas FEM is often built in the variational formulation of the boundary value problem and iteratively couple the equations, based on projection (Guermont et al., 2006), penalty or augmented-Lagrangian (Stokes and Carey, 2008) methods, amongst others, the FVM uses the integral formulation of the Navier-Stokes equations together with one of the various SIMPLE (Patankar, 1980) based methods, to develop and couple pressure and velocity fields along iterations (Oliveira et al., 1998). Although the SIMPLE method is a disguised version of a projection method, results about the implementation of slip boundary conditions making use of FEM and projection methods could not be found in the literature, except for the case of an explicit implementation of slip boundary conditions. This makes it rather difficult to compare the implementation techniques of the slip models.

The aim of this paper is then to present a detailed description of two new different implementations of slip boundary conditions within a FVM approach. These implementations do not need the use of relaxation and work well for all the slip boundary conditions. In addition, two other specific methods, one for the linear Navier slip law and the other for the nonlinear Navier slip law are also presented. The remainder of this paper is organized as follows: the next section presents the governing equations and is followed, in subsection 3, by a detailed description of the implementation of slip velocity in a two dimensional flow using Cartesian coordinates. In subsection 3 we first compare “the classical” fully explicit method (which is applied to the four different slip boundary conditions, namely the linear and especially three non-linear slip boundary conditions) with the fully implicit method for the linear Navier slip law, and then present two new different methods able to deal with all the slip laws studied here. The first of these two methods only works for orthogonal meshes while the second method is able to handle both orthogonal and nonorthogonal meshes. The description of the four methods is followed by the presentation and discussion of results using reference cases for validation, prior to the closure of the paper.

## 5.2 GOVERNING EQUATIONS AND NUMERICAL METHOD

The governing equations for incompressible fluids are the continuity,

$$\nabla \cdot \mathbf{u} = 0 \quad (5.1)$$

and the momentum equations,

$$\frac{\partial \rho \mathbf{u}}{\partial t} + \rho \nabla \cdot \mathbf{u} \mathbf{u} = -\nabla p + \nabla \cdot \boldsymbol{\tau} \quad (5.2)$$

where  $\mathbf{u}$  is the velocity vector,  $\rho$  is the fluid density (assumed to be constant),  $p$  is the pressure and  $\boldsymbol{\tau} = \boldsymbol{\tau}_s + \boldsymbol{\tau}_p$  is the extra stress tensor. The extra stress tensor is divided into solvent  $\boldsymbol{\tau}_s = \eta_s (\nabla \mathbf{u} + (\nabla \mathbf{u})^T)$  (with  $\eta_s$  the solvent viscosity) and polymer  $\boldsymbol{\tau}_p$  contributions, the latter given here by the following differential constitutive equation, called the simplified Phan-Thien—Tanner model (sPTT) (Phan-Thien and Tanner, 1977; Phan-Thien, 1978):

$$\begin{aligned} f(\text{tr} \boldsymbol{\tau}_p) \boldsymbol{\tau}_p + \lambda \left( \frac{\partial \boldsymbol{\tau}_p}{\partial t} + \mathbf{u} \cdot \nabla \boldsymbol{\tau}_p - [(\nabla \mathbf{u})^T \cdot \boldsymbol{\tau}_p + \boldsymbol{\tau}_p \cdot \nabla \mathbf{u}] \right) = \\ = \eta_p \left( \nabla \mathbf{u} + (\nabla \mathbf{u})^T \right) \end{aligned} \quad (5.3)$$

where  $f(\text{tr} \boldsymbol{\tau}_p)$  is a function depending on the trace ( $\text{tr}$ ) of the stress tensor ( $\boldsymbol{\tau}_p$ ),  $\lambda$  is the relaxation time and  $\eta_p$  is the zero shear polymer viscosity. In the literature, there are two possible functions for  $f(\text{tr} \boldsymbol{\tau}_p)$ . The original linear function, presented by (Phan-Thien and Tanner, 1977),

$$f(\text{tr} \boldsymbol{\tau}_p) = 1 + \frac{\varepsilon \lambda}{\eta_p} \text{tr} [\boldsymbol{\tau}_p] \quad (5.4)$$

and the exponential proposed later by (Phan-Thien, 1978), which is given by,

$$f(\text{tr} \boldsymbol{\tau}_p) = \exp \left( \frac{\varepsilon \lambda}{\eta_p} \text{tr} [\boldsymbol{\tau}_p] \right) \quad (5.5)$$

In any case the parameter  $\varepsilon$  is related to the elongational behavior of the modeled fluid ( $\varepsilon$  is inversely proportional to the extensional viscosity).

The UCM model can be derived from the sPTT model by making  $\eta_s = \varepsilon = 0$  and the Oldroyd-B model is obtained when  $\varepsilon = 0$  and  $\eta_s \neq 0$ . The generalized-Newtonian fluid model assumes  $\boldsymbol{\tau} = \boldsymbol{\tau}_s + \boldsymbol{\tau}_p = 2\eta(\dot{\gamma})\mathbf{S}$  in Eq. 2, where  $\eta(\dot{\gamma})$  is a viscosity function which depends on the second invariant ( $\dot{\gamma}$ ) of the rate of deformation tensor  $\mathbf{S} = (\nabla \mathbf{u} + (\nabla \mathbf{u})^T)/2$  with  $\dot{\gamma} = \sqrt{2\mathbf{S} : \mathbf{S}}$ .

A fully-implicit finite volume numerical method is used to solve Eqs. 5.1 to 5.3, which are transformed to generalized coordinates. The method is based on a time marching pressure-correction algorithm formulated with a collocated variable arrangement. The governing equations are integrated in space over the control volumes (cells with volume  $V_p$ ) forming the computational mesh and in time over a time step ( $\Delta t$ ). The volume integration benefits from Gauss Theorem and the subsequent surface integrals are then discretized with help of

the midpoint rule so that sets of linearized algebraic equations are obtained, having the general form:

$$a_P \mathbf{u}_P = \sum_{F=1}^6 a_F \mathbf{u}_F + S_u \quad (5.6)$$

for the velocity components  $u$ ,  $v$ ,  $w$ , and

$$a_P^\tau \boldsymbol{\tau}_P = \sum_{F=1}^6 a_F^\tau \boldsymbol{\tau}_F + S_\tau \quad (5.7)$$

for the extra stress components  $\tau_{xx}$ ,  $\tau_{xy}$ ,  $\tau_{xz}$ ,  $\tau_{yz}$ ,  $\tau_{yy}$ ,  $\tau_{zz}$ . In these equations  $a_P$ ,  $a_F$ ,  $a_P^\tau$  and  $a_F^\tau$  are the coefficients accounting for convection and diffusion influences,  $S_u$  and  $S_\tau$  are source terms encompassing all contributions not included in the coefficients, the subscript  $P$  denotes the cell under consideration and subscript  $F$  its corresponding neighboring cells. The central coefficients of the discretized equations,  $a_P$  and  $a_P^\tau$ , are generally given by the sum of neighbor cell coefficients in addition to the time dependent term in the corresponding governing equation (the time is used here with the purpose of inertial under-relaxation since the interest is only in steady state solutions). As follows, the central coefficient for the momentum equation is given by,

$$a_P = \frac{\rho V_P}{\Delta t} + \sum_{F=1}^6 a_F \quad (5.8)$$

but for the PTT stress equations an additional term is included, resulting from the  $f(tr\boldsymbol{\tau})$  term in Eq. 5.3, which tends to promote stability by increasing the numerical value of the  $a_P$  coefficient,

$$a_P^\tau = \frac{\lambda V_P}{\Delta t} + V_P \left( 1 + \frac{\varepsilon \lambda}{\eta_P} tr[\boldsymbol{\tau}_p] \right) + \sum_{F=1}^6 a_F^\tau. \quad (5.9)$$

The linear set of equations given by Eq. 5.6 are sequentially solved for the Cartesian velocity components by means of a preconditioned bi-conjugate gradient solver (the preconditioner used is LDU decomposition special for indirect addressing). The newly computed velocity field usually does not satisfy the continuity equation (i.e. Eq. 5.1) which needs to be corrected by an adjustment of the pressure differences which drive them. This is accomplished by means of a pressure-correction field obtained from a discrete Poisson equation, derived from a discretized form of the continuity equation (Eq. 5.1) in combination with the momentum equation (Eq. 5.2). This pressure correction equation is then solved by a symmetric conjugate gradient method. The correction of the velocity field follows the SIMPLEC strategy of Van Doormal and Raithby (Van Doormaal and Raithby, 1984) and we may now solve sequentially the implicitly discretized constitutive equations for  $\tau_{xx}$ ,  $\tau_{xy}$ ,  $\tau_{xz}$ ,  $\tau_{yz}$ ,  $\tau_{yy}$ ,  $\tau_{zz}$  (Eq. 5.7). This sys-



tem of equations is solved with the help of the bi-conjugate gradient method.

Most important from the standpoint of accuracy is the representation of the convective terms in the constitutive equations which relies on the SMART scheme of Gaskell and Lau (Gaskell and Lau, 1988). A schematic view of the numerical procedure can be seen in Fig. 5.1, and a detailed description of the code can be found in (Oliveira et al., 1998).

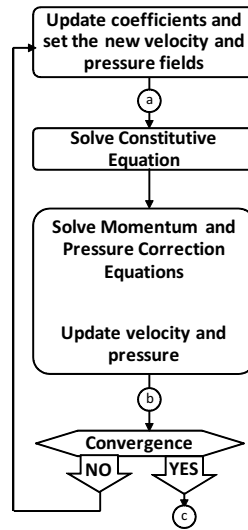


Figure 5.1: Schematic of the numerical procedure.

*Boundary conditions:*

The slip boundary conditions used in this work are the linear (Navier, 1822) and nonlinear (Schowalter, 1988) Navier slip laws as well as the Hatzikiriakos (Hatzikiriakos, 1993) and the asymptotic slip laws, presented next.

Let  $\mathbf{u}_t$  and  $\boldsymbol{\tau}_t$  be the velocity and stress vectors tangent (to the wall), respectively. It is required that the absolute value of the slip velocity must be a function of the absolute value of the tangent stress vector as in Eq.5.10,

$$\|\mathbf{u}_t\| = \|f(\boldsymbol{\tau}_t)\|, \quad (5.10)$$

where  $\|\cdot\|$  stands for the usual  $l^2$  norm and  $f(\cdot)$  represents any real linear or nonlinear function of the tangent stress vector ( $\boldsymbol{\tau}_t$ ). It is also required that the tangent velocity vector,  $\mathbf{u}_t$ , should point in the opposite direction to the tangent stress vector  $\boldsymbol{\tau}_t$ , i.e. the relationship between these two quantities is given by,

$$\mathbf{u}_t = -\|f(\boldsymbol{\tau}_t)\| \|\boldsymbol{\tau}_t\|^{-1} \boldsymbol{\tau}_t, \quad (5.11)$$

where the function  $\|f(\boldsymbol{\tau}_t)\|$  takes the form in Eq. 5.12 for each of the various slip laws

$$\|f(\boldsymbol{\tau}_t)\| = \begin{cases} \text{linear Navier} & k_l \|\boldsymbol{\tau}_t\| & (a) \\ \text{nonlinear Navier} & k_{nl} \|\boldsymbol{\tau}_t\|^m & (b) \\ \text{Hatzikiriakos} & k_{H1} \sinh(k_{H2} \|\boldsymbol{\tau}_t\|) & (c) \\ \text{asymptotic} & k_{A1} \ln(1 + k_{A2} \|\boldsymbol{\tau}_t\|) & (d) \end{cases} \quad (5.12)$$

and the parameters  $k_l, k_{nl}, k_{H1}, k_{H2}, k_{A1}, k_{A2}, m$  are the corresponding slip coefficients. The interested reader is referred to (Ferrás et al., 2012c) for more details about these models.

### 5.3 NUMERICAL IMPLEMENTATION OF SLIP BOUNDARY CONDITIONS

#### 5.3.1 Discretization

To better understand the implementation of slip boundary conditions, a simple 2D channel flow with Cartesian coordinates and orthogonal meshes is used as in Fig. 5.2. At the boundary (the wall at the north cell face), the velocity is tangent to the wall ( $x$ -direction) and the tangent stress vector is determined as,

$$\boldsymbol{\tau}_t = (\mathbf{1} - \mathbf{n} \otimes \mathbf{n}^T) (\boldsymbol{\tau} \mathbf{n}^T) \quad (5.13)$$

where  $\mathbf{n} = (n_1, n_2, n_3)$  is the normal vector to the wall and  $\mathbf{1}$  is the identity matrix.

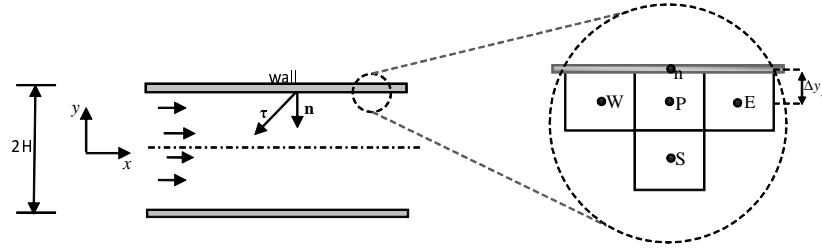


Figure 5.2: Simple geometry: flow between parallel plates (zoomed view of the computational cells near the wall).

The main key for this new implementation of slip boundary conditions is the local assumption of a Couette flow in the vicinity of the wall (Oliveira et al., 1998). If so, the tangent stress vector at the upper wall (for this simple geometry) can be written as,

$$\boldsymbol{\tau}_t = \left( \mu(\dot{\gamma}) \frac{du}{dy} \right)_{wall} \quad (5.14)$$

for all the constitutive equations studied here.

Based on this, what distinguishes one viscoelastic model from another (with respect to the wall boundary treatment) is only the viscosity function  $\mu(\dot{\gamma})_{wall}$  which is given by  $\mu(\dot{\gamma})_{wall} \equiv \eta(\dot{\gamma}_{wall})$  for the generalized Newtonian fluids and is given by  $\mu(\dot{\gamma})_{wall} \equiv \eta_s + \frac{\eta_p}{1 + (\alpha - 1)^2 / 3\alpha}$  (with  $\alpha \equiv (\theta + \sqrt{\theta^2 - 1})^{1/3}$  and  $\theta \equiv 1 + 27\varepsilon(\lambda\dot{\gamma})_{wall}^2$ ) (Azaiez et al., 1996) for the PTT model.

Under these flow conditions the slip law takes the form,

$$u_{ws} = k_{nl} \left( -\mu(\dot{\gamma}) \frac{du}{dy} \right)_{wall}^m \quad (5.15)$$

for the nonlinear Navier slip law. The linear law is recovered for  $m = 1$  in which case  $k_{nl} \equiv k_l$ . The Hatzikiriakos and asymptotic slip laws are given by Eqs. 5.16 and 5.17, respectively.

$$u_{ws} = k_{H1} \sinh \left( -k_{H2} \mu(\dot{\gamma}) \frac{du}{dy} \right)_{wall} \quad (5.16)$$

$$u_{ws} = k_{A1} \ln \left( 1 - k_{A2} \mu(\dot{\gamma}) \frac{du}{dy} \right)_{wall} \quad (5.17)$$

If we assume a one-sided first order approximation for the derivative  $\frac{du}{dy}$  at the wall appearing in Eqs. 5.15, 5.16 and 5.17, then  $\frac{du}{dy} \simeq \frac{u_{ws} - u_p}{\Delta y_f}$ , where  $ws$  stands for “wall slip”,  $u_p$  is the velocity at the center of the control volume adjacent to the wall and  $\Delta y_f$  is half the cell width, as shown in Fig. 5.2. Based on this, Eqs. 5.15, 5.16 and 5.17 can be written in their discretized form as functions of the difference  $u_{ws} - u_p$ , by  $u_{ws} = f_d(u_{ws} - u_p)$  with:

$$f_d(u_{ws} - u_p) \equiv \begin{cases} \text{Navier} & k_{nl} \left( -\frac{\mu(\dot{\gamma})(u_{ws} - u_p)}{\Delta y_f} \right)^m & (a) \\ \text{Hatzikiriakos} & k_{H1} \sinh \left( -\frac{k_{H2} \mu(\dot{\gamma})(u_{ws} - u_p)}{\Delta y_f} \right) & (b) \\ \text{asymptotic} & k_{A1} \ln \left( 1 - \frac{k_{A2} \mu(\dot{\gamma})(u_{ws} - u_p)}{\Delta y_f} \right) & (c) \end{cases} \quad (5.18)$$

where  $f_d(\cdot)$  represents the discretized version of the slip laws.

The discretization of the continuity equation (Eq. 5.1) in a computational cell P (Fig. 5.2) results in the balance of mass fluxes for this cell. These fluxes are normal to the cell faces, therefore, the slip boundary condition has no direct influence on this equation, since the walls are impermeable.

The momentum equation (Eq. 5.2) is directly affected by the slip boundary condition through the term  $\nabla \cdot \tau$ . Notice that the discretization of this term will also change with the assumption of a Couette flow in the vicinity of the wall, Eq. 5.14, as shown in Appendix A.

5.3.2 Explicit and Implicit implementations of the Navier slip law

Explicit formulation:

For the implementation of the slip boundary conditions with an explicit slip formulation, a SIMPLE (Patankar, 1980) type method is used as an example. It can be easily adapted to other algorithms such as the SIMPLEC, SIMPLER or PISO.

Let  $i$  represent the number of the outer iteration (iteration between the linearized momentum equation and the pressure correction equation), then, the discretized slip boundary condition at iteration  $i$  is given for the linear Navier slip law by,

$$u_{ws}^i = k_l \left( -\mu(\dot{\gamma})_{wall}^{i-1} \frac{u_{ws}^{i-1} - u_p^{i-1}}{\Delta y_f} \right) \tag{5.19}$$

where  $\mu(\dot{\gamma})_{wall}^{i-1}$ ,  $u_{ws}^{i-1}$ ,  $u_p^{i-1}$  pertain to the previous iteration.

The proposed modified SIMPLE algorithm (SIMPLE-SLIP-Explicit (SSE)) is given in Fig. 5.1 with the following additional step:

(a) Compute slip velocity with the discretized slip model given by Eq. 5.19.

This slip velocity value  $u_{ws}^i$  goes straight to the source term  $S_u$  of Eq. 5.6 (see Appendix A for more details).

At each iteration  $i$  the boundary condition is updated with the velocity from the previous iteration  $i - 1$ . In order to achieve convergence the variation of this boundary condition along the iterative process must be stable in some sense (sudden changes in the boundary condition along the iterative process will not allow the overall convergence and for a well posed problem we want the flow to depend continuously on the boundary data).

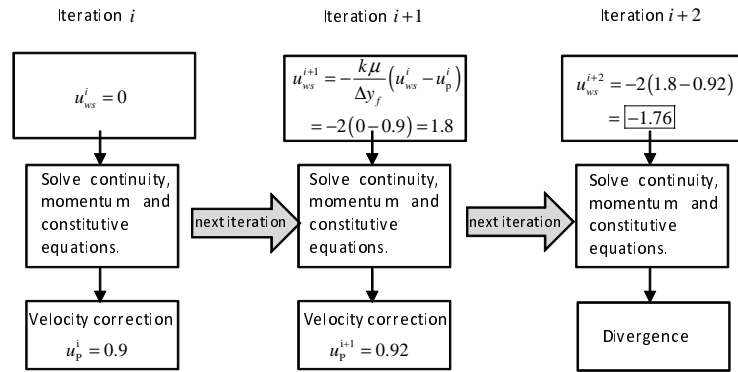


Figure 5.3: Example of the iterative procedure for the explicit formulation of slip velocity.

The example illustrated in Fig. 5.3 shows a case where convergence is not achieved for a situation where the linear Navier slip boundary condition was employed. There we can see the evolution of the velocity

at the center of a control volume with the north face coinciding with a wall, as in Fig. 5.2. The fluid movement is from left to right (with imposed velocity of 1 m/s), but at iteration  $i + 2$  the calculations are made assuming the fluid is slipping at the wall from the right to the left, while just next to the wall the fluid flows in the opposite direction. Due to this inconsistency, non-physical characteristics appear, and the process either diverges or converges to an unacceptable solution.

The relationship  $u_{ws} < u_P$  seems to be the key to the convergence of the process, but this is difficult to guarantee when calculating the slip velocity with the values from the previous iteration. A possible remedy is the classical use of underrelaxation  $u_{ws}^i = R u_{ws}^{i-1} + (1 - R) u_{ws}^i$  with  $R < 1$  when updating the slip velocity in step (a), but for high slip coefficients and nonlinear slip laws this does not work.

Remark: This method can also be applied to any of the other slip laws studied here, provided the right hand side of Eq. 5.19 is evaluated with the values from the previous iteration,  $i - 1$ , by  $u_{ws}^i = f_d \left( u_{ws}^{i-1} - u_P^{i-1} \right)$ .

*Implicit formulation:*

To eliminate the convergence issues of the explicit method a fully-implicit formulation can be implemented, but only the linear Navier slip law allows a fully implicit method without the use of other techniques (such as a deferred correction). The idea is to evaluate Eq.5.19 assuming all variables come from the present iteration. Eq.5.19 can then be rewritten as

$$u_{ws}^{i=k_l} \left( -\mu(\dot{\gamma})_{wall}^i \frac{(u_{ws}^i - u_P^i)}{\Delta y_f} \right) \Leftrightarrow u_{ws}^i = \frac{a}{a+1} u_P^i \text{ with } a = k_l \left( -\frac{\mu(\dot{\gamma})_{wall}^i}{\Delta y_f} \right) \quad (5.20)$$

This ensures the slip velocity is always smaller than the velocity at the center of the adjacent computational cell, so the continuity/monotonicity we searched for is preserved.

The dependency of  $u_{ws}^i$  on  $u_P^i$  leads to modifications in Eqs. 5.6 and 5.8 with the central coefficient  $a_P$  (Eq. 5.8) now being given by,

$$a_P = a_E + a_W + a_S + \frac{a_N}{a+1} + \frac{\Delta V_P \rho_P^0}{\Delta t} \quad (5.21)$$

These equations differ from those for no slip velocity (Eqs. 5.6 and 5.8), in that the term  $a_N u_N$  in Eq. 5.6 does not exist, and the coefficient  $a_N$  in Eq. 5.8 is now multiplied by  $\frac{1}{a+1}$ , therefore in Eq. 5.21  $a_P$  is smaller when compared to the  $a_P$  of Eq. 5.8. Even though this implicit implementation brings a less diagonally dominant system of equations the required conditions for convergence and stability are maintained, such as  $a_P \geq \sum a_F$ .

With this implicit implementation there is no need to specify the value of  $u_{ws}$  along the iterative process and no need to use under-relaxation to solve the discrete system of equations that results from the discretization of the momentum equation. When convergence is achieved the slip velocity can be calculated with Eq. 5.20 at each of the wall computational cells.

The iterative procedure, here called SIMPLE-SLIP-Implicit (SSI) scheme, is given by the scheme of Fig. 5.1 with the following additional step:

(c) After convergence, compute the slip velocity with the discretized slip model  $u_{ws}^i = \frac{a}{a+1} u_p^i$ , for each of the wall computational cells.

Notice that  $\lim_{(\Delta y_f \rightarrow 0)} \frac{1}{a+1} = 0$  and this means that the refinement of the mesh near the wall does not improve the convergence of the iterative matrix solver.

For a formulation with a second order approximation of the derivative  $\frac{du}{dy}_{wall}$  (derivative of the slip law) see Appendix B.

### 5.3.3 Semi-Implicit implementation of slip laws (orthogonal meshes)

As mentioned before, the fully implicit formulation can only be applied to the linear Navier slip law. In order to implement the other slip laws implicitly we devised the method described below.

Consider again the geometry of Fig. 5.2. The idea behind this new method is to assume the slip velocity implicit on both sides of the equation for each of the wall boundary cells at each iteration  $i$ ,

$$u_{ws}^i = f_d \left( u_{ws}^i - u_p^{i-1} \right) \quad (5.22)$$

and then use a numerical scheme to find the roots of the ensuing transcendental equation. It can be proved analytically that with this method  $u_{ws}^i < u_p^{i-1}$  for all the slip boundary conditions studied here (see Appendix C ). In particular, we have the bounds  $[a; b]$  for the solution  $u_{ws}^i$  that are given by Eqs. 5.23, 5.24 and 5.25 for the nonlinear Navier, Hatzikiriakos and asymptotic slip laws, respectively,

$$[a; b] \equiv \left[ 0; u_p^{i-1} \right] \quad (5.23)$$

$$[a; b] \equiv \left[ \frac{k_{H1} k_{H2} \mu(\hat{\gamma})_{wall}^{i-1} / \Delta y_f}{k_{H1} k_{H2} \mu(\hat{\gamma})_{wall}^{i-1} / \Delta y_f + 1}; u_p^{i-1} \right] \quad (5.24)$$

$$[a; b] \equiv \begin{cases} \left[ 0; u_p^{i-1} \right] & \text{if } k_{A1} \geq 1 \\ \left[ 0; \frac{k_{A1} k_{A2} \mu(\hat{\gamma})_{wall}^{i-1} + k_{A1} \Delta y_f}{k_{A1} k_{A2} \mu(\hat{\gamma})_{wall}^{i-1} + \Delta y_f} u_p^{i-1} \right] & \text{if } k_{A1} < 1 \end{cases} \quad (5.25)$$

Here, the bisection method was used to find the roots of the transcendent equation (Eq. 5.22), starting in the range of Eqs. 5.23, 5.24 and 5.25 and stopping after  $n$  iterations such that  $(b - a) / 2^n$  is below a given error.

The canonical equation used to compute the velocity field is still Eq. 5.6 with the central coefficient given by Eq. 5.8.

With this method the new iterative algorithm (SIMPLE-SLIP-Semi-Implicit-transcendent (SSSIT)) follows the SIMPLE scheme, shown in Fig. 5.1, with the following additional step:

(a) Compute slip velocity with the discretized slip model  $u_{ws}^i = f_d(u_{ws}^i - u_p^{i-1})$  by applying the bisection method;

### 5.3.4 Semi-Implicit implementation of slip laws (orthogonal and nonorthogonal meshes)

SSSIT algorithm solves the convergence problems for linear and non-linear slip laws, but only works for orthogonal meshes. A new semi-implicit method is now devised that is able to deal with both orthogonal and nonorthogonal meshes, which is inspired on the linearization used with the Navier slip law (fully implicit formulation).

The slip velocity  $u_{ws}$  can usually be written as a function of the difference  $(u_{ws} - u_p)$  by  $u_{ws} = f_d(u_{ws} - u_p)$ . If we multiply this function by the ratio  $\frac{u_{ws} - u_p}{|u_{ws} - u_p|}$  then our slip law can be rewritten as,

$$u_{ws} = f_d(u_{ws} - u_p) \frac{u_{ws} - u_p}{|u_{ws} - u_p|} \tag{5.26}$$

and, if along the iterative procedure only the slip velocity in the numerator is taken from the present iteration  $\frac{u_{ws}^i - u_p^{i-1}}{|u_{ws}^{i-1} - u_p^{i-1}|}$ , then the general slip boundary condition becomes,

$$u_{ws}^i = \frac{c}{c + 1} u_p^{i-1} \tag{5.27}$$

with  $c = f_d(u_{ws}^{i-1} - u_p^{i-1}) / |u_{ws}^{i-1} - u_p^{i-1}|$ . Since  $\frac{c}{c+1} < 1$  we guarantee once again the continuity/monotonicity of the slip velocity. The specification of  $c$  for each of the slip laws studied here is straightforward.

Notice that although  $\|(u_{ws}^i - u_p^i) / |u_{ws}^i - u_p^i|\| = 1$ , along the calculations  $\|(u_{ws}^i - u_p^{i-1}) / |u_{ws}^{i-1} - u_p^{i-1}|\| \neq 1$ . This ratio should tend to 1 as convergence is approached or else the slip velocity vector will not be pointing in the correct direction. This is another criterion that should be checked for convergence.

The canonical equation used to compute the velocity field is again Eq. 5.6 with the central coefficient given by Eq. 5.8, and the iterative procedure (SIMPLE-SLIP-Semi-Implicit(SSSI)) follows the SIMPLE scheme, shown in Fig. 5.1, with the following additional two steps:

(a) Compute slip velocity with the discretized slip model of Eq. 5.27;

(b) Check for convergence in the residuals of the system of equations and for  $\|(u_{ws}^i - u_p^{i-1}) / (u_{ws}^{i-1} - u_p^{i-1})\| \rightarrow 1$ . If convergence is not achieved proceed to the beginning of the iteration. (The nonlinear Navier slip law can be treated as a special case of this method. For more details see Appendix D).

The generalization to nonorthogonal meshes is straightforward but takes some more work. Let  $\mathbf{u}_t = (u_{1t}, u_{2t}, u_{3t})$  and  $\boldsymbol{\tau}_t = (\tau_{1t}, \tau_{2t}, \tau_{3t})$  be the tangent (to the wall) velocity and stress vectors, both with Cartesian components. By Eq. 5.11 and assuming Couette flow near the wall, we obtain the following general formula for all slip laws,

$$\mathbf{u}_{ws} = \pm f \left( \left\| \left( \mu(\dot{\gamma}) \frac{d\mathbf{u}}{dn} \right)_{wall} \right\| \right) \frac{\left( \mu(\dot{\gamma}) \frac{d\mathbf{u}}{dn} \right)_{wall}}{\left\| \left( \mu(\dot{\gamma}) \frac{d\mathbf{u}}{dn} \right)_{wall} \right\|}, \quad (5.28)$$

where the  $\pm$  depends on the sign of  $\frac{d\mathbf{u}}{dn}$ , and  $\frac{d\mathbf{u}}{dn} = \left( \frac{du_{1t}}{dn}, \frac{du_{2t}}{dn}, \frac{du_{3t}}{dn} \right)$  with  $u_{jt}$ ,  $j = 1, 2, 3$  the components of the tangent vector at the wall.

The discretization of these derivatives is given by,

$$\left( \frac{u_{1t} - u_{1tP}}{\delta n}; \frac{u_{2t} - u_{2tP}}{\delta n}; \frac{u_{3t} - u_{3tP}}{\delta n} \right) \quad (5.29)$$

where  $\delta n$  is the distance between the wall and  $P'$  (as given in Fig. 5.4) and  $u_{jtP} = u_{jP} - n_j \mathbf{u} \cdot \mathbf{n}$ ,  $j = 1, 2, 3$  are the components of the tangent velocity vector at the center of the adjacent cell  $P$ .

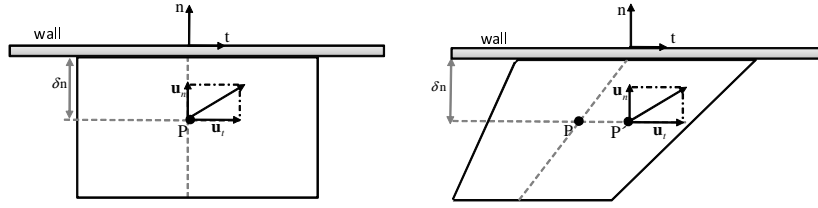


Figure 5.4: Projection of the velocity vector in the center of the computational cell into the tangent and normal part (left - orthogonal mesh; right- nonorthogonal mesh).

The velocity at  $P'$  is not known (Fig. 5.4), so it is assumed that  $\mathbf{u}_P = \mathbf{u}_{P'}$ . This introduces an error in the calculations that will diminish as the mesh quality and refinement are improved.

Considering that  $\mu(\dot{\gamma})_{wall}$  is a positive scalar and that only the slip velocity on the last term of Eq. 5.28 is evaluated implicitly then Eq. 5.28 can be rewritten as,

$$(u_1, u_2, u_3)_{ws}^i = \frac{d}{d+1} (u_{1tP}; u_{2tP}; u_{3tP})^{i-1} \quad (5.30)$$

with



$$d \equiv \begin{cases} \text{Navier} & \frac{k_{nl} \|g\|^{m-1} (\mu(\dot{\gamma})_{wall}^{i-1})^m}{\delta n} & (a) \\ \text{Hatzikiriakos} & \frac{k_{H1} \sinh(k_{H2} \|\mu(\dot{\gamma})_{wall}^{i-1} g\|) \mu(\dot{\gamma})_{wall}^{i-1}}{\|\mu(\dot{\gamma})_{wall}^{i-1} g\| \delta n} & (b) \\ \text{asymptotic} & \frac{k_{A1} \ln(1+k_{A2} \|\mu(\dot{\gamma})_{wall}^{i-1} g\|) \mu(\dot{\gamma})_{wall}^{i-1}}{\|\mu(\dot{\gamma})_{wall}^{i-1} g\| \delta n} & (c) \end{cases} \quad (5.31)$$

and  $g = (u_{1t} - u_{1tP}; u_{2t} - u_{2tP}; u_{3t} - u_{3tP})^{i-1} / \delta n$ .

Notice that  $u_{jws} < u_{jtP}$  seems to be sufficient to obtain a stable computation. In our tests this procedure worked well, except for very high slip coefficients with the Hatzikiriakos law, where convergence was difficult. More details on this issue can be found in the following section.

## 5.4 RESULTS AND DISCUSSION

To assess the performance of the numerical implementations the slip models studied here were first compared with analytical solutions for fully-developed channel flow with wall slip and subsequently tested for the slip-stick and 4:1 contraction flow problems. The analysis is carried out first for Newtonian fluids and subsequently for viscoelastic fluids.

### 5.4.1 Newtonian fluids

Figs.5.5(a) and 5.5(b) compare predictions by the nonlinear Navier slip law (including the particular case of the linear Navier slip law ( $m = 1$ )) for different values of the model parameters (slip coefficient and exponent) with the corresponding analytical solutions. The comparison between the analytical and numerical solutions for the Hatzikiriakos and asymptotic slip laws can be seen in Figs. 5.5(d) and 5.5(e), respectively. The accuracy of the results is quite good as can also be assessed by a zoom of Fig. 5.5(a), shown in Fig. 5.5(c), but more specifically by Figs. 5.6 and 5.7(a) which plot the relative error in the prediction of the slip velocity as a function of the mesh size for the linear and non-linear Navier slip laws, respectively. Fig. 5.6 shows that the accuracy and the order of convergence of the solution both increase with the slip coefficient. For instance, for the linear law the order of convergence increases from 2.14 with  $k_l = 10E - 6 [m.(Pa.s)^{-1}]$  to 2.6 for  $k_l = 1 [m.(Pa.s)^{-1}]$ . This is so because increasing the slip coefficient leads to higher slip velocities, the velocity profile tends to a plug thus reducing the role of diffusion and increasing that of convection where a third-order accurate scheme (Leonard, 1979) is used. Note also that here the error committed in the evaluation of the tangent stress is equal to the error for the slip velocity because the slip velocity depends linearly on the tangent stress  $|u_{ws}^{num} - u_{ws}| / |u_{ws}| = |\tau_{12}^{num} - \tau_{12}| / |\tau_{12}|$ .

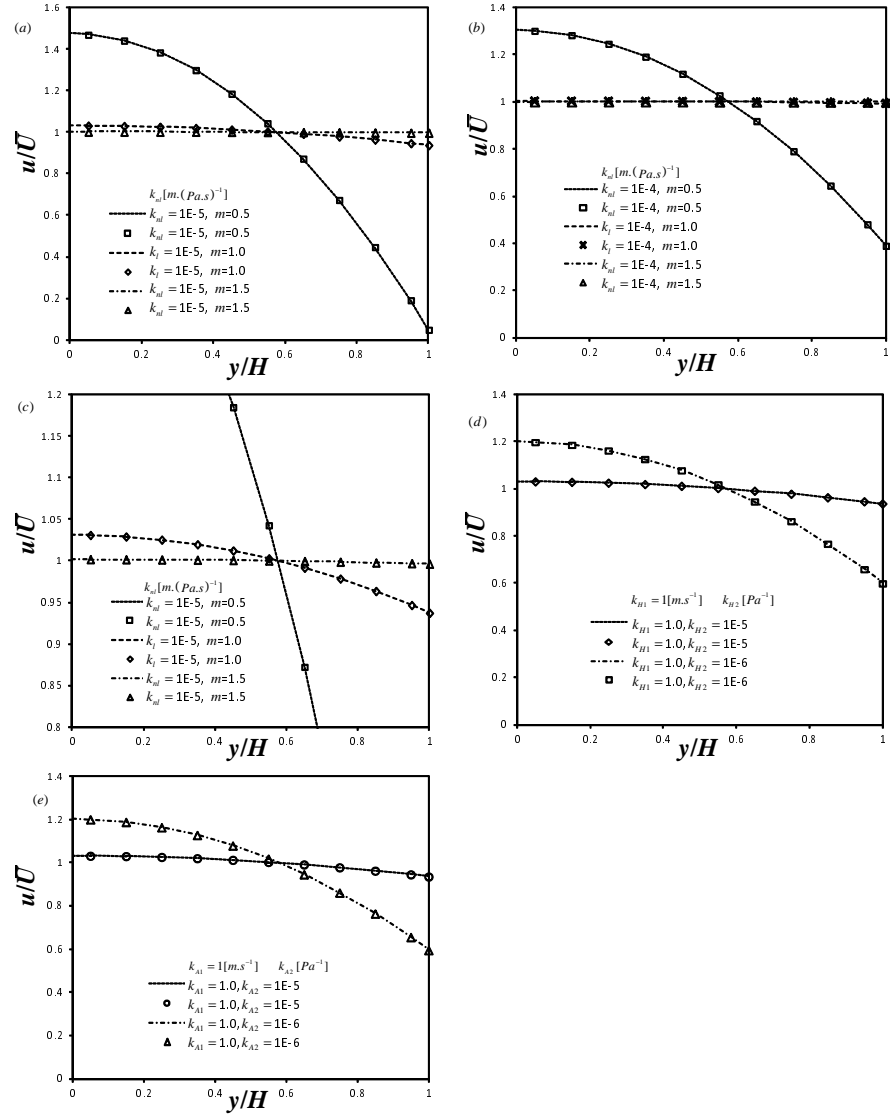


Figure 5.5: Comparison between analytical (lines) and numerical (symbols) solutions for a fully developed channel flow using linear and non-linear slip laws with different slip coefficients (a) non-linear Navier slip law with  $k_{nl} = 1E - 5$  (b) non-linear Navier slip law with  $k_{nl} = 1E - 4$  (c) zoomed view of the non-linear Navier slip law with  $k_{nl} = 1E - 5$  (d) Hatzikiriakos slip law (e) Asymptotic slip law.  $\bar{U}$  is the imposed mean velocity and  $H$  is half the channel width.

These features are observed regardless of the numerical method used to obtain the solution as can be confirmed in Figs. 5.7(a) and 5.7(b), where the order of convergence and error are shown for the predictions obtained with the nonlinear Navier law using the numerical methods SSSIT and SSSI, respectively. Our calculations with the two methods show that the order of convergence increases with the slip coefficient.

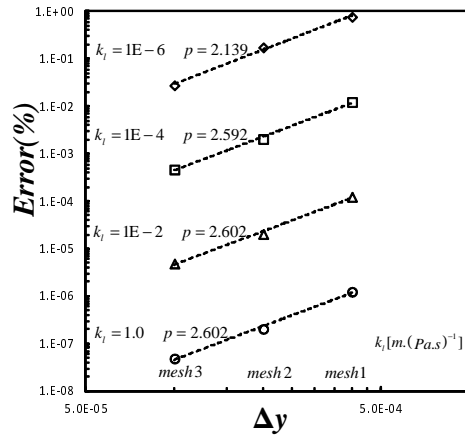


Figure 5.6: Variation of the relative error in slip velocity with mesh spacing  $\Delta y$  for the linear Navier slip law with different slip coefficients and three different meshes ( $Re = 0.003$ ) using the totally implicit scheme ( $p$  stands for the order of convergence).

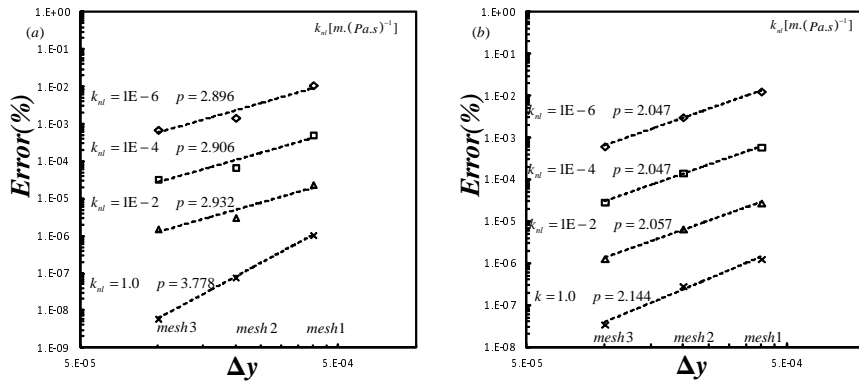


Figure 5.7: Variation of the relative error in slip velocity with mesh spacing  $\Delta y$  for the nonlinear Navier slip law with different slip coefficients and three different meshes ( $Re = 0.003$ ). (a)  $n = 1.5$  SSSIT (b)  $n = 1.5$  SSSI.  $p$  stands for the order of convergence.

Comparing both methods, the order of convergence is larger for the Method SSSIT, where at each iteration the “numerically correct” slip solution is determined by the bisection method, whereas for Method SSSI the solution is only approximated using values from the previous iteration.

After the code assessment, the next step was to compare the various explicit and implicit/semi-implicit schemes using the channel flow of Fig. 5.2 (with the mesh 2 of Table 5.1), at two different Reynolds numbers of 0.003 and 10 for the four different implementations of slip boundary conditions proposed: (1) totally explicit (SSE), (2) totally implicit (SSI), (3) semi-implicit transcendent (SSSIT) and (4) semi-implicit (SSSI). The linear Navier slip model was chosen for the comparison because all the schemes work with it, and the non-linear Navier slip model was chosen to compare scheme (3) and (4).

Table 5.1: Three different uniform meshes were created.  $x$  stands for the number of cells in the  $x$  direction and  $y$  stands for the numbers of cells in the  $y$  direction.

	$x$	$y$	$\Delta x/H = \Delta y/H$
mesh 1	25	5	0.2
mesh 2	50	10	0.1
mesh 3	100	20	0.05

*Linear slip model:*

Fig. 5.8 plots the number of iterations required for convergence, and shows that for the implicit procedure (SSI) and this specific geometry and flow, the larger the slip velocity, the quicker is the convergence. This is so because for large slip the analytical solution is the plug flow, and the guessed initial velocities are very close to the converged values, so only a few iterations are needed to obtain convergence. For the remaining schemes similar results were obtained in terms of number of iterations. It should also be noticed that the error for the totally explicit scheme (SSE) was larger than for any other method, because for high slip coefficients the required relaxation factor was sometimes of the same order as the tolerance used to stop the numerical simulation.

From these results one can conclude that for the linear slip law the best method is the implicit procedure (SSI).

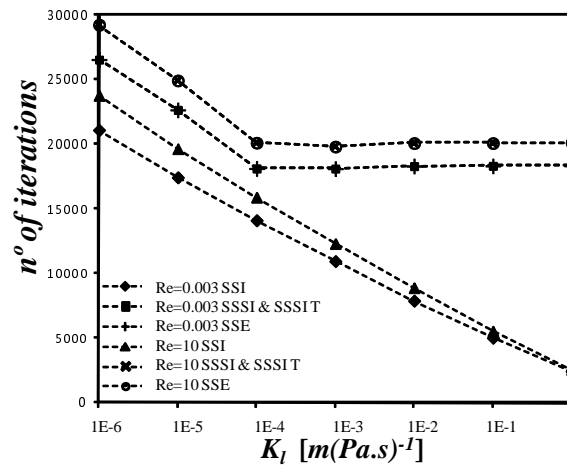


Figure 5.8: Graph representing a comparison for the number of iterations needed to achieve convergence using the schemes: implicit (SSI), explicit (SSE), semi-implicit transcendent (SSSIT) and semi-implicit SSSI (for the linear Navier slip law) with the simple geometry of Fig. 2 (mesh 2).

*Nonlinear slip models:*

The advantages of the semi-implicit procedures can be seen with the nonlinear law SSSIT and SSSI. Table 5.2 shows the number of iterations needed to obtain convergence for  $Re = 0.003, 10$ . The results for the totally explicit method are not shown because convergence

was impossible. This results are for a simple geometry, but for a more complex geometry the capability of the explicit procedure is expected to decrease.

Table 5.2: Number of iterations needed to achieve convergence using the schemes SSSIT and SSSI for the nonlinear Navier slip law with  $n = 1.5$ , for the Hatzikiriakos and for the asymptotic slip laws.

slip coefficient ( $k_{H1}, k_{H2}$ )	nonlinear NS $k_n [m.(Pa.s)^{-1}]$		Hatzikiriakos $k_{H1} = 1 [m.s^{-1}]$ $k_{H2} [Pa^{-1}]$			asymptotic $k_{H1} = 1 [m.s^{-1}]$ $k_{H2} [Pa^{-1}]$		
	Re=0.003	Re=10	Re=0.003	Re=0.003	Re=10	Re=0.003	Re=0.003	Re=10
	SSSIT & SSSI	SSSIT & SSSI	SSSIT	SSSI	SSSIT & SSSI	SSSIT	SSSI	SSSIT & SSSI
1.0E-06	18142	19932	26398	26406	overflow	27204	27198	33049
1.0E-05	17764	20049	22452	22452	overflow	23662	23663	33050
1.0E-04	18266	20094	overflow	17825	overflow	16622	19606	33048
1.0E-03	18327	20111	overflow	18165	overflow	14944	14797	33045
1.0E-02	18344	20130	overflow	18331	overflow	13038	13331	33043
1.0E-01	18348	20162	overflow	18345	overflow	13629	13797	33042
1.0E+00	18351	20157	overflow	18354	overflow	13680	13811	33040

From Table 5.2 it can be seen that for the nonlinear Navier slip law the number of iterations for methods SSSIT and SSSI was the same. For method SSSI we found that when  $d / (d + 1) \approx 1$  (see Eq. 5.30) the code was not able to get out of a periodic sequence where the velocity equals the tangent stress and in order to remedy this issue and obtain convergence a classic relaxation for the slip velocity was used.

For the asymptotic slip law, the schemes SSSIT and SSSI were both efficient and a similar number of iterations were required for convergence. It should be noticed that when starting the outer iterations, the slip velocity was initialized as 90% of the velocity in the center of the nearest computational cell. Starting with null slip velocity and a constant non-zero velocity at the center of the adjacent computational cells may lead to divergence.

For the Hatzikiriakos slip law several convergence issues occur, especially for high slip coefficients. For both methods SSSIT and SSSI the main problem is due to the hyperbolic function, which either gives very high values at the beginning of the calculations leading to  $d / (d + 1) \approx 1$  (SSSI), or gives values that cannot be computed by the CPU (SSSIT).

We tried to solve the problem by controlling the growth of the hyperbolic function by limiting the maximum value of the sinh function argument, however, for high velocities this algorithm does not seem to solve the problem because convergence could only be obtained for mean velocities below  $3 [m.s^{-1}]$  (Re=0.0091). The problem seems to be velocity value and not the Reynolds number itself as one could increase the Reynolds number by imposing a mean velocity smaller than  $3 [m.s^{-1}]$ .

We also tried to initiate the calculations for the Hatzikiriakos model using the converged results from the linearized version of this model,

but convergence was poorly enhanced and the series expansion of the function did not solve the problem either.

For the Hatzikiriakos slip law, with the scheme SSSIT only the first two trials converged. So, the chosen method for this slip law is method SSSI, but even here computations are limited to smaller imposed velocities as with higher imposed velocities the sinh function overflows.

#### 5.4.2 Non-Newtonian fluids

##### 5.4.2.1 Slip-stick

The simplified PTT model was selected for testing the slip-stick problem in a straight channel (cf. Fig. 5.9) using orthogonal and skewed meshes and the linear and nonlinear slip laws. This flow comprises two regions: the initial part (region I) is unbounded (the upper boundary imposed as a symmetry plane) and the second region (region II) has a solid wall. A symmetry plane was considered at the bottom boundary in both regions. The inlet velocity is a plug profile and the mesh used has the properties indicated in Table 5.3 and Fig. 5.9. The meshes (orthogonal and non-orthogonal) are those of (Oliveira et al., 1998) and correspond to their mesh 7, with a skewness of  $30^\circ$  for the non-orthogonal grid.

Table 5.3: Slip constants used in the simulation of the slip-stick flow for the different slip models.

linear Navier	$k_t = 1.0E-a, a \in \{1;2;3;4;5;6\} [m.(Pa.s)^{-1}]$	
nonlinear Navier	$k_{nl} \in \{1.0E-5; 1.0\} [m.(Pa.s)^{-1}]$	
Hatzikiriakos	$k_{H1} = 1.0 [m.s^{-1}]$	$k_{H2} \in \{1.0E-5; 1.0\} [m.s^{-1}]$
Asymptotic	$k_{A1} = 1.0 [Pa^{-1}]$	$k_{A2} \in \{1.0E-5; 1.0\} [Pa^{-1}]$

Tests were made for different values of the slip coefficients (see Table 3), at constant Reynolds number  $Re = \rho UH/\eta = 20$  and a varying Deborah number  $De = \lambda U/H \in \{0.25; 0.5; 1.0; 2.0\}$  with  $\varepsilon = 0.25$ . Convergence could be achieved for all cases when the mesh was orthogonal and all the slip laws whereas for the skewed mesh convergence was only possible for a Deborah number of up to 2. As expected an easier convergence could be seen for high slip velocities (high slip coefficients), because the slip velocity numerically smoothes the singularity at the wall.

In Figure 5.10 one can see the variation (with slip) of the flow variables  $u, \tau_{xx}, \tau_{xy}, \tau_{yy}$  along the line  $y/H = 0.9975$  (near the wall). As expected, near the singularity the variation of all variables tend to smooth with the slip coefficient and this is especially clear with the stresses that develop due to the extensional nature of the flow in the vicinity of the singularity. As the fluid moves away from the singularity, the stresses start to redevelop for shear flow. Increasing the

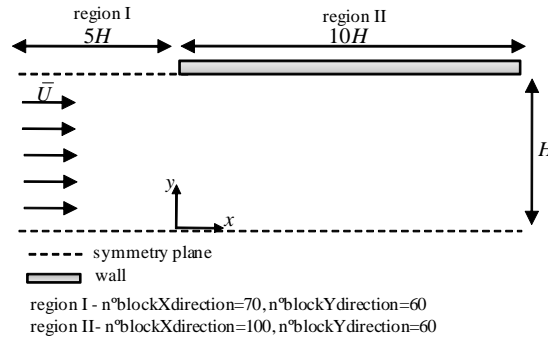


Figure 5.9: Schematic representation of the slip-stick geometry.

slip coefficient, the slip velocity increases and the shear rate tends to zero. This reduces the transverse transfer of momentum by molecular diffusion and flow redevelopment is slowed down. This can be seen especially for the case of  $\tau_{xx}$  with  $k_l = 1E - 4 [m.(Pa.s)^{-1}]$  (Fig. 5.10 (b)).

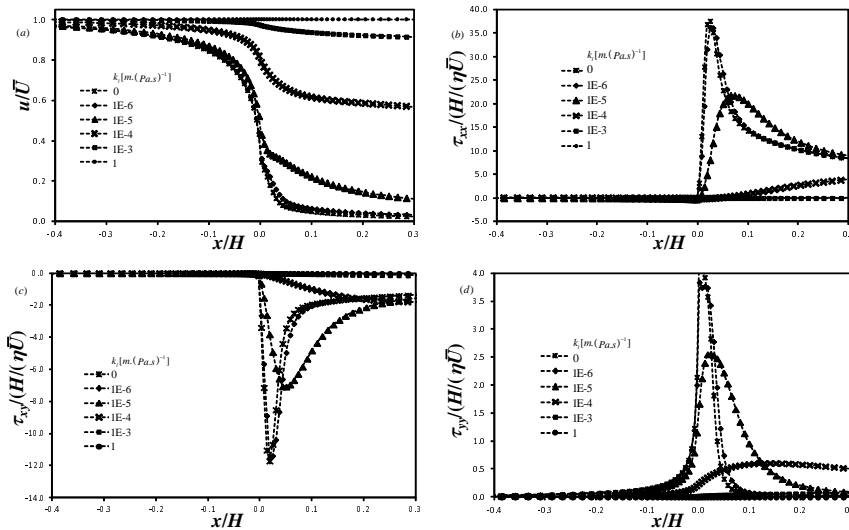


Figure 5.10: Variation of: (a)  $u$ , (b)  $\tau_{xx}$ , (c)  $\tau_{xy}$  and (d)  $\tau_{yy}$  along the slip-stick region near the wall  $y/H = 0.9975$ . Four different slip constants were used  $k_l \in \{1E - 6, 1E - 5, 1E - 4, 1E - 3\}$  and  $De = 2$ ,  $Re = 20$ .

5.4.2.2 Contraction flow

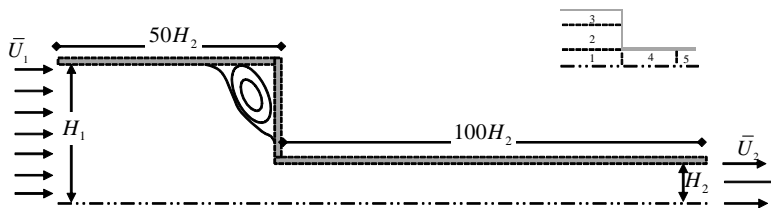


Figure 5.11: Schematic of the 4:1 contraction geometry.

The second benchmark flow problem tested for viscoelastic fluids (under the influence of slip) was the planar 4:1 contraction flow.

The geometry for this problem is given in Fig.5.11 and was divided into five blocks (Table 5.4) with only half of the channel being considered because of symmetry. Based on (Oliveira et al., 1998), (Alves et al., 2003b) and (Ferrás et al., 2012a) we built three different meshes with consistent mesh refinement between consecutive meshes (MC<sub>1</sub>, MC<sub>2</sub> and MC<sub>3</sub> as in Table 5.4). The notation  $n_x$  and  $n_y$  is used to represent the number of cells in the  $x$  and  $y$  directions, respectively,  $f_x$  and  $f_y$  are the corresponding contraction/expansion ratios that allow the concentration of cells in zones where high gradients are expected to occur. The most refined mesh (MC<sub>3</sub>) has almost two hundred thousand cells.

The simulations were performed for the sPTT model with a constant Reynolds number  $Re = \rho U_2 H_2 / \eta = 0.04$  and a varying Deborah number  $De = \lambda U_2 / H_2 \in \{0; 1; 2; 3; 4; 5\}$  with  $\varepsilon = 0.25$  and viscosity ratio  $\beta = \frac{\eta_s}{\eta_0} = \frac{\eta_s}{\eta_s + \eta_p} = \frac{1}{9}$ .

Table 5.4: Mesh properties for the 4:1 contraction geometry.

Zone	M1				M2				M3				M4						
	$f_x$	$f_y$	$n_x$	$n_y$	$f_x$	$f_y$	$n_x$	$n_y$	$f_x$	$f_y$	$n_x$	$n_y$	$f_x$	$f_y$	$n_x$	$n_y$			
1	0.82100	0.84750	24	10	0.90609	0.92060	47	20	0.95189	0.95948	94	40	0.97565	0.97953	188	80			
2	0.82100	1.20910	24	13	0.90609	1.09959	47	25	0.95189	1.04861	94	50	0.97565	1.02402	188	100			
3	0.82100	0.73840	24	5	0.90609	0.85930	47	9	0.95189	0.92699	94	17	0.97565	0.96280	188	34			
4	1.27170	0.84750	20	10	1.12770	0.92060	40	20	1.06193	0.95948	80	40	1.03050	0.97953	160	80			
5	1.00000	0.84750	7	10	1.00000	0.92060	13	20	1.00000	0.95948	25	40	1.00000	0.97953	50	80			
n° cells				942	n° cells				3598	n° cells				14 258	n° cells				57032
$\Delta_{\min}$				0.037	$\Delta_{\min}$				0.020	$\Delta_{\min}$				0.010	$\Delta_{\min}$				0.005

The method that was tested was the SSSI because of its good results in the previous geometries and the chosen viscoelastic model was again the linear PTT model.

For the linear Navier slip law we could obtain convergence only up to a  $De$  number of 5. As expected convergence is reduced with the mesh refinement. It should be noticed that for the no-slip velocity boundary condition no restrictions were found in the  $De$  number for this specific geometry and constitutive equation (Alves et al., 2003b).

Based on the results obtained for the linear Navier slip law it is expectable that the other nonlinear slip laws will again suffer from poor convergence. Because the Hatzikiriakos slip law is the most difficult slip law to compute, we also tested the limits on the  $De$  number for the Hatzikiriakos slip law. We could obtain convergence up to  $De = 1$  with  $k_{H1} = 1$  and  $k_{H2} = 1E - 4$ .

We could also find that the presence of slip velocity leads to an increase of the vortex size, Fig. 5.12 (see (Ferrás et al., 2012a) for more details).



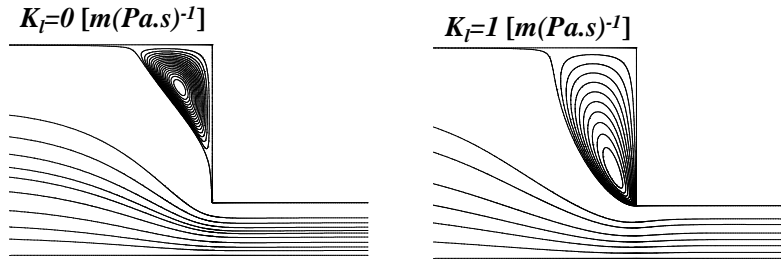


Figure 5.12: Vortex size for the 4:1 contraction flow of a PTT fluid for two different slip coefficients  $k_l = 0$  and  $k_l = 1$ .

## 5.5 CONCLUSIONS

Several new explicit, implicit and semi-implicit numerical techniques were developed to implement slip boundary conditions into a finite volume method based code. These implementations are “stable” for the linear and nonlinear Navier, and asymptotic slip laws. However the Hatzikiriakos slip model leads to unstable behavior for high slip coefficients leading to divergence of the code. Some ad hoc procedures were presented to attenuate this divergence, but these never solve completely the problem which is rooted on the sinh function and the corresponding computer overflow it creates. The predictions given by the numerical code were compared with the analytical solutions and excellent agreements were obtained for Newtonian fluids. Finally the implementations were tested with viscoelastic fluids in the slip-stick and benchmark planar 4:1 contraction flow, evidencing the robustness of the proposed numerical procedures.

## ACKNOWLEDGEMENTS

The authors would like to acknowledge the financial support provided by Fundação para a Ciência e Tecnologia under the project SFRH / BD / 37586 / 2007.

## APPENDIX A: DISCRETIZATION OF THE MOMENTUM EQUATION FOR A SIMPLE 2D GEOMETRY

The continuity and momentum equations can be written in Cartesian coordinates as Eqs. 5.32 and 5.33, respectively,

$$\frac{\partial u}{\partial x} + \frac{\partial v}{\partial y} = 0 \quad (5.32)$$

$$\frac{\partial(\rho\phi)}{\partial t} + \frac{\partial(u\phi)}{\partial x} + \frac{\partial(v\phi)}{\partial y} = -\frac{\partial p}{\partial \Psi} + \frac{\partial}{\partial x} \left( \eta_s \frac{\partial \phi}{\partial x} + \tau_{\Psi x} \right) + \frac{\partial}{\partial y} \left( \eta_s \frac{\partial \phi}{\partial y} + \tau_{\Psi y} \right) \quad (5.33)$$

where  $\phi = u$ ,  $\Psi = x$  in the  $x$ -momentum equation, and  $\phi = v$ ,  $\Psi = y$  in the  $y$ -momentum equation. The discretization of the continuity equation in a computational cell P (Fig. 5.2) results in the balance of mass fluxes for this cell. These fluxes are normal to the cell faces, therefore, the slip boundary condition has no direct influence on this equation (since the walls are impermeable). The momentum equation is directly affected by the slip boundary condition, for that reason its discretization is briefly explained below. The interested reader should consult (Patankar, 1980; Oliveira et al., 1998) for more details.

In the momentum equation (Eq. 5.33), the discretization of the transient, convective and pressure gradient terms is not directly affected by the implementation of slip velocity, but the diffusive term is affected, as explained next.

The discretization of the **transient** term using a first order scheme is given by Eq. ???. The variable  $\phi$  is evaluated at the center of the cell P, meaning that this term is not directly affected by the slip velocity (the superscript "0" indicates the previous time step and compass notation is used, i.e.  $e$  stands for "east",  $w$  for "west",  $n$  for "north" and  $s$  for "south" cell faces).

$$\int_w^e \int_s^n \int_{t_0}^{t_1} \frac{\partial(\rho\phi)}{\partial t} dt dx dy = \int_w^e \int_s^n (\rho\phi) - (\rho\phi)^0 dx dy \approx [\rho\phi]_P - (\rho\phi)_P^0 \Delta V_P \quad (5.34)$$

For the fully implicit method in time used here all other terms are evaluated at the present time step.

Discretization of the **convective** terms results in Eq. 5.35 for the  $x$  and  $y$  momentum equations. Although the variable of interest  $\phi_n$  (cf. Fig.1) appears in Eq. 5.35, for impermeable walls this wall-normal **convective** term has no contribution from the slip boundary condition ( $F_n = \Delta y \rho v = 0$ ).

$$\int_w^e \int_s^n \int_{t_0}^{t_1} \frac{\partial(u\phi)}{\partial x} + \frac{\partial(v\phi)}{\partial y} dt dx dy \approx (F_e \phi_e - F_w \phi_w) \Delta t + (F_n \phi_n - F_s \phi_s) \Delta t \quad (5.35)$$

The discretization of the **diffusive** term for the PTT fluid together with the assumption of Eq. 5.14 leads to the following expression to be incorporated the  $x$  and  $y$  momentum equations,

$$\left[ \left( \mu(\dot{\gamma}) \frac{\partial \phi}{\partial y} \right)_{n \equiv wall} - \left( \eta_s \frac{\partial \phi}{\partial y} + \tau_{\Psi y} \right)_s \right] \Delta x \Delta t + \left[ \left( \eta_s \frac{\partial \phi}{\partial x} + \tau_{\Psi x} \right)_e - \left( \eta_s \frac{\partial \phi}{\partial x} + \tau_{\Psi x} \right)_w \right] \Delta x \Delta t \quad (5.36)$$

Notice that the terms for the north cell face  $(\dots)_n$  at Eq. 5.36 came from Eq. 5.14 (the north cell face is a boundary face). The slip velocity

is then carried via  $\left(\frac{\partial\phi}{\partial y}\right)_{n\equiv wall}$ . Different one-sided approximations to the derivatives can be used, such as the first order scheme of Eq. 5.37, or the second order accurate scheme of Eq. 5.38. Assuming uniform meshes the first order approximation is given by,

$$\left(\frac{\partial\phi}{\partial y}\right)_{wall} = \frac{\phi_{wall} - \phi_P}{\Delta y_f} + O(\Delta y) \quad (5.37)$$

$$\left(\frac{\partial\phi}{\partial y}\right)_{wall} = \frac{8\phi_{wall} - 9\phi_P + \phi_S}{6\Delta y_f} + O(\Delta y)^2 \quad (5.38)$$

Assuming square computational cells and the use of central differences to discretize all diffusion-related derivatives (except at the boundaries) the first term in Eq. 5.36 becomes Eqs. 5.39 and 5.40 for the first and second order approximations, respectively,

$$\left[ \frac{\mu(\dot{\gamma})_{wall}}{\Delta y_f} \phi_n + \frac{(\eta_s)_s}{\Delta y} \phi_S - \left( \frac{\mu(\dot{\gamma})_{wall}}{\Delta y_f} + \frac{(\eta_s)_s}{\Delta y} \right) \phi_P + (\tau_{\Psi y})_s \right] \Delta x \Delta t \quad (5.39)$$

$$\begin{aligned} & \left[ \frac{8\mu(\dot{\gamma})_{wall}}{6\Delta y_f} \phi_n + \left( \frac{\mu(\dot{\gamma})_{wall}}{6\Delta y_f} + \frac{(\eta_s)_s}{\Delta y} \right) \phi_S \right] \Delta x \Delta t + \\ & \left[ - \left( \frac{9\mu(\dot{\gamma})_{wall}}{\Delta y_f} + \frac{(\eta_s)_s}{\Delta y} \right) \phi_P + (\tau_{\Psi y})_s \right] \Delta x \Delta t \end{aligned} \quad (5.40)$$

After grouping all the terms, the discretized momentum equation is rewritten in the standard compact form, (where we have now substituted the general variable  $\phi$  by the specific variable  $u$ , since we are analyzing the  $x$  - momentum equation),

$$a_P u_P = a_E u_E + a_W u_W + a_S u_S + \underbrace{a_N u_N + \frac{\Delta V_P (\rho\phi)_P^0}{\Delta t} + \frac{\delta p}{\delta \Psi} + S_{stress}}_{source\ terms} \quad (5.41)$$

where  $\frac{\delta p}{\delta \Psi}$  represents a general discretization of the pressure gradient and  $a_E$ ,  $a_S$ ,  $a_W$  are given by Eqs. 5.42, 5.43 and 5.44 respectively,

$$a_E = a_E^c + a_E^d = a_E^c + \frac{(\eta_s)_e \Delta y}{\Delta x} \quad (first\ and\ second\ order) \quad (5.42)$$

$$a_S = a_S^c + a_S^d = \begin{cases} a_S^c + \frac{(\eta_s)_s \Delta x}{\Delta y} \quad (first\ order) \\ a_S^c + \left( \frac{\mu(\dot{\gamma})_{wall}}{6\Delta y_f} + \frac{(\eta_s)_s}{\Delta y} \right) \Delta x \quad (second\ order) \end{cases} \quad (5.43)$$

$$a_W = a_W^c + a_W^d = a_W^c + \frac{(\eta_s)_w \Delta y}{\Delta x} \quad (first\ and\ second\ order) \quad (5.44)$$

with the superscripts  $c$  and  $d$  referring to the convective and diffusive contributions, respectively. To account for the slip boundary condition, which affects  $a_N u_N$ , the coefficient  $a_N$  is given by Eqs. 5.45 and 5.46 for first and second order accurate discretization schemes, respectively,

$$a_N = \frac{\mu(\dot{\gamma})_{wall} \Delta x}{\Delta y_f} \quad (5.45)$$

$$a_N = \frac{8\mu(\dot{\gamma})_{wall} \Delta x}{6\Delta y_f} \quad (5.46)$$

Finally the central coefficient  $a_P$  is given as in the standard procedure by,

$$a_P = a_E + a_W + a_S + a_N + \alpha \frac{(\eta_s)_n \Delta x}{6\Delta y} + \frac{\Delta V_P \rho_P^0}{\Delta t} \quad (5.47)$$

with  $\alpha = 0$  and  $\alpha = 1$  for the first and second order approximations, respectively.

#### APPENDIX B: SECOND ORDER DISCRETIZATION OF THE LINEAR NAVIER SLIP LAW

The implicit calculation of the second order accurate linear Navier slip law is given by Eq. 5.48,

$$u_{ws}^i = \frac{9k_l \mu(\dot{\gamma})_{wall}}{6\Delta y_f + 8k_l \mu(\dot{\gamma})_{wall}} u_P^i - \frac{k_l \mu(\dot{\gamma})_{wall}}{6\Delta y_f + 8k_l \mu(\dot{\gamma})_{wall}} u_S^i \quad (5.48)$$

with the restrictions of Eq. 5.49,

$$\begin{cases} u_P^i < \frac{k_l \mu(\dot{\gamma})_{wall}}{k_l \mu(\dot{\gamma})_{wall} - 6\Delta y_f} u_S^i & \text{if } k_l \mu(\dot{\gamma})_{wall} - 6\Delta y_f > 0 \\ u_P^i > \frac{k_l \mu(\dot{\gamma})_{wall}}{k_l \mu(\dot{\gamma})_{wall} - 6\Delta y_f} u_S^i & \text{if } k_l \mu(\dot{\gamma})_{wall} - 6\Delta y_f < 0 \end{cases} \quad (5.49)$$

which are imposed by the need to ensure that  $u_{ws}^i < u_P^i$ . Under these conditions the momentum equation for the control volume P is

$$a_P u_P = a_E u_E + a_W u_W + a_S u_S + \underbrace{\frac{\Delta V_P (\rho \phi)_P^0}{\Delta t} + \frac{\delta p}{\delta \Psi} + S_{stress}}_{\text{source terms}} \quad (5.50)$$

with  $a_S$  given by,

$$a_S = a_S^c + \frac{(\eta_s)_s \Delta x}{\Delta y} - \frac{k_l \mu(\dot{\gamma})_{wall}}{8k_l \mu(\dot{\gamma})_{wall} + 6\Delta y_f} u_S^i \quad (5.51)$$

and  $a_P$  by,

$$a_P = a_E + a_W + a_S + a_N - \frac{8k_I\mu(\dot{\gamma})_{wall}}{8k_I\mu(\dot{\gamma})_{wall} + 6\Delta y_f} + \frac{\Delta V_P \rho_P^0}{\Delta t} \quad (5.52)$$

Eq. 5.51 shows that  $a_S$  can become negative therefore violating the requirement for positive coefficients (Patankar, 1980) needed to obtain physically realistic solutions, and this is an important limitation. The condition for positive values of  $a_S$  cannot be given because it depends on several physical parameters that we do not control.

#### APPENDIX C: EXISTENCE AND UNIQUENESS OF THE DISCRETIZED SLIP VELOCITY

*Hatzikiriakos slip law:*

We postulate that:

(1) The relationship between  $u_{ws}^i$  and  $u_P^{i-1}$  must be

$$u_{ws}^i = k_{H1} \sinh\left(\frac{k_{H2}\mu(\dot{\gamma})}{\Delta y_f} (u_P^{i-1} - u_{ws}^i)\right) \quad (5.53)$$

with  $u_{ws}^i < u_P^{i-1}$  (the physics of the problem requires the slip velocity to be smaller than the velocity at center of the adjacent computational cell), and that  $u_{ws}^i$  and  $u_P^{i-1}$  are both positive or both negative.

Let us assume, without loss of generality, that they are both positive. It must be proved that

$$\begin{aligned} \exists (u_{ws}^i)^1 : u_{ws}^i &= k_{H1} \sinh\left(\frac{k_{H2}\mu(\dot{\gamma})}{\Delta y_f} (u_P^{i-1} - u_{ws}^i)\right) \\ \wedge 0 &\leq u_{ws}^i \leq u_P^{i-1}, \forall k_{H1}, k_{H2}, \mu(\dot{\gamma}), u_P^{i-1} \in \mathbb{R}_0^+ \end{aligned} \quad (5.54)$$

**Proof: (existence)** Because  $0 \leq u_{ws}^i \leq u_P^{i-1}$ , then,  $\exists \delta \in \mathbb{R} : 0 \leq \delta \leq u_P^{i-1}$  in such a way that  $u_{ws}^i$  can be written like  $u_{ws}^i = u_P^{i-1} - \delta$ . The problem can now be stated as,

$$\begin{aligned} \exists (\delta)^1 : \delta + k_{H1} \sinh\left(\frac{k_{H2}\mu(\dot{\gamma})}{\Delta y_f} \delta\right) - u_P^{i-1} &= 0 \\ \wedge 0 &\leq \delta \leq u_P^{i-1}, \forall k_{H1}, k_{H2}, \mu(\dot{\gamma}), u_P^{i-1} \in \mathbb{R}_0^+ \end{aligned} \quad (5.55)$$

Let  $f(\delta) = \delta + k_{H1} \sinh\left(\frac{k_{H2}\mu(\dot{\gamma})}{\Delta y_f} \delta\right) - u_P^{i-1}$ , because  $f(u_P^{i-1})f(0) < 0$  and  $f(\cdot)$  is a real-valued continuous function on the interval  $[0; u_P^{i-1}]$ , the intermediate value theorem implies that  $\exists \delta : f(\delta) = 0$ .

(uniqueness) Rolle theorem states that for a continuous function in some interval  $[a; b]$ ,  $f : [a; b] \rightarrow \mathbb{R}$ , between two zeros (say  $x$  and  $y$ ) that belong to that interval, there exists a value  $\xi \in ]x; y[ : f'(\xi) = 0$  (if  $f'(\xi) \neq 0$  there could exist at most one zero). Since  $f'(\delta) \neq 0 \forall \delta \in \mathbb{R}$ ,

$$f'(\delta) = 1 + k_{H1} \cosh\left(\frac{k_{H2}\mu(\dot{\gamma})}{\Delta y_f} \delta\right) \frac{k_{H2}\mu(\dot{\gamma})}{\Delta y_f} > 0 \quad (5.56)$$

Rolle theorem implies that  $\delta$  is unique. It is now proved the existence and uniqueness of  $u_{ws}^i$ .

More can be said about the bottom bound of  $u_{ws}^i$ . Since:

$$\sinh\left(\frac{k_{H2}\mu(\dot{\gamma})}{\Delta y_f} (u_P^{i-1} - u_{ws}^i)\right) > \frac{k_{H2}\mu(\dot{\gamma})}{\Delta y_f} (u_P^{i-1} - u_{ws}^i), \text{ then,}$$

$$u_{ws}^i > \frac{k_{H1}k_{H2}\mu(\dot{\gamma})}{k_{H1}k_{H2}\mu(\dot{\gamma}) + \Delta y_f} u_P^{i-1} \quad (5.57)$$

and the initial range for the bisection method is given by,

$$\left[ \frac{k_{H1}k_{H2}\mu(\dot{\gamma})}{k_{H1}k_{H2}\mu(\dot{\gamma}) + \Delta y_f} u_P^{i-1}; u_P^{i-1} \right] \quad (5.58)$$

*Asymptotic slip law:*

As for the Hatzikiriakos slip model, first the intermediate value theorem will be used to prove the existence of the solution, and then, with the Rolle theorem we will prove its uniqueness.

Consider the function  $f(u_{ws}^i)$  given by,

$$f(u_{ws}^i) = u_{ws}^i - k_{A1} \ln\left(1 + \frac{k_{A2}\mu(\dot{\gamma})}{\Delta y_f} (u_P^{i-1} - u_{ws}^i)\right) \quad (5.59)$$

Since  $f(u_P^{i-1})f(0) < 0$  and  $f(\cdot)$  is a real-valued continuous function on the interval  $[0; u_P^{i-1}]$ , the intermediate value theorem implies that  $\exists u_{ws}^i : f(u_{ws}^i) = 0$ .

Because  $f'(u_{ws}^i) > 0$  for  $u_{ws}^i \in [0; u_P^{i-1}]$ , by Rolle theorem the solution is unique.

Using the identity  $\ln(x) < x \forall x \in \mathbb{R}$ , it can be seen that,

$$u_{ws}^i < \frac{k_{A1}k_{A2}\mu(\dot{\gamma}) + k_{A1}\Delta y_f}{k_{A1}k_{A2}\mu(\dot{\gamma}) + \Delta y_f} u_P^{i-1} \quad (5.60)$$

The initial range for the bisection method is then given by,

$$\left\{ \begin{array}{l} [0; u_P^{i-1}] \text{ if } k_{A1} > 1 \\ [0; \frac{k_{A1}k_{A2}\mu(\dot{\gamma}) + k_{A1}\Delta y_f}{k_{A1}k_{A2}\mu(\dot{\gamma}) + \Delta y_f} u_P^{i-1}] \text{ if } k_{A1} < 1 \end{array} \right. \quad (5.61)$$

APPENDIX D: IMPLEMENTATION OF THE NONLINEAR NAVIER SLIP LAW

The discretized form of the nonlinear Navier slip law (Eq. 5.18(a)) can be linearized assuming that only the slip velocity of the linear part comes from the actual iteration as,

$$u_{ws}^i = k_{nl} \left( \frac{\mu(\dot{\gamma})^{i-1}}{\Delta y_f} \right)^m \left( u_P^{i-1} - u_{ws}^i \right) \left( u_P^{i-1} - u_{ws}^{i-1} \right)^{m-1}$$

This way we can solve for the slip velocity variable  $u_{ws}^i$ , and obtain,

$$u_{ws}^i = \frac{l}{1+l} u_P^{i-1} \text{ with } l = k_{nl} \left( \frac{\mu(\dot{\gamma})^{i-1}}{\Delta y_f} \right)^m \left( u_P^{i-1} - u_{ws}^{i-1} \right)^{m-1}.$$





## A NUMERICAL AND THEORETICAL STUDY ON VISCOELASTIC FLUID SLIP-FLOWS

---

### Abstract<sup>1</sup>

*This work describes a theoretical and numerical study on viscoelastic fluid slip-flows. The viscoelastic fluid is described by the simplified Phan-Thien—Tanner (sPTT) model, and the governing equations with slip boundary conditions are solved by a finite volume method using a new method to control the growth of the slip velocity along the iterative process, named the SIMPLE-slip method. The numerical results were compared with the analytical solution for a fully-developed slip-flow in planar channel for two nonlinear slip models. Simulations were carried out in a classical benchmark problem employed in computational rheology, the viscoelastic fluid flow in a slip-stick geometry, in order to identify the wall slip influence on the bulk velocity and stress developments at the discontinuity region. Tests were made to investigate the effect of slip on convergence rates and accuracy.*

### 6.1 INTRODUCTION

Wall slip is a relevant phenomenon in many engineering processes, especially those involving long molecular chains, as happens, for example, in polymer processing as demonstrated by a variety of experiments reported in the literature (Potente et al., 2006; Mitsoulis et al., 2005). Among others, fluids that exhibit this type of behavior are the Polyvinyl chloride (PVC), high-density polyethylene, elastomers, suspensions and food products (Denn, 2001).

Given the hyperbolic nature of the constitutive equations used to represent the rheological behavior of viscoelastic fluids, and also the effects of the wall slip, computational simulations of this type of fluids and flows require the use of robust numerical methods. To handle these problems, a new method to solve the pressure equation and to control the growth of the slip velocity along the iterative process, named the SIMPLE-slip method (Ferrás et al., 2012d), was implemented in a well validated computational rheology code (Oliveira et al., 1998), and was subsequently used to predict numerically the slip-stick flow of an sPTT fluid (Phan-Thien and Tanner, 1977; Phan-Thien, 1978) together with the linear and nonlinear Navier slip boundary conditions (?). The SIMPLE-slip method was used with nonlinear slip boundary conditions such as the nonlinear Navier (Schowalter, 1988),

---

<sup>1</sup> L.L. Ferrás, A.M. Afonso, J.M. Nóbrega, M.A. Alves, F.T. Pinho (2012), A numerical and theoretical study on viscoelastic fluid slip-flows, to be submitted to *Theoretical and Computational Fluid Dynamics*;

the (Hatzikiriakos, 1993) and asymptotic slip models, and presented numerical convergence for higher values of the Weissenberg number and the slip coefficient, when compared to the classic explicit implementation of slip (Ferrás et al., 2012d).

In this work, we further extend the use of the SIMPLE-slip method by implementing the slip models given by (Thompson and Troian, 1997) (TT) and by (Lau and Schowalter, 1986) (LS), we also present a detailed study of the slip-stick flow under slip. The slip model derived by (Thompson and Troian, 1997) is controlled by the extent to which the liquid feels corrugations and allows to relate the degree of slip to the underlying static properties and dynamic interactions of the walls and the fluid. The slip model by (Lau and Schowalter, 1986) was derived by applying the concept of junctions at the wall/polymer interface and depends on the shear stress and the temperature. The temperature dependence was assessed with experimental results and a good agreement was obtained, showing the robustness of this model (Lau and Schowalter, 1986).

Additionally, in the analytical study we present closed form solutions for the (Lau and Schowalter, 1986) model (under some simplifications). For the case where an analytical solution was not possible (for both (Thompson and Troian, 1997) and (Lau and Schowalter, 1986) models) we prove the existence of a unique solution and provide the range where the solution lies, thus facilitating the task of finding semi-analytical solutions.

This introduction is preceded by subsection 2, where the relevant governing equations are presented. In subsection 3 we explain the numerical method used to solve and couple the Navier-Stokes equations together with the nonlinear Navier slip boundary condition and present a possible linearization for the TT and Ls slip velocity models. In subsection 4 the results obtained from the simulations of an sPTT fluid on a slip-stick geometry are studied and finally the paper ends with the Conclusions in subsection 5. As a secondary result of this investigation, in Appendix A we derive the full analytical solution for fully developed slip-flow of polymer solutions described by the sPTT or FENE-P (Bird et al., 1987) models in planar channel for the TT and LS non-linear slip models, which is used for validation purposes.

## 6.2 GOVERNING EQUATIONS

The governing equations for incompressible fluids are the mass conservation equation,

$$\nabla \cdot \mathbf{u} = 0 \tag{6.1}$$

and linear momentum equation

$$\rho \frac{\partial \mathbf{u}}{\partial t} + \rho \nabla \cdot \mathbf{u}\mathbf{u} = -\nabla p + \nabla \cdot \boldsymbol{\tau} \quad (6.2)$$

where  $\mathbf{u}$  is the velocity vector,  $p$  is the pressure and  $\boldsymbol{\tau} = \boldsymbol{\tau}_s + \boldsymbol{\tau}_p$  is the extra stress tensor. The extra stress tensor is divided into solvent  $\boldsymbol{\tau}_s = \eta_s (\nabla \mathbf{u} + (\nabla \mathbf{u})^T)$  and polymer,  $\boldsymbol{\tau}_p$ , contributions (elastic part of the stress tensor), the latter given by the following differential constitutive equation, called the simplified Phan-Thien—Tanner model (sPTT) (Phan-Thien and Tanner, 1977; Phan-Thien, 1978):

$$\begin{aligned} f(\text{tr} \boldsymbol{\tau}_p) \boldsymbol{\tau}_p + \lambda \left( \frac{\partial \boldsymbol{\tau}_p}{\partial t} + \mathbf{u} \cdot \nabla \boldsymbol{\tau}_p - [(\nabla \mathbf{u})^T \cdot \boldsymbol{\tau}_p + \boldsymbol{\tau}_p \cdot \nabla \mathbf{u}] \right) = \\ = \eta_p (\nabla \mathbf{u} + (\nabla \mathbf{u})^T) \end{aligned} \quad (6.3)$$

where  $f(\text{tr} \boldsymbol{\tau}_p)$  is a function of the trace of the stress tensor,  $\lambda$  is the relaxation time and  $\eta_p$  is the zero-shear polymer viscosity. In the literature, there are two possible functions for  $f(\text{tr} \boldsymbol{\tau}_p)$ , but only the original linear function (Phan-Thien and Tanner, 1977) is considered here,

$$f(\text{tr} \boldsymbol{\tau}) = 1 + \frac{\varepsilon \lambda}{\eta_p} \text{tr}(\boldsymbol{\tau}_p) \quad (6.4)$$

with  $\varepsilon$  the parameter related to the elongational behavior of the fluid.

When considering slip boundary conditions at the wall, the usual Dirichlet velocity boundary condition  $\mathbf{u} = 0$  is substituted by the nonlinear Navier slip model (Schowalter, 1988)(NNS),

$$\|\mathbf{u}_{ws}\| = k_{nl} \|\boldsymbol{\tau}_w\|^m \quad m > 0 \quad (6.5)$$

where  $\mathbf{u}_{ws}$  is the slip velocity vector ( $ws$  stands for wall slip),  $\boldsymbol{\tau}_w$  is the tangent stress vector,  $k_{nl}$  is the slip coefficient that allows controlling the desired amount of slip for the simulation and  $m$  is the slip exponent that gives the model its nonlinearity ( $k_{nl}$  and  $m$  are both model parameters).

The (Thompson and Troian, 1997) model is given by,

$$\|\mathbf{u}_{ws}\| = \alpha \left( 1 - \frac{\|\boldsymbol{\tau}_w\|}{\|\boldsymbol{\tau}_w\|_c} \right)^{-1/2} \|\boldsymbol{\tau}_w\| \quad (6.6)$$

where  $\|\boldsymbol{\tau}_w\|_c$  is some critical (maximum) tangent stress (its value is such that  $1 - \|\boldsymbol{\tau}_w\| / \|\boldsymbol{\tau}_w\|_c \geq 0$  is always verified) and  $\alpha$  is a model parameter. Following the notation of (Matthews and Hill, 2007) Eq. (6.6) can be rewritten as

$$\|\mathbf{u}_{ws}\| = \alpha (1 - \beta \|\boldsymbol{\tau}_w\|)^{-1/2} \|\boldsymbol{\tau}_w\| \quad (6.7)$$

with  $\beta = \|\boldsymbol{\tau}_w\|_c^{-1}$  and  $\alpha, \beta > 0$ .

The (Lau and Schowalter, 1986) slip velocity model is given by

$$\|\mathbf{u}_{ws}\| = c_1 \|\boldsymbol{\tau}_w\|^m \left[ 1 - c_2 \tanh \left( \frac{E - c_3 \|\boldsymbol{\tau}_w\|}{RT} \right) \right] \quad (6.8)$$

where  $c_1$ ,  $c_2$  and  $c_3$  are empirical constants,  $E$  is the activation energy and  $T$  is the temperature.

### 6.3 ANALYTICAL SOLUTIONS

Assuming a fully developed flow and some simplifications in the slip models, it is possible to present a closed form analytical solution for the LS slip model.

If  $m = 1$  and  $\frac{E+c'_3(p'_x)}{RT} \ll 1$  than,  $\tanh \left( \frac{E+c'_3(p'_x)}{RT} \right) \approx \frac{E+c'_3(p'_x)}{RT}$ . Under this assumptions, and imposing a flow rate,  $Q$ , the solution is given by (as shown in Appendix A),

$$u'(y') = 0.5p'_x(y'^2 - 1) + 0.5\varepsilon Wi^2 p_x'^3 (y'^4 - 1) + c'_1 (-p'_x)^m \left[ 1 - c_2 \tanh \left( \frac{E+c'_3(p'_x)}{RT} \right) \right] \quad (6.9)$$

with

$$p'_x = \sqrt[3]{-\frac{P}{2} + \sqrt{\frac{P^2}{4} + \frac{Q^3}{27}}} + \sqrt[3]{-\frac{P}{2} - \sqrt{\frac{P^2}{4} + \frac{Q^3}{27}}} - \frac{a_1}{3} = 0 \quad (6.10)$$

and

$$\begin{aligned} a_1 &= -\frac{5c'_1 c'_2 c'_3 (-p'_x)^2}{2RT} \\ a_2 &= \frac{-\frac{1}{3}c'_1 + \frac{c'_1 c'_2 E}{RT}}{-\frac{2}{5}\varepsilon Wi^2} \\ a_3 &= \left( \frac{2}{5}\varepsilon Wi^2 p_x'^3 \right)^{-1} \\ P &= a_3 - \frac{a_1 a_2}{3} + \frac{2a_1^3}{27} \\ Q &= a_2 - \frac{a_1^2}{3} \end{aligned} \quad (6.11)$$

where length, velocity and stresses were scaled with  $H$ ,  $\bar{U}$  and  $\eta\bar{U}/H$ , respectively,  $\bar{U}$  is the mean streamwise velocity,  $H$  is the half channel width and  $Wi = \lambda\bar{U}/H$  is the Weissenberg number.

For an higher order truncated series expansion:

$$\frac{E+c'_3(p'_x)}{RT} - \frac{1}{3} \left( \frac{E+c'_3(p'_x)}{RT} \right)^3$$

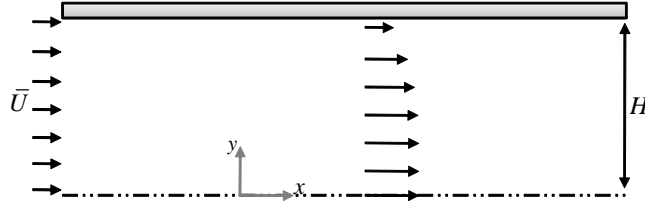


Figure 6.1: Schematic representation of the channel flow geometry.

a closed form solution is still possible because the equation to solve for  $p'_x$  is quartic,

$$\begin{aligned} & \left( -\frac{c'_1 c_2 c_3'^3}{3(RT)^3} \right) p_x'^4 + \left( \frac{c'_1 c_2 c_3'^2 E}{3(RT)^3} - \frac{2}{5} \epsilon Wi^2 \right) p_x'^3 + \left( \frac{c'_1 c_2 c_3'}{RT} + \frac{c'_1 c_2 c_3' E^2}{3(RT)^3} \right) p_x'^2 \\ & + \left( -\frac{1}{3} - c'_1 + \frac{c'_1 c_2 E}{RT} - \frac{c'_1 c_2 E^3}{3(RT)^3} \right) p_x' - 1 = 0 \end{aligned} \quad (6.12)$$

and the procedure to solve this type of equations can be found in any elementary algebra book.

As shown in Appendix A, for the other slip models is still possible to find semi-analytic solutions.

#### 6.4 NUMERICAL METHOD

The in-house code used is a three-dimensional time dependent finite-volume method (FVM) code developed by (Oliveira et al., 1998), with improvements described later in (Oliveira and Pinho, 1999c,b) and (Alves et al., 2001b, 2003a). The FVM code uses collocated non-orthogonal meshes, central differences for discretization of diffusive terms, a second order backward implicit time discretization through the SIMPLEC algorithm (Patankar, 1980) to ensure simultaneously the momentum balance and mass conservation and the Rhie and Chow interpolation method (Rhie and Chow, 1983) to couple the pressure and velocity fields.

The main modifications required to implement the slip boundary condition coupled with the pressure equation correction (the so-called SIMPLE-slip method (Ferrás et al., 2012d)) are briefly explained in the next lines. To illustrate the SIMPLE-slip method implementation, we assume that the equations are solved in a simple 2D flow between parallel plates with Cartesian coordinates and orthogonal meshes, with equal slip at both walls so that symmetry at the channel center plane can be invoked (cf. Fig 6.1). The slip velocity vector is tangent to the wall ( $x$ -direction) and the tangent stress vector is determined as  $\boldsymbol{\tau}_t = (\mathbf{I} - \mathbf{n} \otimes \mathbf{n}^T) (\boldsymbol{\tau} \mathbf{n}^T)$ , where  $\mathbf{n} = (n_1, n_2)$  is the normal vector to the wall and  $\mathbf{I}$  is the identity matrix. Assuming a Couette flow in the vicinity of the wall, the tangent stress vector at the upper wall is given by,

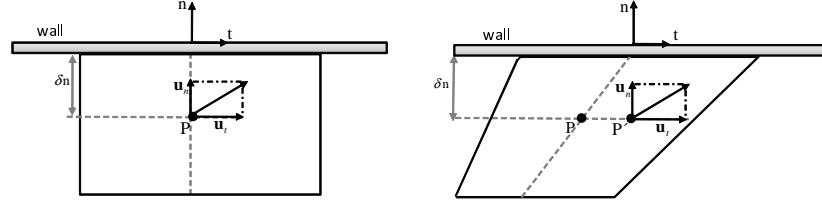


Figure 6.2: Projection of the velocity vector in the center of the computational cell into the tangent and normal part (left- Cartesian mesh; right- non Cartesian mesh).

$$\tau_t = \mu(\dot{\gamma}) \left. \frac{du}{dy} \right|_{wall} \quad (6.13)$$

for any constitutive equation. At the boundary, what will distinguish one constitutive model from the other is only the viscosity function  $\mu(\dot{\gamma})_{wall}$  which is given by  $\mu(\dot{\gamma})_{wall} \equiv \eta_s + \frac{\eta_p}{1 + (\alpha - 1)^{2/3\alpha}}$  (with  $\alpha \equiv (\theta + \sqrt{\theta^2 - 1})^{1/3}$  and  $\theta \equiv 1 + 27\varepsilon(\lambda\dot{\gamma}_{wall}^2)$ ) (Azaiez et al., 1996) for the PTT model. Under these flow conditions the nonlinear Navier slip model takes the form,

$$u_{ws} = k_{nl} \left( -\mu(\dot{\gamma}) \left. \frac{du}{dy} \right|_{wall} \right)^m. \quad (6.14)$$

The linear model is recovered for  $m = 1$  in which case  $k_{nl} \equiv k_l$ .

The continuity and momentum equations can be written in Cartesian coordinates as Eqs. (6.15) and (6.16), respectively,

$$\frac{\partial u}{\partial x} + \frac{\partial v}{\partial y} = 0 \quad (6.15)$$

$$\frac{\partial(\rho\phi)}{\partial t} + \frac{\partial(u\phi)}{\partial x} + \frac{\partial(v\phi)}{\partial y} = -\frac{\partial p}{\partial \Psi} + \frac{\partial}{\partial x} \left( \eta_s \frac{\partial \phi}{\partial x} + \tau_{\Psi x} \right) + \frac{\partial}{\partial y} \left( \eta_s \frac{\partial \phi}{\partial y} + \tau_{\Psi y} \right) \quad (6.16)$$

where  $\phi = u$ ,  $\Psi = x$  in the  $x$ -momentum equation, and  $\phi = v$ ,  $\Psi = y$  in the  $y$ -momentum equation. The discretization of the continuity equation in a computational cell P (Fig. 6.2) results in the balance of mass fluxes for this cell. These fluxes are normal to the cell faces, therefore, the slip boundary condition has no direct influence on this equation (since the walls are impermeable). On the other hand, the momentum equation is directly affected by the slip boundary condition, for that reason its discretization is briefly explained below. The interested reader should consult (Oliveira and Pinho, 1999c,b) for further details.

The discretization of the transient, convective and pressure gradient terms is not directly affected by the implementation of slip velocity, but the diffusive term is, as explained next. The discretization of the

diffusive term for the PTT fluid together with the assumption of Eq. (6.13) leads to the following expression,

$$\left[ \left( \mu(\dot{\gamma}) \frac{\partial \phi}{\partial y} \right)_{n \equiv wall} - \left( \eta_s \frac{\partial \phi}{\partial y} + \tau_{\Psi y} \right)_s \right] \Delta x \Delta t + \left[ \left( \eta_s \frac{\partial \phi}{\partial x} + \tau_{\Psi x} \right)_e - \left( \eta_s \frac{\partial \phi}{\partial y} + \tau_{\Psi x} \right)_w \right] \Delta x \Delta t \quad (6.17)$$

where the subscripts  $n$ ,  $s$ ,  $e$  and  $w$  stand for north, south, east and west faces, respectively.

Notice that the terms for the north cell face  $(\dots)_n$  at Eq. (6.17) came from Eq. (6.13) (the north cell face is a boundary face). The slip velocity is then carried via the term  $\left( \frac{\partial \phi}{\partial y} \right)_{n \equiv wall}$ . Assuming the one-sided approximation to the derivatives, such as the first order scheme of Eq. (6.18),

$$\left( \frac{\partial \phi}{\partial y} \right)_{wall} = \frac{\phi_{wall} - \phi_P}{\Delta y_f} + O(\Delta y) \quad (6.18)$$

together with uniform meshes (square computational cells) and central differences to discretize all diffusion-related derivatives (except at the boundaries), Eq. (6.17) becomes,

$$\left[ \frac{\mu(\dot{\gamma})_{wall}}{\Delta y_f} \phi_n + \frac{(\eta_s)_s}{\Delta y} \phi_s - \left( \frac{\mu(\dot{\gamma})_{wall}}{\Delta y_f} + \frac{(\eta_s)_s}{\Delta y} \right) \phi_P + (\tau_{\Psi y})_s \right] \Delta x \Delta t \quad (6.19)$$

After grouping all the terms, the discretized momentum equation is rewritten in the standard compact form, (where we have now substituted the general variable  $\phi$  by the specific variable  $u$ , since we are analyzing the  $x$  - momentum equation),

$$a_P u_P = a_E u_E + a_W u_W + a_S u_S + a_N u_N + \underbrace{\frac{\Delta V_P (\rho \phi)_P^0}{\Delta t} + \frac{\delta p}{\delta \Psi} + S_{stress}}_{source\ terms} \quad (6.20)$$

where  $\frac{\delta p}{\delta \Psi}$  represents a general discretization of the pressure gradient and  $a_E$ ,  $a_S$ ,  $a_W$  are given by Eqs. (6.21), (6.22) and (6.23) respectively,

$$a_E = a_E^c + a_E^d = a_E^c + \frac{(\eta_s)_e \Delta y}{\Delta x} \quad (6.21)$$

$$a_S = a_S^c + a_S^d = a_S^c + \frac{(\eta_s)_s \Delta x}{\Delta y} \quad (6.22)$$

$$a_W = a_W^c + a_W^d = a_W^c + \frac{(\eta_s)_w \Delta y}{\Delta x} \quad (6.23)$$

with the superscripts  $c$  and  $d$  referring to the convective and diffusive contributions, respectively. To account for the slip boundary condition, which affects  $a_N u_{wall}$ , the coefficient  $a_N$  is given by Eq. (6.24)

$$a_N = \frac{\mu(\dot{\gamma})_{wall} \Delta x}{\Delta y_f} \quad (6.24)$$

Regarding the convective terms, since they are not affected by the slip velocity, they are handled as in (Oliveira et al., 1998). Finally the central coefficient  $a_P$  is given as in the standard procedure (Oliveira and Pinho, 1999b) by,

$$a_P = a_E + a_W + a_S + a_N + \frac{\Delta V_P \rho_P^0}{\Delta t} \quad (6.25)$$

Assuming the approximation of Eq. (6.18), let  $i$  represent the number of the outer iteration (iteration between the linearized momentum equation and the pressure correction equation), then, the discretized slip boundary condition at iteration  $i$  is usually given by,

$$u_{ws}^i = k_{nl} \left( -\mu(\dot{\gamma})_{w}^{i-1} \frac{(u_{ws}^{i-1} - u_P^{i-1})}{\delta n} \right)^m \quad (6.26)$$

At each iteration  $i$  the boundary condition is updated with the velocity from the previous iteration  $i - 1$ . In order to achieve convergence the variation of this boundary condition along the iterative process must be stable in some sense. Sudden changes in the boundary condition along the iterative process will not allow the overall convergence. Due to this inconsistency, non-physical characteristics may appear, and the process either diverges or converges to an unacceptable solution. The relationship  $u_{ws} < u_P$  seems to be the key to the convergence of the process. For the linear Navier slip model, Eq. (6.14) with  $m = 1$ , it was found that if  $k_l \mu(\dot{\gamma})_{wall} / \delta n \leq 1$  the growth of the slip velocity relative to the adjacent cell velocity can be controlled and convergence is achieved, whereas for  $k_l \mu(\dot{\gamma})_{wall} / \delta n > 1$  divergence occurs. Therefore, this provides the restrictions to the converged solution. Near the boundaries the mesh is usually more refined giving a smaller  $\delta n$ , and leading to a larger value of  $k_l \mu(\dot{\gamma})_{wall} / \delta n$ , thus facilitating divergence of the computation. A possible remedy is the classical use of underrelaxation  $u_{ws}^i = R u_{ws}^{i-1} + (1 - R) u_{ws}^i$  with  $R < 1$  when updating the slip velocity in the iterative procedure, but even with this relaxation the computations are not possible for large values of the friction coefficient and a better method proposed below is used.

The nonlinear Navier slip model of Eq. (6.14) can be written as in Eq. (6.27) if the first order approximation to the derivative is used,

$$u_{ws} = k_{nl} \left( \frac{\mu(\dot{\gamma})_w}{\delta n} \right)^m (u_P - u_{ws}) (u_P - u_{ws})^{m-1} \quad (6.27)$$

It is assumed that  $(u_P - u_{ws}) > 0$  which can be guaranteed if in the first iteration the given slip velocity is smaller than the given velocity for the control volume P, and all the coefficients (central and neighbor coefficients) are positive. To obtain a linear numerical equation the term  $(u_P - u_{ws})^{m-1}$  is evaluated explicitly with the values



from the previous iteration  $(u_P^{i-1} - u_{ws}^{i-1})^{m-1}$ , and only in the term  $(u_P^{i-1} - u_{ws}^i)$ ,  $u_{ws}^i$  is evaluated in the present iteration together with the left-hand-side, i.e.,

$$u_{ws}^i = k_{nl} \left( \frac{\mu(\dot{\gamma})_{wall}^{i-1}}{\delta n} \right)^m (u_P^{i-1} - u_{ws}^i) (u_P^{i-1} - u_{ws}^{i-1})^{m-1} \quad (6.28)$$

The method is known semi-implicit in the linearized velocity difference and Eq. (6.28) can be rewritten as,

$$u_{ws}^i = \frac{a}{a+1} u_P^{i-1} \quad (6.29)$$

with  $a = (k_{nl}\mu(\dot{\gamma})_{wall}/\delta n)^m (u_P^{i-1} - u_{ws}^{i-1})^{m-1}$ . In this way, the slip velocity is always bounded by  $u_P$  because  $0 \leq a/(a+1) < 1$ .

The other two slip models can also be linearized in a similar way. For the TT slip model this would be,

$$u_{ws}^i = \alpha \mu \left( \delta n^2 - \delta n \beta \mu (u_P^{i-1} - u_{ws}^{i-1}) \right)^{-1/2} (u_P^{i-1} - u_{ws}^i) \quad (6.30)$$

This equation can be rewritten as,

$$u_{ws}^i = \frac{b}{b+1} u_P^{i-1} \quad (6.31)$$

with  $\beta \mu (u_P^{i-1} - u_{ws}^{i-1}) < \delta n$  and  $b = \alpha \left( \delta n^2 - \delta n \beta \mu (u_P^{i-1} - u_{ws}^{i-1}) \right)^{-1/2}$ .

During the iterative procedure, specially in the beginning of the iterations, the difference  $(u_P^{i-1} - u_{ws}^{i-1})$  can be substantial and eventually lead to  $\beta \mu (u_P^{i-1} - u_{ws}^{i-1}) \geq \delta n$ , resulting in the divergence of the computation or in float errors. To avoid this potential problem, the friction coefficient  $\beta$  at Eq. (6.31) should be replaced by  $(1 - \zeta) \beta$ , with  $\lim_{i \rightarrow +\infty} \zeta = 0$  ( $i$  represents the iteration number).

For the LS slip model, the linearization is given by,

$$u_{ws}^i = \frac{c_1 \mu^m}{\delta n^m} (u_P^{i-1} - u_{ws}^i) (u_P^{i-1} - u_{ws}^{i-1})^{m-1} \left[ 1 - c_2 \tanh \left( \frac{E - \frac{c_3 \mu}{\delta n} (u_P^{i-1} - u_{ws}^{i-1})}{RT} \right) \right] \quad (6.32)$$

which is equivalent to,

$$u_{ws}^i = \frac{c}{c+1} u_P^{i-1} \quad (6.33)$$

with  $c = \frac{c_1 \mu^m}{\delta n^m} (u_P^{i-1} - u_{ws}^{i-1})^{m-1} \left[ 1 - c_2 \tanh \left( \frac{E - \frac{c_3 \mu}{\delta n} (u_P^{i-1} - u_{ws}^{i-1})}{RT} \right) \right]$ .

The main feature of this method is that the slip velocity is always smaller than the velocity in the center of the adjacent computational cell, an indispensable property for convergence. To solve the system of equations we use the following iterative procedure:

1. Set the boundary conditions, the initial velocity and pressure fields;
2. Solve the stress equations for the non-Newtonian model;
3. Compute the slip velocity with the discretized slip model, Eqs. 6.29, 6.31 or 6.33;
4. Solve the linearized momentum equation;
5. Solve the pressure correction equation;
6. Correct velocity and pressure;
7. Check for convergence in the residuals of the system of equations;
8. If convergence is not achieved proceed to step 2.

This method of implementing slip boundary conditions can be generalized for any slip velocity function, provided we can express the slip velocity as a function of the wall tangent stress. Assuming a one-dimensional flow, the slip velocity  $u_{ws}$  can be written as a function of the difference  $u_p - u_{ws}$ , i.e.  $u_{ws} = \pm f(u_p - u_{ws})$ , where the  $\pm$  depends on the direction of the slip velocity and  $u_p$  is the velocity at the computational cell adjacent to the wall. This function can be multiplied by  $(u_p^{i-1} - u_{ws}^i) / |u_p^{i-1} - u_{ws}^{i-1}|$  and solved in a semi-implicit manner. In the iterative procedure only the slip velocity in the numerator comes from the actual iteration, so the general slip boundary condition is given by,

$$u_{ws}^i = \left[ \frac{f(u_p^{i-1} - u_{ws}^{i-1})}{|u_p^{i-1} - u_{ws}^{i-1}| + f(u_p^{i-1} - u_{ws}^{i-1})} \right] u_p^{i-1} \quad (6.34)$$

For the three slip boundary conditions studied here, the function  $f(u_p^{i-1} - u_{ws}^{i-1})$  is given by,

$$f(u_p^{i-1} - u_{ws}^{i-1}) = u_{ws} = k \left( \frac{\mu(\dot{\gamma})_w}{\delta n} \right)^m (u_p^{i-1} - u_{ws}^{i-1}) \quad (6.35)$$

for the NNS model,

$$f(u_p^{i-1} - u_{ws}^{i-1}) = \alpha \left( 1 - \frac{\beta \mu}{\delta n} (u_p^{i-1} - u_{ws}^{i-1}) \right)^{-1/2} \frac{\mu}{\delta n} (u_p^{i-1} - u_{ws}^{i-1}) \quad (6.36)$$

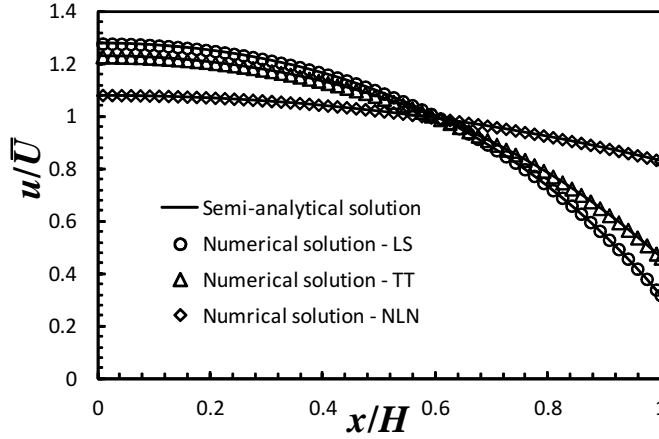


Figure 6.3: Comparison between semi-analytical solutions and the simulated results obtained for a Poiseuille flow, under the influence of three different slip boundary conditions, LS, TT, NLN.

for the TT slip model, and

$$f \left( u_p^{i-1} - u_{ws}^{i-1} \right) = \frac{c_1 \mu^m}{\delta n^m} \left( u_p^{i-1} - u_{ws}^{i-1} \right)^m \cdot \left[ 1 - c_2 \tanh \left( \frac{E}{KT} - \frac{c_3 \mu}{\delta n RT} \left( u_p^{i-1} - u_{ws}^{i-1} \right) \right) \right] \quad (6.37)$$

for the LS slip velocity model.

Providing that the mesh is orthogonal, a semi-implicit method to calculate the slip boundary condition could also be used, as described in Appendix B.

## 6.5 RESULTS AND DISCUSSION

### 6.5.1 Code Verification

To validate the implementation of the non-linear slip models, we compared the analytical and semi-analytical solutions for a fully developed flow (see Appendix A), with the simulation results obtained for the Poiseuille flow between parallel plates (cf. Fig. 6.1). We expect the flow to be fully developed in the center region of the channel where the influence of the inlet and outlet boundary conditions is weaker.

The simulations were performed for the sPTT model with  $Wi = 1$  and  $\varepsilon = 0.25$ , and the slip coefficients used were  $k'_{nl} = 2.53$  and  $m = 1.5$  for the non-linear Navier slip model,  $\alpha' = 0.4$  and  $\beta' = 4.0 \times 10^{-4}$  for the LS slip model, and,  $c'_1 = 0.24$ ,  $c_2 = 0.59 \times 10^{-6}$ ,  $c'_3 = 0.024$ ,  $RT = 3.43 \times 10^3$  J and  $E = 5.0 \times 10^3$  J for the TT slip model. In Fig. 6.3 we show a good agreement between the analytical and numerical results for the three non-linear slip models, showing that the implementation of this models is in agreement with the theoretical results.

To evaluate the influence of the slip velocity in the flow dynamics of viscoelastic fluids flowing in a geometry that possesses a singularity

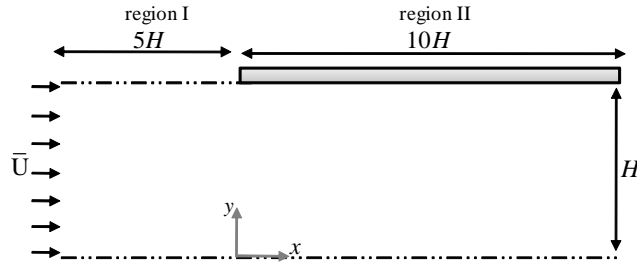


Figure 6.4: Schematic representation of the slip-stick geometry.

Region	M1				M2				M3			
	$f_x$	$f_y$	$n_x$	$n_y$	$f_x$	$f_y$	$n_x$	$n_y$	$f_x$	$f_y$	$n_x$	$n_y$
I	0.79009	0.869698	18	15	0.88887	0.932576	36	30	0.9428	0.9657	72	60
II	1.19938	0.869698	25	15	1.09516	0.932576	50	30	1.0465	0.9657	100	60
	n° cells=			645	n° cells=			2580	n° cells=			10320
	$\Delta_{min}/H=$			0.02	$\Delta_{min}/H=$			0.01	$\Delta_{min}/H=$			0.004

Table 6.1: Mesh characteristics for the slip-stick geometry.

point, we performed additional simulation carried out in a classical benchmark problem in computational rheology, the viscoelastic fluid flow in a slip-stick geometry. In the sake of compactness, only the nonlinear Navier slip boundary condition was used as shown in the next section.

### 6.5.2 Elasticity Effects

Simulations were carried out (for the nonlinear Navier slip model) in a classical benchmark problem in computational rheology, the viscoelastic fluid flow in a slip-stick geometry, illustrated in Fig. 6.4. The computational domain has the following two regions: the inlet region I, bounded by two symmetry lines, and the downstream region II, bounded by a solid wall, the outlet and a symmetry line. The variable  $\bar{U}$  stands for the imposed mean velocity and three meshes were created with its properties described in Table 6.1.

The finer mesh (M<sub>3</sub>) employed is practically the same as the refined mesh used by Oliveira et al. (1998), for which the results were shown to be mesh independent. In Table 6.1  $f_x$  and  $f_y$  stand for the ratio of two consecutive cells while  $n_x$  and  $n_y$  stand for the number of cells in the  $x$  and  $y$  directions, respectively. A zoomed view of our finer mesh can be seen in Fig 6.5.

The simulations were performed for a constant Reynolds number  $Re = \rho \bar{U} H / \mu = 20$  and a varying Weissenberg number  $Wi = \lambda \bar{U} / H \in \{0.25, 0.5, 1.0, 2.0\}$ . For the linear slip model, implemented via Eq. (6.14), convergence could be achieved for all the established Weissenberg numbers. As expected an easier convergence was obtained for high slip velocities (high friction coefficients). This happens because the slip velocity numerically smooths the singularity. For the nonlinear

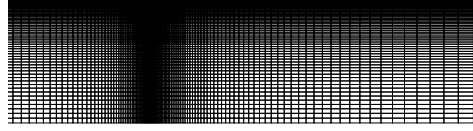


Figure 6.5: Detailed view of mesh  $M_3$  near the singularity point.

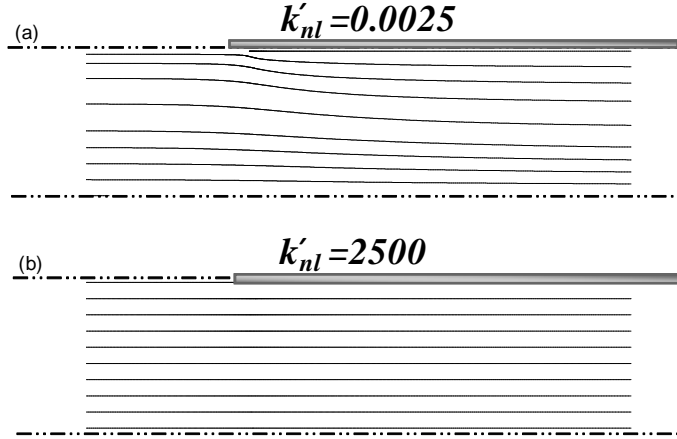


Figure 6.6: Representation of linear slip velocity streamlines for (a)  $k'_{nl} = 0.0025$ , (b)  $k'_{nl} = 2500$ , with  $Re = 20$ ,  $Wi = 2$  for the sPTT model.

model the results were qualitatively very similar to the ones obtained with the linear slip except that convergence was more difficult, not because of the singularity but due to the the method used..

In order to quantify the effect of slip velocity on the flow, the streamlines for two different values of the friction coefficient were plotted in Fig. 6.6. For the case  $k'_{nl} = k_{nl} (\eta_s + \eta_p) / H = 0.0025$  (almost no slip velocity) curved streamlines appear in the slip-friction passage because of the fluid viscosity and the restriction promoted by the wall (Fig. 6.6(a)). The streamlines for the slip coefficient  $k'_{nl} = 2500$  are almost horizontal because for this case a plug flow is obtained. The curved streamlines tend to disappear (Fig. 6.6(b)).

The stress distribution was also studied, together with the characterization of the flow type parameter,  $\zeta$ , defined as (Lee et al., 2007):

$$\zeta = \frac{|\mathbf{D}| - |\mathbf{\Omega}|}{|\mathbf{D}| + |\mathbf{\Omega}|} \quad (6.38)$$

where  $|\mathbf{D}|$  and  $|\mathbf{\Omega}|$  represent the magnitudes of the rate of deformation and vorticity tensors, respectively, given by,

$$\mathbf{D} = \frac{1}{2} [\nabla \mathbf{u} + (\nabla \mathbf{u})^T], \quad \mathbf{\Omega} = \frac{1}{2} [\nabla \mathbf{u} - (\nabla \mathbf{u})^T], \quad (6.39)$$

which can be calculated as

$$|\mathbf{D}| = \sqrt{\frac{1}{2} (\mathbf{D} : \mathbf{D}^T)} = \sqrt{\frac{1}{2} \sum_i \sum_j D_{ij}^2} \quad (6.40)$$

$$|\mathbf{\Omega}| = \sqrt{\frac{1}{2} (\mathbf{\Omega} : \mathbf{\Omega}^T)} = \sqrt{\frac{1}{2} \sum_i \sum_j \Omega_{ij}^2}.$$

The flow type parameter varies from  $-1$ , which corresponds to solid-like rotation, up to  $1$ , for pure extensional flow. Pure shear flow is characterized by  $\zeta = 0$ . In Fig. 6.7 are shown the contour plots

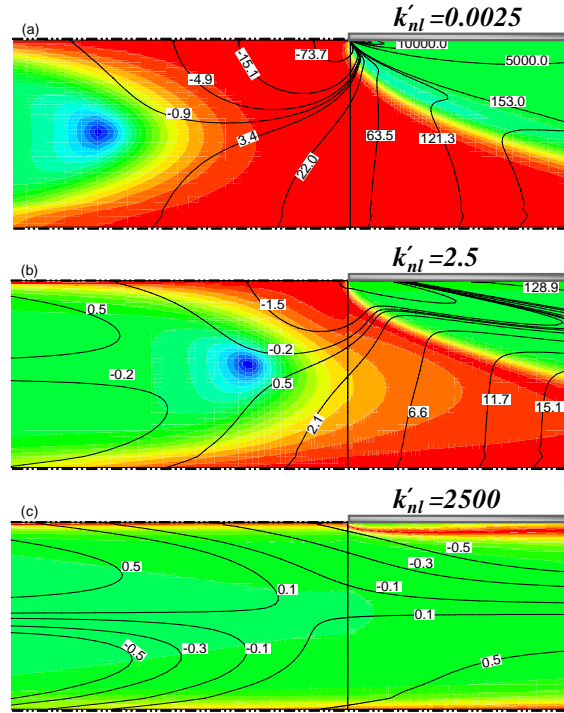


Figure 6.7: Representation of contour lines ( $\tau_{xx}$ ) superimposed with the flow type  $\zeta$  contours for the linear slip model: (a)  $k'_{nl} = 0.0025$ , (b)  $k'_{nl} = 2.5$ , (c)  $k'_{nl} = 2500$ .  $Re = 20$  and  $Wi = 2$ .

for the  $\tau_{xx}$  component and flow type parameter,  $\zeta$ , for three different slip coefficients, whereas Figs. 6.8 and 6.9 show the corresponding contour plots for  $\tau_{xy}$  and  $\tau_{yy}$ . For lower slip coefficients, the region of shear-dominant flow is concentrated near the channel wall, while the extension-dominant flow appears near the stagnation point. Increasing the slip coefficients, the shear-dominated flow increases also in the vicinity of the stagnation point, and eventually, for higher slip coefficients, the extension-dominant flow appears is limited to the thinner region near the walls. The  $\tau_{xx}$  component changes drastically with the increase of slip. Notice that for the Newtonian case this stress component is compressive (negative) in the region of fluid near the

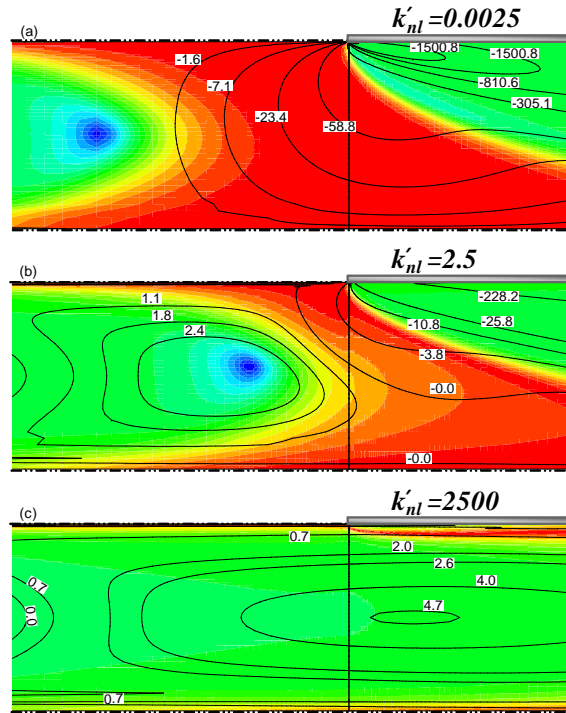


Figure 6.8: Representation of contour lines ( $\tau_{xy}$ ) superimposed with the flow type  $\zeta$  contours for the linear slip model: (a)  $k'_{nl} = 0.0025$ , (b)  $k'_{nl} = 2.5$ , (c)  $k'_{nl} = 2500$ .  $Re = 20$  and  $Wi = 2$ .

wall, as explained by (Oliveira et al., 1998). For this non-Newtonian fluid, in the presence of low slip velocity (Fig. 6.7(a)), this stress component becomes positive (traction), but on increasing the slip velocity it becomes negative as happens for Newtonian fluids (Figure 6.7 (c)). For the  $\tau_{xy}$  component on increasing the slip coefficient the negative stress values decrease in magnitude in the wall region, as shown in Fig. 6.8 (c). This happens because the flow tends to a plug, which corresponds to a null tangent stress as the slip velocity increases (cf. Figs. 6.8(b) and 6.8(c)).

For the contour plots of  $\tau_{yy}$ , plotted in Fig.6.9, the qualitative behavior is essentially the same on increasing the slip velocity but a reduction in magnitude is visible again associated to the progression towards a plug velocity profile, for which there is no shear.

## 6.6 CONCLUSIONS

In this work the numerical implementation of the slip boundary condition in a flow modeling code, based on the Finite Volume Method, was described. The code was then employed to study the effect of the nonlinear Navier, the (Thompson and Troian, 1997) and (Lau and Schowalter, 1986) slip models on the stick-slip flow.

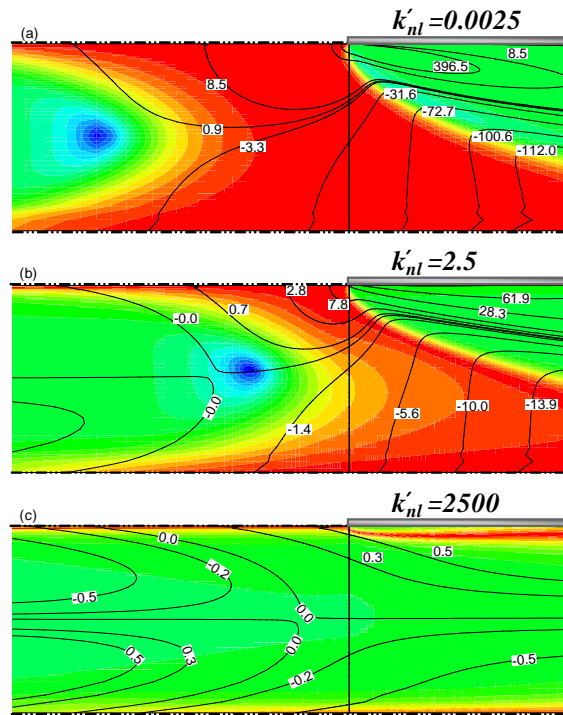


Figure 6.9: Representation of contour lines ( $\tau_{yy}$ ) superimposed with the flow type  $\zeta$  contours for the linear slip model: (a)  $k'_{nl} = 0.0025$ , (b)  $k'_{nl} = 2.5$ , (c)  $k'_{nl} = 2500$ .  $Re = 20$  and  $Wi = 2$ .

As expected, a lower number of iterations was necessary to obtain converged solutions when using higher slip velocities (high friction coefficients), because the slip velocity smooths the flow at the singularity. Identically, by using wall slip, converged solutions are obtained up to higher values of the Weissenberg number than in the absence of slip. However, the use of slip velocity as a method to improve the numerical stability of fluid computations is still under investigation. Regarding the fluid stresses, for the studied stick-slip problem, we found that increasing the slip velocity smooths the stress profiles and increases the relaxation length.

#### ACKNOWLEDGEMENTS

The authors acknowledge funding from COMPETE/FEDER and Fundação para a Ciência e a Tecnologia (FCT), Portugal, through project PTDC/EQU-FTT/113811/2009, and FEDER, via FCT, under the PEstC/CTM/LA0025/2011 (Strategic Project - LA 25 - 2011-2012). LLF would like to thank FCT for financial support through the scholarship SFRH / BD / 37586 / 2007. AMA would also like to thank FCT for financial support through the scholarship SFRH/BPD/75436/2010.



APPENDIX A: ANALYTICAL SOLUTIONS FOR THE SPTT AND FENE-P VISCOELASTIC MODELS

Considering a 2D Cartesian coordinate system  $x, y$  and a fully developed Poiseuille flow (see Fig. 6.1), the governing equations can be simplified because,

$$\partial/\partial x = 0 \text{ (except for pressure)}, \partial v/\partial y = 0, \partial p/\partial y = 0 \quad (6.41)$$

This leads to the following simplification in the momentum equation,

$$\tau_{xy} = p_x y \quad (6.42)$$

where  $p_x$  stands for the pressure gradient in the  $x$  direction and  $\tau_{xy}$  is the shear stress.

The system of rheological constitutive equations for the simplified PTT model can be simplified and is given by,

$$\begin{aligned} f(\tau_{xx} + \tau_{yy}) \tau_{xx} &= 2\lambda \tau_{xy} (\partial u/\partial y) & (a) \\ f(\tau_{xx} + \tau_{yy}) \tau_{yy} &= 0 & (b) \\ f(\tau_{xx} + \tau_{yy}) \tau_{xy} &= \eta (\partial u/\partial y) + \lambda \tau_{yy} (\partial u/\partial y) & (c) \end{aligned} \quad (6.43)$$

From Eq. (6.43)(b) one can see that  $f(\tau_{xx} + \tau_{yy}) = 0 \vee \tau_{yy} = 0$ . If  $f(\tau_{xx} + \tau_{yy}) = 0$  unrealistic results would be obtained, hence  $\tau_{yy} = 0$ .

Dividing Eq. (6.43)(a) by Eq. (6.43)(c), the former becomes  $\tau_{xx} = 2\lambda/\eta (\tau_{xy})^2$ . If Eqs. (6.43)(a), (b), (c) are combined with the momentum equation, the following system is obtained,

$$\begin{aligned} \tau'_{xy} &= p'_x y' & (a) \\ \tau'_{xx} &= 2Wi (p'_x y')^2 & (b) \\ \tau'_{yy} &= 0 & (c) \\ (\partial u'/\partial y') &= p'_x y' + 2\epsilon Wi^2 (p'_x y')^3 & (d) \end{aligned} \quad (6.44)$$

with length, velocity and stresses scaled with  $H, \bar{U}$  and  $\eta \bar{U}/H$ , respectively,  $\bar{U}$  is the mean streamwise velocity,  $H$  is the half channel width (see Fig. 6.1) and  $Wi = \lambda \bar{U}/H$  is the Weissenberg number.

If we assume that the tangent stress vector is given by Eq. (6.13) than the boundary conditions are written in a dimensionless form as:

$$u'_{ws}(\pm 1) = k'_{nl} (-p'_x)^m \quad (6.45)$$

$$u'_{ws}(\pm 1) = \frac{-\alpha' p'_x}{\sqrt{1 + \beta' p'_x}} \quad (6.46)$$

$$u'_{ws}(\pm 1) = c'_1 \left(-p'_x\right)^m \left[ 1 - c_2 \tanh \left( \frac{E + c'_3 \left(p'_x\right)}{RT} \right) \right] \quad (6.47)$$

for the nonlinear Navier, the TT and LS slip models, respectively, and  $k'_{pl} = kU^{m-1}(\eta/H)^m$ ,  $\alpha' = \alpha(\eta/H)$ ,  $\beta' = \beta(\eta U/H)$ ,  $c'_1 = c_1U^{m-1}$ ,  $c_3 = c_3(\eta U/H)$ .

Integrating Eq. (6.44)(d) gives,

$$u' \left( y' \right) = 0.5p'_x y'^2 + 0.5\epsilon Wi^2 p'^3_x y'^4 + d, \quad d \in \mathbb{R} \quad (6.48)$$

where we have two unknowns, the pressure gradient,  $p'_x$ , and the integration constant  $d$ . To find  $d$  we can make use of the slip boundary condition  $u'_{ws}(\pm 1)$  given by Eqs. (??), (6.46) and (6.47). Therefore, the solution for the direct problem is given by,

$$u' \left( y' \right) = 0.5p'_x \left( y'^2 - 1 \right) + 0.5\epsilon Wi^2 p'^3_x \left( y'^4 - 1 \right) + u'_{ws} \left( 1 \right) \quad (6.49)$$

By applying a constant flow rate  $Q = 2UH$  and integrating Eq. (6.49) over half the channel width,

$$\int_0^1 u' \left( y' \right) dy' = 1 \quad (6.50)$$

the following equation is obtained,

$$\left(-2/5\right) \epsilon Wi^2 p'^3_x - \left(1/3\right) p'_x - 1 + u'_{ws} \left( 1 \right) = 0 \quad (6.51)$$

The strong nonlinearity of Eq. (6.51), mainly due to the  $u'_{ws} \left( 1 \right)$  term, makes difficult the work of finding closed form solutions for this equation.

For the nonlinear Navier slip model, these solutions were already reported in the literature and can be found in the work of ?. For the other two slip models one can only prove the existence and uniqueness of a solution and provide the range where the solution lies (for the LS slip model an approximate particular solution can still be devised), this way is easy to find the solution using a method to solve transcendent equations.

*TT slip model*

Let  $f \left( p'_x \right) = \left(-2/5\right) \epsilon Wi^2 p'^3_x - \left(1/3\right) p'_x - 1 - \frac{\alpha' p'_x}{\sqrt{1+\beta' p'_x}}$  then,

$$\frac{df(p'_x)}{dp'_x} = \frac{-6}{5}\varepsilon Wi^2 p_x'^2 - \frac{1}{3} - \frac{\alpha' \sqrt{1+\beta' p_x'}}{1+\beta' p_x'} + \frac{\alpha\beta p_x'}{2(1+\beta' p_x')\sqrt{1+\beta' p_x'}} < 0 \quad (6.52)$$

Since  $f(0) = -1 < 0$  and  $f(-3) > 0$  ( $\beta' > 1/3$ ), the intermediate value theorem together with Rolle theorem guarantees the existence of a unique solution in the range  $[-3, 0]$ .

*LS slip model*

Let  $g(p'_x) = (-2/5)\varepsilon Wi^2 p_x'^3 - (1/3)p_x' - 1 + c_1'(-p_x')^m \left[ 1 - c_2 \tanh\left(\frac{E+c_3'(p_x')}{RT}\right) \right]$  then,

$$\frac{dg(p'_x)}{dp'_x} = \frac{-6}{5}\varepsilon Wi^2 p_x'^2 - \frac{1}{3} - mc_1'(-p_x')^{m-1} \left[ 1 - c_2 \tanh\left(\frac{E+c_3'(p_x')}{RT}\right) \right] - \frac{c_1'c_2c_3'(-p_x')^m}{RT \cosh^2} < 0 \quad (6.53)$$

Since  $g(0) = -1$  and  $g(-3) > 0$ , the intermediate value theorem together with Rolle theorem, guarantees again the existence of a unique solution in the range  $[-3, 0]$ .

For small values of the tanh argument,  $\frac{E+c_3'(p_x')}{RT} \ll 1$ , we can approximate  $\tanh\left(\frac{E+c_3'(p_x')}{RT}\right)$  by:

$$\frac{E+c_3'(p_x')}{RT} \text{ (linear), and,} \\ \frac{E+c_3'(p_x')}{RT} - \frac{1}{3} \left( \frac{E+c_3'(p_x')}{RT} \right)^3 \text{ (truncated series expansion).}$$

With these approximations, and assuming  $m = 1$  in Eq. (6.51), the following equation is obtained

$$-\frac{2}{5}\varepsilon Wi^2 p_x'^3 + \frac{c_1'c_2c_3'}{RT} p_x'^2 + \left( -\frac{1}{3} - c_1' + \frac{c_1'c_2E}{RT} \right) p_x' - 1 = 0 \quad (6.54)$$

This equation can be written in a more compact form as,

$$p_x'^3 + a_1 p_x'^2 + a_2 p_x' + a_3 = 0 \quad (6.55)$$

and its solution is given by the Cardano-Tartaglia formula,

$$p_x' = \sqrt[3]{-\frac{P}{2} + \sqrt{\frac{P^2}{4} + \frac{Q^3}{27}}} + \sqrt[3]{-\frac{P}{2} - \sqrt{\frac{P^2}{4} + \frac{Q^3}{27}}} - \frac{a_1}{3} = 0 \quad (6.56)$$

with

$$\begin{aligned}
a_1 &= -\frac{5c'_1c'_2c'_3(-p'_x)^2}{2RT'} \\
a_2 &= \frac{-\frac{1}{3}-c'_1+\frac{c'_1c'_2E}{KT'}}{-\frac{2}{5}\varepsilon Wi^2} \\
a_3 &= \left(\frac{2}{5}\varepsilon Wi^2 p'_x\right)^{-1} \\
P &= a_3 - \frac{a_1 a_2}{3} + \frac{2a_1^3}{27} \\
Q &= a_2 - \frac{a_1^2}{3}
\end{aligned} \tag{6.57}$$

The second viscoelastic model used in this work is the FENE-P equation, based on the kinetic theory for finitely extensible dumbbells with a Peterlin approximation for the average spring force. In this case the polymer extra-stress is given by

$$\begin{aligned}
Z (tr\boldsymbol{\tau}_p) \boldsymbol{\tau}_p + \lambda \left( \frac{\partial \boldsymbol{\tau}_p}{\partial t} + \mathbf{u} \cdot \nabla \boldsymbol{\tau}_p - [(\nabla \mathbf{u})^T \cdot \boldsymbol{\tau}_p + \boldsymbol{\tau}_p \cdot \nabla \mathbf{u}] \right) = \\
= \lambda \left( \boldsymbol{\tau} - \frac{b}{b+2} nkT \mathbf{I} \right) \frac{D \ln Z}{DZ} + \eta_p \left( \frac{b+5}{b+2} \right) (\nabla \mathbf{u} + (\nabla \mathbf{u})^T)
\end{aligned} \tag{6.58}$$

where  $\mathbf{I}$  is the identity tensor,  $b$  is a parameter that measures the extensibility of the dumbbell,  $k_B$  is the Boltzmann constant,  $T$  is the absolute temperature and  $n$  is a parameter of the model (Bird et al., 1987). The stress coefficient function,  $Z(\boldsymbol{\sigma}_{kk})$ , can be expressed by

$$Z(\tau_{kk}) = 1 + 3 \left( \frac{1}{b+2} + \frac{\lambda}{3\eta} \frac{\tau_{kk}}{b+5} \right) \tag{6.59}$$

Note that for fully-developed flows  $D \ln Z / Dt \approx 0$  and equation (6.58) becomes considerably simplified. Since that for steady fully developed channel flow, the sPTT and the FENE-P models exhibit similar behavior, as found by (Oliveira, 2002), then there is an exact equivalence between the sPTT and the FENE-P models in the sense of a parameter to parameter match, as explained in detail in Cruz et al. (Cruz et al., 2005), with the following change of variables,

$$\begin{aligned}
Z(\tau_{xx}) &\rightarrow \left( \frac{b+5}{b+2} \right) f(\tau_{xx}) \\
\lambda &\rightarrow \lambda \left( \frac{b+2}{b+5} \right) \\
\varepsilon &\rightarrow \frac{\varepsilon}{b+5} \\
\eta_p &\rightarrow \eta_p
\end{aligned} \tag{6.60}$$

Then, providing these substitutions are made, the results of this Appendix remain valid for the FENE-P fluid.

APPENDIX B: ANALYTICAL SOLUTIONS FOR THE SPTT AND FENE-P MODELS WITH NONLINEAR SLIP BOUNDARY CONDITIONS

The slip boundary conditions could be implemented assuming that an implicit slip velocity on both sides of the equation for each of the wall boundary cells at each iteration  $i$ ,

$$u_{ws}^i = \alpha\mu \left( \delta n^2 - \delta n \beta \mu \left( u_P^{i-1} - u_{ws}^i \right) \right)^{-1/2} \left( u_P^{i-1} - u_{ws}^i \right) \quad (6.61)$$

$$u_{ws}^i = \frac{c_1 \mu^m}{\delta n^m} \left( u_P^{i-1} - u_{ws}^i \right)^m \left[ 1 - c_2 \tanh \left( \frac{E}{KT} - \frac{c_3 \mu}{\delta n RT} \left( u_P^{i-1} - u_{ws}^i \right) \right) \right] \quad (6.62)$$

and then use a numerical method to find the solution of these transcendent equations (Eq. (6.61) for the TT and Eq. (6.62) for the LS slip models).

The iterative procedure is very similar to the one presented in Section 3, except that step 3 is now: “3. Compute the slip velocity by solving the transcendent equation for the boundary (Eq. (6.61) for the TT model and Eq. (6.62) for the LS model);”.

The bisection method was the selected algorithm to find the roots of these equations. In the overall numerical procedure for each wall boundary cell and each iteration  $i$  the solution is chosen after  $n$  iterations (bisection method iterations) such that  $(b - a) / 2^n$  is below a given error ( $[a; b]$  are the initial bounds for the solution  $u_{ws}^i$ ).

It can be proved analytically (for these two slip boundary conditions) that a unique solution,  $u_{ws}^i$ , exists, and that this solution verifies the condition  $u_{ws}^i < u_P^{i-1}$ .

Proof of existence of a unique solution for the LS model:

First, the intermediate value theorem will be used to prove the existence of the solution, and then, with the Rolle theorem we will prove its uniqueness.

We want to prove that :

$$\begin{aligned} \exists (u_{ws}^i)^1 : u_{ws}^i &= \frac{c_1 \mu^m (u_P^{i-1} - u_{ws}^i)^m}{\delta n^m} \left[ 1 - c_2 \tanh \left( \frac{E}{KT} - \frac{c_3 \mu (u_P^{i-1} - u_{ws}^i)}{\delta n RT} \right) \right] \\ \wedge 0 &\leq u_{ws}^i \leq u_P^{i-1}, \forall c_1, c_2, c_3, R, T, m, E, \delta n, u_P^{i-1} \in \mathbb{R}_0^+ \end{aligned} \quad (6.63)$$

Without loss of generality assume that the solution,  $u_{ws}^i$ , is positive. Let us create a function  $f(u_{ws}^i)$  given by,

$$f(u_{ws}^i) = u_{ws}^i - \frac{c_1 \mu^m (u_P^{i-1} - u_{ws}^i)^m}{\delta n^m} \left[ 1 - c_2 \tanh \left( \frac{E}{KT} - \frac{c_3 \mu (u_P^{i-1} - u_{ws}^i)}{\delta n RT} \right) \right] \quad (6.64)$$

Since  $f(u_p^{i-1})f(0) < 0$  and  $f(\cdot)$  is a real-valued continuous function on the interval  $[0; u_p^{i-1}]$ , the intermediate value theorem implies that  $\exists u_{ws}^i : f(u_{ws}^i) = 0$ .

Because  $f'(u_{ws}^i) < 0$  for  $u_{ws}^i \in [0; u_p^{i-1}]$ , by Rolle theorem the solution is unique.

For  $m = 1$  we can narrow down the range where the solution lies.

Assuming  $c_2 \tanh\left(\frac{E}{KT} - \frac{c_3\mu}{\delta n RT} (u_p^{i-1} - u_{ws}^i)\right) < 1$ , then,

$$u_{ws}^i = \frac{c_1\mu^m}{\delta n^m} (u_p^{i-1} - u_{ws}^i) \left[ 1 - c_2 \tanh\left(\frac{E}{KT} - \frac{c_3\mu}{\delta n RT} (u_p^{i-1} - u_{ws}^i)\right) \right] \leq \frac{c_1\mu^m}{\delta n^m} (u_p^{i-1} - u_{ws}^i) \quad (6.65)$$

meaning that,

$$u_{ws}^i < \frac{\frac{c_1\mu^m}{\delta n^m} u_p^{i-1}}{1 + \frac{c_1\mu^m}{\delta n^m}} u_p^{i-1} \quad (6.66)$$

The initial range for the bisection method is then given by,

$$[a; b] \equiv \begin{cases} \left[ 0; \frac{\frac{c_1\mu^m}{\delta n^m} u_p^{i-1}}{1 + \frac{c_1\mu^m}{\delta n^m}} u_p^{i-1} \right] & \text{if } m = 1 \\ [0; u_p^{i-1}] & \text{if } m \neq 1 \end{cases} \quad (6.67)$$

For the TT model we can use a similar procedure to prove that the existence of a unique solution  $u_{ws}^i \in [0; u_p^{i-1}]$ . Furthermore, we have that,

$$u_{ws}^i = \alpha \frac{\mu}{\delta n} \left( 1 - \frac{\beta\mu}{\delta n} (u_p^{i-1} - u_{ws}^i) \right)^{-1/2} (u_p^{i-1} - u_{ws}^i) \geq \alpha \frac{\mu}{\delta n} (u_p^{i-1} - u_{ws}^i) \quad (6.68)$$

This sets a new initial range for the bisection method, given by,

$$[a; b] \equiv \left[ \frac{\alpha \frac{\mu}{\delta n} u_p^{i-1}}{1 + \alpha \frac{\mu}{\delta n}}; u_p^{i-1} \right] \quad (6.69)$$

By using this ranges as initial guess for the bisection method (used to obtain the solutions of these transcendent equations) we gain computational time.

## SLIP FLOWS OF NEWTONIAN AND PTT FLUIDS IN A 4:1 PLANAR CONTRACTION

---

### Abstract<sup>1</sup>

*This work presents numerical results regarding the simulation of the 4:1 planar contraction flow for a viscoelastic fluid modeled by the simplified Phan-Thien–Tanner (sPTT) model under the influence of slip boundary conditions at the channel walls. The linear Navier slip law was considered with the dimensionless slip coefficient varying in the range  $[0; 4500]$ . The simulations were carried out for a small constant Reynolds number of 0.04 and different Deborah numbers,  $De = 0; 1; 2; 3; 4; 5$ . Convergence could not be achieved for higher values of the Deborah number, especially for large values of the slip coefficient, due to the large stress gradients near the singularity of the reentrant corner. Increasing the slip velocity leads to the formation of two vortices, a corner and a lip vortex. The lip vortex grows with increasing slip until it absorbs the corner vortex, creating a single vortex that continues to increase in size and intensity. In the range  $De = 3 - 5$  no lip vortex was formed. The results are intensively investigated for the  $De = 1$  case as function of the slip coefficient, while for the remaining  $De$  only the main features are shown for specific values of the slip coefficient.*

### 7.1 INTRODUCTION

In industrial processes, such as those involved in polymer processing, the existence of contraction flows is very common. The development of vortices in these flows affects the smoothness of the flow and promotes the appearance of instabilities, as reported by (Kim and Dealy, 2002; Dealy and Kim, 2005) and (Meller et al., 2002). In fact, the flow through a 4:1 planar sudden contraction under conditions of creeping flow and no wall slip is a long standing classic benchmark problem in computational rheology (Owens and Phillips, 2002).

A wide range of experimental, theoretical and numerical studies have been carried out in the past regarding contraction flows of Newtonian and non-Newtonian fluids. For the experimental work we highlight the work of (Boger and Walters, 1993) where most of the relevant non-Newtonian flow phenomena are illustrated. In terms of theoretical investigations of viscoelastic flow in the vicinity of the reentrant corner in a planar contraction we cite the works by Hinch (Hinch, 1993), (Renardy, 1995) and a series of investigations by Evans

---

<sup>1</sup> L.L. Ferrás, A.M. Afonso, M.A. Alves, J.M. Nóbrega, O.S. Carneiro, F.T. Pinho (2012). Flow of Newtonian and Phan-Thien–Tanner fluids in a 4:1 planar contraction with slip boundary conditions, submitted to the *Journal of Non-Newtonian Fluid Mechanics*.

and co-workers (Evans and Sibley, 2008, 2009; Evans, 2010). In terms of numerical simulation the monograph by (Owens and Phillips, 2002) gives a detailed overview of the progress in numerical analysis. Other contributions of note include the comparison between numerical and experimental results for a Boger fluid by Cochrane et al. (Cochrane et al., 1981) and by (Walters and Webster, 1982), who found no significant vortex activity for a 4:1 contraction. Marchal and Crochet (1986) studied numerically the 4:1 contraction flow with the UCM and Oldroyd-B viscoelastic models, while (Keunings and Crochet, 1984) used the PTT model. In their revision papers, (White et al., 1987) and (Boger, 1987) emphasize the critical role of the extensional viscosity in contraction flows and (Boger, 1987) also showed the presence of a lip vortex. Marchal and Crochet (1987) (numerical), and (Nguyen and Boger, 1979) (experimental) studied the growth of the main vortex with the Deborah number ( $De$ ). Debbaut and Crochet (1988) studied the contraction flow of fluids described by the Oldroyd-B, PTT and Giesekus-Leonov models. Luo and Tanner (1989) studied the 4:1 contraction flow of UCM and Oldroyd-B fluids. There are several other important works on contraction flows, such as references (Yul Yoo and Na, 1991; Keiller, 1993; Olsson, 1994; Xue et al., 1998a,b; Wapperom and Webster, 1999; Aboubacar and Webster, 2001; Aboubacar et al., 2002; Alves et al., 2003b, 2005, 2008; Fu et al., 2010; Kwon and Han, 2010; Afonso et al., 2011b). All these works assume the typical no-slip boundary condition at the walls. The few exceptions that we are aware of regarding contraction flows assuming wall slip, are the works of (Sunarso et al., 2006, 2007) where they perform numerical simulations to investigate the effect of wall slip on the flow behavior in macro and micro contraction channels, the work of (Yasuda and Sugiura, 2008) that is based on experimental and numerical studies of contractions with the nonlinear Navier slip boundary condition, and the work of (Joshi and Denn, 2003) that presents an analytical study of inertialess planar contraction flow with the linear Navier slip boundary condition.

The challenge of establishing quantitative agreement between the numerical results and the experimental observations is a demanding need (Nigen and Walters, 2002) and this cannot be achieved if the correct boundary conditions are not applied. It is known that various polymer melts exhibit wall slip (Ramamurthy, 1986; Kalika and Denn, 1987; Hatzikiriakos and Dealy, 1991, 1992; Migler et al., 1993; Chen et al., 1993; Awati et al., 2000; Münstedt et al., 2000; Gevgilili and Kalyon, 2001) but when developing constitutive equations and determining the parameters that best fit the fluid rheology, slip velocity is not usually taken into account.

It is therefore important to assess the influence of the slip velocity on the fluid flow and, for that reason, this work studies numerically the 4:1 contraction flow with the Navier slip boundary condition for a large range of slip coefficients,  $k_l^* \in [0; 4500]$ , and Deborah



numbers,  $De \in \{0; 1; 2; 3; 4; 5\}$ . This geometry was chosen in order to investigate the direct influence of the slip velocity by analyzing the vortex dimensions. We study both Newtonian and non-Newtonian fluids modeled by the simplified PTT model.

Although (Sunarso et al., 2006, 2007) have analyzed this problem, they used a different constitutive equation. Their investigation is limited to a set of values of the slip coefficient and they do not assess convergence with mesh refinement, a fundamental issue with viscoelastic fluids. In our calculations we present a detailed study of the flow characteristics and there is no need for any direct relaxation of the slip velocity as used by (Sunarso et al., 2006, 2007). Instead, we use an efficient procedure that calculates the slip velocity along iterations, adjusting the calculations depending on the solution's proximity to convergence. When convergence is eminent the calculated slip velocity converges to the correct slip velocity, while when far from the solution the new procedure guarantees that the slip velocity is always smaller than the velocity at the center of the adjacent control volume, a necessary condition to avoid numerical divergence.

This introduction is followed by subsection 2 where the governing equations are presented together with the slip boundary condition. In subsection 3 we briefly describe the algorithm used to couple velocity, pressure and the slip boundary condition and we describe also the geometry and the characteristics of the flow. The results are presented in three parts in subsection 4. First, the slip flow is analyzed for Newtonian fluids, followed by a detailed investigation of the flow of the sPTT fluid at  $De = 1$  and finally for the remaining Deborah numbers. The main conclusions close the paper.

## 7.2 GOVERNING EQUATIONS

The governing equations for confined flow of incompressible fluids are the continuity,

$$\nabla \cdot \mathbf{u} = 0 \quad (7.1)$$

and the momentum,

$$\rho \frac{\partial \mathbf{u}}{\partial t} + \rho \nabla \cdot \mathbf{u} \mathbf{u} = -\nabla p + \nabla \cdot \boldsymbol{\tau} \quad (7.2)$$

equations, where  $\mathbf{u}$  is the velocity vector,  $p$  is the pressure,  $\rho$  is the density and  $\boldsymbol{\tau} = \boldsymbol{\tau}_s + \boldsymbol{\tau}_p$  is the deviatoric stress tensor. The stress tensor is divided into a solvent contribution,  $\boldsymbol{\tau}_s = \eta_s (\nabla \mathbf{u} + (\nabla \mathbf{u})^T)$  (with  $\eta_s$  being the solvent viscosity) and a polymer contribution,  $\boldsymbol{\tau}_p$ , which in this case is given by the simplified Phan-Thien–Tanner (sPTT) model (Phan-Thien and Tanner, 1977):

$$\begin{aligned} f(tr\boldsymbol{\tau}_p) \boldsymbol{\tau}_p + \lambda \left( \frac{\partial \boldsymbol{\tau}_p}{\partial t} + \mathbf{u} \cdot \nabla \boldsymbol{\tau}_p - [(\nabla \mathbf{u})^T \cdot \boldsymbol{\tau}_p + \boldsymbol{\tau}_p \cdot \nabla \mathbf{u}] \right) = \\ = \eta_p \left( \nabla \mathbf{u} + (\nabla \mathbf{u})^T \right) \end{aligned} \quad (7.3)$$

where  $f(tr\boldsymbol{\tau})$  is a function depending on the trace of the stress tensor,  $\lambda$  is the relaxation time and  $\eta_p$  is the polymer viscosity coefficient. For the function  $f(tr\boldsymbol{\tau})$  we use its linear form, given by

$$f(tr\boldsymbol{\tau}) = 1 + \frac{\varepsilon \lambda}{\eta_p} tr(\boldsymbol{\tau}_p) \quad (7.4)$$

where  $\varepsilon$  is the extensibility parameter that bounds the extensional viscosity of the PTT fluid. This model was chosen because it has been extensively studied in the contraction flow in the absence of slip with the PTT model (see Alves et al. (Alves et al., 2003b) and the literature cited therein).

In order to include the wall slip boundary condition, the usual Dirichlet (no-slip) boundary condition was replaced by the Navier slip law (Navier, 1822). Assuming Cartesian coordinates for the velocity  $[u_{1t}, u_{2t}, u_{3t}]$  and stress wall tangent vectors  $[\tau_{1t}, \tau_{2t}, \tau_{3t}]$ , the Navier slip boundary condition can be written as,

$$[u_{1t}, u_{2t}, u_{3t}] = -k_l [\tau_{1t}, \tau_{2t}, \tau_{3t}] \quad (7.5)$$

where  $k_l \in [0, +\infty[$  is the slip coefficient (also known as slip length) that allows increasing or decreasing the intensity of slip velocity. Eq. 7.5 states that the tangent velocity vector points in the stress opposite direction, both variables referring to the wall.

### 7.3 NUMERICAL METHOD AND GEOMETRY

The system of Eqs. 7.1, 7.2 and 7.3 is solved using a methodology based on the finite volume method algorithm. The SIMPLEC method of van Doormal and Raithby (Van Doormaal and Raithby, 1984), extended by (Oliveira et al., 1998) to incorporate viscoelastic fluids, is used to couple velocity, pressure and stress fields (Oliveira et al., 1998). The inclusion of slip boundary conditions promotes some changes in the overall procedure that are described in detail by (Ferrás et al., 2012d).

The main key for the implementation of slip boundary conditions is the assumption of a Couette flow in the vicinity of the wall,

$$\boldsymbol{\tau}_t = \eta (\dot{\gamma})_w \left. \frac{d\mathbf{u}}{d\mathbf{n}} \right|_w \quad (7.6)$$

where  $\mathbf{n}$  is the unit normal velocity vector (cf. Fig. 7.1),  $\boldsymbol{\tau}_t$  is the tangent stress vector and the subscript "w" means that the variables are evaluated at the wall.

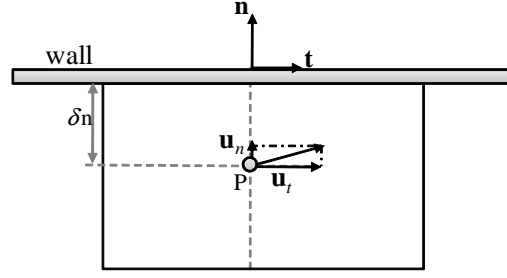


Figure 7.1: Computational cell near the wall.

Combining Eqs. 7.5 and 7.6, the discretized slip boundary condition (assuming a one-sided first order approximation for the wall derivative) is given by

$$\left[ u_{1t}^i, u_{2t}^i, u_{3t}^i \right] = -k_l \eta (\dot{\gamma})_w^{i-1} \left[ \frac{u_1^i - u_{1tP}^{i-1}}{\delta n}, \frac{u_2^i - u_{2tP}^{i-1}}{\delta n}, \frac{u_3^i - u_{3tP}^{i-1}}{\delta n} \right] \quad (7.7)$$

where  $\delta n$  is the distance between the wall and P (as given in Fig. 7.1),  $u_{jtP}$  ( $j = 1, 2, 3$ ) are the components of the tangent velocity vector at the center of the adjacent cell P,  $i$  is the iteration number and  $\eta (\dot{\gamma})_{wall}^{i-1}$  is the shear-rate dependent shear viscosity,  $\dot{\gamma}$ , evaluated at the wall. This shear viscosity is evaluated for the particular constitutive equation adopted, here the sPTT.

To solve the system of equations the following iterative procedure is used:

- (1) Set the boundary conditions, the initial (tentative) velocity and pressure fields;
- (2) Solve the stress equations for the non-Newtonian model;
- (3) Compute the slip velocity with the discretized slip model:

$$(u_1, u_2, u_3)_{ws}^i = \frac{d}{1+d} (u_{1P}, u_{2P}, u_{3P})_t^{i-1},$$

where  $d = k_l \eta (\dot{\gamma})_w^{i-1} / \delta n$  with :

$$\eta (\dot{\gamma})_w^{i-1} = \eta_s + \frac{\eta_p}{1 + (\alpha - 1)^2 / 3\alpha},$$

$$\alpha = \left( \theta + \sqrt{\theta^2 - 1} \right)^{1/3}, \quad \theta = 1 + 27\epsilon (\lambda \dot{\gamma})_w^2;$$

- (4) Solve the linearized momentum equations;
- (5) Solve the pressure correction equation;
- (6) Correct the velocity and pressure fields;
- (7) Check for convergence of the residuals of the linear system of discretized equations and for convergence of the vector direction (see Eq. 7.8);
- (8) If convergence is not achieved return to step 2 and repeat until convergence.

Since we are looking for the steady state solution a pseudo time evolution is employed, thus time is only used for relaxation purposes; this means that each time step represents one iteration  $i$ . Based on (Ferrás et al., 2012d) it is known that during the first iterations the slip velocity vector may not have the correct direction, but is expected that when convergence is achieved the correct direction is obtained. This is achieved when

$$\lim_{i \rightarrow \infty} \frac{\left\| \left( u_1^i - u_{1P}^{i-1}, u_2^i - u_{2P}^{i-1}, u_3^i - u_{3P}^{i-1} \right) \right\|}{\left\| \left( u_1^{i-1} - u_{1P}^{i-1}, u_2^{i-1} - u_{2P}^{i-1}, u_3^{i-1} - u_{3P}^{i-1} \right) \right\|} = 1 \quad (7.8)$$

With this method there is no need for direct relaxation in the slip velocity and the computations are stable (Ferrás et al., 2012d).

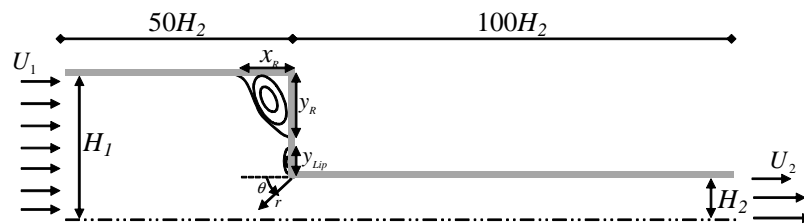


Figure 7.2: Schematic representation of the 4:1 contraction geometry.

The geometry of the 4:1 contraction used in the present study is given in Fig.7.2. The computational domain was divided into five blocks (see Table 7.1 and Fig. 7.2) and only half of the channel is considered because of symmetry. Based on the work of (Oliveira et al., 1998) and (Alves et al., 2003b) we built three different meshes named MC1, MC2 and MC3 (Table 7.1) that were used for Newtonian and non-Newtonian fluids.

Table 7.1: Mesh Characteristics for MC1, MC2, MC3.

Zone	MC1				MC2				MC3					
	$f_x$	$f_y$	$n_x$	$n_y$	$f_x$	$f_y$	$n_x$	$n_y$	$f_x$	$f_y$	$n_x$	$n_y$		
1	0.93500	0.95950	87	36	0.96695	0.97950	174	72	0.98334	0.98972	348	144		
2	0.93500	1.04860	87	47	0.96695	1.02400	174	94	0.98334	1.01193	348	188		
3	0.93500	0.92700	87	18	0.96695	0.96280	174	36	0.98334	0.98123	348	72		
4	1.06952	0.95950	87	36	1.03418	0.97950	174	72	1.01694	0.98972	348	144		
5	1.00000	0.95950	15	36	1.00000	0.97950	30	72	1.00000	0.98972	60	144		
n <sup>o</sup> cells				12459	n <sup>o</sup> cells				49836	n <sup>o</sup> cells				199344
$(\Delta/H)_{min}$				0.010	$(\Delta/H)_{min}$				0.005	$(\Delta/H)_{min}$				0.002

Refinement between consecutive meshes is consistently done by doubling the number of cells in each direction and using square-rooted cell contraction/expansion factors. The notation  $n_x$  and  $n_y$  is used to represent the number of cells in the  $x$  and  $y$  directions, respectively,  $f_x$  and  $f_y$  are the contraction/expansion ratios between consecutive cells that allow the concentration of cells in zones where

high gradients are expected to occur. The most refined mesh (MC<sub>3</sub>) has 199344 cells and a zoomed view of the more refined zone can be seen in Fig.7.3. More details regarding these three meshes can be found in Table 7.1.

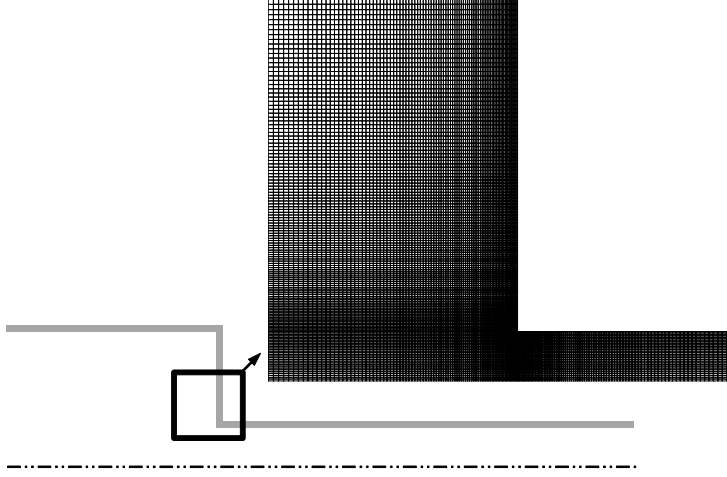


Figure 7.3: Zoomed view of mesh MC<sub>3</sub>.

The simulations were performed for the sPTT model at a constant Reynolds number,  $Re = \rho U_2 H_2 / \eta_0 = 0.04$  and a varying Deborah number  $De = \lambda U_2 / H_2$  ( $De = 0; 1; 2; 3; 4$  and  $5$ ) with  $\varepsilon = 0.25$  and a viscosity ratio  $\beta = \frac{\eta_s}{\eta_0} = \frac{\eta_s}{\eta_s + \eta_p} = \frac{1}{9}$ .

## 7.4 RESULTS AND DISCUSSION

### 7.4.1 Newtonian Fluids

#### 7.4.1.1 Vortex size and intensity

For Newtonian fluids ( $De = 0$ ) one could find that the increase in the slip coefficient leads to a significant variation in the vortex intensity  $\Psi_R$  and vortex dimensions  $X_R = x_R / H_2$  and  $Y_R = y_R / H_2$  (cf. Fig. 7.2). The vortex intensity is defined as the flow rate inside the vortex normalized by the flow rate at the entrance,  $U_1 H_1$ :

$$\Psi_R = \frac{\psi_R - U_1 H_1}{U_1 H_1} \times 10^3 \quad (7.9)$$

where  $\psi_R$  is the streamfunction value at the vortex center (we assume  $\psi_R = 0$  at the centerline,  $y = 0$ ).

As shown in Figs. 7.4 and 7.5 the vortex decreases with the increase of the slip coefficient and it disappears at  $k_l^* = k_l \eta_0 / H_2 \approx 4500$ . As for the vortex intensity we found that it increases from 1.125 for  $k_l^* = 0$  to 1.829 with  $k_l^* = 0.45$  and then decreases to 0 as  $k_l^*$  continues to increase.

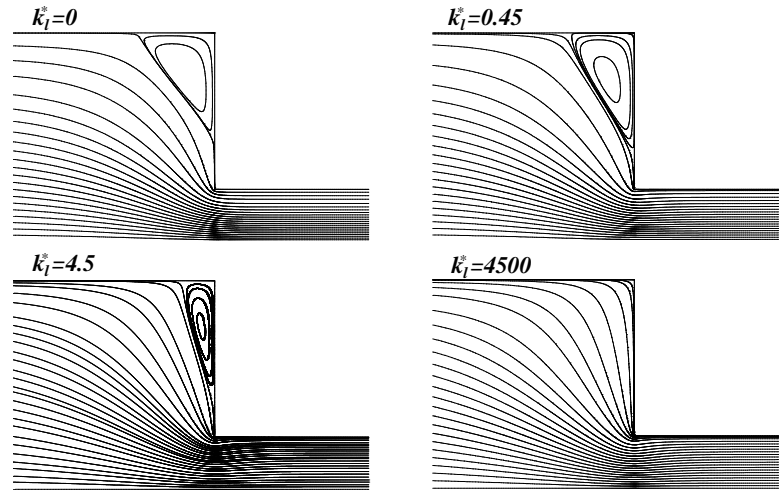


Figure 7.4: Variation of the vortex dimensions and strength with the fiction coefficient  $k_l^*$  for a Newtonian fluid at a constant  $Re = 0.04$ .

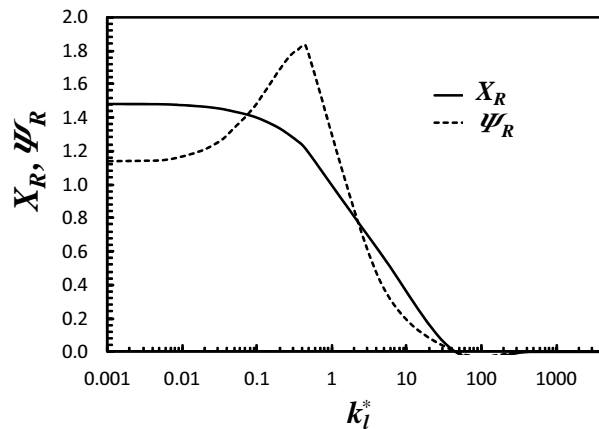


Figure 7.5: Variation of the vortex dimension  $X_R$  and vortex intensity  $\Psi_R$  with the dimensionless slip coefficient  $k_l^*$  for  $Re = 0.04$  and  $De = 0$ .

For small slip intensity the flow is essentially affected in the vicinity of the wall where there is a reduction of the shear rates with concomitant reductions in dissipative friction, thus increasing the vortex strength while the vortex remains essentially unchanged (cf. Fig. 7.4). As  $k_l^*$  is further increased the slip effect penetrates further into the channel and leads to a reduction in size and consequently in the strength of the recirculation. With a very large slip the flow behaves essentially as an inviscid fluid, which is able to negotiate all the obstacles and no recirculation exists.

7.4.1.2 Singularity (variation along the line  $\theta = \pi/2$ )

In all Newtonian fluid cases there was no lip vortex and this allowed the measurement of the asymptotic variation of the stress and velocity

components on their approach to the reentrant corner at  $\theta = \pi/2$  measured counterclockwise from the incoming flow direction (cf. Fig. 7.2). This way we can compare our results with the theoretical studies of (Moffatt, 1964), and (Dean and Montagnon, 1949), for the asymptotic behavior of a fluid near the reentrant corner (Fig. 7.6). More precisely,

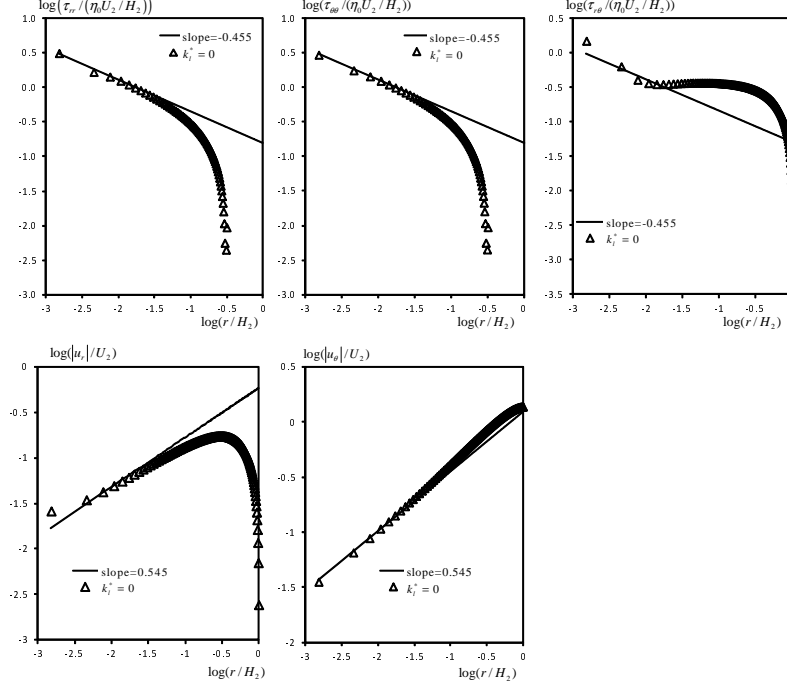


Figure 7.6: Asymptotic behavior for the velocity and stress components near the reentrant corner of a 4:1 contraction, for a Newtonian fluid with  $Re = 0.04$  and  $k_l^* = 0$ .

these authors found that the asymptotic behavior of velocity and stress components near the reentrant corner are given by (Dean and Montagnon, 1949),

$$u_i \propto r^{0.545}, \tau_{ij} \propto r^{-0.455} \quad (7.10)$$

where  $r$  is the distance measured from the reentrant corner. In Fig. 7.6 we can see a good agreement between our results ( $k_l^* = 0$ ) and the results obtained by (Dean and Montagnon, 1949; Moffatt, 1964). This allows us to assess the accuracy of our results.

#### 7.4.1.3 Couette correction

In order to investigate the viscous losses, we also studied the variation of the Couette correction with the slip coefficient. The Couette correction is given by (Coates et al., 1992),

$$C = \frac{\Delta p - \Delta p_{1FD} - \Delta p_{2FD}}{2\tau_w} \quad (7.11)$$

where  $\Delta p$  represents the pressure drop between the entrance and the exit of the contraction (in regions where the flow is well full-

developed),  $\Delta p_{1FD}$ ,  $\Delta p_{2FD}$  denote the pressure drop for fully developed Poiseuille flow in the entry and exit channels (between the same points considered for  $\Delta p$ ), with widths  $H_1$  and  $H_2$ , respectively, and  $\tau_w$  is the wall shear stress for the fluid in question (encompassing both solvent and polymer contributions) for fully-developed flow in the exit channel. We could find a non-linear relationship between  $C$  and  $k_l^*$  as can be seen in Fig. 7.7 (a). For small values of the slip coefficient

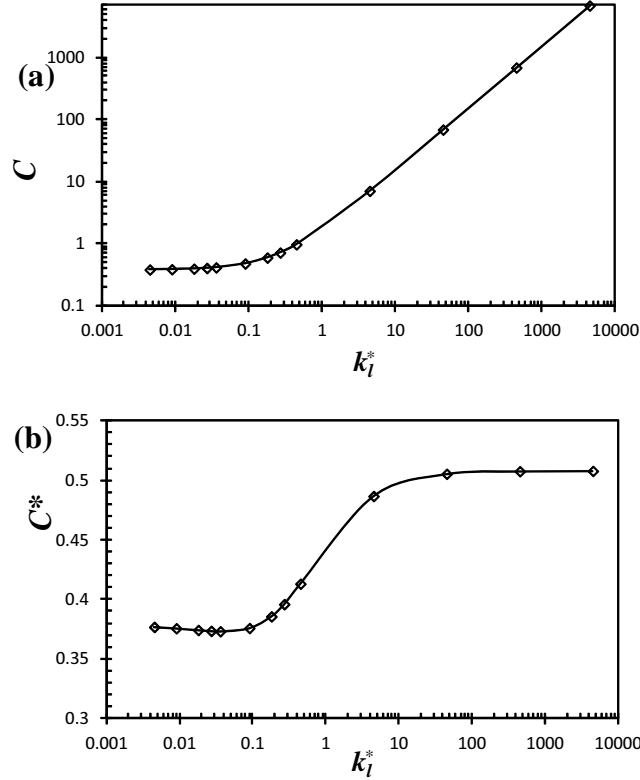


Figure 7.7: Variation of the Couette correction with the slip coefficient for a Newtonian fluid at  $Re = 0.04$ . (a) Couette correction ( $C$ ) normalized with  $2\tau_w$ . (b) Couette correction ( $C^*$ ) normalized with the wall stress from the no-slip case  $2\tau_{w-no\ slip}$

we observe a slight increase in  $C$  followed by a sudden exponential increase. For  $k_l^* = 0$  we obtained a value of  $C = 0.3786$  ( $C = 0.3741$  was obtained in the work of Alves et al. (Alves et al., 2003b) for  $Re = 0$ ) while for  $k_l^* = 4500$  we obtained a value of  $C = 6856$ . These high values of the Couette correction are mainly an outcome of the small values of  $\tau_w$  (a consequence of the increase of the slip coefficient) used in the normalization of  $\Delta p$ . Therefore we also plotted in Fig 7.7 (b) the modified Couette correction,  $C^*$ , normalized with the wall stress obtained from the no-slip case,  $\tau_{w-no\ slip}$ . In this case, for  $k_l^* = 4500$  we obtained a value of  $C^* = 0.5078$ .

In order to understand why  $C^*$  increases with  $k_l^*$ , we plotted separately in Fig. 7.8 the three terms that make up  $C^*$ , i.e., the normalized real pressure drop ( $\Delta p$ ) and the normalized  $\Delta p$  corresponding



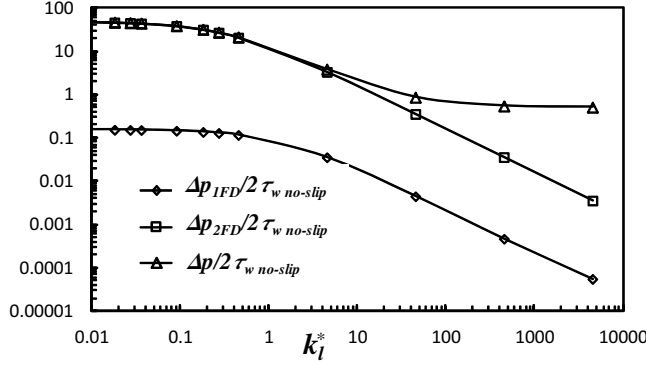


Figure 7.8: Variation of the normalized real pressure drop,  $\Delta p$ , normalized  $\Delta p_{1FD}$  and normalized  $\Delta p_{2FD}$ , with the slip coefficient, for a Newtonian fluid at  $Re = 0.04$ .

to fully-developed flow in the whole of the upstream ( $\Delta p_{1FD}$ ) and downstream channels ( $\Delta p_{2FD}$ ). It is clear that by increasing the slip coefficient these extrapolated fully-developed pressure drops decrease significantly faster (and even tend to go to zero) than the reduction in the overall pressure drop.

#### 7.4.2 Viscoelastic fluids

##### 7.4.2.1 Small elastic effects: $De=1$

##### 7.4.2.2 Vortex size and intensity and Couette correction

Table 7.2 presents the vortex dimension  $X_R$ , vortex intensity  $\Psi_R$  and Couette correction  $C$  together with the relative error (relative difference between the results obtained with the mesh MC<sub>3</sub> and the extrapolated values, in percentage) for the 4:1 contraction flow at  $De = 1$ . The extrapolated values were obtained with the Richardson extrapolation technique (Richardson, 1910; Richardson and Gaunt, 1927) using the three consecutively refined meshes presented in Table 7.1.

As shown in Fig. 7.9(a) the variation of  $X_R$  with  $k_l^*$  is nonmonotonic with a local minimum at  $k_l^* = 0.36$  and subsequent increase in length, in strong contrast to the Newtonian behavior. This is a consequence of the competition between viscous and elastic effects, both coupled with slip. At low values of  $k_l^*$ , and as for Newtonian fluids, the viscous effects predominate over the elastic effects and the reduction of the near wall shear rates associated with slip leads to a local reduction of dissipative effects and to a small decrease in  $X_R$  (note that a region of separated flow is a fairly effective means of locally dissipating energy). However, as  $k_l^*$  increases the elastic effects also intensify and these are translated into the formation of a lip vortex which grows slowly at low values of  $k_l^*$  and more intensely as  $k_l^*$  increases, engulfing the corner vortex and increasing in size. The increase in  $X_R$  with  $k_l^*$  is asymptotic because the growth of the elastic recirculation is not dominated by

Table 7.2: Vortex dimensions, intensity and Couette correction for an sPTT fluid flow with  $\varepsilon = 0.25$ ,  $Re = 0.04$ ,  $De = 1$ .

$k_l^*$	$X_R$ ext.	error(%)	$\Psi_R$ ext.	error(%)	$C$ ext.	error(%)	$C^*$ ext.	error(%)
0.0000	1.5197	0.0026	1.2509	0.0014	0.1025	0.3982	0.1025	0.3982
0.0045	1.5177	0.0038	1.2862	0.0018	0.1046	0.1271	0.1041	0.1271
0.0090	1.5155	0.0005	1.3201	0.0077	0.1067	0.0394	0.1056	0.0394
0.0180	1.5114	0.0002	1.3872	0.0094	0.1111	0.0243	0.1088	0.0243
0.0270	1.5077	0.0004	1.4552	0.0009	0.1156	0.0663	0.1121	0.0664
0.0360	1.5044	0.0049	1.5231	0.0184	0.1202	0.0195	0.1154	0.0194
0.0450	1.5015	0.0132	1.5916	0.0720	0.1251	0.0105	0.1189	0.0103
0.0900	1.4903	0.0488	1.9384	0.5512	0.1516	0.5156	0.1371	0.5253
0.1800	1.4804	0.1359	-	-	0.2159	1.5807	0.1770	1.6118
0.2700	1.4803	0.2595	-	-	0.2878	0.9700	0.2146	0.9824
0.3600	1.4855	0.4547	-	-	0.3696	0.8151	0.2516	0.8254
0.4500	1.4906	0.5197	-	-	0.4584	0.6989	0.2860	0.7078
4.5000	1.5496	0.0071	-	-	5.1278	0.8711	0.5843	0.9163
45.000	1.5650	0.0107	-	-	51.131	1.8501	0.6228	2.0732
450.00	1.5668	0.0171	-	-	504.44	0.7583	0.6173	0.7873
4500.0	1.5669	0.0174	-	-	5060.2	1.0925	0.6200	1.1686

the near wall forces, but by the normal stresses associated with the extensional flow in the central region of the contraction, so the vortex ceases to grow above  $k_l^* \approx 100$ . Since the increase of slip reduces both the viscous shear stress and the elastic shear-induced normal stress, we show in this way that the corner vortex is essentially determined by viscous forces and that the lip vortex and its growth is essentially determined by the extensional elastic stresses in the central region of the geometry.

As for the corner vortex intensity we see in Fig. 7.9(b) that it increases with the increase of the slip coefficient and this increase is due at low values of  $k_l^*$  to the reduction of viscous losses within the vortex, already observed with Newtonian fluids, followed subsequently to the increasing intensity of the elastically driven lip vortex. The specific values of  $\Psi_R$  have to be looked at with care especially when the corner and lip vortices co-exist given the distortion induced by each one on the other, with obvious consequences in terms of accuracy.

For the three meshes used we find that for  $k_l^* \simeq 0.027$  the two vortices begin to merge until a single and larger vortex is formed at  $k_l^* \simeq 0.45$ . Further, increasing  $k_l^*$  leads to vortex growth and curvature changes, as shown in the streamline plots of Fig 7.10 (obtained for the mesh MC3).

For the lip vortex dimension  $Y_{lip}$ , accurate results are much more difficult to obtain and require very refined meshes. This happens because the top part of the increasing vortex starts to rotate in the counterclockwise direction (as seen in Fig. 7.11 ) meaning that the results obtained for the  $Y_{lip}$  are deceived by that rotation.

Regarding the lip vortex intensity,  $\Psi_{lip}$ , Fig. 7.12 shows that it increases with the slip coefficient, but we could find the existence of a region of higher uncertainty,  $k_l^* \in [0.09; 0.45]$ . This happens in the cases where the two vortices coexist and because their specific location is very sensitive to the mesh characteristics. Finally, the lip vortex

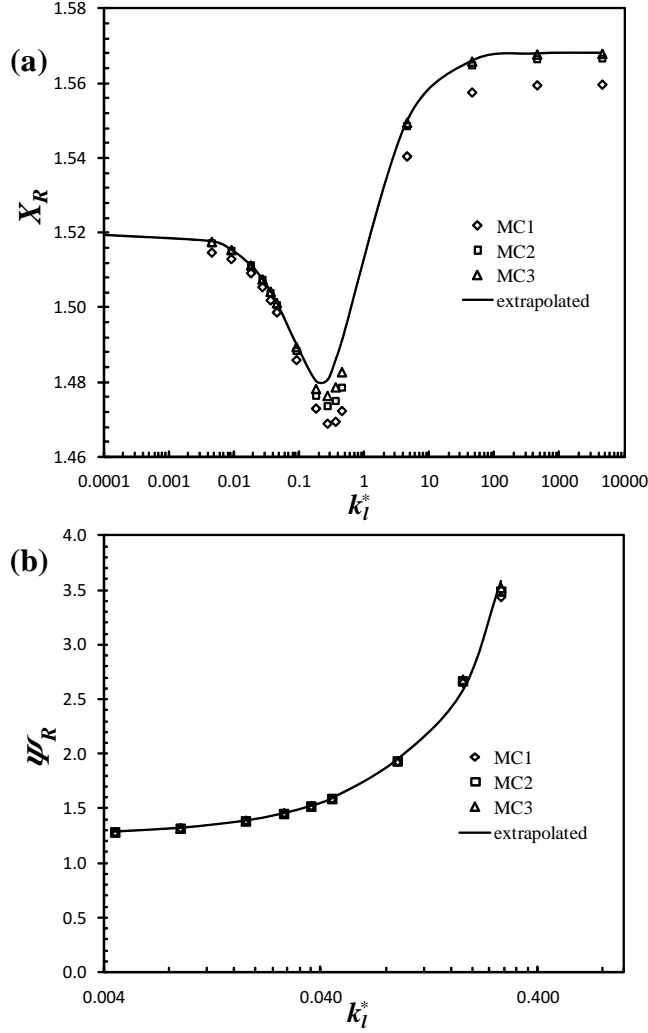


Figure 7.9: Variation of the vortex dimension  $X_R$  (a) and vortex intensity  $\Psi_R$  (b) with the slip coefficient  $k_l^*$  for an sPTT fluid with  $\varepsilon = 0.25$ ,  $Re = 0.04$  and  $De = 1$ .

becomes the main vortex above  $k_l^* \simeq 0.4$  and high levels of vortex intensity are obtained.

The existence of two vortices with one vortex engulfing and absorbing the other while increasing the elasticity was also found by (Xue et al., 1998a) for an Oldroyd-B fluid employing the no-slip boundary condition. These features were also present in the nonlinear dynamics at high Deborah-number flows described by (Afonso et al., 2011b), in which the elastic lip vortex increases in size and eventually reaches the corner vortex region, and merges with it in a fairly complex dynamic process. This merging-growth regime occurs at  $De \simeq 4.5$  for the Oldroyd-B model with no slip, corresponding to the minimum value of  $X_R$  (Afonso et al., 2011b).

The Couette correction was also calculated and we found a similar behavior to the one obtained for the Newtonian results. The Couette

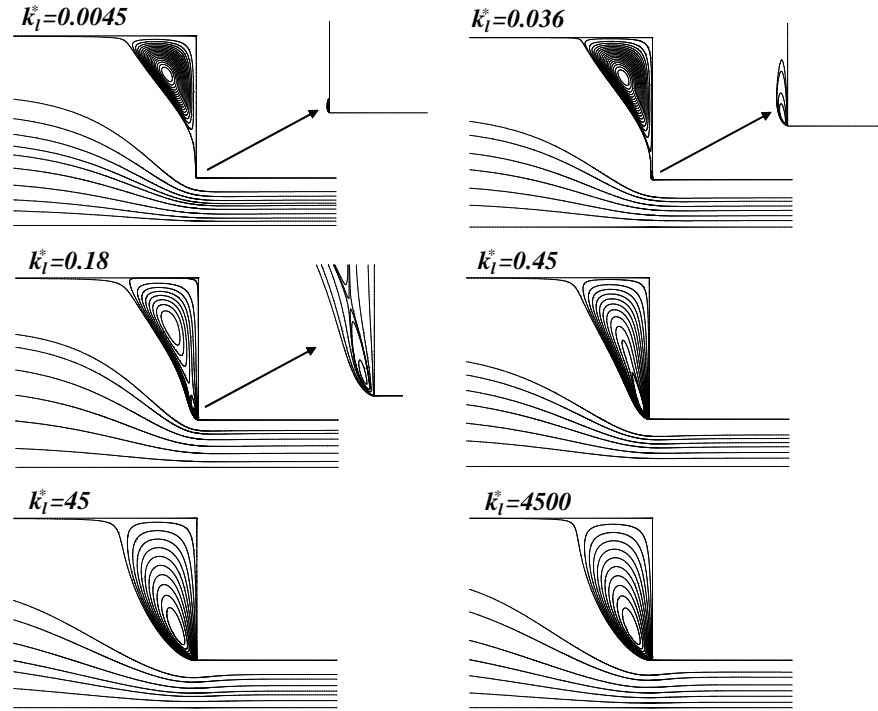


Figure 7.10: Visualization of the corner and lip vortex growth with the slip coefficient  $k_l^*$  for an sPTT fluid with  $\varepsilon = 0.25$ ,  $Re = 0.04$  and  $De = 1$ .

correction increases with the slip coefficient as shown in Fig. 7.13 and in Table 7.2.

#### 7.4.2.3 Variation of velocity and stresses near the wall

In order to assess the effects of slip velocity on the distribution of velocity and stresses, the streamwise components of these variables were monitored near the downstream channel walls, at  $y/H_2 = 0.9985$ .

For the velocity Fig. 7.14(a) shows its smoothing with the increase of the slip velocity, except near the reentrant corner where a large gradient is usually found. For the dimensionless shear stress  $\tau_{xy}$  (normalized with  $3\eta_0 U_2/H_2$ ) we see, in Fig. 7.14(b), that the increase of the slip velocity leads to a decrease of the shear stress (in absolute value), as expected. The normalized first normal stress difference  $N_1 \equiv \tau_{xx} - \tau_{yy}$  given in Fig. 7.14 follows the same trend as the normalized  $\tau_{xy}$  showing a decrease but presenting higher values near the singularity when compared to the no-slip boundary condition case.

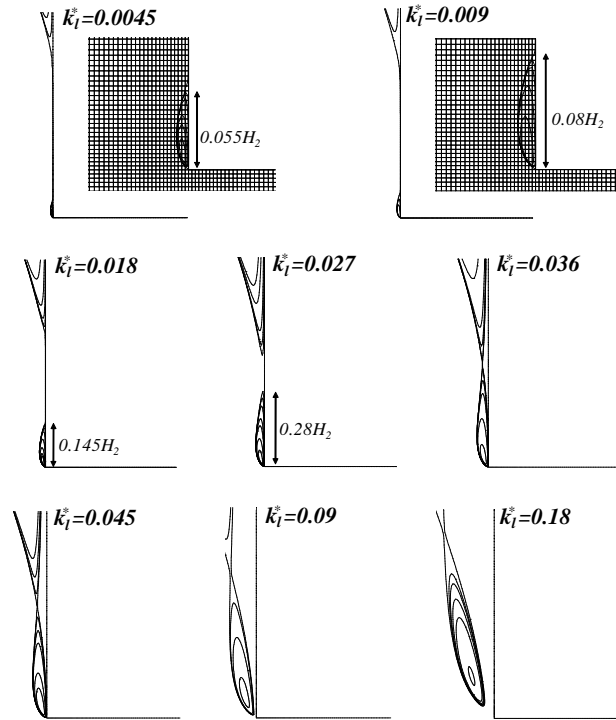


Figure 7.11: Lip vortex growth for increasing values of the slip coefficient  $k_l^*$  for an sPTT fluid with  $\varepsilon = 0.25$ ,  $Re = 0.04$  and  $De = 1$ .

#### 7.4.3 Effect of elasticity

In addition to  $De = 0$  and  $De = 1$ , the 4:1 contraction flow was also simulated for  $De = 2, 3, 4$  and 5. For higher values of  $De$  convergence could not be achieved (especially for high slip coefficients). This contrasts with the no-slip simulations of (Alves et al., 2003b) with the sPTT fluid, which converged up to values of  $De$  of at least 100, using essentially the same code. However in the absence of slip the presence of the lip vortex is not observed, i.e., the dynamics seen here for the sPTT fluids with slip is more akin to that observed for the Oldroyd-B fluid without slip by Alves et al. (Alves et al., 2003b). These results thus show that the slip velocity strongly influences the convergence properties of the sPTT fluid mainly due to the higher normal strain/stress gradients that appear near the reentrant corner.

For Deborah numbers ranging from 6 to 9 the code was not able to decrease the residuals of the iterative procedure and convergence was not possible, an indication of possible inherent unsteady behavior. For higher values of  $De$  the computations diverged. Note also that the computations were performed on half domain, but it is known that the viscoelastic flow through a sudden contraction of some viscoelastic

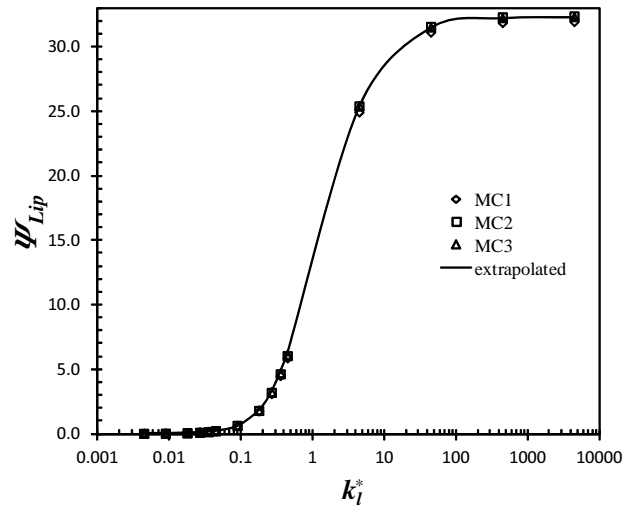


Figure 7.12: Variation of the lip vortex intensity  $\Psi_{lip}$  with the slip coefficient  $k_l^*$  for an sPTT fluid with  $\varepsilon = 0.25$ ,  $Re = 0.04$  and  $De = 1$ .

fluids, like Oldroyd-B fluid, exhibits time dependency and is no longer symmetric above certain critical  $De$  (Afonso et al., 2011b).

For  $De = 0, 2, 3, 4$  and  $5$  the results qualitatively follow the same trends of the  $De = 1$  case. We can see in Fig 7.15 that the vortex intensity  $\Psi_R$  and the vortex dimension  $X_R$  both increase with the Deborah number for the constant value of slip coefficients  $k_l^* = 0; 0.18; 45$ , and also increase with slip at constant  $De$ . As an example, for  $De = 5$   $\Psi_R \approx 3$  for the no-slip case, and increases to  $\Psi_R \approx 50$  for  $k_l^* = 45$  (see Fig. 7.15(b)). For the Couette correction  $C$  we see that the presence of slip velocity leads to an extra pressure loss ( $C > 0$ ) (Fig. 7.15(c)).

## 7.5 CONCLUSIONS

Numerical simulations were performed for the flow of Newtonian and non-Newtonian fluids past an abrupt 4:1 planar contraction in the presence of wall slip. To model the non-Newtonian fluid the sPTT constitutive equation was used and slip on all walls was described by the Navier slip law.

For the Newtonian fluid the vortex decreases in size until it eventually disappears with increasing slip velocity, even though for weak values of slip a slight increase in vortex intensity was observed. Although it seems unlikely for a Newtonian fluid to present these high levels of slip velocity, the results are helpful for the interpretation of the slip effects.

For non-Newtonian fluids the corner vortex tends to decrease with slip, with lower values of the slip coefficient, along with the formation of a lip vortex. As slip increases the lip vortex engulfs and absorbs the corner vortex, promoting an increase in size and curvature modifica-

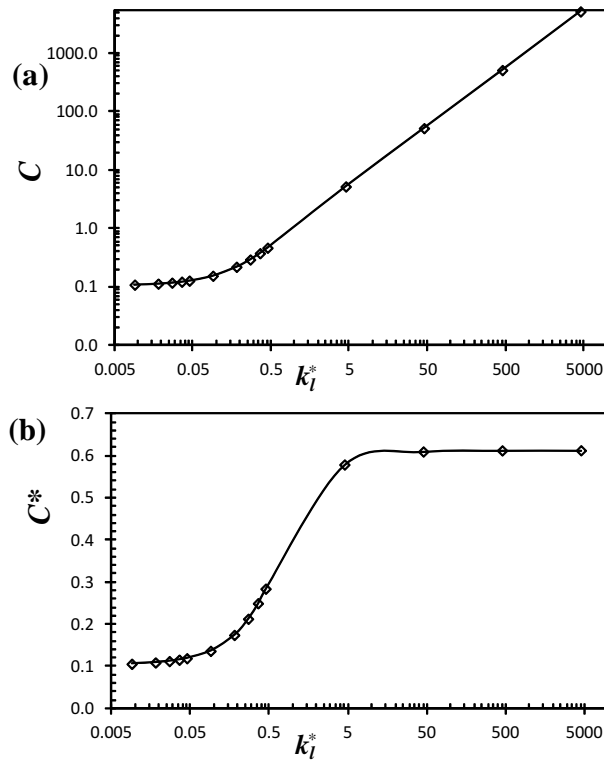


Figure 7.13: Variation of the Couette correction with the slip coefficient  $k_l^*$  for an sPTT fluid with  $\varepsilon = 0.25$ ,  $Re = 0.04$  and  $De = 0, 1$ . (a) Couette correction ( $C$ ) normalized with  $2\tau_w$ . (b) Couette correction ( $C^*$ ) normalized with the wall shear stress from the no-slip case,  $2\tau_{w-no\ slip}$

tion of the flow recirculation, very much as had been observed with Oldroyd-B fluids without wall slip. It was also found that the vortex dimensions increase with  $De$ . Hence, slip enhances significantly the effect of elasticity observed in the no-slip cases. For  $De > 5$  it was not possible to achieve convergence, mainly due to the higher gradients that appear near the re-entrant corner. Considering that in the absence of slip and for the same model Alves et al. (Alves et al., 2003b) were able to obtain converged solutions up to  $De$  of 100 it is clear the the high Deborah-number problem is enhanced by the presence of slip.

These results are useful to interpret and model fluids subjected to slip boundary conditions such as some polymer systems used in polymer processing industries.

#### ACKNOWLEDGEMENTS

The authors gratefully acknowledge funding by COMPETE, FEDER and Fundação para a Ciência e Tecnologia (FCT) through projects PEst-C/CTM/LA0025/2011 (Strategic Project - LA 25 - 2011-2012) and PTDC/EME-MFE/114322/2009. LLF and AMA would also like to

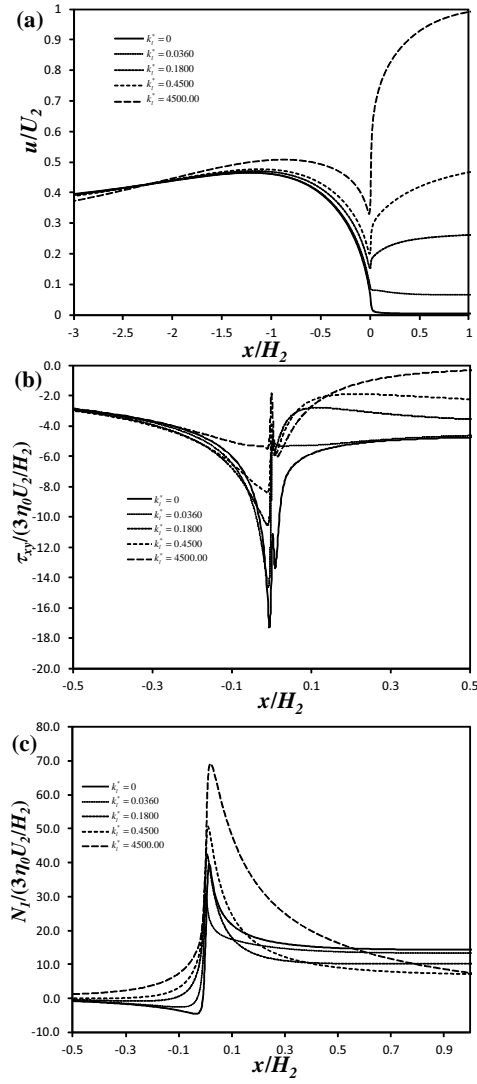


Figure 7.14: Variation of the normalized velocity and stress fields along the line  $y/H_2 = 0.9985$  as function of the slip coefficient  $k_1^*$  for an sPTT fluid with  $\varepsilon = 0.25$  and  $De = 1$  : (a)  $u/u_2$ (b)  $\tau_{xy}/(3\eta_0 u_2/H_2)$  and (c)  $N_1/(3\eta_0 u_2/H_2)$ .

thank FCT for financial support through the scholarships SFRH/BD/37586/2007 and SFRH/BPD/75436/2010, respectively.



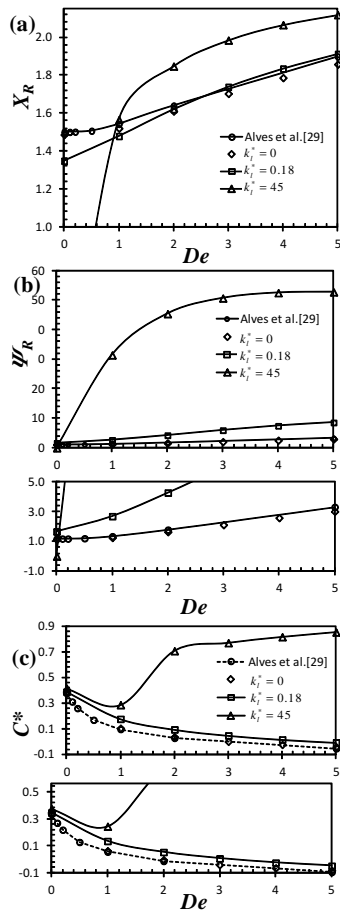


Figure 7.15: Variation of the vortex dimension  $X_R$  (a), vortex intensity  $\Psi_R$ (b) and the Couette correction  $C$  (c) for three different values of the slip coefficient:  $k_l^* = 0$  ,  $k_l^* = 0.18$  and  $k_l^* = 45$  (the lines are only a guide to the eye and the reference Alves et al. ? refers to no-slip case).



## THE INFLUENCE OF SLIP ON VISCOELASTIC FLUID FLOW THROUGH AN EXPANSION

---

### Abstract<sup>1</sup>

*In this work we present a systematic numerical investigation of the 1:4 planar expansion creeping flow for a Newtonian and a viscoelastic fluid modeled by the simplified Phan-Thien–Tanner (sPTT) constitutive equations and under the influence of slip boundary conditions. The linear and nonlinear Navier slip laws were considered with the dimensionless slip coefficient  $k_1^*$  varying in the range  $[0, 4500]$  and the slip exponents  $m = 0.5, 1$  and  $2$ . The simulations were carried out for creeping flow (we used a Reynolds number of  $0.001$ ) with different Deborah numbers,  $De = \lambda U/H = 0, 1, 2, 3, 4, 5, 10, 50$  and  $100$ . Convergence could not be achieved for higher values of the Deborah number, specially for large values of the slip coefficient, due to the large stress gradients near the singularity point. The increase of slip velocity leads to the vortex suppression for all  $De$ . The results are intensively investigated for low values of Deborah number,  $De = 0, 1, 2, 3, 4$  and  $5$ , while for the remaining  $De$  the main features are only shown for specific values of the slip coefficient.*

### 8.1 INTRODUCTION

The incompressible laminar flow in a symmetric plane sudden expansion is an intriguing benchmark problem. Although the geometry is rather simple, the resulting flows are dynamically complex, depending on several factors such as the inlet boundary conditions, the Reynolds ( $Re$ ) and Deborah ( $De$ ) numbers and the length of the inlet channel. This geometry is found in several industrial and biomedical processes and injection molding of polymer melts. In order to better understand this problem, several studies have been done leading to new results and improved knowledge of the expansion flow dynamics for both Newtonian and non-Newtonian fluids.

Halmos and Boger (1975, 1976) present an experimental and numerical study of flows of viscoelastic polymer solutions flows through an abrupt expansion. They found good agreement between the experimental results obtained for polymers melts and the numerical simulations performed with a power-law model. Townsend and Walters (1994) and (Baloch et al., 1996) both used the PTT model (Phan-Thien and Tanner, 1977) to compare their numerical results with the experi-

---

<sup>1</sup> L.L. Ferrás, A.M. Afonso, J.M. Nóbrega, M.A. Alves, F.T. Pinho (2012), The Influence of Slip Velocity on the Newtonian and Viscoelastic Fluid Flow Through an Abrupt 1:4 Expansion, to be submitted to *Journal of Non-Newtonian Fluid Mechanics*.

mental results obtained by (Townsend and Walters, 1994). In all these studies the conclusions were unanimous: viscoelasticity suppresses the secondary flows that appear at the corner, and this is justified with some kind of “extrudate swell” phenomenon that occurs to the main flow upon entry to the expansion (the fluid releases some of the stored energy resulting in the expansion of the main flow and the compression of the recirculation region). More recently (Poole et al., 2007) provided a numerical study of the 1:3 two dimensional expansion flow for the upper-convected Maxwell (UCM), Oldroyd-B and PTT models. They found that the previous results published in the literature by (Darwish et al., 1992) and (Missirlis et al., 1998) were only qualitatively correct because of the poor mesh refinement used. In (Poole et al., 2007) the degree of recirculation suppression is much weaker than suggested previously and for high Deborah numbers a significant recirculation region still exists.

The study of flow bifurcations in fluid mechanics has also received considerable interest as it enables a better understanding of the problems of stability and transition to turbulent flow. For this specific topic, experimental results are given in the work of (Durst et al., 1974) and (Cherdron et al., 1978) whereas numerical predictions, as well as a good review of the literature regarding the bifurcation phenomena for Newtonian and non-Newtonian fluids, can be found in the work of (Wahba, 2007).

For the bifurcation phenomenon in viscoelastic fluids we highlight the works of (Rocha et al., 2007), where a numerical investigation of viscoelastic flows (FENE–CR constitutive model) through a planar 1:4 sudden expansion is presented. They found that the viscoelasticity stabilizes the flow and results in symmetric flow patterns up to a Reynolds number of about 46 . Poole et al. (2005) arrived at similar conclusions based on experimental results obtained for the laminar flow of a viscoelastic liquid through a symmetrical plane sudden expansion preceded by a gradual contraction from a square duct. Therefore, because creeping flow conditions are employed in this work, we assume the existence of symmetry.

For turbulent flows there is the experimental work of (Abbott and Kline, 1962), about the subsonic turbulent flow over a single and double backward facing steps, and the experimental works of (Escudier et al., 2002), (Poole and Escudier, 2003, 2004) and (Dales et al., 2005).

All the previous works were done either for Newtonian or non-Newtonian inelastic and viscoelastic fluids. The viscoelastic fluids usually present a more rheologic and dynamic complex behavior when compared to the Newtonian fluids, and one of these complex features is the ability for the fluid to slip (Ramamurthy, 1986; Dealy and Kim, 2005; Kalika and Denn, 1987; Denn, 2001) along the wall, found in some polymer melt flows. However, in the literature we could not find the influence of slip boundary conditions on the fluid flow behavior through an abrupt expansion, and this feature is very

important in polymer processing where contraction and expansion flows are often encountered. For this reason, this work presents a numerical study looking at the influence of slip velocity (linear and nonlinear Navier slip boundary conditions) on the flow through an abrupt 1:4 expansion for a large range of dimensionless slip coefficients  $k_l^* \in [0, 4500]$  and Deborah numbers,  $De \in \{0, 1, 2, 3, 4, 5, 10, 50, 100\}$ . We study both Newtonian and non-Newtonian fluids modeled by the simplified PTT model, and we present a detailed study of the flow characteristics such as the influence of the slip velocity on the vortex dimensions, vortex intensity and Couette correction.

In our calculations there is no need for any direct relaxation of the slip velocity. Instead, we use an efficient procedure, proposed in (Ferrás et al., 2012d), that calculates the slip velocity along iterations, adjusting the calculations depending the proximity to the final solution. When convergence is eminent the calculated slip velocity converges to the correct slip velocity while far from the solution the new procedure guarantees that the slip velocity is always smaller than the velocity at the center of the adjacent control volume, an important requirement for convergence since divergence occurs when this necessary condition for continuity (between the boundary and the bulk data) is not satisfied.

In contrast to the contraction flows (Alves et al., 2003b; Ferrás et al., 2012a; Afonso et al., 2011b) it was possible to obtain convergence for higher values of the Deborah number, where we found the complete suppression of recirculation for high slip coefficients. Based on the fact that wall slip reduces both the amount of extrudate swell and the critical Deborah number, (Phan-Thien, 1988) we confirm the correctness of the previous proposed hypothesis for the suppression of recirculation (Townsend and Walters, 1994; Baloch et al., 1996).

This introduction is preceded by subsection 2, where the governing equations are presented together with the linear and nonlinear Navier slip boundary conditions. In subsection 3 we briefly describe the solver used to couple velocity, pressure and the slip boundary condition and we also describe the geometry and the characteristics of the flow. In subsection 4 the results obtained for the Newtonian fluid case  $De = 0$  are discussed, while the remaining Deborah numbers studied here are treated in subsection 5. The closure of the paper is made with the conclusions in subsection 6.

## 8.2 GOVERNING EQUATIONS

The governing equations for the laminar and incompressible fluid flow are those expressing the conservation of mass,

$$\nabla \cdot \mathbf{u} = 0 \quad (8.1)$$

and momentum,

$$\rho \frac{\partial \mathbf{u}}{\partial t} + \rho \nabla \cdot \mathbf{u} \mathbf{u} = -\nabla p + \nabla \cdot \boldsymbol{\tau} \quad (8.2)$$

Additionally, an appropriate constitutive relation for the the extra stress tensor  $\boldsymbol{\tau}$  is used. The stress tensor ( $\boldsymbol{\tau} = \boldsymbol{\tau}_s + \boldsymbol{\tau}_p$ ) is split into a Newtonian solvent contribution,  $\boldsymbol{\tau}_s$ ,

$$\boldsymbol{\tau}_s = \eta_s \left( \nabla \mathbf{u} + (\nabla \mathbf{u})^T \right) \quad (8.3)$$

and a polymer contribution,  $\boldsymbol{\tau}_p$ , (for a Newtonian fluid  $\boldsymbol{\tau} = \boldsymbol{\tau}_s$ ) that is given here by a widely used model, the simplified Phan-Thien and Tanner equation (sPTT) (Phan-Thien and Tanner, 1977),

$$\begin{aligned} f(tr\boldsymbol{\tau}_p) \boldsymbol{\tau}_p + \lambda \left( \frac{\partial \boldsymbol{\tau}_p}{\partial t} + \mathbf{u} \cdot \nabla \boldsymbol{\tau}_p - \left[ (\nabla \mathbf{u})^T \cdot \boldsymbol{\tau}_p + \boldsymbol{\tau}_p \cdot \nabla \mathbf{u} \right] \right) = \\ = \eta_p \left( \nabla \mathbf{u} + (\nabla \mathbf{u})^T \right) \end{aligned} \quad (8.4)$$

For the function  $f(tr\boldsymbol{\tau}_p)$  we use its linear form,

$$f(tr\boldsymbol{\tau}) = 1 + \frac{\varepsilon \lambda}{\eta_p} tr(\boldsymbol{\tau}_p) \quad (8.5)$$

In Eqs. (8.1)-(8.5),  $\mathbf{u}$  is the velocity vector,  $p$  is the pressure,  $\boldsymbol{\tau} = \boldsymbol{\tau}_s + \boldsymbol{\tau}_p$  is the extra stress tensor,  $\eta_s$  and  $\eta_p$  are the solvent and zero shear polymer viscosity contributions, respectively,  $\lambda$  is the relaxation time and  $\varepsilon$  is the extensibility parameter related to the elongational behavior of the PTT fluid.

In order to consider the possibility of slip at the boundary wall we use the linear ( $m = 1$ ) (Navier, 1822) and nonlinear Navier slip boundary conditions ( $m \neq 1$ ) (Schowalter, 1988),

$$\|\mathbf{u}_{ws}\| = k \|\boldsymbol{\tau}_w\|^m \quad \text{and} \quad \mathbf{u}_{ws} = -k \|\boldsymbol{\tau}_w\|^m \frac{\boldsymbol{\tau}_w}{\|\boldsymbol{\tau}_w\|^{-1}} \quad (8.6)$$

where the parameter  $k_l \in [0, +\infty)$  is the slip coefficient (it will depend on the material employed and on the flow conditions and is normally computed through the adjustment of experimental observations) that allows to control the amount of slip in the simulation (for  $m = 1$  the slip coefficient can also be interpreted as the slip length). The second condition in Eq. (8.6) refers to the fact that the slip velocity vector  $\mathbf{u}_{ws}$  (the subscript “ws” stands for “wall slip”) points in the tangent stress  $\boldsymbol{\tau}_w$  (the subscript “w” stands for “wall”) opposite direction.

### 8.3 NUMERICAL PROCEDURE AND GEOMETRY

The system of differential equations, Eqs. (8.1-8.6), is solved with a finite volume method code (see (Oliveira et al., 1998)), using the SIMPLEC method of (Van Doormaal and Raithby, 1984) to couple velocity

and pressure fields. For the implementation of the slip boundary conditions we use two slightly different methods, one for the linear Navier slip law and the other for the nonlinear Navier slip law. In both cases we assume the flow near the wall is mostly viscometric so that the tangent stress at the wall can be approximated by (Azaiez et al., 1996),

$$\boldsymbol{\tau}_w = \eta(\dot{\gamma})_w \left. \frac{d\mathbf{u}}{dn} \right|_w \quad (8.7)$$

where  $\eta(\dot{\gamma})_w = \eta_s + \frac{\eta_p}{1 + (\alpha^{-1})^2 / 3\alpha}$ ,  $\alpha \equiv (\theta + \sqrt{\theta^2 - 1})^{1/3}$ ,  $\theta \equiv 1 + 27\epsilon(\lambda\dot{\gamma})_w^2$  is the viscosity as a function of the shear rate,  $\dot{\gamma}$ , evaluated at the wall, and  $\frac{d\mathbf{u}}{dn}$  is the velocity derivative in the wall normal direction.

Assuming Cartesian coordinates, orthogonal meshes and a one-sided first order approximation for the velocity derivative, the relationship between the slip velocity and the tangent stress vector can be written as,

$$u_{wsj} = k_{nl} \left( \eta(\dot{\gamma})_w \frac{u_{pj} - u_{wsj}}{\delta n} \right)^m \quad j = 1, 2 \quad \text{and} \quad u_{pj} > u_{wsj} \quad (8.8)$$

where  $(u_{ws1}; u_{ws2})$  are the components of the slip velocity vector  $\mathbf{u}_{ws}$ ,  $u_{pj}$  is the velocity at the center of the adjacent computational cell and  $\delta n$  is the distance between the center (P) of the adjacent cell and the wall boundary (see Fig. 8.1).

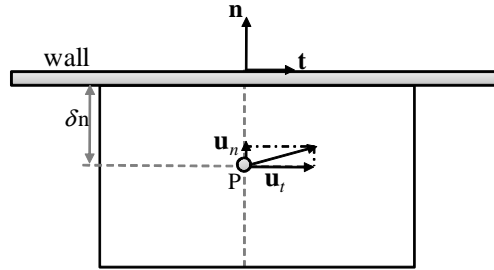


Figure 8.1: Schematic of a computational cell.

Let  $i$  represent one iteration of the SIMPLE method. For the implementation of the slip boundary condition two different linearizations were used, depending on the exponent  $m$ . For  $m = 1$  we assume that only the slip velocity variable comes from the present iteration,  $i$ , thus allowing to obtain the following relationship between  $u_{ws}^i$  and  $u_p^{i-1}$ ,

$$u_{ws}^i = k_l \left( -\eta(\dot{\gamma})_w^{i-1} \frac{(u_{ws}^i - u_p^{i-1})}{\Delta y_f} \right) = \frac{a}{a+1} u_p^{i-1} \quad \text{with} \quad a = k_l \left( -\frac{\eta(\dot{\gamma})_w^{i-1}}{\Delta y_f} \right) \quad (8.9)$$

For  $m \neq 1$  the discretized form of the nonlinear Navier slip law can be linearized assuming that only the slip velocity of the linear part comes from the actual iteration ( $i$ ) as,

$$u_{ws}^i = k_{nl} \left( \frac{\eta(\dot{\gamma})_w^{i-1}}{\Delta y_f} \right)^m \left( u_P^{i-1} - u_{ws}^i \right) \left( u_P^{i-1} - u_{ws}^{i-1} \right)^{m-1} \quad (8.10)$$

leading to,

$$u_{ws}^i = \frac{l}{1+l} u_P^{i-1} \quad \text{with} \quad l = k_{nl} \left( \frac{\eta(\dot{\gamma})_w^{i-1}}{\Delta y_f} \right)^m \left( u_P^{i-1} - u_{ws}^{i-1} \right)^{m-1}. \quad (8.11)$$

The main feature of this method is that the slip velocity is always smaller than the velocity at the center of the adjacent computational cell, a required condition for convergence. To solve the system of equations we use the following iterative procedure (Ferrás et al., 2012d):

- (1) Set the boundary conditions, the initial velocity and pressure fields;
- (2) Solve the stress equations for the non-Newtonian model;
- (3) Compute the slip velocity with the discretized slip model Eqs. (8.9) or (8.11).
- (4) Solve the linearized momentum equations;
- (5) Solve the pressure correction equation;
- (6) Correct velocity and pressure fields;
- (7) Check for convergence in the system of equations residuals;
- (8) If convergence is not achieved proceed to step 2.

In this work we are interested only in the stationary solution, so the time evolution is fictitious. Each time step represents one iteration  $i$ . With this method there is no need for direct relaxation of the slip velocity and the computations are stable.

A schematic of the 1:4 expansion geometry is given in Fig. 8.2. We assume the flow is two-dimensional and impose symmetry at the centerline. At the inlet, a uniform velocity profile  $U$  is imposed together with null stress components. To perform the numerical simulations for the expansion flow we built three different meshes ME1, ME2 and ME3 (cf. Table 8.1),



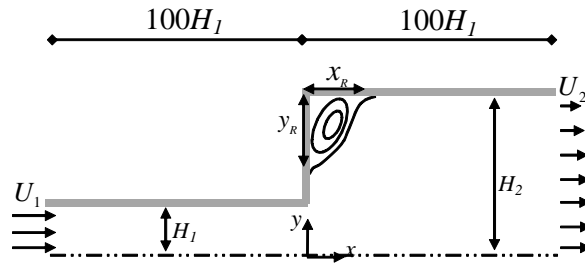


Figure 8.2: Schematic of the expansion geometry.

Table 8.1: Mesh Characteristics for ME1, ME2, ME3.

Zone	ME1		ME2		ME3	
	$n_x$	$n_y$	$n_x$	$n_y$	$n_x$	$n_y$
1	15	36	30	72	60	144
2	87	36	174	72	348	144
3	87	36	174	72	348	144
4	87	47	174	94	348	188
5	87	18	174	36	348	72
6	15	36	30	72	60	144
7	15	47	30	94	60	188
8	15	18	30	36	60	72
NC	13974		55896		223584	
$\Delta x_{\min}/H_1$	0.01		0.005		0.002	
Zones					5	8
					4	7
	1	2	3	6		

with consistent consecutive refinement, in the sense that the number of cells was doubled in each direction, with mesh spacing being approximately halved. This way we can measure the accuracy of our results by using Richardson’s extrapolation technique (Richardson, 1910; Richardson and Gaunt, 1927). The computational domain was divided into eight blocks, the notation  $n_x$  and  $n_y$  is used to represent the number of cells in the  $x$  and  $y$  directions, respectively. The mesh data are provided in Table 8.1.

We performed a large number of simulations, mostly because of the large range of slip coefficients used (for each  $De$  we used 15 different slip coefficients) to capture the influence of slip velocity on the flow behavior. Most results shown here were obtained for mesh ME2. Mesh ME3 was also used to test the accuracy of the method but only for a limited number of simulations, because of the high computation times and convergence issues.

The simulations were performed for the sPTT model at a constant Reynolds number,  $Re = \rho U_1 H_1 / \eta_0 = 0.001$ , and a varying Deborah number  $De = \lambda U_1 / H_1$  ( $De = 0, 1, 2, 3, 4, 5, 10, 50$  and  $100$ ) with  $\varepsilon =$

0.25 and viscosity ratio  $\beta = \frac{\eta_s}{\eta_0} = \frac{\eta_s}{\eta_s + \eta_p} = \frac{1}{9}$ . Several values of the normalized slip coefficient,  $k_i^* = k_i \eta_0 / H_1$ , are used.

The numerical results were analyzed in terms of the vortex sizes  $X_R = x_R / H_1$  and  $Y_R = y_R / H_1$  (cf. Fig. 8.2), the vortex intensity, defined here as the recirculating flow rate inside the vortex normalized by the flow rate in the entrance channel,  $U_1 H_1$ :

$$\Psi_R = \frac{\psi_R - U_1 H_1}{U_1 H_1} \times 10^3 \quad (8.12)$$

where  $\psi_R$  is the streamfunction value at the vortex center (we assume  $\psi_R = 0$  at the centerline,  $y = 0$ ), and also the Couette correction given by,

$$C = \frac{\Delta p - \Delta p_{1FD} - \Delta p_{2FD}}{2\tau_w} \quad (8.13)$$

where  $\Delta p$  represents the pressure drop between two points located far away from the expansion plane, one upstream and another downstream of the expansion plane,  $\Delta p_{1FD}$ ,  $\Delta p_{2FD}$  the pressure drop for the fully developed Poiseuille flow obtained for the entry and exit channels, with widths  $H_1$  and  $H_2$ , respectively, and  $\tau_w$  is the wall shear stress encompassing both the solvent and polymer contributions (for fully-developed flow in the entrance channel).

Additional plots are also presented, such as the variations of velocity and stresses along the centerline, streamlines, together with the characterization of the flow type parameter,  $\zeta$ , defined as (Lee et al., 2007):

$$\zeta = \frac{|\mathbf{D}| - |\mathbf{\Omega}|}{|\mathbf{D}| + |\mathbf{\Omega}|} \quad (8.14)$$

where  $|\mathbf{D}|$  and  $|\mathbf{\Omega}|$  represent the magnitudes of the rate of deformation and vorticity tensors, respectively

$$\mathbf{D} = \frac{1}{2} [\nabla \mathbf{u} + (\nabla \mathbf{u})^T], \quad \mathbf{\Omega} = \frac{1}{2} [\nabla \mathbf{u} - (\nabla \mathbf{u})^T], \quad (8.15)$$

which are given by,

$$\begin{aligned} |\mathbf{D}| &= \sqrt{\frac{1}{2} (\mathbf{D} : \mathbf{D}^T)} = \sqrt{\frac{1}{2} \sum_i \sum_j D_{ij}^2} \\ |\mathbf{\Omega}| &= \sqrt{\frac{1}{2} (\mathbf{\Omega} : \mathbf{\Omega}^T)} = \sqrt{\frac{1}{2} \sum_i \sum_j \Omega_{ij}^2}. \end{aligned} \quad (8.16)$$

The flow type parameter varies from  $-1$ , which corresponds to solid-like rotation, up to  $1$ , for pure extensional flow. Pure shear flow is characterized by  $\zeta = 0$ .

## 8.4 RESULTS AND DISCUSSION

## 8.4.1 Newtonian Fluids

For Newtonian fluids ( $De = 0$ ) we observed that the axial vortex dimension,  $X_R$ , presents a non monotonic behaviour with the slip coefficient,  $k_l^*$ , while the vortex intensity,  $\Psi_R$ , decreases with  $k_l^*$ , as shown in Fig. 8.3. This means that for  $k_l^* > 0.45$ , the vortex is at the

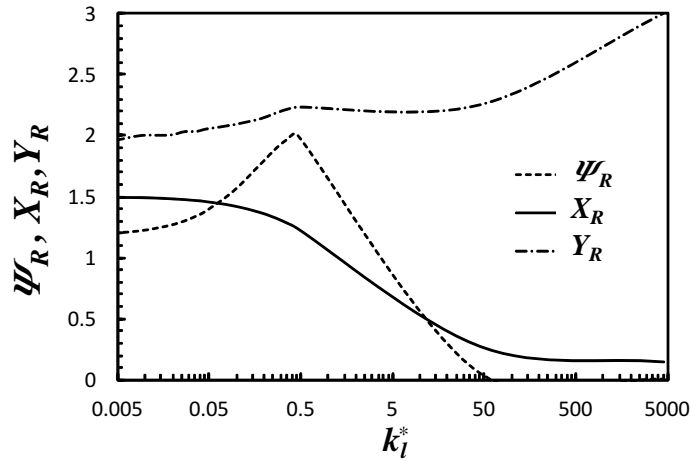


Figure 8.3: Variation of the vortex dimension,  $X_R$  and  $Y_R$ , and vortex intensity,  $\Psi_R$ , with  $k_l^*$  for a Newtonian fluid ( $De = 0$ ).

same time reducing his size ( $X_R$ ) and intensity. This is also clear in Fig. 8.4, where the streamlines are superimposed on contour plots of the flow type parameter,  $\xi$ , showing that the increase of the slip coefficient leads to an increase of  $Y_R$  and a decrease of  $X_R$ . For small slip coefficients only  $Y_R$  increases and  $X_R$  only experiences small changes. For  $k_l^* > 0.45$  significant changes in the vortex dimensions are seen,  $X_R$  is abruptly reduced while  $Y_R$  is of the size of the corner wall aligned with the  $y$  direction. This is in contradiction with the behaviour observed for viscoelastic fluids (see Section 8.4.2), where the vortex does not disappear for high slip velocity. We can also observe, in Fig. 8.4, a region of shear flow located near the walls for no-slip velocity and low slip coefficients ( $k_l^* = 0.0045$  and  $k_l^* = 0.045$ ), while for  $k_l^* \geq 0.45$  a region of extensional flow develops near the expansion corner, which spreads over the domain with the increase of  $k_l^*$ , thus reducing the vortex size.

We also plotted the variation of the dimensionless stream wise velocity component along the channel for  $y/H_1 = 0.99$  (Fig. 8.5(a)) and  $y/H_1 = 0$  (Fig. 8.5(b)). For both cases we see that the slip velocity smoothes the velocity profile across the vicinity of the singular point. Notice that for high slip coefficients there is also an abrupt change in the velocity profile, especially for the case  $y/H_1 = 0.99$ , where the normalized velocity is almost unitary (plug flow) in the smaller

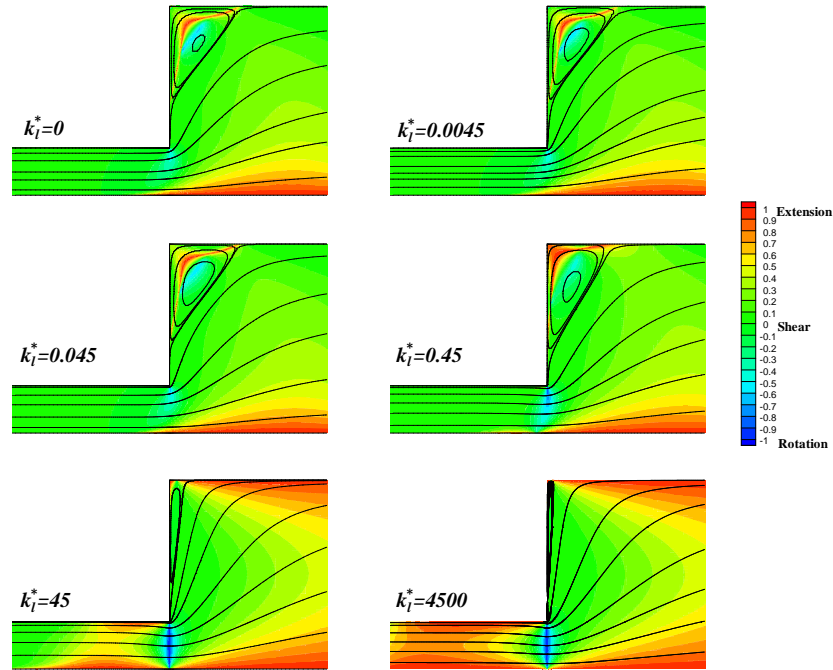


Figure 8.4: Streamlines and flow type  $\zeta$  for a Newtonian fluid ( $De = 0$ ) and different values of the slip coefficient  $k_l^*$ .

channel and then drastically reduces when passing to the expansion zone.

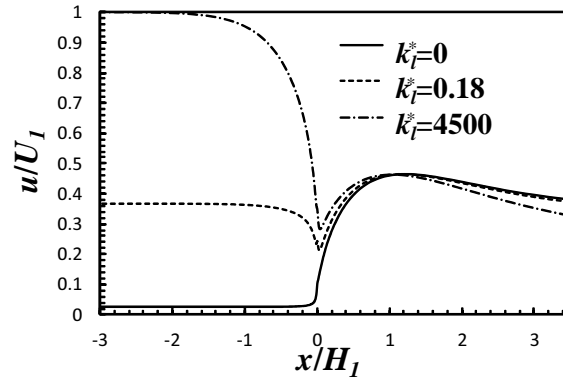
#### 8.4.2 Viscoelastic fluids

##### 8.4.2.1 Effect of elasticity and slip

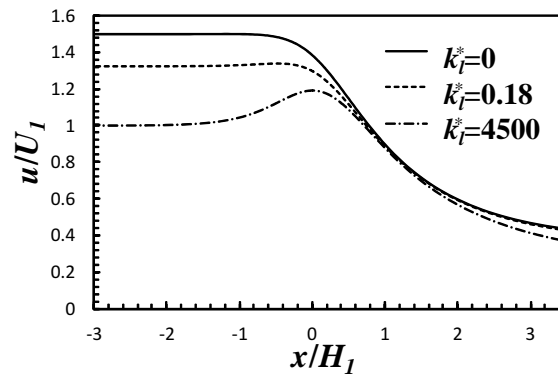
In addition to Newtonian fluid limit ( $De = 0$ ) the 4:1 expansion flow was also simulated for  $De = 1, 2, 3, 4$  and 5 using a vast range of slip coefficients and for  $De = 10, 50$  and 100 using only two different slip coefficients, due to the significant computational times required for these cases.

Fig. 8.6 presents the variation of  $X_R$  and  $\Psi_R$  with  $De$ , for several slip coefficients,  $k_l^*$ . We see that both properties decrease with  $De$  and  $k_l^*$ , with the vortex vanishing for smaller values of the slip coefficient as elasticity increases. These results can also be seen in Tables 8.2 and 8.3 (for the case  $De = 1$ ) where the accuracy of the results was assessed with the Richardson extrapolation technique for three different values of the slip coefficient. The variations of  $X_R$  and  $\Psi_R$  for higher values of  $De$  are also shown for a constant slip coefficient  $k_l^* = 0.09$ . We see that  $\Psi_R$  decreases with  $De$  while  $X_R$  presents a non-monotonic behaviour, in agreement with the conclusions of (Poole et al., 2007).

In Fig. 8.7 we show the streamlines superimposed on contour plots of  $\zeta$  for different values of the slip coefficient and two different values



(a)

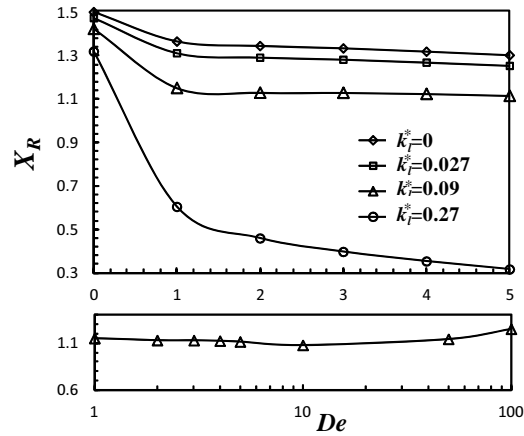


(b)

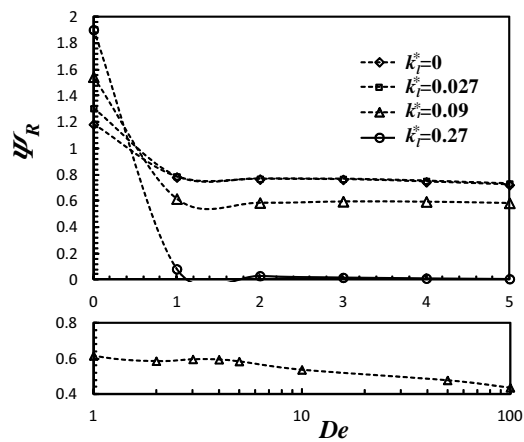
Figure 8.5: Dimensionless axial velocity profiles along the channel for a Newtonian fluid ( $De = 0$ ) (a)  $y/H_1 = 0.99$  (b)  $y/H_1 = 0$ .

of the Deborah number,  $De = 1$  and  $5$ . Contrarily to the Newtonian case the vortex totally disappears with the increase of the slip velocity, and considerable changes in the vortex dimensions appear first for the viscoelastic case, especially for high Deborah numbers ( $De = 5$ ). Notice also that for  $De = 5$  we obtain a wider region of extensional flow near the centerplane for all slip coefficients used, which can be justified by the higher relaxation time of the fluid that delays its deceleration in the expansion region, thus increasing the area where the flow is extensionally dominant. The overall conclusion, based on these figures, is that the vortex dimensions decrease with the increase of elasticity and slip intensity.

Regarding the Couette correction,  $C$ , Figs. 8.8 show the variation of  $C$  and  $C^*$  with  $De$ , for different values of the slip coefficient. The variable  $C^*$  represents the Couette correction normalized with the wall tangent stress,  $\tau_w$ , obtained for the case of no-slip velocity at the walls. This normalization is used because when  $k_l^*$  is very large, the value of  $\tau_w$  vanishes, leading to unbounded values of  $C$ . For a Newtonian fluid our results match the results obtained by (Poole et al., 2009). In Tables 8.4 (a) and (b) we can also see the Couette correction  $C$  and  $C^*$



(a)



(b)

Figure 8.6: Variation of (a) vortex dimension,  $X_R$ , and (b) vortex intensity,  $\Psi_R$ , with  $De$ , for different values of  $k_l^*$ .

obtained for different slip coefficients at  $De = 1$ . For the viscoelastic fluids, we can observe that both  $C$  and  $C^*$ , increase with  $De$ , as also observed in the data for the 1:3 expansion flow (Poole et al., 2007). The Couette correction increases with  $k_l^*$  (a side effect of the chosen normalization) while the alternative Couette correction,  $C^*$ , decreases. This means that, contrarily to the behaviour observed in data obtained by (Ferrás et al., 2012a) for the 4:1 contraction flow, slip reduces  $C^*$ .

The dimensionless axial velocity profiles along the channel at two different positions  $y/H_1 = 0$  and  $y/H_1 = 0.99$ , were studied for two different Deborah numbers,  $De = 1$  and  $5$  as shown in Fig. 8.9. For both  $De$ , the velocity near the wall increases with the slip coefficient,  $k_l^*$ , and higher velocities are attained for the smaller Deborah number,  $De = 1$ . This is more notorious for intermediate values of  $k_l^*$  and at the smaller channel. When the fluid is at the wider channel, the influence of the slip boundary condition is weakened by the larger distance

Table 8.2: Variation of vortex dimension  $Xr$  with the slip coefficient  $k_l^*$  for  $De = 1$ .

$k_l^*$	ME1	ME2	ME3	ext. $X_R$	Percent error
0	1.3625	1.3664	1.3672	1.3673	0.012
0.0045		1.3586			
0.009	1.3470	1.3497	1.3502	1.3503	0.007
0.018		1.3319			
0.027		1.3126			
0.036	1.2872	1.2920	1.2928	1.2929	0.01
0.045		1.2704			
0.09		1.1527			
0.18	0.8723	0.8911			
0.27		0.6047			
0.36		0.2656			
0.45	0	0			
45	0	0			
4500	0	0			

Table 8.3: Variation of the vortex intensity  $\Psi_R$  with the slip coefficient  $k_l^*$  for  $De = 1$ .

$k_l^*$	ME1	ME2	ME3	ext. $\Psi_R$	Percent error
0	0.7775	0.7816	0.7827	0.7831	0.05
0.0045		0.7874			
0.009	0.7871	0.7899	0.7903	0.7904	0.01
0.018		0.7922			
0.027		0.7863			
0.036	0.7687	0.7747	0.7755	0.7756	0.014
0.045		0.7561			
0.09		0.6169			
0.18	0.2716	0.2936			
0.27		0.0824			
0.36		0.0044			
0.45	0	0			
45	0	0			
4500	0	0			

between the centerplane and the wall, and the velocity profiles for the different  $De$  and  $k_l^*$  vary from each other in a smaller range.

In order to see the influence of the slip exponent,  $m$ , on the flow characteristics, we performed simulations for two different slip exponents, six different slip coefficients and a constant  $De = 1$  (see Fig. 8.10). We can observe that for  $m = 0.5$  the influence of  $k_l^*$  on the flow is small, while for  $m = 1.5$  the influence of  $k_l^*$  is enhanced. Notice that for the case  $k_l^* = 0.36$  and  $m = 1.5$  we have an extensional flow near the vortex corner that smears the vortex, while for the case  $m = 0.5$  a rotation flow is still present indicating the existence of a vortex. This result is the expected since the increase of the slip law exponent enhances the slip velocity.

#### 8.4.2.2 The vortex size reduction

In order to try to explain the vortex size reduction and its link to the extrudate swell phenomenon, we performed simulations assuming slip velocity only at the entrance channel walls. With this we wanted to decrease the extrudate swell when the flow passes from the narrow

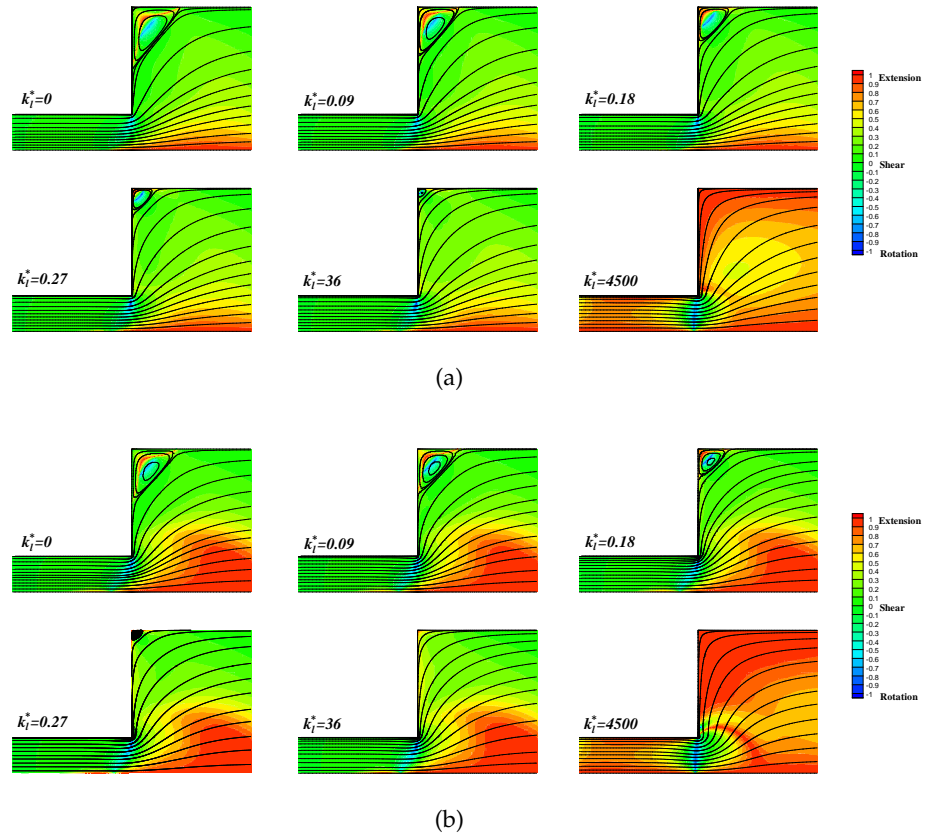


Figure 8.7: Streamlines and flow type,  $\zeta$ , for different values of the slip coefficient  $k_i^*$ . (a)  $De = 1$  (b)  $De = 5$ .

channel to the expansion zone. We found that when the inlet channel has slip the vortex dimensions decrease, as observed in the comparison shown in Fig. 8.11. For the case of no-slip velocity at the walls (c.f. Fig. 8.12) we can observe a region of shear flow near the walls, in deep contrast with the flow with high slip velocity where the flow is mainly extensional, thus explaining the vortex suppression. When slip is only present at the inlet channel walls, we can observe a region of rotation flow near the singularity point due to the passage from high slip to no-slip, and also an extensional flow approaching the singularity point, that increases with elasticity.

The dimensionless stress contour plots are shown in Fig. 8.13 and the variation of the stresses along the channel for  $y/H_1 = 0.99$  is shown in Fig. 8.14. We can see that the presence of wall slip in the entrance channel leads to a sudden increase of the axial polymer normal stress  $\tau_{xx}$  near the singular point (cf. Fig. 8.14(a) and Fig. 8.13). This results in compression of the flow in the  $x$  direction, by an enhanced curvature of the velocity streamlines. As expected, the shear stress,  $\tau_{xy}$ , is almost null in the entrance channel because of the high slip velocity attained (see Fig. 8.14(b) and Fig. 8.13). For  $\tau_{yy}$  we can observe that it increases



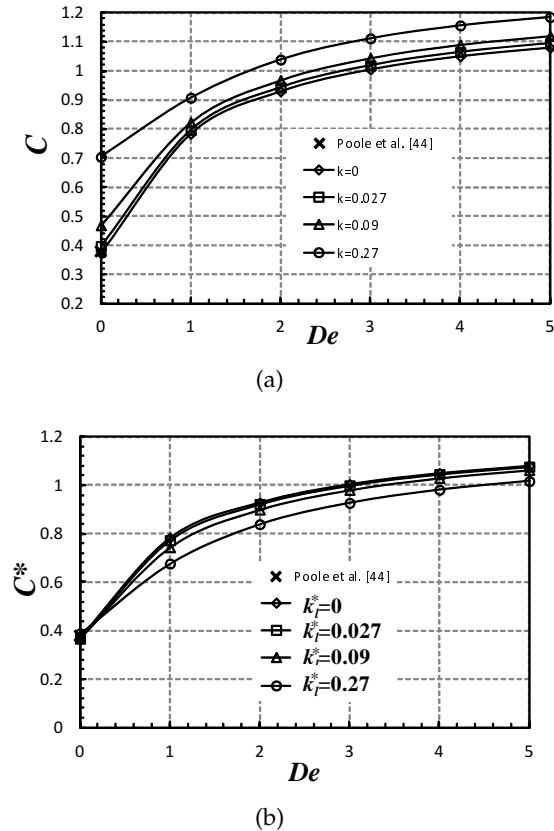


Figure 8.8: Couette correction,  $C$ , as function of  $De$ . (a)  $C$  (b)  $C^*$ .

(for the case with slip velocity) before the fluid reaches the singularity point (see Fig.8.14(c) and Fig. 8.13), followed by a smooth transition to a fully developed state. In the expansion zone we obtain higher values of  $\tau_{yy}$  for the no-slip case, and this leads to an increase of the vortex size in the presence of slip.

## 8.5 CONCLUSIONS

Simulations were performed to evaluate the influence of the slip boundary condition on the 1:4 expansion flow of Newtonian and viscoelastic fluids. The presence of slip velocity leads to a reduction of the vortex size and intensity, together with the reduction of the Couette correction. The influence of the slip exponent on the flow was also studied and we found that a small slip exponent weakens the slip effect on the flow properties. Simulations with high slip velocity in the inlet channel and no slip in the outlet channel were performed which helped relate the vortex size reduction with the weakening of the transverse normal stress, i.e., with the weakening of the mechanism associated with extrudate swell. Consequently we found that the vortex size reduction is higher when the slip velocity in the inlet channel is higher.

Table 8.4: Variation of the Couette correction with  $k_l^*$  for  $De = 1$ . (a)  $C$  (b)  $C^*$ .

$k_l^*$	ME1	ME2	ME3	ext. $C$	Percent error
0	0.7851	0.7832	0.7826	0.7822	0.046
0.0045		0.7859			
0.009	0.7907	0.7883	0.7874	0.7867	0.084
0.018		0.7927			
0.027		0.7967			
0.036	0.8104	0.8006	0.7991	0.7989	0.034
0.045		0.8056			
0.09		0.8230			
0.18	0.8669	0.8627			
0.27		0.9075			
0.36		0.9574			
0.45	1.0152	1.0123			
45	47.2465	47.4563			
4500	4718.17	4736.24			

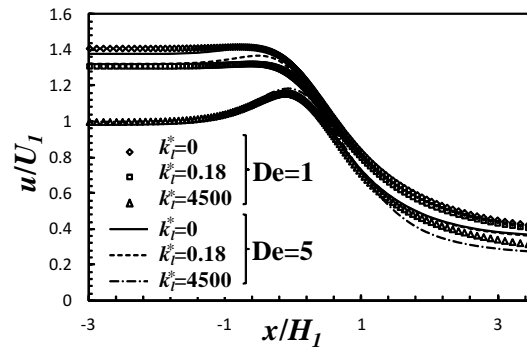
(a)

$k_l^*$	ME1	ME2	ME3	ext. $C^*$	Percent error
0	0.7851	0.7833	0.7826	0.7822	0.046
0.0045		0.7820			
0.009	0.7827	0.7804	0.7796	0.7867	0.084
0.018		0.7768			
0.027		0.7729			
0.036	0.7782	0.7688	0.7676	0.7674	0.026
0.045		0.7656			
0.09		0.7442			
0.18	0.7107	0.7072			
0.27		0.6767			
0.36		0.6518			
0.45	0.6334	0.6317			
45	0.5765	0.5747			
4500	0.5795	0.5778			

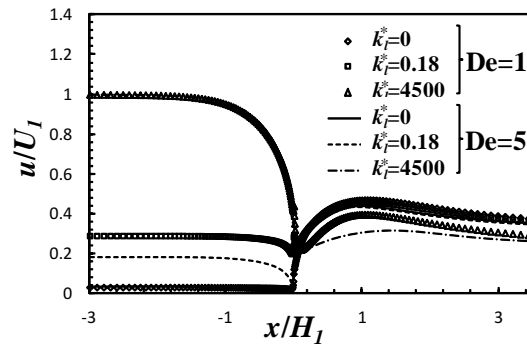
(b)

## ACKNOWLEDGEMENTS

The authors acknowledge funding from FEDER and Fundação para a Ciência e a Tecnologia (FCT), Portugal, through projects PTDC/EQU-FTT/70727/2006 and PTDC/EQU-FTT/113811/2009, and FEDER, via FCT, under the PEst-C/CTM/LA0025/2011 (Strategic Project - LA 25 - 2011-2012). LLF and AMA would like to thank FCT for financial support through scholarships SFRH/BD/37586/2007 and SFRH/BPD/75436/2010, respectively.

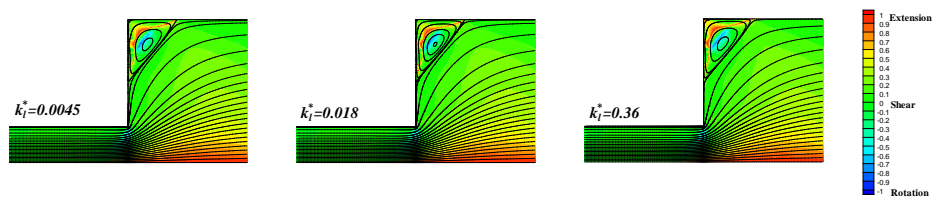


(a)

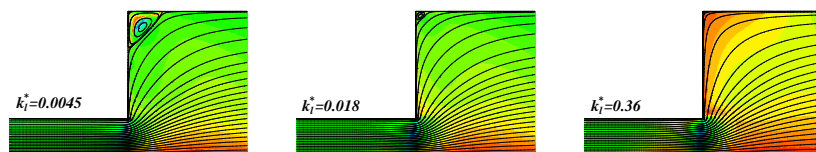


(b)

Figure 8.9: Dimensionless axial velocity profiles along the channel for  $De = 1$  and  $5$  and three different slip coefficients (a)  $y/H_1 = 0$  (b)  $y/H_1 = 0.99$ .



(a)



(b)

Figure 8.10: Streamlines and flow type  $\zeta$ , for the evolution of the vortex dimensions with the slip coefficient  $k_i^*$  for a constant  $De = 1$  and two different slip exponents: (a)  $m = 0.5$  (b)  $m = 1.5$ .

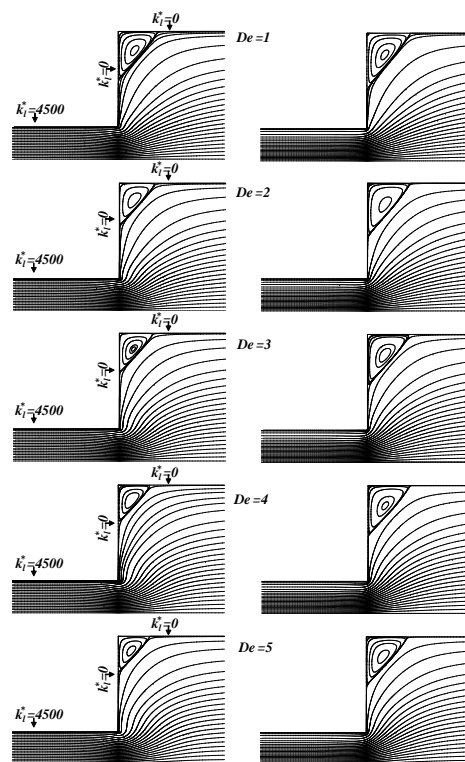
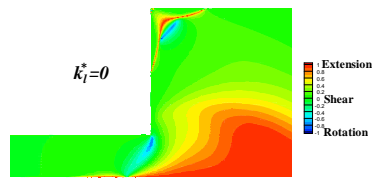
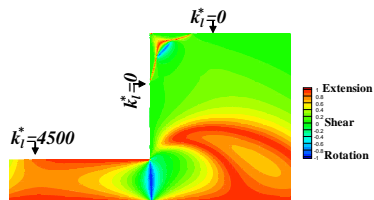


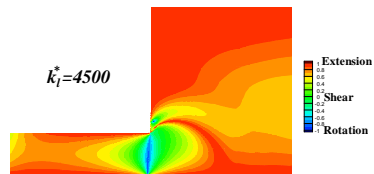
Figure 8.11: Streamlines for five different values of the  $De$  number: (a) slip velocity only in the entrance channel wall and (b) no-slip velocity.



(a)



(b)



(c)

Figure 8.12: Flow type,  $\zeta$ , for  $De = 5$  (a) no slip velocity (b) slip velocity in the entrance of the channel walls ( $k_l^* = 4500$ ) (c) slip velocity at all walls ( $k_l^* = 4500$ ).

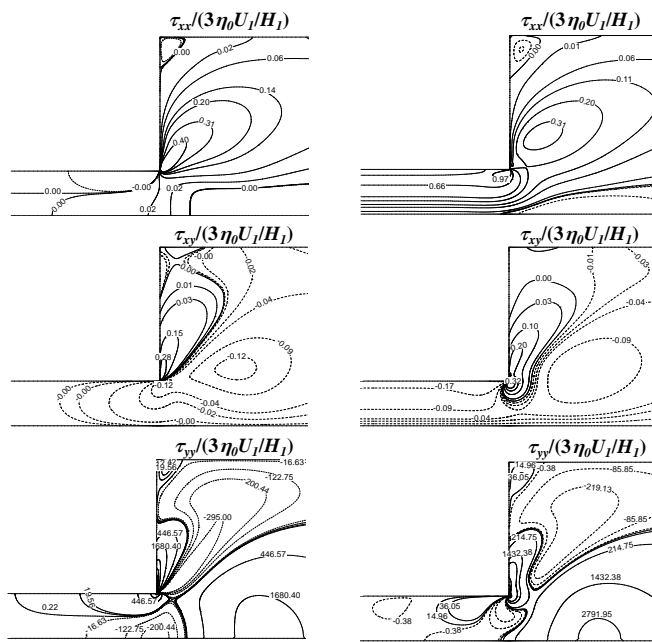
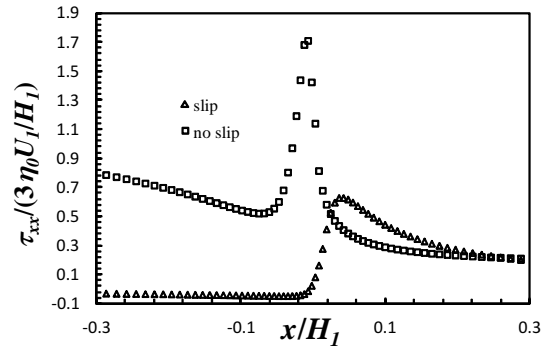
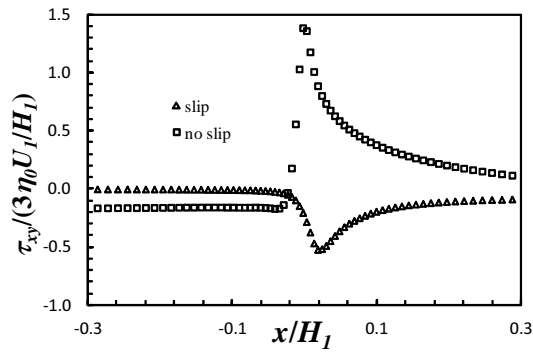


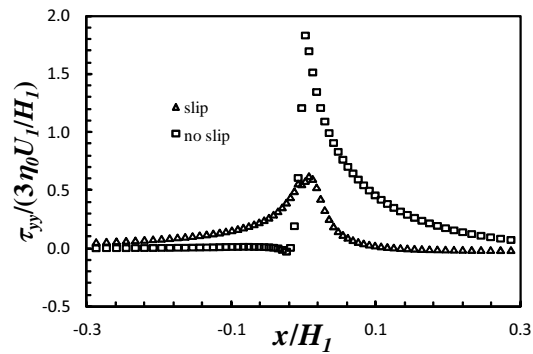
Figure 8.13: Contour plots for the dimensionless stress components near the singularity point, for  $De = 5$ : (a) slip velocity only in the entrance channel wall and (b) no-slip velocity.



(a)



(b)



(c)

Figure 8.14: Dimensionless stress profiles along the coordinate  $y/H_1 = 0.99$  at  $De = 5$  (a)  $\tau_{xx}$  (b)  $\tau_{xy}$  and (c)  $\tau_{yy}$ . Note that slip velocity is only considered in the entrance channel wall.





## DEVELOPMENT LENGTH OF NEWTONIAN FLUIDS UNDER THE INFLUENCE OF WALL SLIP

---

### Abstract<sup>1</sup>

*This technical brief presents a numerical study regarding the required development length ( $\mathcal{L} = L_{fd}/H$ ) to reach fully-developed flow conditions at the entrance of a planar channel for Newtonian fluids under the influence of slip boundary conditions. The linear Navier slip law is used with the dimensionless slip coefficient  $\bar{k}_l = k_l (\frac{\mu}{H})$  varying in the range  $0 < \bar{k}_l \leq 1$ . The simulations were carried out for low Reynolds number flows in the range  $0 < Re \leq 100$ , making use of a rigorous mesh refinement with an accuracy error below 1%. The development length is found to be a non-monotonic function of the slip velocity, increasing up to  $\bar{k}_l \approx 0.1 - 0.4$  (depending on  $Re$ ), and decreasing for higher  $\bar{k}_l$ . We present a new non-linear relationship between  $\mathcal{L}$ ,  $Re$  and  $\bar{k}_l$  that can accurately predict the development length for Newtonian fluid flows with slip velocity at the wall, for  $Re$  of up to 100 and  $\bar{k}_l$  up to 1.*

### 9.1 INTRODUCTION

The relevance of the development length is well known in engineering. The assumption that the flow is fully developed in regions where it remains under strong influence of the inlet boundary conditions, can seriously under-estimate the design of flow systems and incorrectly assume specific velocity profile shapes, in addition to lead to wrong conclusions in the interpretation of data. Another relevant aspect in system flow design is the fact that some flows of Newtonian fluids in micro-channels exhibit slip velocity at the walls, especially if they are hydrophobic, as shown in several experimental (Tretheway and Meinhart, 2002; Watanabe et al., 1998; Zhu and Granick, 2001; Ligrani et al., 2010) and numerical (Barrat and Bocquet, 1999) investigations. A detailed review of experiments on Newtonian fluids showing the existence of slip velocity is given by Neto et al. (Neto et al., 2005). Correlations to predict the development length for Newtonian fluid flows, as function of the Reynolds number, and under no-slip boundary conditions are available in the literature. Recent accurate correlations (Durst et al., 2005; Poole and Ridley, 2007; Poole and Chhabra, 2010) indicate that the development length varies non-linearly with the Reynolds number, while experimental data of flows in micro-channels

---

<sup>1</sup> L.L. Ferrás, A.M. Afonso, M.A. Alves, J.M. Nóbrega, F.T. Pinho (2012). Development length in planar channel flows of Newtonian fluids under the influence of wall slip, accepted for publication in the *Journal of Fluids Engineering*.

with a rectangular cross section at low Reynolds numbers (Lee et al., 2008) showed shorter developing lengths compared to conventional correlations for 2D channel flows. To the best of our knowledge there is no literature on development lengths for Newtonian fluids in the presence of wall slip. The inclusion of slip boundary conditions in the modeling process is very important, mainly due to the emergence of industrial micro and nano technologies using Newtonian fluids that exhibit wall slip (Neto et al., 2005; Lauga et al., 2005). This justifies the present contribution, where a numerical study is presented on the required development lengths for Newtonian fluid flow in planar channels under the influence of slip boundary conditions, using the linear Navier slip law (Navier, 1822), with the dimensionless slip coefficient  $\bar{k}_l$  varying in the range  $0 < \bar{k}_l \leq 1$  ( $\bar{k}_l = 1$  corresponds to a significant slip, close to a plug velocity profile, and these high slip lengths can be found in experimental results and attributed to the presence of gaseous material at the interface (Neto et al., 2005)).

## 9.2 EQUATIONS, NUMERICAL ANALYSIS AND GEOMETRY

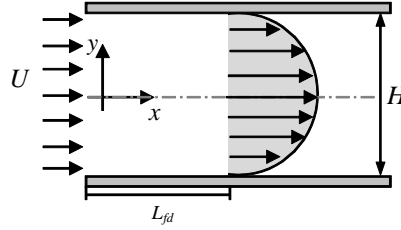


Figure 9.1: Schematic representation of the geometry.

It is assumed that this internal flow is two dimensional, incompressible, laminar, isothermal and steady. The governing equations for such flow conditions are the continuity,

$$\nabla \cdot \mathbf{u} = 0 \quad (9.1)$$

and the momentum,

$$\rho \left( \frac{\partial \mathbf{u}}{\partial t} + \mathbf{u} \cdot \nabla \mathbf{u} \right) = -\nabla p + \nabla \cdot \boldsymbol{\tau} \quad (9.2)$$

equations, where  $\mathbf{u}$  is the velocity vector,  $p$  is the pressure,  $\rho$  is the fluid density and  $\boldsymbol{\tau}$  is the Newtonian extra-stress tensor, which is given by

$$\boldsymbol{\sigma} = \mu \left( \nabla \mathbf{u} + (\nabla \mathbf{u})^T \right) = 2\mu \mathbf{D} \quad (9.3)$$

where  $\mathbf{D}$  is the symmetric rate of deformation tensor and  $\mu$  is the dynamic viscosity.

The channel geometry and Cartesian coordinate system are represented in Fig. 9.1. A uniform velocity profile,  $U$ , is imposed at the inlet of the planar channel, with all other variables set to zero. Vanishing streamwise gradients are applied to all variables at the outlet plane, except for the pressure which is linearly extrapolated to the outlet from the two nearest upstream cells. At the wall the usual no-slip boundary condition was replaced by a wall slip law, in this case, the linear Navier slip law (Navier, 1822):

$$\bar{u}_{ws} = -\bar{k}_l \bar{\tau}_{xy,w} \quad (9.4)$$

where  $\bar{u}_{ws} = u_{ws}/U$  is the dimensionless slip velocity,  $\bar{k}_l$  is the dimensionless slip coefficient that allows to control the intensity of the slip velocity and  $\bar{\tau}_{xy,w} = \tau_{xy,w}(H/U\mu)$  stands for the dimensionless tangent stress vector. Eq. 9.4 states that the tangent velocity vector points in the tangent stress opposite direction, both variables calculated at the wall. Hence, the Navier slip boundary condition can be written as  $\bar{u}_{ws} = \mp \bar{k}_l \frac{d\bar{u}}{d\bar{y}}$  (with  $\bar{y} = y/H$  and  $\bar{u} = u/U$ ), where the signs (-) and (+) are used for the upper and lower walls, respectively.

The system of Eqs. (9.1-9.3) is solved by the finite volume method using the SIMPLE procedure of Patankar (Patankar, 1980) to couple velocity and pressure fields (Oliveira et al., 1998). The inclusion of slip boundary conditions changes the overall procedure as explained in detail by Ferrás et al. (Ferrás et al., 2012d). With their semi-implicit method, on the verge of convergence the calculated slip velocity converges to the correct slip velocity, and when it is far from the solution this new procedure guarantees that the slip velocity is always smaller than the velocity at the center of the adjacent control volume (divergence of the numerical method occurs when this necessary condition is not verified), therefore there is no need to use direct relaxation in the slip velocity and the computations are stable.

In order to achieve accurate mesh independent results, the physical domain depicted in Fig. 9.1 was discretized into three meshes with increasing mesh refinement by doubling the number of cells in the streamwise and transverse directions. Due to symmetry, only half of the domain was used in the numerical simulations. A non-uniform distribution of the cell sizes was used, with the ratio of the geometric progression of the cell sizes in the streamwise direction being 1.05 and 1.01 for the coarse and refined meshes, respectively. For the transverse direction, the cells were concentrated near the channel wall and at the centerplane region to quantify accurately the streamwise variation of the velocity to define well the fully-developed flow condition. For details about the meshes used in the numerical calculations see Table 9.1.

Table 9.1: Mesh characteristics.

	$NC$	$\Delta x_{min}/H$	$\Delta y_{min}/H$
M1	100x40	$3.8 \times 10^{-3}$	$1.2 \times 10^{-3}$
$L=10H$ M2	200x80	$1.9 \times 10^{-3}$	$6.2 \times 10^{-4}$
M3	400x160	$9.6 \times 10^{-4}$	$3.1 \times 10^{-4}$

The present mesh refinement strategy was designed to provide a detailed and accurate measure of uncertainty in our simulations, by using the Richardson extrapolation to the limit technique (Richardson, 1910; Richardson and Gaunt, 1927). This method allows the estimation of the order of accuracy of the simulations (an overall second order was attained in the mesh convergence studies) and an accurate mesh-independent extrapolated  $\mathcal{L}_{ext}$  value. More details on this can be found in Table 9.2, where we provide the results obtained for three specific Reynolds numbers of 0.001, 5 and 100, and four different slip friction coefficients (the “% error” in the table is a quantification of the relative difference between the predictions of  $\mathcal{L}$  on the finest mesh (M3) and the extrapolated results ( $\mathcal{L}_{ext}$ ) obtained from Richardson’s extrapolation technique).

Table 9.2: Development length and estimated error for the three different meshes.

	$Re$	M1	M2	M3	$\mathcal{L}_{ext}$	% error
$\bar{k}_l=0.0001$	0.001	0.6394	0.6308	0.6289	0.6284	0.08
	5	0.7160	0.7007	0.6958	0.6934	0.34
	100	4.9945	4.7927	4.7252	4.6912	0.73
$\bar{k}_l=0.001$	0.001	0.6402	0.6316	0.6298	0.6293	0.08
	5	0.7171	0.7018	0.6969	0.6945	0.34
	100	4.9986	4.7971	4.7296	4.6955	0.72
$\bar{k}_l=0.01$	0.001	0.6483	0.6397	0.6381	0.6377	0.06
	5	0.7283	0.7132	0.7085	0.7065	0.29
	100	5.0468	4.8484	4.7814	4.7474	0.72
$\bar{k}_l=0.1$	0.001	0.6893	0.6832	0.6819	0.6816	0.05
	5	0.8004	0.7873	0.7831	0.7811	0.25
	100	5.5846	5.4168	5.3546	5.3179	0.69
$\bar{k}_l=1$	0.001	0.5568	0.5560	0.5561	-	-
	5	0.6856	0.6818	0.6806	0.6799	0.10
	100	4.9682	4.9347	4.9235	4.9180	0.11

### 9.3 RESULTS AND DISCUSSION

The results obtained showed that the development length varies non-monotonically with the slip coefficient, as observed in Fig. 9.2, showing that the development length increases at low dimensionless slip coefficients and decreases at high values of  $\bar{k}_l$ . For  $Re = 10^{-3}$  the peak development length occurs for  $\bar{k}_l = 0.1$ . The development length,  $\mathcal{L}$ , is here defined as the length from the inlet required for the velocity in the center plane to attain a value of 99% of the corresponding fully-developed value. As shown in Table 9.2 and Fig. 9.2, for creep-

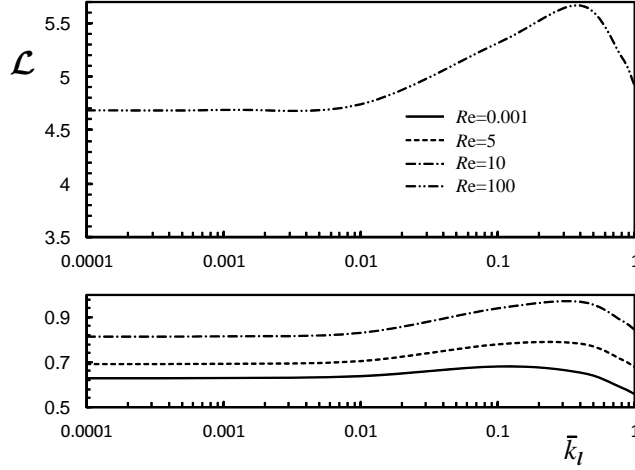


Figure 9.2: Variation of the development length ( $\mathcal{L}$ ) with the slip coefficient ( $\bar{k}_l$ ) for three different values of  $Re$ .

ing flow conditions ( $Re = 10^{-3}$ ) and  $\bar{k}_l = 0.1$  an asymptotic limit of  $\mathcal{L}_{ext|Re \rightarrow 0} = 0.682$  was obtained, while for the no-slip boundary condition the corresponding asymptotic limit is  $\mathcal{L}_{ext|Re \rightarrow 0} = 0.628$ , as show in Table 9.3

Table 9.3: Development length ( $\mathcal{L}$ ) obtained for different values of the slip coefficient ( $\bar{k}_l$ ) and different Reynolds numbers ( $Re$ ) for the mesh M2 (the extrapolated values are in bold).

$Re$	$\bar{k}_l=0.0001$	$\bar{k}_l=0.001$	$\bar{k}_l=0.01$	$\bar{k}_l=0.1$	$\bar{k}_l=0.4$	$\bar{k}_l=0.8$	$\bar{k}_l=1$
0.001	<b>0.6284</b>	<b>0.6293</b>	<b>0.6377</b>	<b>0.6816</b>	0.6546	0.5860	0.5560
0.002	0.6308	0.6316	0.6397	0.6832	0.6546	0.5860	0.5560
0.005	0.6308	0.6317	0.6398	0.6833	0.6547	0.5861	0.5561
0.01	0.6309	0.6317	0.6398	0.6833	0.6548	0.5862	0.5562
0.02	0.631	0.6318	0.6399	0.6835	0.6550	0.5864	0.5564
0.05	0.6313	0.6321	0.6403	0.684	0.6557	0.5870	0.5570
0.1	0.6317	0.6326	0.6408	0.6848	0.6568	0.5881	0.5581
0.2	0.6327	0.6335	0.6419	0.6863	0.6591	0.5903	0.5603
0.5	0.6356	0.6364	0.6452	0.6911	0.6658	0.5970	0.5667
1	0.6411	0.642	0.6509	0.7	0.6773	0.6085	0.5779
2	0.6532	0.6541	0.6638	0.7189	0.7020	0.6327	0.6013
5	<b>0.6934</b>	<b>0.6945</b>	<b>0.7065</b>	<b>0.7811</b>	0.7881	0.7162	<b>0.6799</b>
10	0.8144	0.8159	0.831	0.9388	0.9680	0.8860	0.8441
20	1.156	1.1579	1.1779	1.3456	1.4180	1.3003	1.2366
50	2.4968	2.4995	2.5303	2.8361	2.9924	2.7324	2.5888
100	<b>4.6912</b>	<b>4.6955</b>	<b>4.7474</b>	<b>5.3179</b>	5.7238	5.2161	<b>4.9180</b>

(which is in agreement with Durst et al.). For the same inertialess conditions and higher values of  $\bar{k}_l$ , the asymptotic limit decreases, with  $\mathcal{L}_{ext|Re \rightarrow 0} = 0.556$  at  $\bar{k}_l = 1$ . Regarding the comparison between the development lengths for the no-slip and the slip cases, we could find differences of the order of 15% for high slip coefficients and below 3% for small slip coefficients. These differences increased with Reynolds number and slip coefficient, as seen in Table 9.3 and Fig. 9.3. For small slip coefficients and small Reynolds number ( $Re \leq 10$ ) these differences are less pronounced.

We propose a correlation (Fig. 9.4), which is able to predict the development length of Newtonian fluid flows under slip ( $0 \leq \bar{k}_l \leq 1$ ) for

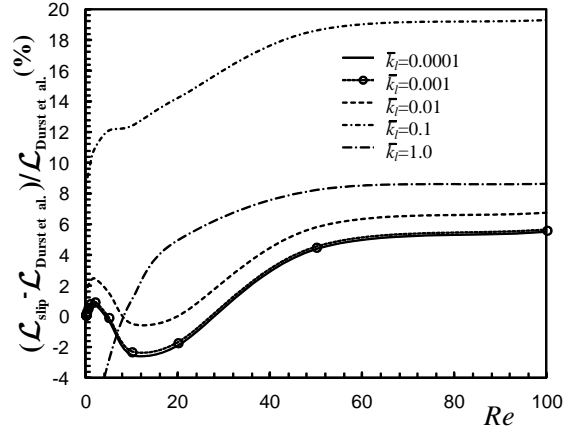


Figure 9.3: Variation with  $Re$  of the difference in  $\mathcal{L}$  relative to the no-slip case results of Durst et al. [8] as a function of the slip coefficient  $\bar{k}_l$ .

the low Reynolds number range studied here  $Re \leq 100$ . The model is inspired on the works of Durst et al. (Durst et al., 2005) and Barber and Emerson (Barber and Emerson, 2001) and is given by

$$\mathcal{L}_{slip} = \frac{1 + 3.15\bar{k}_l^{-1.2} + 0.28\bar{k}_l Re^{0.5}}{1 + 3.82\bar{k}_l^{-1.5} + 0.018\bar{k}_l Re} \left[ 0.631^{1.8} + (0.047Re)^{1.8} \right]^{\frac{1}{1.8}} \quad (9.5)$$

for  $0 \leq Re \leq 100$  and  $\bar{k}_l \leq 1$ .

We quantified the error as the average of the relative errors (for each slip coefficient and Reynolds number) and a global error below 0.01 was obtained.

In Fig. 9.5 we plot the profiles of the dimensionless streamwise velocity component along the axial direction at several transverse positions for two distinct values of the slip coefficient ( $\bar{k}_l = 0.0001$  and  $0.1$ ). We can observe in both cases that the dimensionless velocity increases as we move towards the symmetry axis ( $y = 0$ ). The conservation of mass, together with the fact that the slip velocity increases with the slip coefficient, forces the centerplane velocity to decrease inversely with  $\bar{k}_l$ . From the inset on Fig. 9.5 we can also see that the development length for  $\bar{k}_l = 0.1$  is longer than the development length obtained for  $\bar{k}_l = 0.0001$ . For  $\bar{k}_l = 0.0001$  the dimensionless axial velocity component presents a pronounced local maximum close to the channel wall, that increases as the Reynolds number increases. For higher values of  $\bar{k}_l$ , we found that the introduction of the slip velocity tends to suppress the appearance of this near-wall velocity overshoot. To better understand this behavior, we also plotted the transverse profiles of the dimensionless streamwise velocity for various positions along the channel, shown in Fig. 9.6, for creeping flow conditions ( $Re = 10^{-3}$ ) and  $Re = 100$ . When the contribution from the slip velocity is negligible ( $\bar{k}_l = 0.0001$ ), the development of the axial velocity profiles is not

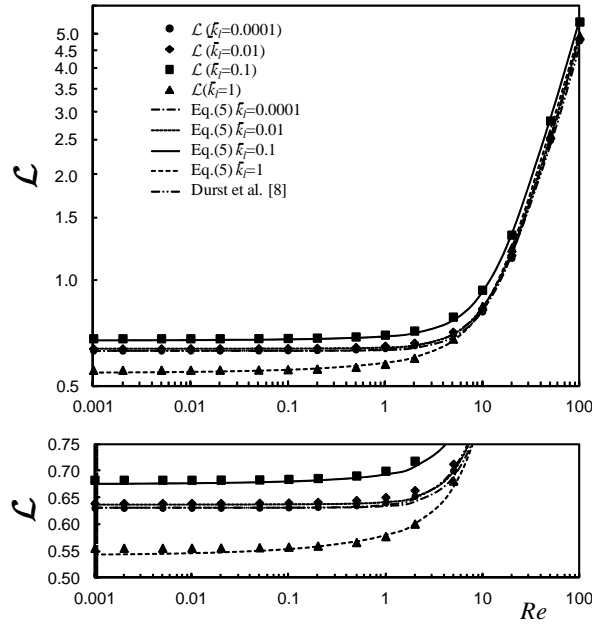


Figure 9.4: Non-linear functional correlations for  $\mathcal{L} = f(Re, \bar{k}_l)$  for channel flows.

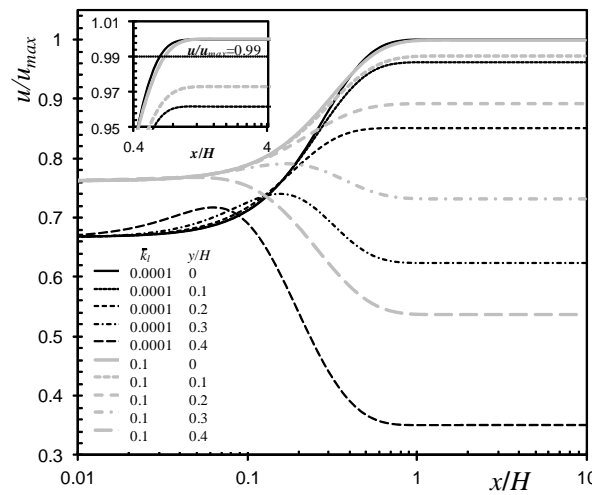
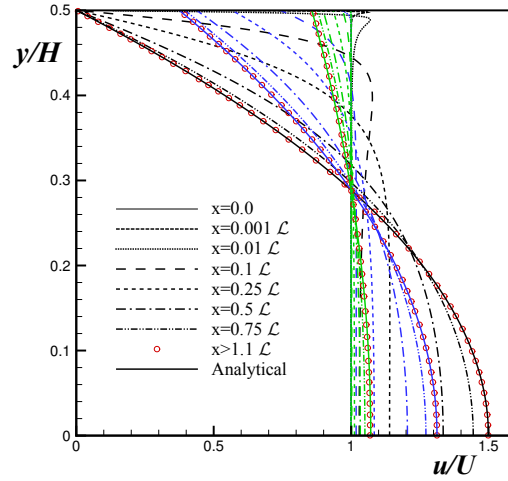
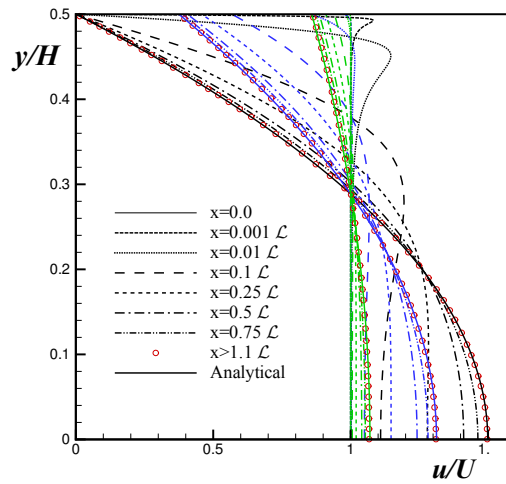


Figure 9.5: Dimensionless velocity profiles along the channel for two different values of the slip coefficient ( $\bar{k}_l = 0.0001$  and  $0.1$ ) and  $Re = 10^{-3}$ , at five different positions  $y/H$ . Inset: detailed view near the wall.

purely convex and shows a local minimum on the symmetry axis and a local maximum near the walls. These overshoots are generated as a result of the abrupt fluid deceleration happening near the wall at the inlet that happens faster than diffusion is able to transport momentum to the centerplane. As slip increases this deceleration effect is reduced and the local maximum disappears (for the full slip condition there is no fluid deceleration). A more in-depth description of this velocity overshoot for non-slip conditions is reported in (Darbandi and



(a)



(b)

Figure 9.6: Velocity profiles at different axial locations for  $\bar{k}_l = 0.0001$  (black), 0.1 (blue) and 1.0 (green): (a)  $Re = 10^{-3}$  and (b)  $Re = 100$ .

Schneider, 1998). Comparing Figs. 9.6a and 9.6b, we can conclude that for small slip velocities the overshoots are present even when inertia is negligible, with their magnitudes (measured by  $(u_{y_{max}} - u_{sa}) / u_{sa}$ , where  $u_{y_{max}}$  is the local maximum velocity in the profile and  $u_{sa}$  is the corresponding velocity at the symmetry axis) increasing with inertia. For all the simulations, the maximum overshoot magnitude is attained for  $Re = 100$  with a value of 15.83% (close to 15.8% obtained with  $\bar{k}_l = 0$  by (Darbandi and Schneider, 1998)). For higher values of the slip coefficient the appearance of the velocity overshoots is almost suppressed, as also observed in Figs. 9.6a and 9.6b, where we can see that for inertialess conditions there is no overshoot (since  $Re$  is the ratio between diffusive and advective time scales, the effect of viscosity is transmitted to the whole channel very quickly when  $Re = 0$ ), while



for higher Reynolds number ( $Re = 100$ ) a very small overshoot is present only for  $\bar{k}_l = 0.1$ . This can be explained as a result of a smaller deceleration effect of the fluid elements near the channel walls due to the slip condition, allowing both the convection and diffusion to transport momentum to the centerplane. The velocity in the centerplane is also affected (and indirectly the development length), as observed in the dimensionless velocity profiles along the centerplane for different slip coefficients and  $Re \rightarrow 0$ , plotted in Fig. 9.7, showing smaller  $\mathcal{L}$  for  $\bar{k}_l > 0.1$ .

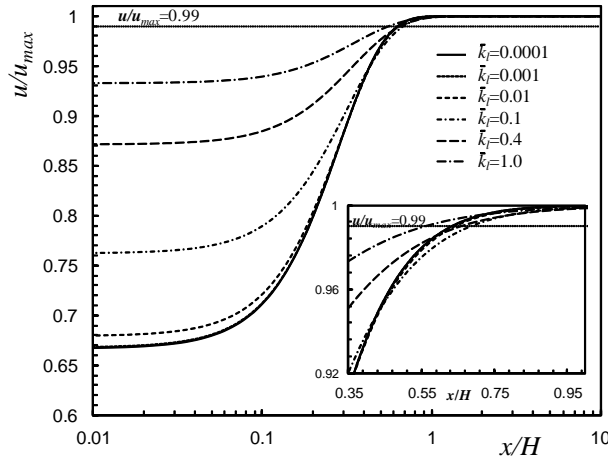


Figure 9.7: Variation along the channel of the dimensionless centreplane velocity as a function of the slip coefficients for  $Re = 10^{-3}$ . Inset: detailed view of the development length for the different slip coefficients.

#### 9.4 CONCLUSIONS

We conducted a detailed and systematic numerical investigation of the development length in planar channels flows of Newtonian fluids under laminar flow conditions and under the presence of hydrodynamic wall slip. We show that a judicious choice of mesh refinement and highly accurate numerical methods allow the prediction of highly accurate development length values. A new non-linear correlation for  $\mathcal{L}(\bar{k}_l, Re)$  is proposed, which shows good accuracy over the range  $\bar{k}_l \leq 1$  and  $Re \leq 100$ . This non-linear correlation predicts a non-monotonic behavior between the wall slip coefficient and the development length, with the development length increasing up to  $\bar{k}_l \approx 0.1$  and  $\bar{k}_l \approx 0.4$  for creeping flow and higher inertia ( $Re = 100$ ) flows, respectively, and decreasing for higher values of  $\bar{k}_l$ .

## ACKNOWLEDGEMENTS

The authors acknowledge funding from COMPETE/FEDER and Fundação para a Ciência e a Tecnologia (FCT), Portugal, through project PTDC/EQU-FTT/113811/2009. L.L. F. would like to thank FCT for financial support through the scholarship SFRH/BD/37586/2007 and A.M. A. through the scholarship SFRH/BPD/75436/2010.

## DEVELOPMENT LENGTH OF UCM VISCOELASTIC FLUIDS UNDER SLIP

---

### Abstract<sup>1</sup>

*In this work we present a numerical study of the channel development length,  $\mathcal{L}$ , required to obtain the fully developed flow conditions, for a viscoelastic fluid modeled by the Upper Convected Maxwell (UCM) model. Instead of the usual Dirichlet no-slip boundary condition, we consider the linear Navier slip model as boundary condition at the wall, with the normalized slip length ( $\bar{k}_1$ ) varying in the range  $[0, 1]$ . To perform the simulations we used an in house finite volume code that couples velocity, pressure and stress fields by solving iteratively the Cauchy and the rheological constitutive equation (Oliveira et al., (1998) "Numerical simulation of non-linear elastic flows with a general collocated finite-volume method", Journal of Non-Newtonian Fluid Mechanics, 79 pp. 1-43.). To deal with the discontinuity issues at the entrance region close to the channel wall, where steep stress variations are expected to occur, we use the Log-Conformation tensor approach. The simulations were carried out for two different elasticity numbers,  $El = 0.1$  and  $1$  with Reynolds ( $Re$ ) and Deborah ( $De$ ) numbers varying in the range  $[0.1, 5]$  and  $[0.01, 0.5]$ , respectively. We also performed simulations for creeping flow conditions ( $Re = 0.001$ ) with a varying Deborah number  $De \in [0.01, 0.5]$ . For each of these simulations five different dimensionless slip coefficients were employed,  $\bar{k}_1 = 0, 0.001, 0.3, 0.1$  and  $1$ . We found that the development length decreases with the increase of the slip coefficient.*

### 10.1 INTRODUCTION

The real nature and type of interaction between a liquid and a solid is a subject of intense research. Even with the great advances in technology that occurred over the last decade, it seems impossible to find a physical law that describes accurately the flow characteristics at the interface between solids and liquids, valid for all types of fluids and wall materials. Even the friction law for solids is empirical.

In the absence of such universal law for the boundary between liquids and solids, the empirical law proposed by Navier (1822) seems to be a good approximation, specially for polymer melts, for which several studies indicate the existence of slip velocity at the wall (Ra-

---

<sup>1</sup> L.L. Ferrás, A.M. Afonso, J.M. Nóbrega, M.A. Alves, F.T. Pinho (2012), Development length in planar channel flows of UCM viscoelastic fluids under slip, to be submitted to *Journal of Fluids Engineering*;

mamurthy, 1986; Kalika and Denn, 1987; Mitsoulis et al., 2005; Dealy and Kim, 2005; Denn, 2001) .

The Nature of the boundary conditions is of major importance to accurately describe the fluid flow, as is also the development length required for the fluid to attain the the fully developed flow conditions. As an example we have the production of thermoplastic profiles by extrusion. If the length of the extrusion die parallel zone is not long enough for the fluid to attain its fully developed condition, the process is more prone to be unstable and more sensitive to the variations of the upstream flow conditions. This applies to several other flow systems.

In the available literature we can find several works regarding the development length for Newtonian fluids with no-slip boundary conditions. A good review is given by (Durst et al., 2005), where a correlation that predicts the development length as a function of the Reynolds number is also presented, valid in the range  $0 < Re < \infty$  (provided that the flow remains laminar). Considering slip velocity at the wall, it seems that we only have the work of (Ferrás et al., 2012b). This happened because the no-slip boundary condition was for long time universally accepted as a physical “law”, and because only for specific wall materials and fluids apparent slip was detected (Neto et al., 2005).

For Non-Newtonian flows, assuming no-slip velocity at the wall, the literature is scarcer and only few works could be found. For inelastic fluids modelled by the “power law” model most of the available works are summarized in the work of (Poole and Ridley, 2007). In his work, (Poole and Ridley, 2007), develops a new correlation that outstands the previous works published in the literature by presenting a correlation valid in the range  $0.4 < n < 1.5$  and  $0 < Re < 1000$ . For the case of yield stress fluids, (Poole and Chhabra, 2010) presents a systematic numerical investigation of developing laminar pipe flow of yield stress fluids for models of the Bingham-type.

For viscoelastic fluids, (Liang, 1998), investigated the entry flow of a viscoelastic fluid in a channel experimentally, (Alves et al., 2003b) studied the 4:1 contraction flow of a fluid obeying the Phan Thien Tanner (PTT) linear viscoelastic model, expressing the entry length as a function of the Deborah (De) number, (Na and Yoo, 1991) examined the effects of the elasticity and inertia on the entry length and more recently Kerim et al. (Yapici et al., 2012) studied the flow development of steady flow of Oldroyd-B and Phan-Thien-Tanner (PTT) fluids through a two-dimensional rectangular channel considering the effects of effects of mesh refinement, inlet boundary conditions, constitutive equation parameters, and Reynolds number. In their (Yapici et al., 2012) work they used a regularization function to account for the discontinuities at the channel entrance. For the same urpose in this study we use the log-conformation tensor approach (Fattal and Kupferman, 2004; Afonso et al., 2009a).

The development length,  $\mathcal{L} = L_{fd}/H$ , is here defined as the length (measured from the entrance of the channel) required for the fluid to reach 99% of its fully developed velocity at the center of the channel. The stress relaxation length,  $\mathcal{L}_{\bar{\tau}_{xx}}$ , was also studied and is here de-

defined by  $|\bar{\tau}_{xx} - \bar{\tau}_{xx-fd}| \leq 0.01$  with  $\bar{\tau}_{xx} = \tau_{xx}/(\eta_0 U/H)$  and  $\bar{\tau}_{xx-fd}$  representing the fully developed (fd) solution.

The paper starts with this brief introduction. In the next section we present the governing equations and boundary conditions, together with the transformation needed in the momentum equation to implement the log-conformation tensor approach. In Section 3 we briefly describe the solver used to couple velocity, pressure and the slip boundary condition and we also describe the geometry and flow characteristics. In Section 4 the results obtained for a viscoelastic fluid modeled by the UCM model are presented and discussed. The closure of the paper is made with the conclusions in Section 5.

## 10.2 GOVERNING EQUATIONS

The flow is assumed to be laminar and the fluid is incompressible. The governing equations are those expressing the conservation of mass,

$$\nabla \cdot \mathbf{u} = 0 \quad (10.1)$$

and momentum,

$$\rho \left[ \frac{\partial \mathbf{u}}{\partial t} + \nabla \cdot \mathbf{u}\mathbf{u} \right] = -\nabla p + \beta \eta_0 \nabla^2 \mathbf{u} + \frac{\eta_0}{\lambda} (1 - \beta) \nabla \cdot \mathbf{A} \quad (10.2)$$

where  $\mathbf{u}$  is the Cartesian velocity vector,  $p$  is the pressure,  $\rho$  is the fluid density,  $t$  is the time,  $\mathbf{A}$  is the polymer conformation tensor and  $\lambda$  is the relaxation time of the polymer. The total fluid extra stress tensor is the sum of a solvent and a polymer contributions and  $\eta_0 = \eta_s + \eta_p$  is the zero shear rate total viscosity with  $\eta_s$  and  $\eta_p$  being the solvent and polymer contributions, respectively. The coefficient  $\beta$  is defined as  $\beta = \frac{\eta_s}{\eta_0}$ , in such a way that if  $\beta = 1$  we have a Newtonian fluid and for  $\beta = 0$  we have only the contribution from the polymeric part of the total stress tensor. The polymer stress contribution is here described by the Oldroyd-B constitutive equation, which includes the particular case of the UCM model.

The extra stress tensor  $\boldsymbol{\tau}$  can be written in terms of  $\mathbf{A}$  by,

$$\boldsymbol{\tau} = \frac{\eta_p}{\lambda} (\mathbf{A} - \mathbf{I}) \quad (10.3)$$

leading to an evolution equation for  $\mathbf{A}$  of the form,

$$\mathbf{A} + \lambda \left[ \frac{\partial \mathbf{A}}{\partial t} + \nabla \cdot \mathbf{u}\mathbf{A} \right] = \mathbf{I} + \lambda \left[ (\nabla \mathbf{u})^T \cdot \mathbf{A} + \mathbf{A} \cdot \nabla \mathbf{u} \right] \quad (10.4)$$

where  $\mathbf{I}$  is the unitary tensor. If  $\beta = 0$  than the UCM model is recovered.

Fattal and Kupferman (Fattal and Kupferman, 2004) suggested a simple tensor-logarithmic transformation that features the decomposition of the velocity gradient  $(\nabla \mathbf{u})^T$  into a traceless extensional component,  $\mathbf{E}$ , and a pure rotational component,  $\mathbf{R}$ , together with the transformation  $\mathbf{\Theta} = \log \mathbf{A}$ , leading to the following evolution equation in  $\mathbf{\Theta}$ ,

$$\frac{\partial \mathbf{\Theta}}{\partial t} + (\mathbf{u} \cdot \nabla) \mathbf{\Theta} - [\mathbf{R} \cdot \mathbf{\Theta} - \mathbf{\Theta} \cdot \mathbf{R}] = \frac{(e^{-\mathbf{\Theta}} - \mathbf{I})}{\lambda} \quad (10.5)$$

To recover  $\mathbf{A}$  from  $\mathbf{\Theta}$  the inverse transformation is used  $\mathbf{A} = e^{\mathbf{\Theta}}$ . This transformation is important because it increases the critical Deborah number at which divergence occurs.

Additionally, an appropriate boundary condition that considers the slippery characteristic of some polymer melts was assumed. The chosen slip model was the linear Navier slip model (Navier, 1822),

$$\mathbf{u}_{ws} = -k_l \boldsymbol{\tau}_w \quad (10.6)$$

where  $\mathbf{u}_{ws}$  is the slip velocity vector (the subscript “ws” stands for “wall slip”) that points in the tangent stress  $\boldsymbol{\tau}_w$  (the subscript “w” stands for “wall”) opposite direction, and  $k_l$  is a positive slip coefficient, known as the slip length, that allows to control the amount of slip in the simulation.

### 10.3 NUMERICAL METHOD

The system of differential equations, Eqs. (10.1-10.6), is discretized and solved within a finite volume method framework, described with great detail in the work of (Oliveira et al., 1998). The code is based on the SIMPLEC method of (Van Doormaal and Raithby, 1984) to couple velocity and pressure fields, and uses high resolution methods for the representation of the convective terms in the constitutive equation (Alves et al., 2000). The implementation of the log-conformation tensor approach is well described in the work of Afonso et al. (Afonso et al., 2009a).

For the implementation of the slip boundary conditions we assume a Couette flow in the vicinity of the wall (the flow near the wall is mostly viscometric) (Azaiez et al., 1996) thus,

$$\boldsymbol{\tau}_w = \eta_0 \left. \frac{d\mathbf{u}}{dn} \right|_w \quad (10.7)$$

leading to the following slip boundary condition,

$$\mathbf{u}_{ws} = -k_l \eta_0 \left. \frac{d\mathbf{u}}{dn} \right|_w \quad (10.8)$$

For the discretization of Eq. 10.8 we use a one-sided finite difference approximation for the derivative,

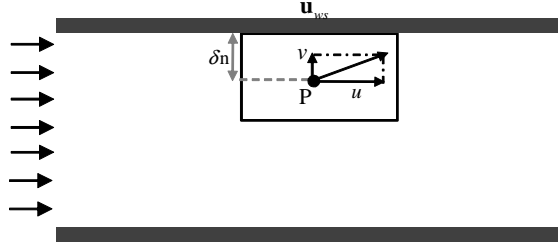


Figure 10.1: Typical computational cell near the wall.

$$u_{ws} = k_l \eta_0 \frac{u_P - u_{ws}}{\delta n} \quad (10.9)$$

where  $u_{ws}$ ,  $u_P$  are the first component of the slip velocity vector and the velocity at the center of the adjacent computational cell, respectively,  $\delta n$  is the distance between the center (P) of the adjacent cell and the wall boundary (see Fig. 10.1).

To couple this equation with the momentum equation we use two slightly different methods. The first one, more stable (but more iteration consuming), corresponding to the implicit implementation of the slip boundary condition,

$$u_{ws} = \frac{k_l \eta_0}{\delta n + k_l \eta_0} u_P \quad (10.10)$$

into the discretized system of equations, and a second method, that uses a similar approach, but the boundary condition is updated at each iteration  $i$ , with the velocity of the adjacent computational cell,  $u_P^{i-1}$ , that comes from the previous iteration,

$$u_{ws}^i = \frac{k_l \eta_0}{\delta n + k_l \eta_0} u_P^{i-1} \quad (10.11)$$

where  $i$  is the iteration number. For a detailed description see (Ferrás et al., 2012d).

To solve the system of equations the following iterative procedure was used:

- (1) Set the boundary conditions, the initial velocity and pressure fields;
- (2) Solve Eq. 10.5 to obtain the discretized version of  $\Theta$  at the new time level;
- (4) Recover the discretized version of the the conformation tensor  $\mathbf{A}$  and calculate the extra stress tensor  $\boldsymbol{\tau}$  with Eq.

- (a) Compute the slip velocity with the discretized slip model Eq.10.11.
- (4) Solve the linearized momentum equations and the equation for pressure using the SIMLEC method;
- (6) Correct velocity and pressure fields;
- (7) Check for convergence in the system of equations residuals;
- (8) If convergence is not achieved proceed to step 2.
- (b) If convergence is achieved then calculate the slip velocity values at each wall cell using Eq. 10.10.

In this work we are interested only in the stationary solution, so the time evolution is fictitious, being used just for relaxation purposes. Each time step represents one iteration  $i$ . With this method there is no need for direct relaxation of the slip velocity and the computations are stable. In the algorithm Step (b) is employed just for the implicit implementation of the slip boundary condition, while Step (a) is used just for the explicit implementation.

A schematic of the geometry used in our simulations is given in Fig. 10.2. The flow is two-dimensional and we impose symmetry at

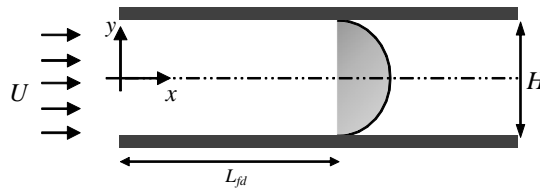


Figure 10.2: Schematic of the geometry.

the centerline, therefore only half of the geometry was considered in the simulations. At the inlet, a mean velocity profile,  $U$ , is imposed together with null stress components, and at the outflow a zero gradient boundary condition is assumed.

The problem was solved using three meshes, designated by  $M_1$ ,  $M_2$  and  $M_3$ , with consistent consecutive refinement, in the sense that the number of cells was doubled in each direction, with mesh spacing being approximately halved. This way we can measure the accuracy of our results by using Richardson's extrapolation technique (Richardson, 1910; Richardson and Gaunt, 1927). The mesh refinement near the walls and at the channel centerplane was intensified, in order to capture well the development length,  $\mathcal{L}$ . More details on the mesh characteristics are given in Table 10.1 where the notation  $n_x$  and  $n_y$  is used to represent the number of cells in the  $x$  and  $y$  directions, respectively, and  $f_x, f_y$  are the mesh ratio of expansion/contraction between two consecutive cells in the  $x$  and  $y$  direction, respectively.



	$f_x$	$f_y$	$n_x$	$n_y$
M1	1.0200	1.1000	200	40
M2	1.0100	1.0488	400	80
M3	1.0050	1.0241	800	160

Table 10.1: Mesh Characteristics for ME<sub>1</sub>, ME<sub>2</sub>, ME<sub>3</sub>.

For this study a large number of simulations was performed. Two different elasticity numbers,  $El = \frac{De}{Re}$ , were used,  $El = 0.1$  and  $El = 1$  together with several different numbers of  $De = \lambda U/H$  and  $Re = \rho UH/\eta_0$ . For  $El = 0.1$  we have used the following set of  $De$  and  $Re$  numbers ratio,  $\frac{De}{Re} \in \{ \frac{0.01}{0.1}, \frac{0.1}{1}, \dots, \frac{0.5}{5} \}$ , and for  $El = 1$  we have  $De = Re$  with  $\frac{De}{Re} \in \{0.0, 0.1, \dots, 0.5\}$ . Additionally we also performed simulations for creeping flow conditions ( $Re = 0.001$ ) and a varying Deborah number,  $De \in \{0.0, 0.1, \dots, 0.5\}$ . For each of these simulations we have also used five different dimensionless slip coefficients,  $\bar{k}_l = k_l \frac{\eta_0}{H}$ , with  $\bar{k}_l = 0, 0.01, 0.1, 0.3, 1$ .

10.4 RESULTS AND DISCUSSION

The aforementioned numerical method was applied to the study of the development-length requirements for fully developed laminar channel flow of a viscoelastic fluid modeled by the UCM model. The results are discussed in terms of elasticity and inertia effects, combined with the slip boundary condition.

10.4.1 Slip and elasticity effects

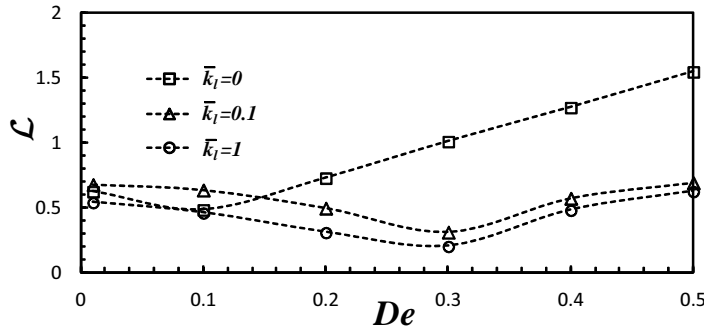
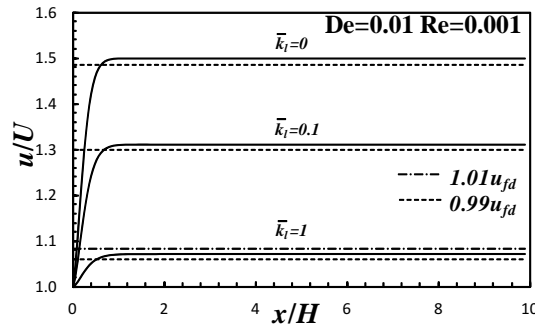


Figure 10.3: Variation of the streamwise velocity component development length,  $\mathcal{L}$ , with  $De$  and  $\bar{k}_l$ .

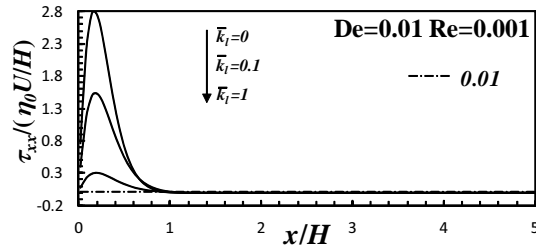
In this subsection we present the study of the elasticity effect on the development length of the velocity,  $u$ , and normal stress,  $\tau_{xx}$ , assuming creeping flow ( $Re = 0.001$ ) and using three different slip coefficients,  $\bar{k}_l = 0$  (no-slip boundary condition) and  $\bar{k}_l = 0.1, 1$ .

For the development of the streamwise velocity component,  $u$ , Fig. 10.3 shows that for small values of  $De$  ( $0 < De < 0.1$ ) it decreases, and that starts to increase for  $0.1 < De < 0.5$ . This happens for the no-slip velocity case, assuming slip velocity at the wall, the minimum of  $\mathcal{L}$  shifts to  $De \approx 0.3$  for both slip coefficients used here.

The minimum value of  $\mathcal{L}$  shifts from  $De$  0.1 to  $De$  0.3, when slip is considered. This result evidences that the presence of slip affects the diffusion of momentum along the flow channel thickness, as reported in Ferrás et al. (Ferrás et al., 2012b) for Newtonian fluids. As shown also in Fig. 10.3, the difference between the no-slip and slip boundary conditions increase with the growth of elasticity. While for the no-slip boundary  $\mathcal{L}$  increases significantly with  $De$ , when slip is considered, for high values of  $De$ , the influence of elasticity is less pronounced. This is a direct consequence of the steep stress variation that occur near the flow channel inlet (see Fig. 10.4), which is faded by the presence and increase of slip.



(a)



(b)

Figure 10.4: Variation of the development length,  $\mathcal{L}$ , with  $De$  and  $\bar{k}_l$  for  $Re = 0.001$  and  $De = 0.01$ . (a) dimensionless streamwise velocity component,  $u/U$  (b) dimensionless normal stress,  $\tau_{xx} / (\eta_0 U/H)$ .

It is also interesting that for very small Deborah numbers, the fluid behaves as a Newtonian fluid, and for this case the development length increases with the slip velocity (Fig. 10.3), in agreement with the results obtained for Newtonian fluids in (Ferrás et al., 2012b). For the no-slip case with  $Re \rightarrow 0$  and  $De \rightarrow 0$  we obtained a development length value of  $\mathcal{L} = 0.6270$ , which is in agreement with Durst et al. (Durst et al., 2005).

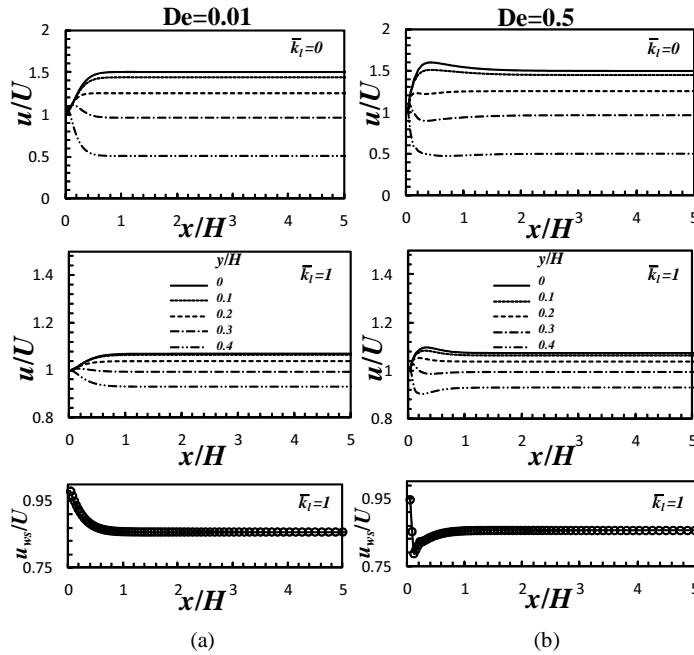


Figure 10.5: Variation of velocity along the streamwise direction at different positions  $y/H$ , for different values of the slip coefficient,  $\bar{k}_l = 0, 1$ . (a)  $De = 0.01$  (b)  $De = 0.5$ .

In Figs. 10.4 (a), (b), we can see the variation of velocity and normal stress at the channel centerplane for  $Re = 0.001$  and  $De = 0.01$ . Notice that the fully developed solution depends on the slip coefficient, with the centerplane velocity and stress decreasing with  $\bar{k}_l$ . These results evidence that the presence of slip counteracts the effect of elasticity, being the development length a balance between slip and elasticity intensities, with a minimum value that depend on both properties values (see Fig. 10.3 ).

Fig. 10.5 shows the variation of velocity along the streamwise direction at different positions  $y/H$ , for different values of the slip coefficient,  $\bar{k}_l = 0, 1$  and different Deborah numbers,  $De = 0.01, 0.5$ . As expected, the velocity decreases as we increase  $y/H$  for both  $\bar{k}_l = 0$  and  $\bar{k}_l = 1$ . For  $\bar{k}_l = 1$ , due to high slip velocity, the range of the velocity field is smaller. The slip velocity profile shows a different behavior depending on the Deborah number. For  $De = 0.5$  it decreases drastically in the entrance of the the channel and then suddenly increases until it converges to the fully developed state, while for  $De = 0.01$  it decreases smoothly to the fully developed solution. The streamwise velocity at different positions along the flow channel thickness shows a similar behaviour ( see Fig. 10.5).

Fig. 10.6 shows the transverse profiles of the dimensionless streamwise velocity for various positions along the  $x$ -direction for  $De = 0.5$  and two slip coefficients. The non-monotonic evolution of the velocity for this  $De$  is again evident, initially the velocity increases, but as we

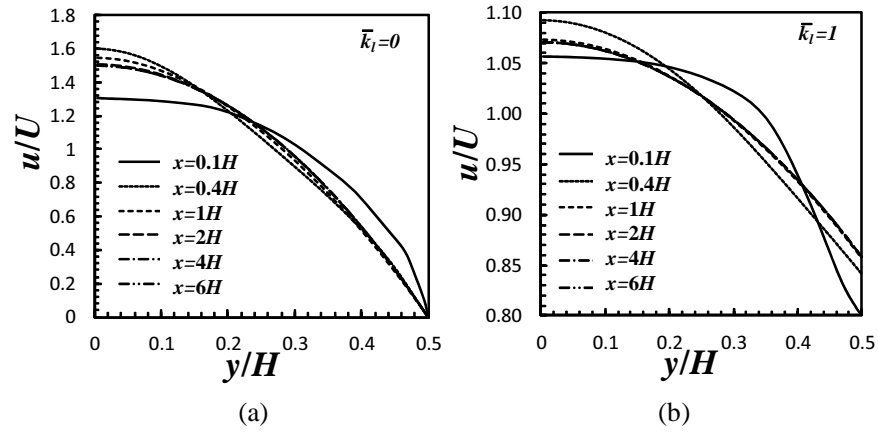


Figure 10.6: Velocity profiles at different axial locations for  $Re = 0.001$ ,  $De = 0.5$  and  $\bar{k}_l = 0, 1$ .

move towards the exit of the channel it stabilizes. This happens for both cases considered, with and without slip velocity. For  $\bar{k}_l = 1$  we obtain an almost plug like profile, meaning that the transfer of momentum by diffusion and convection occurs mainly in the streamwise direction which leads to a reduction of the development length.

We also studied the effect of slip velocity and Deborah number on the development length,  $\mathcal{L}_{\bar{\tau}_{xx}}$ , required for the dimensionless normal stress to become fully developed. From the analysis of Fig. 10.7 we see

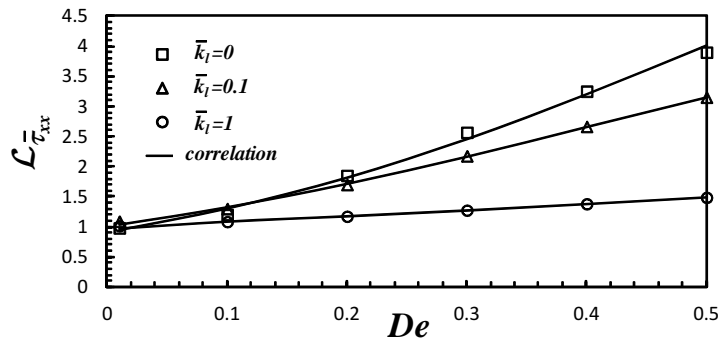


Figure 10.7: Variation of the normal stress development length,  $\mathcal{L}_{\bar{\tau}_{xx}}$ , with  $De$  and  $\bar{k}_l$ .

that  $\mathcal{L}_{\bar{\tau}_{xx}}$  increases with  $De$  and decreases with  $\bar{k}_l$ , except for very small  $De$ . This can be explained as a result of a smaller deceleration near the wall due to the existence of slip velocity. This way the “relaxation time” is reduced, in comparison to  $\bar{k}_l = 0$ , because the fluid suffers a smaller deformation, resulting in a faster transport of momentum to the centerplane.

We propose a correlation (see Fig. 10.7) that is able to predict the development length of the dimensionless normal stress  $\tau_{xx}/(\eta_0 U/H)$  in the range  $0 \leq \bar{k}_l \leq 1$  for low Deborah numbers of  $0 \leq De \leq 0.5$ .

$$\mathcal{L}_{\bar{\tau}_{xx}} = \frac{1.254 \left( \frac{1 - 0.873\bar{k}_l^{4.477}}{1 + 0.002De\bar{k}_l^{-2.538}} \right)}{0.157 + 1.204 \exp(-4.086De)} + \bar{k}_l De^{0.003} \quad (10.12)$$

The error was quantified as the sum of the square relative errors, for each slip coefficient and Debora number tested, and a global error of 0.015 was obtained.

10.4.2 Slip and inertia effects

$\bar{k}_l$	$De=0.01$	$De=0.1$	$De=0.2$	$De=0.3$	$De=0.4$	$De=0.5$
0	0.6279	0.4821	0.7299	0.9339	1.8959	3.0248
0.01	0.6375	0.5008	0.7166	0.9477	1.8605	2.5912
0.1	0.6830	0.6444	0.4886	0.5746	1.4358	2.4050
0.3	0.6675	0.6324	0.4682	0.3861	1.0006	1.9079
1	0.5453	0.4743	0.3073	0.3597	0.8435	1.3041

Table 10.2: Development length values for a constant elasticity number,  $El$ , of 0.1 and five different slip coefficients,  $\bar{k}_l$ .

To study the inertia effects combined with the slip velocity two different elasticity numbers,  $El$ , of 0.1 and 1, were used.

For the first two Deborah numbers shown in Table 10.2 ( $El = 0.1$ ) we see that the Newtonian behavior is present. The velocity development length values obtained for  $De = 0.01$  match the data from (Ferrás et al., 2012b) for  $De = 0$ . For  $De = 0.1$  the development length starts to deviate from the Newtonian behavior but the results are qualitatively similar. The development length varies non-monotonically with the slip coefficient, with a maximum in the range  $0 \leq \bar{k}_l \leq 1$ .

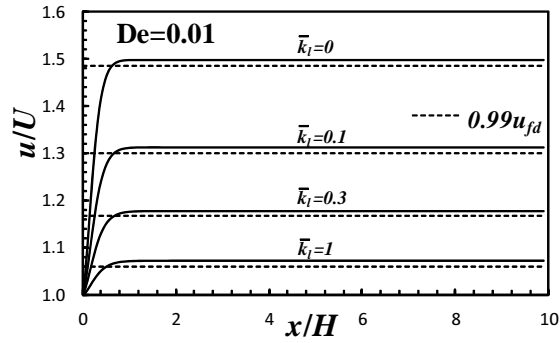
For higher Deborah and Reynolds numbers, the development length increases with  $Re$  and  $De$ , and decreases with  $\bar{k}_l$ .

$\bar{k}_l$	$De=0.01$	$De=0.1$	$De=0.2$	$De=0.3$	$De=0.4$	$De=0.5$
0	0.6271	0.4869	0.7318	1.0089	1.2683	1.5415
0.1	0.6817	0.6399	0.4994	0.3076	0.5737	0.6757
1	0.5434	0.4644	0.3120	0.2033	0.4950	0.6230

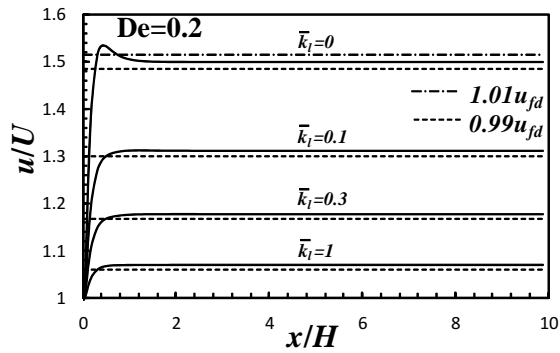
Table 10.3: Development length values for a constant elasticity number,  $El$ , of 1 and three different slip coefficients,  $\bar{k}_l$ .

As expected (Barbosa, 2012), the presence of inertia leads to the appearance of oscillations (see Figs. 10.8 and 10.9) in both velocity and normal stress. These oscillations are smoothed by the presence of slip velocity. In Fig. 10.8, specially for  $De = 0.5$  these oscillations are very intense for  $\bar{k}_l = 0$  and become smother as  $\bar{k}_l$  increases. According to (Barbosa, 2012), these oscillations occur because of the convective velocity and the characteristic time for convection. These two prproperties

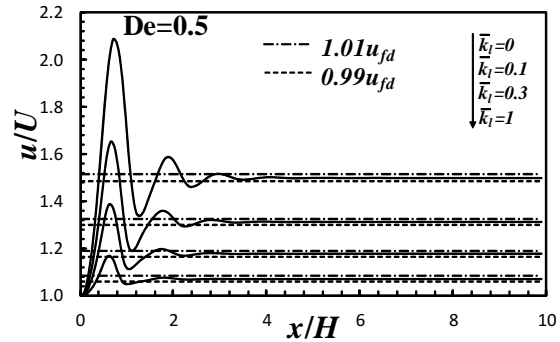
enhance the importance of the elastic Mach number,  $Ma_e = \sqrt{Re \cdot De}$ . Based on (Barbosa, 2012), these oscillations occur for  $Ma_e \geq 1$ .



(a)



(b)



(c)

Figure 10.8: Variation of velocity,  $u$ , along the centerplane of the channel, for a constant elasticity number,  $El = 0.1$ , and three different Deborah numbers,  $De = 0.01, 0.2, 0.5$ .

These oscillations require a different criterion for determine  $\mathcal{L}$ , which is given by  $|u - u_{fd}| \leq 0.01u_{fd}$ .

For  $El = 1$  the results are qualitatively similar to the ones obtained for  $El = 0.1$ . We see in Table 10.3 that the development length is smaller for  $El = 1$ , specially for high values of  $De$ . Notice that the oscillations shown for  $El = 0.1$  are not present for  $El = 1$  and  $0 \leq$

$De \leq 0.5$ . This happens because the Reynolds numbers used for  $El = 1$  are smaller than the the ones used for  $El = 0.1$ , thus reducing the effect of inertia.

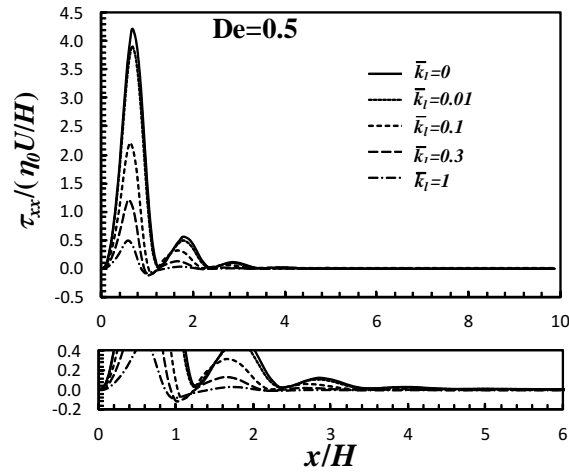


Figure 10.9: Variation of the dimensionless normal stress,  $\tau_{xx}/(\eta_0 U/H)$ , along the centerplane of the channel, for a constant elasticity number,  $El = 0.1$ , and three different Deborah numbers,  $De = 0.01, 0.2, 0.5$ .

## 10.5 CONCLUSIONS

Simulations were performed to evaluate the influence of the slip boundary condition on the entry flow of viscoelastic fluids, following a UCM stress model. Except for very small Deborah numbers, the presence of slip velocity leads to a reduction of the development length for both streamwise velocity component and normal stress. This was verified both for creeping flow and for an elasticity number of 0.1 and 1. For very small Deborah numbers the behaviour approaches the one of the Newtonian fluids, showing a maximum of the development length. For a Mach number greater than one,  $Ma_e \geq 1$ , oscillations occur for both velocity and normal stress, and the presence of slip velocity smooths the oscillations.

## ACKNOWLEDGEMENTS

The authors acknowledge funding from FEDER and Fundação para a Ciência e a Tecnologia (FCT), Portugal, through projects PTDC/EQU-FTT/70727/2006 and PTDC/EQU-FTT/113811/2009, and FEDER, via FCT, under the PEst-C/CTM/LA0025/2011 (Strategic Project - LA 25 - 2011-2012). LLF and AMA would like to thank FCT for financial support through scholarships SFRH/BD/37586/2007 and SFRH/BPD/75436/2010, respectively.





Part V

ELECTRO OSMOTIC FLOW



## INTRODUCTION TO PART V

In this Part, the following papers based on analytical solutions for mixed electro-osmotic/pressure driven slip-flows of Newtonian and viscoelastic fluids, are presented:

▷A.M. Afonso, L.L. Ferrás, J.M. Nóbrega, M.A. Alves, F.T. Pinho (2012), Mixed electro-osmotic/pressure driven slip-flows of viscoelastic fluids in hydrophobic microchannels, to be submitted to *Journal of Non-Newtonian Fluid Mechanics*;

▷A.M. Afonso, L.L. Ferrás, J.M. Nóbrega, M.A. Alves, F.T. Pinho (2012), Pressure-driven electrokinetic slip-flows of viscoelastic fluids in hydrophobic microchannels with assymmetric zeta potential, to be submitted to *Journal of Colloid and Interface Science*;



## MIXED EO/PD SLIP-FLOWS OF VISCOELASTIC FLUIDS

---

### Abstract<sup>1</sup>

*Analytical solutions are presented for the flow of viscoelastic fluids in hydrophobic microchannels under the combined influences of electrokinetic and pressure forcings using the Debye-Hückel approximation and accounting for wall slip. The viscoelastic fluids used are described by the simplified Phan-Thien-Tanner model with linear kernel for the stress coefficient function, or the FENE-P model based on the kinetic theory for finitely extensible dumbbells with a Peterlin approximation for the average spring force. The slip boundary conditions are described using the linear and nonlinear Navier slip laws. The combined effects of the slip boundary conditions, fluid rheology, electro-osmotic and pressure gradient forcings on the fluid velocity distribution and streaming potential are discussed.*

### 11.1 INTRODUCTION

The no-slip boundary condition is usually accepted as a law, and not as an empirical formula (Lamb, 1932). This happens because of the good agreement between experiments and theory over a large number of experiments made with Newtonian fluids since the early stages of fluid dynamics. With the evolution of fluid mechanics toward micro and nano-scales together with evidence of wall slip during experimental works with Newtonian and non-Newtonian fluids, and with the help of numerical simulations, the validity of the no-slip law was questioned. Nowadays, the wall slip velocity phenomenon in fluids is an accepted fact and the observation of wall slip in viscoelastic fluid flows is a fact that has been reinforced consistently in the literature over the years. Denn (2001) and (Lauga et al., 2005) provided a good account of slip effects including measurements and theoretical approaches for Newtonian and non-Newtonian fluids. Kazatchkov and Hatzikiriakos (2010) and (Hatzikiriakos, 2012) provide new physical models that are able to capture the slippery characteristics of certain viscoelastic fluids. Hatzikiriakos (2012) also showed the good agreement between numerical and physical data for the multimode dynamic slip boundary conditions. All these works refer to for pressure-driven flows.

For electro-osmotic driven flows the existence of slip velocity was more readily accepted (Zhu and Granick, 2001; Tretheway and Meinhart,

---

<sup>1</sup> A.M. Afonso, L.L. Ferrás, J.M. Nóbrega, M.A. Alves, F.T. Pinho (2012), Mixed electro-osmotic/pressure driven slip-flows of viscoelastic fluids in hydrophobic microchannels, to be submitted to *Journal of Non-Newtonian Fluid Mechanics*;

2002, 2004; Tandon et al., 2008; Park and Kim, 2009). For flows with charged walls and polar fluids a thin electric double layer (EDL) is formed in the vicinity of the walls, where the imbalance of positive and negative ions results in an electric force that affects the fluid flow. At the scales typical in microfluidics, the interaction between the wall and the fluid leads to electrokinetics phenomena, which are strongly dependent on surface and fluid chemistry, the possible existence of gas near the wall, wall roughness and other local properties. If the wall surface is treated either by physical or chemical means, with the purpose of modifying its surface properties, the wall hydrophobicity or the slip characteristic can be tuned. This modification of the interfacial condition may result in a change in the wall zeta potential, but since it is difficult to model the details of the surface condition, such as roughness or gas bubble attached, the resultant fluid slippage is usually described by using the Navier law (Navier, 1822) with slip length as an index just like the slippage data listed by (Voronov et al., 2008). Churaev et al. (2002) presented a simple linear relationship between zeta potential and slip length. In a study of simultaneously determining slip and zeta potential, (Yang and Kwok, 2002) obtained a modified expression by introducing a modification factor, appropriate for low zeta potentials in the Debye-Hückel model. Using molecular dynamics simulations, (Joly et al., 2004) disclosed that the immobile layer disappears in the cases of non-wetting (i.e., hydrophobic) surfaces, and the zeta potential deduced from electrokinetic effects is thus considerably amplified by the existence of slippage at the solid surface. More recently, a nonlinear expression for a dilute  $z$ - $z$  symmetric electrolyte was proposed in the review article by Tandon et al. (Tandon et al., 2008).

In order to assess if the proposed slip models are reliable, analytical solutions and numerical simulations are important tools, and, even for the latter, the analytical solutions are again of major importance for code verification under simplified flow conditions. These facts, together with the urge of understanding slip in fluid flows, are the main motivations of this work. On what concerns analytical solutions for viscoelastic fluids with slip boundary conditions, we can distinguish two cases: the pressure-driven viscoelastic fluid motion and the viscoelastic fluid motion driven by a combination of electro-osmotic and pressure forcings. For the first case we have a wide range of literature contributions, such as (Fujita, 2002) who looked at the well-posedness of the Navier-Stokes system of equations with slip boundary conditions, (Mitsoulis and Hatzikiriakos, 2009; Hatzikiriakos and Mitsoulis, 2009) who investigated generalized non-Newtonian fluid flows and the non-linear Navier slip boundary condition and (Pereira, 2009) who analysed microfluidic flows for Newtonian, generalized Newtonian and viscoelastic fluids governed by the White-Metzner model using the linear Navier slip boundary condition. For the simplified Phan-

Thien—Tanner (sPTT) (Phan-Thien and Tanner, 1977; Phan-Thien, 1978) and Giesekus (Giesekus, 1982) models, analytical solutions with slip boundary conditions were discussed by (Ferrás et al., 2012c), who extended several previous investigations to other common slip laws (four different slip boundary conditions were used). Naturally, in the absence of wall slip there is a wealth of analytical solutions and for the PTT fluid we single out the solutions for channel and pipe flows (Oliveira and Pinho, 1999a; Alves et al., 2001a).

For the second case, viscoelastic fluid motion driven by a combination of electro-osmotic and pressure forcings in the presence of wall slip, we are only aware of analytic solutions for Newtonian fluids. Ngoma and Erchiqui (2007) investigated numerically and analytically the effects of heat flux and boundary slip on electrokinetic flows invoking the Debye-Hückel approximation. Yang and Kwok (2004) presented analytical solutions of time-dependent microfluidic flow in rectangular hydrophobic microchannels by combining electrokinetic effect with wall slip. Soong et al. (2010) analysed pressure-driven electrokinetic flows in hydrophobic microchannels using a nonlinear slip-dependent zeta potential for dilute  $z$ - $z$  symmetric electrolytes, and (Jamaati et al., 2010) investigated pressure-driven electrokinetic slip-flow in planar microchannels. For non-Newtonian fluids the existing analytical solutions are for no-slip at the wall. Here, (Zhao and Yang, 2011) report a theoretical analysis of electro-osmotic mobility of non-Newtonian fluids and (Afonso et al., 2009b, 2011a) present analytical solutions of mixed electro-osmotic/pressure driven viscoelastic fluids in microchannels, including for the case of electro-osmotic flow under asymmetric zeta potential. (Sousa et al., 2011) considered the formation of a skimming layer without polymer additives near the walls, and (Dhinakaran et al., 2010) analysed the channel flow for the full PTT model with non-zero second normal stress difference, but only considering EOF without an imposed pressure gradient. Recently, (Afonso et al., 2012) derived the analytical solution for fully-developed electro-osmosis driven flow of polymer solutions described by the sPTT and FENE-P (Bird et al., 1980) models with a Newtonian solvent.

The objectives of this work are then to fill this gap in the literature and to add some enlightenment to the understanding of the slip velocity phenomena in combined electro-osmotic/pressure-driven viscoelastic flows. The paper starts with the set of governing equations, including the nonlinear Poisson–Boltzmann equation governing the EDL field and the added body force to the momentum equation caused by the applied electrical potential field. The simplifications required to obtain the analytical solution are discussed, the solutions are presented and a discussion of the effects of the various relevant nondimensional parameters upon the flow characteristics are presented before the conclusions of the work.

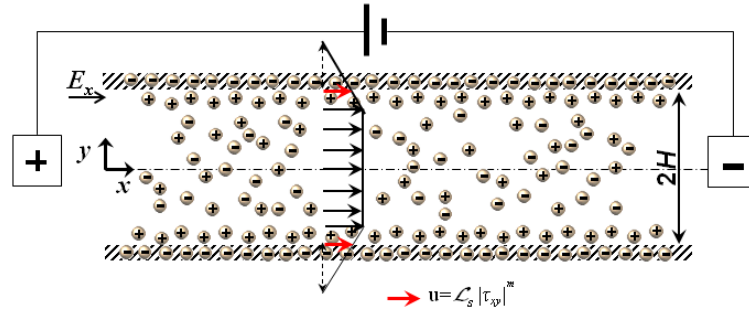


Figure 11.1: Schematic of the flow in a microchannel.

## 11.2 GOVERNING EQUATIONS

The steady, isothermal and fully-developed flow of an incompressible viscoelastic fluid is sketched in Figure 12.1. The basic governing equations describing this fully-developed flow for incompressible fluids are the continuity equation,

$$\nabla \cdot \mathbf{u} = 0 \quad (11.1)$$

and the momentum equation,

$$-\nabla p + \nabla \cdot \boldsymbol{\tau} + \rho_e \mathbf{E} = \mathbf{0} \quad (11.2)$$

where  $\mathbf{u}$  is the velocity vector,  $p$  the pressure,  $\rho$  the fluid density and  $\boldsymbol{\sigma}$  the polymeric extra-stress contribution. The  $\rho_e \mathbf{E}$  term of equation (11.2) represents a body force per unit volume, where  $\mathbf{E}$  is the applied external electric field and  $\rho_e$  is the net electric charge density in the fluid. The electric field is related to the electric potential,  $\Phi$ , by

$$\mathbf{E} = -\nabla \Phi \quad (11.3)$$

while the electric potential is governed by,

$$\nabla^2 \Phi = -\frac{\rho_e}{\epsilon} \quad (11.4)$$

where  $\epsilon$  is the electrical permittivity of the solution. Two electric fields are relevant in EOF flows: one is the applied electric field,  $\phi$ , generated by the electrodes at the inlet and outlet of the flow geometry; the other electric field is due to the net charge distribution in the EDL,  $\psi$ , associated to the charge acquired by the fluid near the walls. The total electric field is given by linear superposition of these two contributions,

$$\Phi = \phi + \psi \quad (11.5)$$

Equations (11.4) and (11.5) can be rewritten as two separate equations (Bruss, 2008),

$$\nabla^2 \phi = 0 \quad (11.6)$$



and

$$\nabla^2 \psi = -\frac{\rho_e}{\epsilon}. \quad (11.7)$$

In many circumstances, when the flow (and the ionic distribution) is stationary, the electric double layer does not overlap at the center of the channel and significant variations of  $\psi$  occur only in the normal direction to the channel walls, in which case the stable Boltzmann distribution of ions in the electric double layer can be assumed. In this situations the electric charge density can be obtained by a Poisson–Boltzmann equation, by the following distribution (Bruss, 2008):

$$\rho_e = -2n_0 e z \sinh\left(\frac{e z}{k_B T} \psi\right) \quad (11.8)$$

where  $n_0 = CN_A$  is the bulk number concentration of ions in the electrolyte solution,  $C$  is the molar concentration of ions,  $N_A$  is Avogadro's number,  $T$  is the absolute temperature and  $k_B$  is the Boltzmann constant. For small values of  $e z \zeta_s / k_B T$ , synonymous of a small ratio of electrical to thermal energies, equation (11.8) can also be linearized, since  $\sinh x \approx x$  ( $\zeta_s$  is the maximum value of  $\psi$ , at the wall). This is the so-called Debye–Hückel approximation for which the electric charge density equation becomes

$$\rho_e = -\epsilon \kappa^2 \psi \quad (11.9)$$

where  $\kappa^2 = \frac{2n_0 e^2 z^2}{\epsilon k_B T}$  is the Debye–Hückel parameter, related to the thickness of the Debye layer, (also referred to as the EDL thickness,  $\lambda_D = \kappa^{-1}$ ).

### 11.2.1 Constitutive equations

The polymer extra-stress  $\boldsymbol{\sigma}$  tensor in equation (11.2) needs to be described by an appropriate constitutive equation, and in this work we consider two models to be described in the next sections.

#### *PTT model*

The first model here considered was proposed by Phan-Thien and Tanner (Phan-Thien and Tanner, 1977; Phan-Thien, 1978), based on network theory arguments, in the form:

$$f(\tau_{kk}) \boldsymbol{\tau} + \lambda \overset{\nabla}{\boldsymbol{\tau}} = 2\eta \mathbf{D} \quad (11.10)$$

where  $\mathbf{D} = (\nabla \mathbf{u}^T + \nabla \mathbf{u}) / 2$  is the rate of deformation tensor,  $\lambda$  is the relaxation time of the fluid,  $\eta$  is a polymer viscosity coefficient and  $\overset{\nabla}{\boldsymbol{\sigma}}$  represents the upper-convected derivative of  $\boldsymbol{\sigma}$ , defined as

$$\overset{\nabla}{\boldsymbol{\tau}} = \frac{D\boldsymbol{\tau}}{Dt} - \nabla \mathbf{u}^T \cdot \boldsymbol{\tau} - \boldsymbol{\tau} \cdot \nabla \mathbf{u} \quad (11.11)$$

The stress coefficient function,  $f(\tau_{kk})$ , is given by the linear form (Phan-Thien and Tanner, 1977)

$$f(\tau_{kk}) = 1 + \frac{\varepsilon\lambda}{\eta} \tau_{kk} \quad (11.12)$$

where  $\tau_{kk}$  represents the trace of the extra-stress tensor and  $\varepsilon$  is the extensibility parameter that imposes an upper limit to the elongational viscosity. For  $\varepsilon = 0$  the upper-convected Maxwell model (UCM) is recovered.

#### 11.2.1.1 FENE-P model

The second viscoelastic model used in this work is the FENE-P equation, based on the kinetic theory for finitely extensible non-linear elastic (FENE) dumbbells with a Peterlin approximation for the average spring force. In this case the polymer extra-stress is given by (Bird et al., 1980):

$$Z(\tau_{kk})\boldsymbol{\tau} + \lambda \overset{\nabla}{\boldsymbol{\tau}} - \lambda \left( \boldsymbol{\tau} - \frac{b}{b+2} n k_B T \mathbf{I} \right) \frac{D \ln Z}{Dt} = 2\eta \left( \frac{b+5}{b+2} \right) \mathbf{D} \quad (11.13)$$

where  $\mathbf{I}$  is the identity tensor,  $b$  is a parameter that measures the extensibility of the dumbbell,  $k_B$  is the Boltzmann constant,  $T$  is the absolute temperature and  $n$  is a parameter of the model (Bird et al., 1980). The stress coefficient function,  $Z(\tau_{kk})$ , is given by (Bird et al., 1980),

$$Z(\tau_{kk}) = 1 + 3 \left( \frac{1}{b+2} + \frac{\lambda}{3\eta} \frac{\tau_{kk}}{b+5} \right) \quad (11.14)$$

Note that for fully-developed flows  $D \ln Z / Dt = 0$  and equation (11.13) becomes considerably simplified.

#### 11.2.2 Boundary conditions and slip-flow assumptions

Since we assume that the microchannel walls are hydrophobic, and therefore the immobile layer disappears in the cases of non-wetting surface, we have the necessity of slip boundary conditions at the wall. The chosen slip boundary condition is the non-linear Navier slip law (Navier, 1822; Schowalter, 1988) given by

$$u_{\parallel y=H} = \mathcal{L}_s \text{sign} \left( \frac{du}{dy} \Big|_{y=H} \right) \left| \tau_{xy} \Big|_{y=H} \right|^m \quad (11.15)$$

where  $\mathcal{L}_s$  represents the non-linear Navier slip coefficient. For  $m = 1$ , the classical linear Navier slip law (Navier, 1822) is recovered.

## 11.3 ANALITICAL SOLUTION

## 11.3.1 Analytical solution for the PTT model

For fully developed channel flow of viscoelastic fluids driven mixed electro-osmotic/pressure driving forcings, the momentum equation - equation (11.2) - reduces to

$$\frac{d\tau_{xy}}{dy} = -\rho_e E_x + p_{,x} \quad (11.16)$$

where  $y$  is the transverse coordinate,  $p_{,x} \equiv dp/dx$ ,  $E_x \equiv -d\phi/dx$  and  $\phi$  is the electric potential of the applied external field, which is characterized by a constant streamwise gradient under fully-developed flow conditions. Note that in this flow the external electrical field is positive according to Fig. 12.1, and negative otherwise. In this flow the Poisson-Boltzmann distribution is valid and additionally we invoke the Debye-Hückel approximation (see (Afonso et al., 2009b) for justifications). Since eq. (11.7) can be solved subjected to  $d\psi/dy = 0$  at the symmetry plane/axis and the zeta potential at the wall,  $\zeta_s$ , leading to

$$\psi = \zeta_s \frac{\cosh(\kappa y)}{\cosh(\kappa H)} \quad (11.17)$$

for  $0 \leq |y| \leq H$ . The net charge density distribution, equation (11.9), in conjunction with equation (11.17) reduces to

$$\rho_e = -\epsilon \zeta_s \kappa^2 \frac{\cosh(\kappa y)}{\cosh(\kappa H)} \quad (11.18)$$

which is a positive quantity for a negatively charged wall ( $\zeta_s < 0$ ).

Noting that the shear stress at the centerline is zero, Eq. (11.16) can be integrated to yield the following linear contribution of electro-osmotic and pressure gradient contributions to the shear stress distribution

$$\tau_{xy} = \epsilon \zeta_s E_x \kappa \frac{\sinh(\kappa y)}{\cosh(\kappa H)} + p_{,x} y \quad (11.19)$$

For the same fully-developed flow conditions, the non-zero extra-stress components for the PTT model are defined as,

$$f(\tau_{kk})\tau_{xx} = 2\lambda \frac{du}{dy} \tau_{xy} \quad (11.20)$$

$$f(\tau_{kk})\tau_{xy} = \eta_p \frac{du}{dy} \quad (11.21)$$

where  $\tau_{kk} = \tau_{xx}$ , since  $\tau_{yy} = \tau_{zz} = 0$  (Phan-Thien and Tanner, 1977), and  $\frac{du}{dy}$  is the velocity gradient. Then, upon division of equation (11.20) by equation (11.21) the specific function  $f(\tau_{xx})$  cancels out, and the following relation between the normal and shear stresses is obtained,

$$\tau_{xx} = 2 \frac{\lambda}{\eta_p} \tau_{xy}^2. \quad (11.22)$$

Using these relations, an explicit expression for the normal stress component can be obtained,

$$\tau_{xx} = 2\frac{\lambda}{\eta} \left( \epsilon\zeta_s E_x \kappa \frac{\sinh(\kappa y)}{\cosh(\kappa H)} + p_{,x} y \right)^2 \quad (11.23)$$

To determine the velocity gradient, equations (11.21), (11.19) and (11.23) are combined to give

$$\dot{\gamma} \equiv \frac{du}{dy} = \left[ 1 + 2\epsilon\lambda^2 \left( \frac{\kappa\epsilon\zeta_s E_x}{\eta} \frac{\sinh(\kappa y)}{\cosh(\kappa H)} + \frac{p_{,x}}{\eta} y \right)^2 \right] \left( \frac{\kappa\epsilon\zeta_s E_x}{\eta} \frac{\sinh(\kappa y)}{\cosh(\kappa H)} + \frac{p_{,x}}{\eta} y \right) \quad (11.24)$$

It is often more convenient to work with the dimensionless form of equation (11.24). Introducing the normalizations,  $\bar{u} = u/u_{sh}$ ,  $\bar{y} = y/H$  and  $\bar{\kappa} = \kappa H$ , the dimensionless velocity gradient can be written as

$$\frac{\dot{\gamma}}{u_{sh}/H} \equiv \frac{d\bar{u}}{d\bar{y}} = \left[ 1 + 2\frac{\epsilon De_\kappa^2}{\bar{\kappa}^2} \left( \Gamma \bar{y} - \bar{\kappa} \frac{\sinh(\bar{\kappa} \bar{y})}{\cosh(\bar{\kappa})} \right)^2 \right] \left( \Gamma \bar{y} - \bar{\kappa} \frac{\sinh(\bar{\kappa} \bar{y})}{\cosh(\bar{\kappa})} \right) \quad (11.25)$$

where  $De_\kappa = \frac{\lambda u_{sh}}{\xi} = \lambda \kappa u_{sh}$  is the Deborah number based on the EDL thickness and on the Helmholtz-Smoluchowski electro-osmotic velocity, defined as  $u_{sh} = -\frac{\epsilon\zeta_s E_x}{\eta}$ . In Poiseuille flows a different Deborah number is usually defined (Oliveira and Pinho, 1999a) based on the bulk velocity for the Newtonian flow under the sole influence of pressure gradient and the channel half-height,  $De_N = \frac{\lambda U_N}{H}$  with  $U_N = -\frac{H^2 p_{,x}}{3\eta}$ . A third alternative Deborah number for electro-osmotic flow is based again on  $u_{sh}$ , but considers the channel half-height,  $De_{sh} = \frac{\lambda u_{sh}}{H}$ . These three Deborah numbers are related by  $De_\kappa = \bar{\kappa} De_{sh} = -\frac{3}{\Gamma} \bar{\kappa} De_N$ , where the dimensionless parameter  $\Gamma = -\frac{H^2 p_{,x}}{\epsilon\zeta_s E_x}$  represents the ratio of pressure to electro-osmotic driving forcings. Equation (11.25) can be integrated subject to the dimensionless slip boundary condition at the wall,

$$\frac{u}{u_{sh}} \Big|_{\bar{y}=1} = \bar{\mathcal{L}}_s (\bar{\kappa} \bar{D} - \Gamma)^m \quad (11.26)$$

where  $\bar{\mathcal{L}}_s = \mathcal{L}_s \left( \frac{\eta}{H} \right)^m (u_{sh})^{m-1}$  and the resulting dimensionless velocity profile is

$$\begin{aligned} \frac{u}{u_{sh}} &= \bar{\mathcal{L}}_s (\bar{\kappa} \bar{D} - \Gamma)^m + (1 - 2\bar{\mathcal{C}}\epsilon De_\kappa^2)(1 - \bar{A}) + \frac{2}{3}\epsilon De_\kappa^2(1 - \bar{A}^3) \\ &\quad - \frac{1}{2}\Gamma(1 - \bar{y}^2) \left[ 1 + \frac{\epsilon De_\kappa^2}{\bar{\kappa}^2} \Gamma^2 (1 + \bar{y}^2) \right] \\ &\quad + \frac{3}{2} \frac{\epsilon De_\kappa^2}{\bar{\kappa}^2} \Gamma \left[ 1 - \bar{A}^2 + (\bar{\kappa}^2 - (\bar{\kappa} \bar{y})^2) \bar{\mathcal{C}} + 2\bar{\kappa} \bar{D} (\bar{y} \bar{A} \bar{B} - 1) \right] \\ &\quad - \frac{12\epsilon De_\kappa^2}{\bar{\kappa}^4} \Gamma^2 \left[ \bar{\kappa} \bar{D} (1 - \bar{y} \bar{B}) + (1 + \frac{1}{2} (\bar{\kappa} \bar{y})^2) \bar{A} - (1 + \frac{1}{2} \bar{\kappa}^2) \right] \end{aligned} \quad (11.27)$$

where  $\bar{A} = \frac{\cosh(\bar{\kappa}\bar{y})}{\cosh(\bar{\kappa})}$ ,  $\bar{B} = \frac{\sinh(\bar{\kappa}\bar{y})}{\sinh(\bar{\kappa})}$ ,  $\bar{C} = \frac{1}{\cosh^2(\bar{\kappa})}$  and  $\bar{D} = \tanh(\bar{\kappa})$ .

Equation (11.27) couples the Poiseuille and electro-osmotic flows with terms that are simultaneously proportional to  $p_{,x}$  and  $E_x$ . This contribution only exists because the fluid is nonlinear, i.e., no such effect is present if the fluid is Newtonian or a quasi-linear viscoelastic fluid, such as UCM fluid. Equation (11.27) shows that the superposition principle valid for Newtonian and quasi-linear viscoelastic fluids is no longer valid for the PTT and FENE-P fluids, as proposed by (Afonso et al., 2009b, 2011a).

Flow problems are usually of direct or indirect/inverse type. In a direct problem the pressure gradient  $p_{,x}$  and the applied electric potential gradient  $E_x$  are known (or instead the ratio of pressure to electro-osmotic driving forces is known) and the flow rate, or the cross-sectional average velocity, is required. The flow rate can be determined from integration of the normalized velocity profile, equation (11.27), thinking ahead on the benefit this brings to the inverse problem, where the aim is the determination of  $\Gamma$  for a given dimensionless flow rate. The expression for the normalized flow rate is

$$\begin{aligned} \bar{Q} &= \frac{Q}{Hu_{sh}} = \frac{2\bar{u}}{u_{sh}} = \int_{-1}^1 \frac{u}{u_{sh}} d\bar{y} = 2 \int_0^1 \frac{u}{u_{sh}} d\bar{y} = 2\bar{\mathcal{L}}_s (\bar{\kappa}\bar{D} - \Gamma)^m \\ &\quad + 2(1 - 2\bar{C}\varepsilon De_\kappa^2) \left(1 - \frac{\bar{D}}{\bar{\kappa}}\right) + \frac{4}{3}\varepsilon De_\kappa^2 \left(1 - \frac{1}{3}\frac{\bar{D}}{\bar{\kappa}}(1 + 2\bar{C})\right) \\ &\quad - 2\Gamma \left(\frac{2}{5}\frac{\varepsilon De_\kappa^2}{\bar{\kappa}^2}\Gamma^2 + \frac{1}{3}\right) + 3\frac{\varepsilon De_\kappa^2}{\bar{\kappa}^2}\Gamma \left(2 - \frac{\bar{D}}{\bar{\kappa}} - \bar{C} + \frac{2}{3}\bar{C}\bar{\kappa}^2 - 2\bar{\kappa}\bar{D}\right) \\ &\quad - \frac{24\varepsilon De_\kappa^2}{\bar{\kappa}^4}\Gamma^2 \left(-3 + 3\frac{\bar{D}}{\bar{\kappa}} + \frac{3}{2}\bar{\kappa}\bar{D} - \frac{1}{2}\bar{\kappa}^2\right) \end{aligned} \quad (11.28)$$

For Navier slip coefficient with  $m = 1, 2$  and  $3$ , this is a cubic equation on  $\Gamma$  and the solution of the inverse problem (calculation of  $\Gamma$  for a given  $\bar{Q}$ ) involves the determination of  $\Gamma$ , which can be done using the Cardan-Tartaglia solution for cubic algebraic equations. Within the assumptions invoked in the previous sections, the analysis in this section is general, but relies on the Debye-Hückel approximation. Here, as in many practical applications the finite electric double layer is very small, about 1 to 3 orders of magnitude smaller than the thickness of the microfluidic channel ( $10 \lesssim \bar{\kappa} \lesssim 10^3$ ). In these circumstances  $\cosh(\bar{\kappa}) \gg 1$  and  $\bar{D} = \tanh(\bar{\kappa}) \approx 1$ , so the above equations for the velocity profile can be further simplified. In particular the normalized flow rate becomes

$$\begin{aligned} \bar{Q} &\simeq 2\bar{\mathcal{L}}_s (\bar{\kappa} - \Gamma)^m + 2 \left(\frac{\bar{\kappa} - 1}{\bar{\kappa}}\right) + \frac{4}{3}\varepsilon De_\kappa^2 \left(\frac{3\bar{\kappa} - 1}{3\bar{\kappa}}\right) - \left(\frac{4\varepsilon De_\kappa^2 \Gamma^3}{5\bar{\kappa}^2} + \frac{2\Gamma}{3}\right) \\ &\quad + 3\frac{\varepsilon De_\kappa^2}{\bar{\kappa}^2}\Gamma \left(\frac{2\bar{\kappa} - 1 - 2\bar{\kappa}^2}{\bar{\kappa}}\right) - \frac{24\varepsilon De_\kappa^2}{\bar{\kappa}^4}\Gamma^2 \left(\frac{\bar{\kappa}}{2}(3 - \bar{\kappa}) + \frac{3 - 3\bar{\kappa}}{\bar{\kappa}}\right) \end{aligned} \quad (11.29)$$

which is simpler than equation (??), but still cubic in  $\Gamma$  for  $m = 1, 2$  and  $3$ . This expression can be written in compact as

$$\Gamma^3 + a_1\Gamma^2 + a_2\Gamma + a_3 = 0 \quad (11.30)$$

for  $m = 1, 2$  or  $3$ . The explicit solution of the inverse problem, giving the ratio of pressure to electro-osmotic driving forces as a function of the dimensionless flow rate, viscoelastic model parameters and relative microchannel ratio is obtained using the Cardan-Tartaglia solution,

$$\begin{aligned} \Gamma &= \sqrt[3]{-\frac{b_1}{2} + \sqrt{\frac{b_1^2}{4} + \frac{a^3}{27}}} + \sqrt[3]{-\frac{b_1}{2} - \sqrt{\frac{b_1^2}{4} + \frac{a^3}{27}}} - \frac{a_1}{3} \\ a &= a_2 - \frac{a_1^2}{3} \\ b_1 &= a_3 - \frac{a_1 a_2}{3} + \frac{2a_1^3}{27} \end{aligned} \quad (11.31)$$

with

$$\begin{aligned} a_1 &= \frac{24 \frac{\varepsilon D e_\kappa^2}{\bar{\kappa}^4} \left( \frac{\bar{\kappa}}{2} (3 - \bar{\kappa}) + \frac{3-3\bar{\kappa}}{\bar{\kappa}} \right) - 2(m-1) \bar{\mathcal{L}}_s \left( \frac{3}{2} \bar{\kappa} \right)^{m-2}}{\left( \frac{4}{5} \frac{\varepsilon D e_\kappa^2}{\bar{\kappa}^2} + 2\delta_{m3} \bar{\mathcal{L}}_s \right)} \\ a_2 &= \frac{\frac{2}{3} - 3 \frac{\varepsilon D e_\kappa^2}{\bar{\kappa}^2} \left( \frac{2\bar{\kappa}-1-2\bar{\kappa}^2}{\bar{\kappa}} \right) + 2m \bar{\mathcal{L}}_s \bar{\kappa}^{m-1}}{\left( \frac{4}{5} \frac{\varepsilon D e_\kappa^2}{\bar{\kappa}^2} + 2\delta_{m3} \bar{\mathcal{L}}_s \right)} \\ a_3 &= \frac{\bar{Q} - 2 \left( \frac{\bar{\kappa}-1}{\bar{\kappa}} \right) - \frac{4}{3} \varepsilon D e_\kappa^2 \left( \frac{3\bar{\kappa}-1}{3\bar{\kappa}} \right) - 2 \bar{\mathcal{L}}_s \bar{\kappa}^m}{\left( \frac{4}{5} \frac{\varepsilon D e_\kappa^2}{\bar{\kappa}^2} + 2\delta_{m3} \bar{\mathcal{L}}_s \right)} \end{aligned} \quad (11.32)$$

where  $\delta_{m3}$  is a Kronecker delta that assumes the value of 1 only for  $m = 3$  and 0 for  $m = 1$  and  $2$ .

The explicit expressions for the dimensionless shear and normal stress components are obtained from normalization of equations (11.19) and (11.23),

$$\frac{\tau_{xy}}{3\eta u_{sh}\kappa} = \frac{1}{3} \left[ \Gamma \frac{\bar{y}}{\bar{\kappa}} - \frac{\sinh(\bar{\kappa}\bar{y})}{\cosh(\bar{\kappa})} \right] \quad (11.33)$$

$$\frac{\tau_{xx}}{3\eta u_{sh}\kappa} = \frac{2}{3} D e_\kappa \left( \Gamma \frac{\bar{y}}{\bar{\kappa}} - \frac{\sinh(\bar{\kappa}\bar{y})}{\cosh(\bar{\kappa})} \right)^2 \quad (11.34)$$

Wall values for all these quantities are useful and are obtained after setting  $\bar{y} = 1$  (and  $\tanh(\bar{\kappa}) \approx 1$  for  $\bar{\kappa} \gtrsim 10$ ):

$$\begin{aligned} \frac{\tau_{xy}}{3\eta u_{sh}\kappa} \Big|_w &\simeq \frac{1}{3} \left( \frac{\Gamma}{\bar{\kappa}} - 1 \right) \\ \frac{\tau_{xx}}{3\eta u_{sh}\kappa} \Big|_w &\simeq \frac{2}{3} D e_\kappa \left( \frac{\Gamma}{\bar{\kappa}} - 1 \right)^2 \end{aligned} \quad (11.35)$$

## 11.3.2 Streaming potential solution

In the solution of the previous section, the electrical field  $E_x$  can be applied externally or be a consequence of electric potentials created by the flow. In the absence of an externally applied electrical field, the imposed pressure difference causes a flow containing ions in motion, hence it causes an electrical current, called the streaming current,  $I'_s$ . The streaming current accumulates counter-ions at the end of the channel therefore setting up an electric field,  $E_{x,sp}$  which is associated with the so-called streaming potential,  $\phi_{sp}$  via  $E_{x,sp} = -\Delta\phi_{sp}/l$ . Therefore, this induced electric field opposes the flow and creates an opposite current,  $I'_c$ , called conduction current. The net electrical current,  $I'$ , is the sum of the streaming current with the electrical conduction current and in steady-state should be zero:

$$I' = I'_s + I'_c \equiv 0 \quad (11.36)$$

The electrical streaming current (per unit of width) is of the form:

$$I'_s = 2 \int_0^H u(y)\rho_e(y)dy \quad (11.37)$$

which for the particular case of the PTT fluid leads to

$$\begin{aligned} \frac{I'_s}{\epsilon\zeta_s} &= 2\mathcal{L}_s (\epsilon\zeta_s E_x \kappa \bar{D} + p_{,x} H)^m (\kappa \bar{D}) \\ &+ \kappa \left[ \frac{\epsilon\zeta_s E_{x,sp}}{\eta} \right] \left[ \bar{D} - \kappa H \bar{C} + \kappa^2 \epsilon \lambda^2 \left[ \frac{\epsilon\zeta_s E_{x,sp}}{\eta} \right]^2 \left[ \bar{D} + \frac{3}{2} \kappa H \bar{C}^2 - \frac{5}{2} \bar{D} \bar{C} \right] \right] \\ &+ \frac{2}{\kappa} \left[ \frac{p_{,x}}{\eta} \right] \left[ \kappa H - \bar{D} + \frac{\left[ \frac{p_{,x}}{\eta} \right]^2 2\epsilon \lambda^2}{\kappa^2} (\kappa^3 H^3 - 6\bar{D} - 3\kappa^2 H^2 \bar{D} + 6\kappa H) \right] \\ &+ 4\kappa \epsilon \lambda^2 \left[ \frac{\epsilon\zeta_s E_{x,sp}}{\eta} \right]^2 \left[ \frac{p_{,x}}{\eta} \right] \left[ -\frac{1}{3} \bar{D} + \kappa H \bar{D}^2 - 2\kappa H \bar{C} + \frac{7}{3} \bar{D} \bar{C} \right] + \\ &\frac{2\epsilon \lambda^2}{\kappa} \left[ \frac{\epsilon\zeta_s E_{x,sp} p_{,x}^2}{\eta^3} \right] \left[ 3\kappa^2 H^2 \bar{D} - 12\kappa H \bar{D}^2 + \frac{3\bar{D}}{2} - (\kappa H)^3 \bar{C} + 9\kappa H - \frac{21}{2} \kappa H \bar{C} \right] \end{aligned} \quad (11.38)$$

The electrical conduction current in the channel can now be expressed as:

$$I'_c = 2\sigma_t E_{x,sp} H \quad (11.39)$$

where  $\sigma_t$  is the total electric conductivity. Note that the conduction current can now flow back through both the fluid as well as the channel walls, depending on the corresponding electrical conductivities. The total electrical conductivity can be calculated as  $\sigma_t = \sigma_{fluid} + \sigma_{sur} P_{sur} / A_{chan}$ , where  $P_{sur}$  and  $A_{chan}$  are the wetting perimeter and cross section area of the channel, respectively and  $\sigma_{fluid}$  and  $\sigma_{sur}$  are the fluid bulk and wall surface conductivities, respectively. This equation and the condition imposed by equation (11.36) leads finally to the expression that defines the relation between the imposed pressure gradient and the ensuing streaming electric field,  $E_{x,sp}$ . This ratio is  $\Gamma_{sp} = -\frac{H^2}{\epsilon\zeta_s} \frac{p_{,x}}{E_{x,sp}}$  and such relation is given by equation (11.40)

$$\begin{aligned}
 -2Y_1 &= 2\overline{\mathcal{L}}_s\overline{\kappa}\overline{D} (\overline{\kappa}\overline{D} - \Gamma_{sp})^m \\
 &\overline{\kappa}\overline{D} - \overline{\kappa}^2\overline{C} + 9\frac{\overline{\kappa}^3\varepsilon De_N^2}{\Gamma_{sp}^2} \left( \overline{D} + \frac{3}{2}\overline{\kappa}\overline{C}^2 - \frac{5}{2}\overline{D}\overline{C} \right) \\
 &- \frac{2}{\overline{\kappa}}\Gamma_{sp} \left[ \overline{\kappa} - \overline{D} + \frac{18\varepsilon De_N^2}{\overline{\kappa}^2} (\overline{\kappa}^3 - 6\overline{D} - 3\overline{\kappa}^2\overline{D} + 6\overline{\kappa}) \right] \\
 &- 36\frac{\overline{\kappa}\varepsilon De_N^2}{\Gamma_{sp}} \left[ -\frac{1}{3}\overline{D} + \overline{\kappa}\overline{D}^2 - 2\overline{\kappa}\overline{C} + \frac{7}{3}\overline{D}\overline{C} \right] \\
 &+ 18\frac{\varepsilon De_N^2}{\overline{\kappa}} \left[ 3\overline{\kappa}^2\overline{D} - 12\overline{\kappa}\overline{D}^2 + \frac{3}{2}\overline{D} - \overline{\kappa}^3\overline{C} + 9\overline{\kappa} - \frac{21}{2}\overline{\kappa}\overline{C} \right] \quad (11.40)
 \end{aligned}$$

with  $Y_1 = \frac{H^2\eta\sigma_i}{\varepsilon^2\zeta_s^2}$ . This new dimensionless number quantifies the effect of electric conductivity. Equation (11.40) is a cubic equation in  $\Gamma_{sp}$  for  $m = 1$ , and for such linear Navier slip law can be rewritten in compact form as

$$\Gamma_{sp}^3 + a_1\Gamma_{sp}^2 + a_2\Gamma_{sp} + a_3 = 0 \quad (11.41)$$

with coefficients

$$\begin{aligned}
 a_1 &= \frac{2Y_1 + \overline{\kappa}\overline{D} - \overline{\kappa}^2\overline{C} + 2\overline{\mathcal{L}}_s\overline{\kappa}^2\overline{D}^2}{2\left(\frac{\overline{D}-\overline{\kappa}}{\overline{\kappa}}\right) - 2\overline{\mathcal{L}}_s\overline{\kappa}\overline{D} - \frac{36\varepsilon De_N^2}{\overline{\kappa}^3} (\overline{\kappa}^3 - 6\overline{D} - 3\overline{\kappa}^2\overline{D} + 6\overline{\kappa})} + \\
 &+ \frac{18\frac{\varepsilon De_N^2}{\overline{\kappa}} \left[ 3\overline{\kappa}^2\overline{D} - 12\overline{\kappa}\overline{D}^2 + \frac{3}{2}\overline{D} - \overline{\kappa}^3\overline{C} + 9\overline{\kappa} - \frac{21}{2}\overline{\kappa}\overline{C} \right]}{2\left(\frac{\overline{D}-\overline{\kappa}}{\overline{\kappa}}\right) - 2\overline{\mathcal{L}}_s\overline{\kappa}\overline{D} - \frac{36\varepsilon De_N^2}{\overline{\kappa}^3} (\overline{\kappa}^3 - 6\overline{D} - 3\overline{\kappa}^2\overline{D} + 6\overline{\kappa})} \\
 a_2 &= \frac{-36\overline{\kappa}\varepsilon De_N^2 \left[ -\frac{1}{3}\overline{D} + \overline{\kappa}\overline{D}^2 - 2\overline{\kappa}\overline{C} + \frac{7}{3}\overline{D}\overline{C} \right]}{2\left(\frac{\overline{D}-\overline{\kappa}}{\overline{\kappa}}\right) - 2\overline{\mathcal{L}}_s\overline{\kappa}\overline{D} - \frac{36\varepsilon De_N^2}{\overline{\kappa}^3} (\overline{\kappa}^3 - 6\overline{D} - 3\overline{\kappa}^2\overline{D} + 6\overline{\kappa})} \\
 a_3 &= \frac{9\overline{\kappa}^3\varepsilon De_N^2 \left( \overline{D} + \frac{3}{2}\overline{\kappa}\overline{C}^2 - \frac{5}{2}\overline{D}\overline{C} \right)}{2\left(\frac{\overline{D}-\overline{\kappa}}{\overline{\kappa}}\right) - 2\overline{\mathcal{L}}_s\overline{\kappa}\overline{D} - \frac{36\varepsilon De_N^2}{\overline{\kappa}^3} (\overline{\kappa}^3 - 6\overline{D} - 3\overline{\kappa}^2\overline{D} + 6\overline{\kappa})} \quad (11.42)
 \end{aligned}$$

Equation (11.31) is also the solution of equation (11.41) for  $\Gamma_{sp}$ , but with the coefficients  $a_1$ ,  $a_2$  and  $a_3$  given by equation (11.42). For large  $\overline{\kappa}$ ,  $\cosh(\overline{\kappa}) \gg 1$  and  $\overline{D} = \tanh(\overline{\kappa}) \approx 1$ , and the above equations simplify to become

$$\begin{aligned}
 a_1 &= \frac{2Y_1 + \overline{\kappa} + 18\frac{\varepsilon De_N^2}{\overline{\kappa}} \left[ 3\overline{\kappa}^2 - 12\overline{\kappa} + \frac{3}{2} + 9\overline{\kappa} \right] + 2\overline{\mathcal{L}}_s\overline{\kappa}^2}{2\left(\frac{1-\overline{\kappa}}{\overline{\kappa}}\right) - 2\overline{\mathcal{L}}_s\overline{\kappa} - \frac{36\varepsilon De_N^2}{\overline{\kappa}^3} (\overline{\kappa}^3 - 3\overline{\kappa}^2 + 6\overline{\kappa} - 6)} \\
 a_2 &= \frac{-36\overline{\kappa}\varepsilon De_N^2 \left[ \overline{\kappa} + \frac{6}{3} \right]}{2\left(\frac{1-\overline{\kappa}}{\overline{\kappa}}\right) - 2\overline{\mathcal{L}}_s\overline{\kappa} - \frac{36\varepsilon De_N^2}{\overline{\kappa}^3} (\overline{\kappa}^3 - 3\overline{\kappa}^2 + 6\overline{\kappa} - 6)} \\
 a_3 &= \frac{9\overline{\kappa}^3\varepsilon De_N^2}{2\left(\frac{1-\overline{\kappa}}{\overline{\kappa}}\right) - 2\overline{\mathcal{L}}_s\overline{\kappa} - \frac{36\varepsilon De_N^2}{\overline{\kappa}^3} (\overline{\kappa}^3 - 3\overline{\kappa}^2 + 6\overline{\kappa} - 6)} \quad (11.43)
 \end{aligned}$$

As expected, equations (11.41) -(11.42) reduce to the solution without slip, as found in (Afonso et al., 2009b), when  $\overline{\mathcal{L}}_s \rightarrow 0$ , and to the Newtonian fluid solution, when  $\varepsilon \rightarrow 0$ :



$$\Gamma_{sp} = Y_1 \left[ \frac{1 + \frac{1}{2} \frac{\bar{\kappa}^2}{Y_1} \left( \frac{\bar{D}}{\bar{\kappa}} - \bar{C} \right)}{1 - \bar{D}/\bar{\kappa}} \right] \quad (11.44)$$

## 11.3.3 Analytical solutions for the FENE-P model

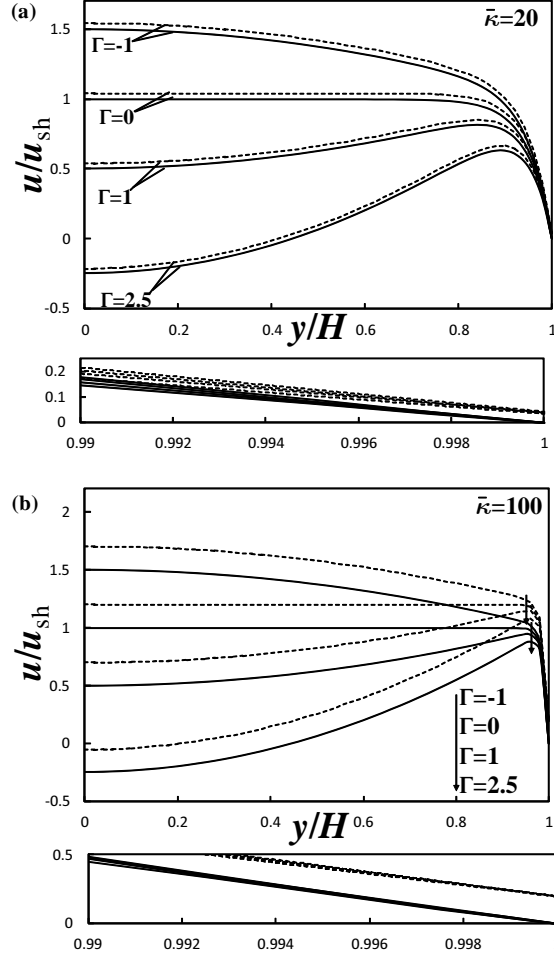


Figure 11.2: Velocity profiles for various ratios of pressure to electro-osmotic driving forcings,  $\Gamma$ , and various slip coefficients,  $\bar{\mathcal{L}}_s = 0$  and  $0.002$ , for Newtonian fluids with relative microchannell ratio of (a)  $\bar{\kappa} = 20$  and (b)  $\bar{\kappa} = 100$ .

For the FENE-P fluid in fully-developed shear flow between two parallel plates, i.e., subjected to the velocity field  $\mathbf{u} = \{u(y), 0, 0\}$ , equations (11.13) and (11.14) reduce to

$$Z(\tau_{kk})\tau_{xx} = 2\lambda\dot{\gamma}\tau_{xy} \quad (11.45)$$

$$Z(\tau_{kk})\tau_{xy} = \left( \frac{b+5}{b+2} \right) \eta\dot{\gamma} \quad (11.46)$$

Again, the trace of the extra-stress tensor becomes  $\boldsymbol{\sigma}_{kk} = \boldsymbol{\sigma}_{xx}$ , thus

$$Z(\tau_{xx}) = \left( \frac{b+5}{b+2} \right) \left[ 1 + \frac{\lambda}{\eta} \frac{(b+2)}{(b+5)^2} \tau_{xx} \right] \quad (11.47)$$

The relation between the normal and shear stresses is,

$$\tau_{xx} = 2 \frac{\lambda}{\eta} \left( \frac{b+2}{b+5} \right) \tau_{xy}^2 \quad (11.48)$$

For fully-developed channel flow there is similarity between the solutions for the PTT and the FENE-P models as found by (Oliveira, 2002). Comparing the equations for the PTT model with equations (11.45) and (11.46) for the FENE-P model, and since the momentum equation (11.16) is independent of the constitutive equation, there is an exact equivalence of the solution in the sense of a parameter to parameter match, as explained in detail in (Cruz et al., 2005). Hence, the solution of the previous sections also applies to the flow of FENE-P fluids, provided the following change of variables are made:

$$\begin{aligned} f(\tau_{xx}) &\rightarrow \left( \frac{b+2}{b+5} \right) Z(\boldsymbol{\sigma}_{xx}) \\ \lambda &\rightarrow \lambda \left( \frac{b+2}{b+5} \right) \\ \varepsilon &\rightarrow \frac{1}{b+5} \\ \eta &\rightarrow \eta \end{aligned} \quad (11.49)$$

#### 11.4 RESULTS AND DISCUSSION

In the previous section, general equations were derived for fully-developed flow of viscoelastic fluids, described by the sPTT and FENE-P models, under the mixed influence of electrokinetic and pressure-gradient forcings, including the account of microchannel wall hydrophobicity. The different influences of the driving forces and fluid rheology on the velocity profile have been identified in equation (11.27) and in this section we discuss in detail some limiting cases in order to understand the fluid dynamics. The following cases included in the general solution that will be discussed next are: (a) Newtonian fluid with mixed electro-osmotic/pressure driving forcings with wall slip; (b) Viscoelastic fluid under the sole influence of an electro-osmotic driving forcing with wall slip; (c) Poiseuille flow of a viscoelastic fluid with wall slip; (d) Viscoelastic fluid with mixed electro-osmotic/pressure driving forcings with wall slip. Case (c) was studied in detail by (Ferrás et al., 2012c), and so was case (a) by (Soong et al., 2010) and (Jamaati et al., 2010), but this latter situation is briefly revisited here as a starting point.

## 11.4.1 Newtonian fluid with mixed driving forcings with wall slip

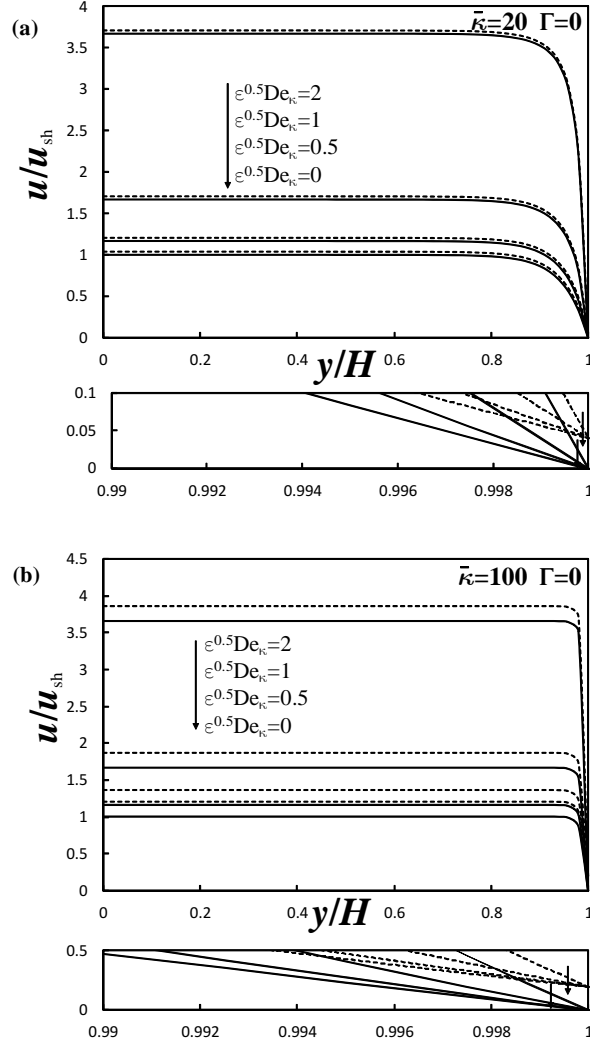


Figure 11.3: Dimensionless velocity profiles of a PTT fluid for various values of  $\sqrt{\epsilon}De_\kappa$  under pure electro-osmotic flow ( $\Gamma = 0$ ) ( $\bar{\mathcal{L}}_s = 0$  solid lines,  $\bar{\mathcal{L}}_s = 0.02$  dashed lines). (a)  $\bar{\kappa} = 20$  and (b)  $\bar{\kappa} = 100$ .

For a Newtonian fluid the relaxation time is zero and the Deborah number vanishes ( $De_\kappa = 0$ ), thus equation (11.27) becomes

$$\frac{u}{u_{sh}} = \bar{\mathcal{L}}_s (\bar{\kappa}\bar{D} - \Gamma)^m + (1 - \bar{A}) - \frac{1}{2}\Gamma(1 - \bar{y}^2) \quad (11.50)$$

under the mixed influence of electro-osmotic and pressure driving forcings. For linear Navier slip law ( $m = 1$ ), equation (11.50) reduces to that shown in (Jamaati et al., 2010). For  $\Gamma \rightarrow 0$ , the last term on the right-hand-side of equation (11.50) vanishes, the flow becomes governed solely by the electro-osmosis and the velocity profile is only a function of the wall distance and the relative microchannel ratio,  $\bar{\kappa}$ . For  $\frac{1}{\Gamma} \rightarrow 0$ , pressure forcing dominates the momentum transport,

and the classical laminar parabolic velocity profile is recovered. Figure 11.2 shows velocity profiles for various ratios of pressure gradient to electro-osmotic driving forcings at  $\bar{\kappa} = 20$  and  $\bar{\kappa} = 100$  for two different values of the slip coefficient,  $\bar{\mathcal{L}}_s = 0$  and 0.002. When  $\Gamma = 0$  the velocity profiles correspond to a *pluglike flow*. The cases  $\Gamma < 0$  and  $\Gamma > 0$  correspond to Poiseuille electro-osmotic flows with favorable and adverse pressure gradients, respectively. Equation (11.50) predicts negative velocities at  $\bar{y} = 0$  when  $\Gamma > \frac{2}{2\bar{\mathcal{L}}_s+1} \left( \frac{\cosh(\bar{\kappa})-1}{\cosh(\bar{\kappa})} \right) + \frac{2\bar{\mathcal{L}}_s}{2\bar{\mathcal{L}}_s+1} \bar{\kappa} \tanh(\bar{\kappa})$  for linear Navier slip law,  $m = 1$ . For small Debye lengths,  $\bar{\kappa} \gtrsim 10$ , the velocity becomes negative in the central region of the channel for  $\Gamma \gtrsim \frac{2+2\bar{\mathcal{L}}_s\bar{\kappa}}{2\bar{\mathcal{L}}_s+1}$ , which, as expected, reduces to the solution without slip,  $\Gamma \gtrsim 2$ , as found in (Afonso et al., 2009b) when  $\bar{\mathcal{L}}_s \rightarrow 0$ . When comparing with the no-slip solutions, we can see that the presence of slip velocity changes the velocity profile and requires larger adverse pressure gradients to obtain negative velocities.

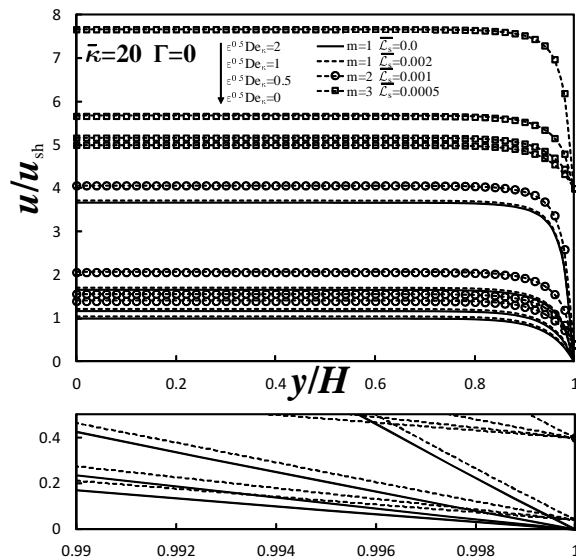


Figure 11.4: Dimensionless velocity profiles of a PTT fluid for various values of  $\sqrt{\epsilon}De_\kappa$ ,  $m$  and  $\bar{\mathcal{L}}_s$  and constant  $\bar{\kappa} = 20$  under pure electro-osmotic flow ( $\Gamma = 0$ ).

### 11.4.2 Viscoelastic fluid driven by electro-osmosis with wall slip

The discussion in this paper on viscoelastic flows is for a PTT fluid, but the analysis is identical for a FENE-P model provided the substitutions given before are made. For pure electro-osmotic flow ( $\Gamma = 0$ ) of a viscoelastic fluid, equation (11.27) reduces to

$$\frac{u}{u_{sh}} = \bar{\mathcal{L}}_s (\bar{\kappa}\bar{D} - \Gamma)^m + (1 - 2\bar{C}\epsilon De_\kappa^2)(1 - \bar{A}) + \frac{2}{3}\epsilon De_\kappa^2(1 - \bar{A}^3) \tag{11.51}$$

Figs. 11.3(a) and (b) show the dimensionless velocity profiles as a function of  $\sqrt{\varepsilon}De_\kappa$  for two relative microchannel ratios  $\bar{\kappa} = 20$  and  $\bar{\kappa} = 100$ , with and without slip velocity. By comparing with the Newtonian case we see that a *pluglike* velocity profile is again obtained, but now  $\sqrt{\varepsilon}De_\kappa$  and  $\bar{\mathcal{L}}_s$  both contribute to an increase of the velocity plateau, especially for  $\bar{\kappa} = 100$  where the effect of the slip velocity is more significant. The influence of  $\bar{\kappa}$  on the velocity profile is restricted to the effective EDL thickness, with the velocity profiles for higher values of  $\bar{\kappa}$  exhibiting thinner EDL layers and consequently stronger velocity gradients (or shear rates). In Fig. 11.4 we analyse the effect of the slip law exponent  $m$  on the velocity profile. The profiles shown that an increase in  $m$  leads to an increase of the velocity plateau, with the influence of  $m$  being more important than  $\bar{\mathcal{L}}_s$  in the increase of the flow rate.

#### 11.4.3 Viscoelastic fluid with mixed driving forcings with wall slip

The viscoelastic flow characteristics under the combined action of electro-osmosis and pressure gradient forcings are discussed in this section, based on equation (11.27). Figs. 11.5(a) and (b) present dimensionless velocity profiles for flows with favorable and adverse pressure gradients, respectively. For both  $\Gamma < 0$  and  $\Gamma > 0$  the velocity profiles increase with  $\sqrt{\varepsilon}De_\kappa$  and  $\bar{\mathcal{L}}_s$ , and, as also shown in Fig. 11.3, the increase due to the slip coefficient  $\bar{\mathcal{L}}_s$  contribution is more intense for higher values of  $\sqrt{\varepsilon}De_\kappa$ .

The effect of the slip velocity on the velocity profile can be easily seen when imposing a constant flow rate  $\bar{Q}$ . Figs. 11.6(a) and (b) present velocity profiles as a function of  $\bar{\mathcal{L}}_s$  at flow rate  $\bar{Q} = 1$ , for the cases  $\sqrt{\varepsilon}De_\kappa = 0$  and  $\sqrt{\varepsilon}De_\kappa = 2$ . The presence of viscoelasticity leads to a decrease of the centerline velocity (see Fig. 11.6(b)) when compared to the Newtonian case (see Fig. 11.6(a)), and the slip velocity enhances this effect. Simultaneously, an increase of the velocity gradients in the EDL layers are observed in for higher  $\sqrt{\varepsilon}De_\kappa$  and  $\bar{\mathcal{L}}_s$ . Figs. 11.6(c) and (d) show similar results, but now for a higher dimensionless flow rate,  $\bar{Q} = 3$ .

In order to see the influence of  $\Gamma$  on the flow rate  $\bar{Q}$ , in Fig. 11.7 we show the variation of  $\bar{Q}/\bar{Q}_N$  ( $\bar{Q}_N$  is the flow rate that would be observed for a Newtonian fluid with no slip velocity for each  $\Gamma$ ) with  $\Gamma$  for  $\bar{\kappa} = 20$  and different values of  $\bar{\mathcal{L}}_s$  and  $\sqrt{\varepsilon}De_\kappa$ . For  $\sqrt{\varepsilon}De_\kappa = 0$  (Newtonian fluid) we can see that the dimensionless flow rate always increases with  $\Gamma$  while for the other values of  $\sqrt{\varepsilon}De_\kappa$  and  $\bar{\mathcal{L}}_s$  the dimensionless flow rate is non-monotonic. Again, we obtain higher flow rates for the case with slip velocity. This can also be seen in Figs. 11.8(a) and (b) which illustrate the variation of  $\bar{Q}/\bar{Q}_N$  as a function of  $\sqrt{\varepsilon}De_\kappa$  and  $\bar{\mathcal{L}}_s$ , for two different values of  $\Gamma$ . The parameter  $\sqrt{\varepsilon}De_\kappa$  leads to a

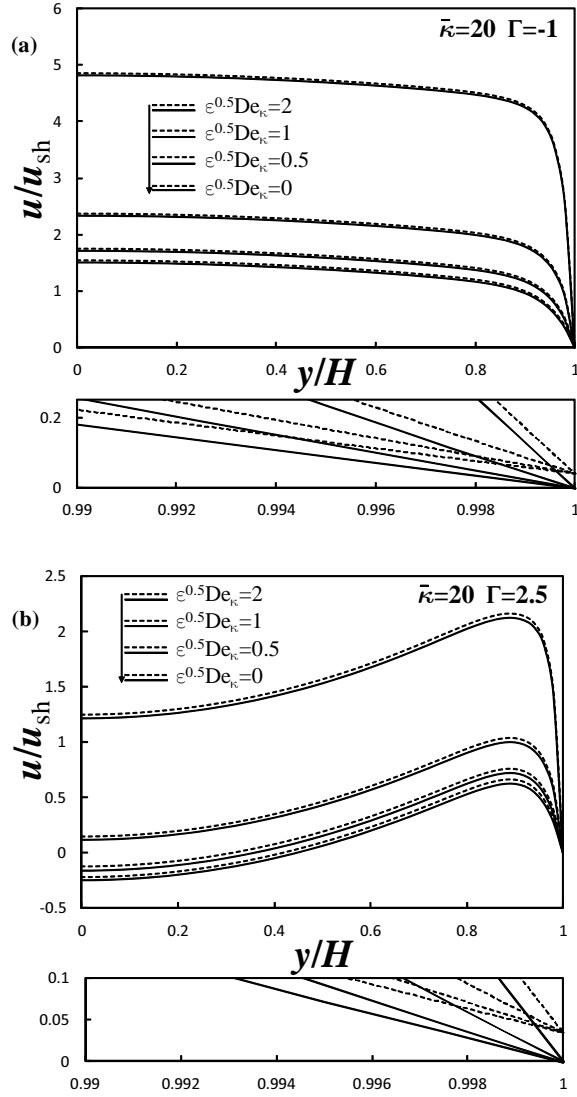


Figure 11.5: Dimensionless velocity profiles for a PTT fluid under the mixed influence of electro-osmotic/pressure driving forcings as function of  $\sqrt{\epsilon}De_{\kappa}$  and  $\bar{\mathcal{L}}_s$  with a relative microchannel ratio of  $\bar{\kappa} = 20$ : (a) favorable pressure gradient ( $\Gamma = -1$ ) and (b) adverse pressure gradient ( $\Gamma = 2.5$ ).

significant increase of  $\bar{Q}/\bar{Q}_N$  and an increase of the slip velocity also enhances  $\bar{Q}/\bar{Q}_N$  as expected.

We now discuss the streaming potential, working with the reciprocal of  $\Gamma_{SP}$ ,  $\Gamma_{SP}^{-1}$ . Figs. 11.9(a) and (b) show that  $\Gamma_{SP}^{-1}$  increases with the viscoelasticity for different values of  $\bar{\mathcal{L}}_s$ ,  $Y_1$  and  $\bar{\kappa}$ , and that the amount of electrical streaming current asymptotically converges to a saturation point. We can also see that the increase of  $Y_1$  leads to a decrease of  $\Gamma_{SP}^{-1}$  as also discussed by (Afonso et al., 2009b), but now the slip velocity has a nonlinear relationship with both  $Y_1$  and  $\bar{\kappa}$ . In Fig. 11.9(a) we see that for  $Y_1 = 1$  the slip velocity leads to a decrease

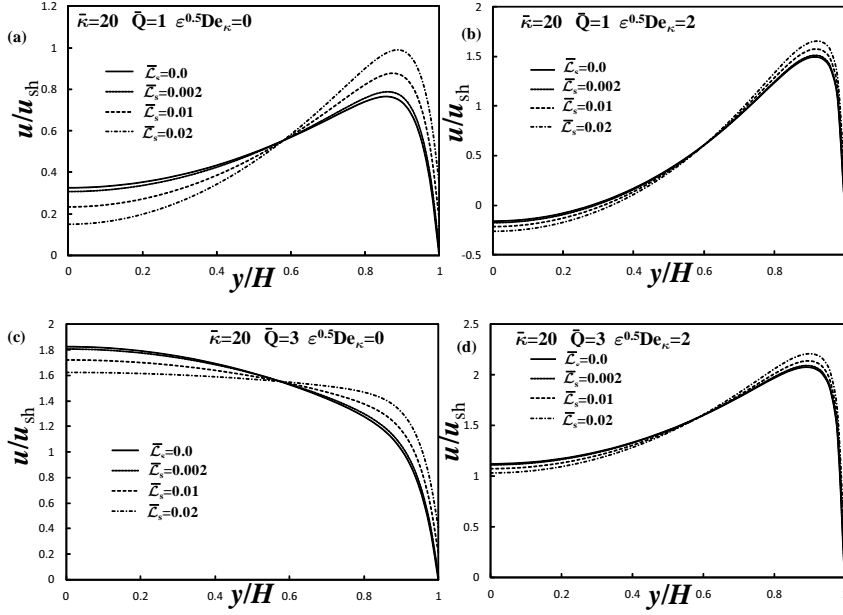


Figure 11.6: Dimensionless velocity profiles for Newtonian ( $\sqrt{\varepsilon}De_\kappa = 0$ ) and PTT fluids ( $\sqrt{\varepsilon}De_\kappa = 2$ ) under the mixed influence of electro-osmotic/pressure driving forcings for different values of the slip coefficient  $\bar{\mathcal{L}}_s$  and  $\bar{\kappa} = 20$ : (a)  $\bar{Q}=1$  and  $\sqrt{\varepsilon}De_\kappa = 0$ ; (b)  $\bar{Q}=1$  and  $\sqrt{\varepsilon}De_\kappa = 2$ ; (c)  $\bar{Q}=3$  and  $\sqrt{\varepsilon}De_\kappa = 0$ ; (d)  $\bar{Q}=3$  and  $\sqrt{\varepsilon}De_\kappa = 2$ .

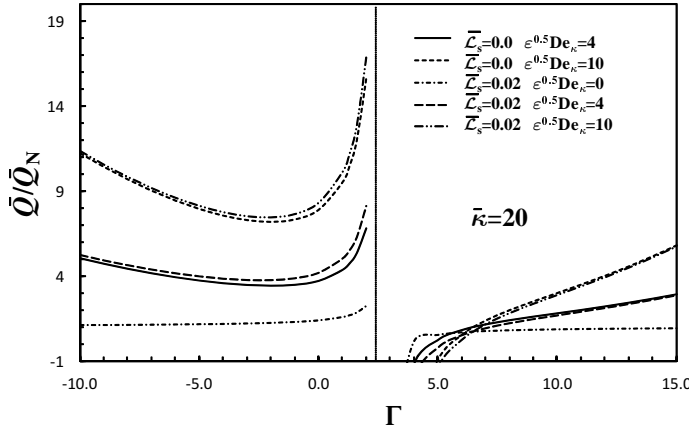


Figure 11.7: Dimensionless flow rate  $\bar{Q}/\bar{Q}_N$  as a function of  $\Gamma$  for pressure driven/electro-osmotic flow of a PTT fluid for  $\bar{\kappa} = 20$  and different values of the slip coefficient,  $\bar{\mathcal{L}}_s$ , and  $\sqrt{\varepsilon}De_\kappa$ .

of  $\Gamma_{SP}^{-1}$ , but for  $Y_1 = 100$ ,  $\Gamma_{SP}^{-1}$  increases with  $\bar{\mathcal{L}}_s$ . For  $\bar{\kappa} = 100$  (Fig. 11.9(b)),  $\Gamma_{SP}^{-1}$  decreases with  $\bar{\mathcal{L}}_s$  for both  $Y_1 = 1$  and  $Y_1 = 100$ .

11.5 CONCLUSIONS

In this work, we derived analytical solutions for channel flows of viscoelastic fluids in hydrophobic microchannels under the combined influence of electrokinetic and pressure forcings using the Debye-

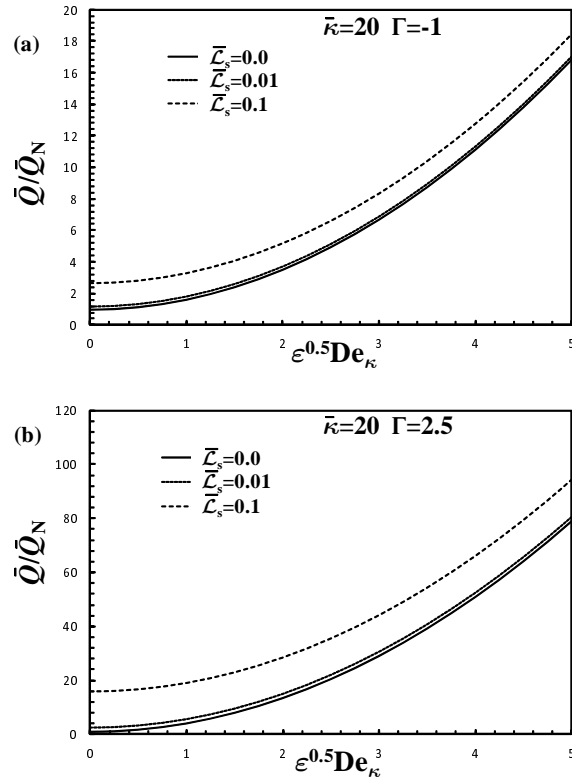


Figure 11.8: Variation of the dimensionless flow rate  $\bar{Q}/\bar{Q}_N$  rate with  $\sqrt{\varepsilon}De_\kappa$  and the slip coefficient  $\bar{\mathcal{L}}_s$  for the pressure driven/electro-osmotic flow of a PTT fluid for relative microchannel ratio  $\bar{\kappa} = 20$ : (a) favorable pressure gradient ( $\Gamma = -1$ ) and (b) adverse pressure gradient ( $\Gamma = 2.5$ ).

Hückel approximation, including the limiting case of pure electro-osmotic flow and the account of wall slip. The analysis is restricted to cases with small electric double-layer, where the distance between the walls of a microfluidic device is at least one order of magnitude larger than the EDL. The viscoelastic fluids used are described by the sPTT model, with linear kernel for the stress coefficient function and the FENE-P model.

The combined effects of the slip boundary conditions, fluid rheology, electro-osmotic and pressure gradient forcings on the fluid velocity distribution and streaming potential are also discussed. We results demonstrate that the presence of the slip velocity and viscoelasticity both induce an increase the in dimensionless velocity profiles and the flow rate.

#### ACKNOWLEDGEMENTS

The authors acknowledge funding from FEDER and Fundação para a Ciência e a Tecnologia (FCT), Portugal, through project PTDC/EQU-FTT/113811/2009. A.M.A. and L.L.F. would also like to thank FCT for



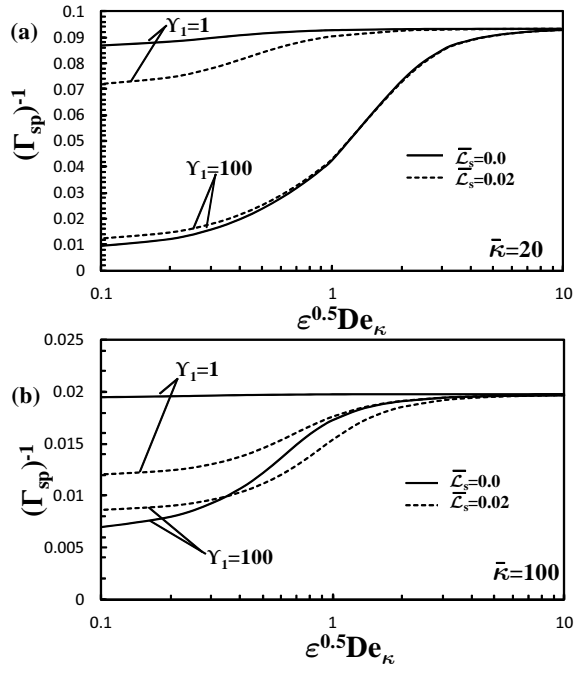


Figure 11.9: Streaming Potential: variation of  $\Gamma_{SP}^{-1}$  with  $\sqrt{\varepsilon}De_{\kappa}$  as a function of  $\bar{L}_s$  and  $Y_1$ : (a)  $\bar{k} = 20$ ; (b)  $\bar{k} = 100$ .

financial support through scholarships SFRH/BPD/75436/2010 and SFRH/BD/37586/2007, respectively.



## EO/PD SLIP-FLOWS OF VISCOELASTIC FLUIDS IN HM WITH ASSYMETRIC ZP

**Abstract**<sup>1</sup>*This work investigates the slip flow of viscoelastic fluids in hydrophobic microchannels under the combined influence of electro-osmotic and pressure gradient forcings with asymmetric zeta potentials at the walls. For the analytic solutions, the Debye-Hückel approximation for weak potential is assumed. To model the viscoelastic fluids, the simplified Phan-Thien-Tanner (sPTT) and the Finitely Extensible Non-linear Elastic model with a Peterlin approximation for the average spring force (FENE-P), constitutive equations were chosen. Because of the different hydrophobic characteristics of the microchannels walls, we study the influence of the Navier slip boundary condition on the fluid flow, by considering different slip coefficients at the walls and varying the electrical double-layer thickness, the ratio between the applied streamwise gradients of electrostatic potential and pressure, and the ratio of the zeta potentials.*

## 12.1 INTRODUCTION

The exponential growth of technology, together with a rapid dissemination of knowledge, made us question the validity of some “empirical laws” that were considered an absolute truth in the past. The no-slip boundary condition is one of these cases. Based on experiments with Newtonian fluids, the no-slip boundary condition became popular and above all, it became a law, as stated in many books on the subject of fluid Mechanics. The truth is that the no-slip boundary condition is nothing but an empirical model.

For non-Newtonian fluids such as polymer melts, it is nowadays a known fact the existence of slip velocity between the fluid and the solid wall (Brochard and De Gennes, 1992; De Gennes, 1979; Denn, 2001; Inn and Wang, 1996; Kraynik and Schowalter, 1981; Migler et al., 1993; Schowalter, 1988; Wang, 1999). The same applies to electro-osmotic flow (Marry et al., 2003; Herr et al., 2000), flow in microfluidic devices (Gad-el Hak, 1999; Stone et al., 2004), biological processes (Zhang et al., 2003; Beebe et al., 2002), and Gas flow (the assumption that gases may exhibit wall slip was first introduced by (Maxwell, 1879)).

Even for Newtonian fluids, where the no-slip boundary condition fits well the macroscopic experimental data, new experiments in microfluidics showed that for specific cases such boundary condition are

<sup>1</sup> A.M. Afonso, L.L. Ferrás, J.M. Nóbrega, M.A. Alves, F.T. Pinho (2012), Pressure-driven electrokinetic slip-flows of viscoelastic fluids in hydrophobic microchannels with assymetric zeta potential, to be submitted to *Journal of Colloid and Interface Science*;

inaccurate (Pit et al., 2000; Craig et al., 2001; Zhu and Granick, 2001; Horn et al., 2000; Baudry et al., 2001; Bonaccorso et al., 2002).

In the last decade we have witnessed a fast evolution in micro and nanofluidics and therefore the electro-osmotic flow has attracted the scientific community, specially due to its applicability to chemical analysis, medical research and possibly in the mixing of fluids at microscales.

Several works have been published on the subject of electro-osmotic flow, such as the works of (Soong et al., 2010) and (Jamaati et al., 2010) regarding the Newtonian pressure-driven electrokinetic flows in hydrophobic and planar microchannels. For non-Newtonian fluids, (Afonso et al., 2009b, 2011a) presented analytical solutions of mixed electro-osmotic/pressure driven viscoelastic fluids in microchannels for the case of electro-osmotic flow under symmetric and asymmetric zeta potential (they used the Phan-Thien and Tanner model (Phan-Thien and Tanner, 1977; Phan-Thien, 1978) to describe the viscoelasticity), (Dhinakaran et al., 2010) analysed the full PTT model with non-zero second normal stress differences, and (Afonso et al., 2012) derived the full analytical solution for fully developed electro-osmosis driven flow of polymer solutions described by the sPTT and FENE-P models with a Newtonian solvent.

The existence of slip velocity between the fluid and the wall is an interfacial phenomenon that influences the hydrodynamics of micro and nano flows, as explained in the works of (Tretheway and Meinhart, 2002, 2004; Tandon et al., 2008), and, therefore, appropriate boundary conditions should be used to model such physical phenomenon. The Navier slip boundary condition, (Navier, 1822), is the most widely used formula to describe such effect.

In microfluidics it is common to find channel with walls made from different materials. For instance, in soft lithography the channels are often made polydimethylsiloxane (PDMS) except for the top wall that is often made of glass for optical access, therefore the need to study asymmetric flows.

In this work we present an analytical solution for pressure-driven electrokinetic slip-flows of viscoelastic fluids in hydrophobic microchannels with asymmetric zeta potential, and under the influence of the Navier slip boundary condition at the channel wall.

The paper starts with the set of governing equations including the nonlinear Poisson–Boltzmann equation governing the electric double layer (EDL) field and the added body force to the momentum equation caused by the applied electrical potential field. In subsection 3 we present the analytical solution for the PTT and FENE-P models, including the particular case of streaming potential. A discussion of the effects of the Navier slip coefficient upon the flow characteristics closes this work.

## 12.2 GOVERNING EQUATIONS

The basic equations describing the flow are the continuity equation,

$$\nabla \cdot \mathbf{u} = 0 \quad (12.1)$$

and the momentum equation,

$$\rho \frac{D\mathbf{u}}{Dt} = \nabla \cdot \boldsymbol{\tau} - \nabla p + \mathbf{F} \quad (12.2)$$

where  $\mathbf{u}$  is the velocity vector,  $p$  the pressure,  $t$  the time,  $\rho$  the fluid density (assumed constant) and  $\boldsymbol{\tau}$  the polymeric extra stress contribution. The body force  $\mathbf{F}$  in the momentum equation (12.2) is given as

$$\mathbf{F} = \rho_e \mathbf{E} \quad (12.3)$$

where  $\mathbf{E}$  is the applied external electric field and  $\rho_e$  is the net electric charge density associated with the spontaneously formed electric double layers, which are assumed here not to be affected by the imposed electric field. The electric field is related to a potential ( $\Phi$ ), by  $\mathbf{E} = -\nabla \Phi$ , with  $\Phi = \psi + \phi$ , where  $\phi$  is the applied streamwise potential and  $\psi$  is the equilibrium/ induced potential at the channel walls, associated with the interaction between the ions of the fluid and the dielectric properties of the wall.

## 12.2.1 Slip boundary conditions

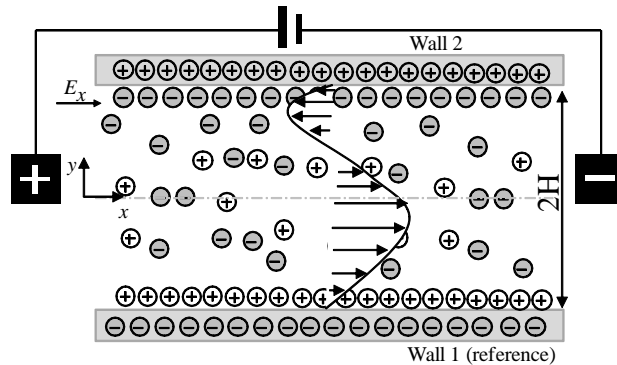


Figure 12.1: Schematic of the flow in a parallel plate microchannel.

In this work, we assume that the microchannel walls are made of different materials (e.g. glass and PDMS), leading to different hydrophobic characteristics, different zeta wall potentials (see Fig. 12.1) and different slip boundary conditions. For this work, we chose the

linear Navier slip law with different slip coefficients (Navier, 1822),  $\mathcal{L}_1$  and  $\mathcal{L}_2$ , for the bottom and top walls, respectively,

$$\begin{cases} \mathbf{u}_{\parallel wall1} = -\mathcal{L}_1 \boldsymbol{\tau}_{t\parallel wall1} \\ \mathbf{u}_{\parallel wall2} = -\mathcal{L}_2 \boldsymbol{\tau}_{t\parallel wall2} \end{cases} \quad (12.4)$$

These slip models are written in vector notation and basically state that the slip velocity vector,  $\mathbf{u}_{\parallel wall}$ , points in the tangent stress,  $\boldsymbol{\tau}_{t\parallel wall}$ , opposite direction.

### 12.2.2 Constitutive equations

#### 12.2.2.1 sPTT model

The sPTT model (Phan-Thien and Tanner, 1977; Phan-Thien, 1978), can be expressed by

$$f(\tau_{kk})\boldsymbol{\tau} + \lambda \overset{\nabla}{\boldsymbol{\tau}} = 2\eta \mathbf{D}, \quad (12.5)$$

where  $\mathbf{D}$  is the rate of deformation tensor ( $\mathbf{D} = \frac{1}{2}(\nabla \mathbf{u} + \nabla \mathbf{u}^T)$ ),  $\lambda$  is a relaxation time,  $\eta$  is the constant viscosity coefficient,  $\boldsymbol{\sigma}_{kk} = \boldsymbol{\sigma}_{xx} + \boldsymbol{\sigma}_{yy} + \boldsymbol{\sigma}_{zz}$  is the trace of the extra stress tensor, and  $\overset{\nabla}{\boldsymbol{\tau}}$  represents the upper-convected derivative, defined by

$$\overset{\nabla}{\boldsymbol{\tau}} = \frac{D\boldsymbol{\tau}}{Dt} - \nabla \mathbf{u}^T \cdot \boldsymbol{\tau} - \boldsymbol{\tau} \cdot \nabla \mathbf{u}. \quad (12.6)$$

For the stress coefficient function,  $f(\boldsymbol{\sigma}_{kk})$ , the linear form was chosen,

$$f(\tau_{kk}) = 1 + \frac{\varepsilon \lambda}{\eta} \tau_{kk}, \quad (12.7)$$

#### 12.2.2.2 FENE-P model

The FENE-P constitutive equation is based on the kinetic theory for finitely extensible dumbbells with a Peterlin closure for the average spring force (Bird et al., 1980), and can be written as,

$$Z(\tau_{kk})\boldsymbol{\tau} + \lambda \overset{\nabla}{\boldsymbol{\tau}} - \lambda \left( \boldsymbol{\tau} - \frac{b}{b+2} n k_B T \mathbf{I} \right) \frac{D \ln Z}{Dt} = 2 \frac{b}{b+2} n k_B T \lambda \mathbf{D} \quad (12.8)$$

where  $\overset{\nabla}{\boldsymbol{\tau}}$  represents the upper convected derivative defined by equation (12.5),  $b$  is a parameter that measures the extensibility of the dumbbell,  $k_B$  is the Boltzmann constant,  $T$  is the absolute temperature and  $n$

is a parameter of the model (Bird et al., 1980). The stress coefficient function,  $Z(\tau_{kk})$  can be expressed as

$$Z(\tau_{kk}) = 1 + 3 \left( \frac{1}{b+2} + \frac{\lambda}{3\eta} \frac{\tau_{kk}}{(b+5)} \right). \quad (12.9)$$

### 12.2.3 Poisson-Boltzmann equation and slip-dependent zeta potentials

One of the most significant effects of the charged surface is the attraction of ions with opposite sign of the charge (counter-ions) and the repulsion of the ions with the same sign (co-ions). Near the charged wall we can distinguish two different types of layers. The first layer is called Stern layer and is composed of counter-ions. The second layer is called diffusive layer where the ions have the ability to move around freely. This two layers near the wall form what is called the Electrical Double Layer (EDL, see (Bruss, 2008) for more details. The different concentrations of counter-ions and co-ions leads to the creation of a varying potential field within the electric double layer, that can be expressed by means of a Poisson equation:

$$\nabla^2 \psi = -\frac{\rho_e}{\epsilon} \quad (12.10)$$

where  $\psi$  denotes the EDL potential and  $\epsilon$  is the dielectric constant of the solution. The net electric charge density in the fluid,  $\rho_e$ , is described by the following Boltzmann distribution

$$\rho_e = -2n_0 e z \sinh \left( \frac{e z}{k_B T} \psi \right) \quad (12.11)$$

where,  $n_0$  is the ion density,  $e$  is the electronic charge and  $z$  the valence of the ions. In order to obtain the velocity field, first we need to solve for the net charge density distribution ( $\rho_e$ ). The charge density field can be calculated by combining equation (12.10), which for fully-developed steady flow conditions reduces to

$$\frac{d^2 \psi}{dy^2} = -\frac{\rho_e}{\epsilon}, \quad (12.12)$$

and equation (12.11) to obtain the the well-known Poisson–Boltzmann equation,

$$\frac{d^2 \psi}{dy^2} = \frac{2n_0 e z}{\epsilon} \sinh \left( \frac{e z}{k_B T} \psi \right). \quad (12.13)$$

If we assume a flow between parallel plates with charged walls and the existence of a current potential difference between two electrodes at the inlet and outlet, than an electric field is generated that exerts a body force on the counter-ions of the EDL, which move along the channel dragging the neutral liquid core. The distribution of the

charged species in the domain is governed by the potential at the walls and by the externally applied electric field. However, when the EDL thickness is small and the charge at the walls is not large, this distribution is essentially governed by the potential at the wall,  $\psi_0$ , and the charge distribution near the walls can be determined independently of the applied external electric field.

In this work, the charge redistribution is exactly null as is also the inertial term of the momentum equation. Then, for small values of  $\psi$  it is also possible to conduct further simplifications because the Debye–Hückel linearization principle ( $\sinh x \approx x$ ) can be invoked. This means that the electrical potential is small compared with the thermal energy of the ions, and the Poisson–Boltzmann equation for the channel flow under investigation becomes:

$$\frac{d^2\psi}{dy^2} = \kappa^2\psi, \quad (12.14)$$

where  $\kappa^2 = \frac{2n_0e^2z^2}{\epsilon\kappa_B T}$  is the Debye–Hückel parameter, related with the thickness of the Debye layer,  $\zeta = \frac{1}{\kappa}$  (normally referred as the EDL thickness). This approximation is valid for  $10 \lesssim H/\zeta \lesssim 10^3$ .

Equation (12.14) can be integrated subject to different zeta potential at the walls,  $\psi|_{y=-H} = \zeta_1$  and  $\psi|_{y=H} = \zeta_2$  (cf. Fig. 12.1), leading to:

$$\psi(y) = \zeta_1 (\Psi_1 e^{\kappa y} - \Psi_2 e^{-\kappa y}) \quad (12.15)$$

with  $\Psi_1 = \frac{(R_\zeta e^{\kappa H} - e^{-\kappa H})}{2 \sinh(2\kappa H)}$  and  $\Psi_2 = \frac{(R_\zeta e^{-\kappa H} - e^{\kappa H})}{2 \sinh(2\kappa H)}$ , and where  $R_\zeta = \zeta_2/\zeta_1$  denotes the ratio of the zeta potentials of the two walls with  $-H \leq y \leq H$ . For  $R_\zeta = 1$  the symmetric potential profile of (Afonso et al., 2009b) is recovered.

A combination of Eqs. (12.11) and (12.15) gives the net charge density distribution,

$$\rho_e = -\epsilon\kappa^2\zeta_1 (\Psi_1 e^{\kappa y} - \Psi_2 e^{-\kappa y}) = -\epsilon\kappa^2\zeta_1 \Omega_1^-(y), \quad (12.16)$$

where the operator  $\Omega_p^\pm(y) = \Psi_1^p (e^{\kappa y})^p \pm \Psi_2^p (e^{-\kappa y})^p$  is a hyperbolic function of the transverse variable  $y$ , and depends on the ratio of zeta potentials and on the thickness of the Debye layer.

### 12.3 ANALYTICAL SOLUTION

#### 12.3.1 sPTT constitutive equation

Assuming the fully developed flow of a fluid modeled by the sPTT model, Eqs. (12.6) and (12.7), can be further simplified leading to,

$$f(\tau_{kk})\tau_{xx} = 2\lambda\dot{\gamma}\tau_{xy} \quad (12.17)$$



$$f(\tau_{kk})\tau_{xy} = \eta\dot{\gamma}, \quad (12.18)$$

where  $\tau_{kk} = \tau_{xx}$  is the trace of the stress tensor and  $\dot{\gamma} = du/dy$  is the velocity gradient. If we consider  $\tau_{yy} = 0$  unphysical solutions may appear (Oliveira et al., 1998), so the stress coefficient function becomes an explicit function of the normal stress  $\tau_{xx}$  only. Upon division of the expressions for the two nonvanishing stresses (equations (12.17) and (12.18)) the following relation is obtained,

$$\tau_{xx} = 2\frac{\lambda}{\eta}\tau_{xy}^2 \quad (12.19)$$

### 12.3.2 FENE-P constitutive equation

For the FENE-P fluid in fully developed channel flow conditions, equations (12.8) and (12.9) reduce to

$$Z(\tau_{kk})\tau_{xx} = 2\lambda\dot{\gamma}\tau_{xy} \quad (12.20)$$

$$Z(\tau_{kk})\tau_{xy} = \left(\frac{b+5}{b+2}\right)\eta\dot{\gamma}. \quad (12.21)$$

with  $\tau_{kk} = \tau_{xx}$ , and

$$Z(\tau_{xx}) = \left(\frac{b+5}{b+2}\right) \left[1 + \frac{\lambda}{\eta} \frac{(b+2)}{(b+5)^2} \tau_{xx}\right]. \quad (12.22)$$

The relation between the normal and shear stresses is given by,

$$\tau_{xx} = 2\frac{\lambda}{\eta} \left(\frac{b+2}{b+5}\right) \tau_{xy}^2. \quad (12.23)$$

### 12.3.3 Analytical solution for the sPTT model

From the previous simplifications, the momentum equation (12.2), for fully developed channel flow reduces to

$$\frac{d\tau_{xy}}{dy} = -\rho_e E_x + p_{,x}, \quad (12.24)$$

where  $p_{,x} \equiv dp/dx$ ,  $E_x \equiv -d\phi/dx$  and  $\phi$  is the electric potential of the applied external field, which is characterized by a constant streamwise gradient. Note that in this flow the external electrical field is positive according to Fig. 12.1, and negative otherwise.

Integration of Eq. (12.24) yields the following expression for the shear stress,

$$\tau_{xy} = \epsilon\kappa\zeta_1 E_x \Omega_1^+(y) + p_{,x}y + \tau_1, \quad (12.25)$$

and making use of Eq.12.19 the normal stress component is given by,

$$\tau_{xx} = 2\frac{\lambda}{\eta} \left( \epsilon\kappa\zeta_1 E_x \Omega_1^+(y) + p_{,x}y + \tau_1 \right)^2 \quad (12.26)$$

where  $\tau_1$  is a shear stress integration constant to be quantified later from the slip boundary conditions.

If we combine Eqs. (12.18), (12.25) and (12.26) we arrive to the velocity gradient distribution, given by

$$\dot{\gamma} \equiv \frac{du}{dy} = \left[ 1 + 2\epsilon\lambda^2 \left( \frac{\epsilon E_x \zeta_1}{\eta} \kappa \Omega_1^+(y) + \frac{p_{,x}}{\eta} y + \dot{\gamma}_1 \right)^2 \right] \left( \frac{\epsilon E_x \zeta_1}{\eta} \kappa \Omega_1^+(y) + \frac{p_{,x}}{\eta} y + \dot{\gamma}_1 \right) \quad (12.27)$$

where for compactness we use the *shear rate asymmetry coefficient* defined as  $\dot{\gamma}_1 = \tau_1/\eta$ . Equation (12.27) can be integrated subject to the slip boundary condition at  $y = -H$  (where we assume, for the sake of simplicity, that  $\tau_{xy}|_{y=-H} > 0$ ),

$$u|_{y=-H} = \mathcal{L}_1 \tau_{xy}|_{y=-H} \quad (12.28)$$

and the resulting velocity profile is given by,

$$\begin{aligned} u = & \mathcal{L}_1 \left( \epsilon\kappa\zeta_1 E_x \Omega_1^+(-H) - p_{,x}H + \tau_1 \right) \\ & + \dot{\gamma}_1 (y+H) \left( 1 + 2\epsilon\lambda^2 \dot{\gamma}_1^2 \right) + \left[ \frac{\epsilon E_x \zeta_1}{\eta} \right] \left( 1 + 6\dot{\gamma}_1^2 \epsilon\lambda^2 \right) \Omega_{1,1}^-(y) \\ & + 2\epsilon\lambda^2 \left[ \frac{\epsilon E_x \zeta_1}{\eta} \right]^2 \dot{\gamma}_1 \left( 6\Psi_1\Psi_2\kappa (y+H) + \frac{3}{2}\Omega_{2,1}^-(y) \right) \\ & + 2\epsilon\lambda^2 \left[ \frac{\epsilon E_x \zeta_1}{\eta} \right]^3 \kappa^2 \left( \frac{1}{3}\Omega_{3,1}^-(y) + 3\Psi_1\Psi_2\Omega_{1,1}^-(y) \right) \\ & + \frac{1}{2} \left[ \frac{p_{,x}}{\eta} \right] (y^2 - H^2) \left( 1 + 6\epsilon\lambda^2 \dot{\gamma}_1^2 + \epsilon\lambda^2 \left[ \frac{p_{,x}}{\eta} \right]^2 (y^2 + H^2) \right) \\ & + 2\dot{\gamma}_1 \epsilon\lambda^2 \left[ \frac{p_{,x}}{\eta} \right]^2 (y^3 + H^3) + \frac{12\epsilon\lambda^2 \left[ \frac{\epsilon E_x \zeta_1}{\eta} \right] \left[ \frac{p_{,x}}{\eta} \right] \dot{\gamma}_1 \left( \Omega_{1,2}^-(y) - \Omega_{1,1}^+(y) \right)}{\kappa} \\ & + 6 \frac{\epsilon\lambda^2 \left[ \frac{\epsilon E_x \zeta_1}{\eta} \right] \left[ \frac{p_{,x}}{\eta} \right]^2}{\kappa^2} \left( \Omega_{1,3}^-(y) + 2\Omega_{1,1}^-(y) - 2\Omega_{1,2}^+(y) \right) \\ & + 6\epsilon\lambda^2 \left[ \frac{\epsilon E_x \zeta_1}{\eta} \right]^2 \left[ \frac{p_{,x}}{\eta} \right] \left( \Psi_1\Psi_2\kappa^2 (y^2 - H^2) + \frac{1}{2}\Omega_{2,2}^-(y) - \frac{1}{4}\Omega_{2,1}^+(y) \right) \end{aligned} \quad (12.29)$$

where the operator  $\Omega_{p,q}^\pm(y)$  is defined as

$$\Omega_{p,q}^\pm(y) = (\kappa y)^{(q-1)} \Omega_p^\pm(y) - (-1)^{(q+1)} (\kappa H)^{(q-1)} \Omega_p^\pm(-H). \quad (12.30)$$

The second slip boundary condition, at  $y = H$ , is given by

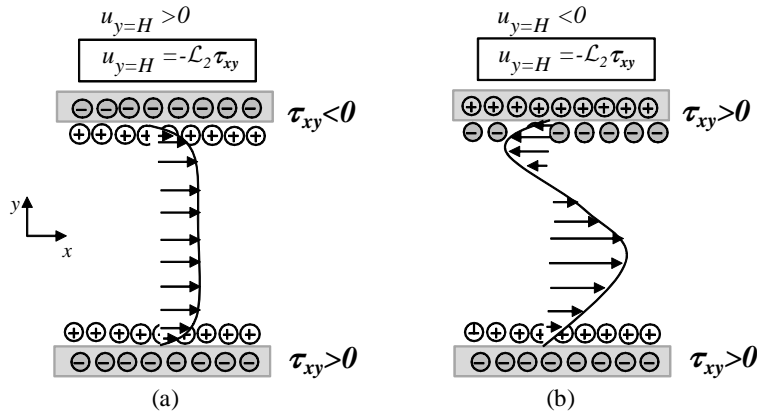


Figure 12.2: Schematic of the slip flow at the upper wall.

$$u_{\parallel y=H} = -\mathcal{L}_2 \tau_{xy \parallel y=H} \quad (12.31)$$

and this can be understood by looking at Fig. 12.2 (a), (b). Depending on the flow direction,  $\tau_{xy \parallel y=H}$  can be either positive or negative. The slip velocity vector points in the tangent stress opposite direction, and because of that Eq. 12.31 works for both flow directions.

The restriction imposed by the second slip boundary condition allows us to obtain an equation for  $\dot{\gamma}_1$ :

$$\dot{\gamma}_1^3 + a_1 \dot{\gamma}_1^2 + a_2 \dot{\gamma}_1 + a_3 = 0. \quad (12.32)$$

which solution is given by the Cardan-Tartaglia (12.32) formula,

$$\begin{aligned} \dot{\gamma}_1 &= \sqrt[3]{-\frac{b_1}{2} + \sqrt{\frac{b_1^2}{4} + \frac{a^3}{27}}} + \sqrt[3]{-\frac{b_1}{2} - \sqrt{\frac{b_1^2}{4} + \frac{a^3}{27}}} - \frac{a_1}{3} \\ a &= a_2 - \frac{a_1^2}{3} \\ b_1 &= a_3 - \frac{a_1 a_2}{3} + \frac{2a_1^3}{27} \end{aligned} \quad (12.33)$$

with coefficients

$$\begin{aligned}
a_1 &= \frac{3}{2} \frac{\epsilon E_x \zeta_1}{\eta H} \Omega_{1,1}^-(H) \\
a_2 &= \frac{1}{2\epsilon\lambda^2} + \left(\frac{p_{,x}}{\eta}\right)^2 H^2 + 6 \left(\frac{f\bar{f} E_x \zeta_1}{J}\right)^2 \Psi_1 \Psi_2 + \frac{3}{4} \left(\frac{\epsilon E_x \zeta_1}{\eta} \kappa\right)^2 \Omega_{2,1}^-(H) \\
&\quad + 3 \frac{\left(\frac{\epsilon E_x \zeta_1}{\eta} \kappa\right) \frac{p_{,x}}{\eta}}{\kappa^2 H} \left(\Omega_{1,2}^-(H) - \Omega_{1,1}^+(H)\right) + \frac{\eta (\mathcal{L}_1 + \mathcal{L}_2)}{4H\epsilon\lambda^2} \quad (12.34) \\
a_3 &= \frac{1}{2} \frac{\epsilon E_x \zeta_1}{\eta} \frac{\Omega_{1,1}^-(H)}{2\epsilon\lambda^2 H} + \frac{1}{2} \frac{\left(\frac{\epsilon E_x \zeta_1}{\eta} \kappa\right)^3}{\kappa H} \left(\frac{1}{3} \Omega_{3,1}^-(H) + 3\Psi_1 \Psi_2 \Omega_{1,1}^-(H)\right) \\
&\quad + \frac{3}{2} \frac{\left(\frac{f\bar{f} E_x \zeta_1}{J}\right)^2 \frac{p_{,x}}{\eta}}{\kappa^2 H} \left(\frac{1}{2} \Omega_{2,2}^-(H) - \frac{1}{4} \Omega_{2,1}^+(H)\right) \\
&\quad + \frac{3}{2} \frac{\left(\frac{\epsilon E_x \zeta_1}{\eta} \kappa\right) \left(\frac{p_{,x}}{\eta}\right)^2}{\kappa^3 H} \left(\Omega_{1,3}^-(H) + 2\Omega_{1,1}^-(H) - 2\Omega_{1,2}^+(H)\right) \\
&\quad + \frac{\epsilon k E_x \zeta_1}{4H\epsilon\lambda^2} (\mathcal{L}_1 \Omega_1^+(-H) + \mathcal{L}_2 \Omega_1^+(H)) + \frac{p_{,x} (-\mathcal{L}_1 + \mathcal{L}_2)}{H\epsilon\lambda^2}
\end{aligned}$$

It is often more convenient to work with the dimensionless form of equation (12.29). Introducing the normalizations  $\bar{y} = y/H$  and  $\bar{\kappa} = \kappa H$ , the dimensionless velocity profile can be written as

$$\begin{aligned}
\frac{u}{u_{sh}} &= -\bar{\mathcal{L}}_1 \left( \bar{\kappa} \bar{\Omega}_1^+(-1) + \Gamma - \bar{\gamma}_1 \right) \\
&\quad + \bar{\gamma}_1 (\bar{y} + 1) \left( 1 + 2\bar{\gamma}_1 \frac{\bar{\epsilon} De_\kappa^2}{\bar{\kappa}^2} \right) - \left( 1 + 6\bar{\gamma}_1 \frac{\bar{\epsilon} De_\kappa^2}{\bar{\kappa}^2} \right) \bar{\Omega}_{1,1}^-(\bar{y}) \\
&\quad + 2\bar{\gamma}_1 \frac{\bar{\epsilon} De_\kappa^2}{\bar{\kappa}} \left( 6\Psi_1 \Psi_2 \bar{\kappa} (\bar{y} + 1) + \frac{3}{2} \bar{\Omega}_{2,1}^-(\bar{y}) \right) \\
&\quad - 2\bar{\epsilon} De_\kappa^2 \left( \frac{1}{3} \bar{\Omega}_{3,1}^-(\bar{y}) + 3\Psi_1 \Psi_2 \bar{\Omega}_{1,1}^-(\bar{y}) \right) \\
&\quad + \frac{1}{2} \Gamma (\bar{y}^2 - 1) \left( 1 + 6\bar{\gamma}_1 \frac{\bar{\epsilon} De_\kappa^2}{\bar{\kappa}^2} + \frac{\bar{\epsilon} De_\kappa^2}{\bar{\kappa}^2} \Gamma^2 (\bar{y}^2 + 1) \right) \\
&\quad + 2\bar{\gamma}_1 \frac{\bar{\epsilon} De_\kappa^2}{\bar{\kappa}^2} \Gamma^2 (\bar{y}^3 + 1) \\
&\quad - 12\bar{\gamma}_1 \frac{\bar{\epsilon} De_\kappa^2}{\bar{\kappa}^3} \Gamma \left( \bar{\Omega}_{1,2}^-(\bar{y}) - \bar{\Omega}_{1,1}^+(\bar{y}) \right) \\
&\quad + 6 \frac{\bar{\epsilon} De_\kappa^2}{\bar{\kappa}^2} \Gamma \left( \Psi_1 \Psi_2 \bar{\kappa}^2 (\bar{y}^2 - 1) + \frac{1}{2} \bar{\Omega}_{2,2}^-(\bar{y}) - \frac{1}{4} \bar{\Omega}_{2,1}^+(\bar{y}) \right) \\
&\quad - 6 \frac{\bar{\epsilon} De_\kappa^2}{\bar{\kappa}^4} \Gamma^2 \left( \bar{\Omega}_{1,3}^-(\bar{y}) + 2\bar{\Omega}_{1,1}^-(\bar{y}) - 2\bar{\Omega}_{1,2}^+(\bar{y}) \right) \quad (12.35)
\end{aligned}$$

where  $\overline{\Omega}_{p,q}^{\pm}(\bar{y})$  is the normalization of the operator introduced by equation (12.30), defined as

$$\overline{\Omega}_{p,q}^{\pm}(\bar{y}) = (\bar{\kappa}\bar{y})^{(q-1)}\overline{\Omega}_p^{\pm}(\bar{y}) - (-1)^{(q+1)}\bar{\kappa}^{(q-1)}\overline{\Omega}_p^{\pm}(-1). \quad (12.36)$$

with  $\overline{\Omega}_p^{\pm}(\bar{y}) = \Psi_1^p(e^{\bar{\kappa}\bar{y}}) \pm \Psi_2^p(e^{-\bar{\kappa}\bar{y}})^p$ .

with the dimensionless shear rate asymmetry coefficient calculated from

$$\bar{\gamma}_1 + \bar{a}_1\bar{\gamma}_1 + \bar{a}_2\bar{\gamma}_1 + \bar{a}_3 = 0, \quad (12.37)$$

with coefficients

$$\begin{aligned} \bar{a}_1 &= -\frac{3}{2}\overline{\Omega}_{1,1}^-(1) \\ \bar{a}_2 &= \frac{\bar{\kappa}^2}{2\varepsilon D e_{\kappa}^2} + \Gamma^2 + 6\bar{\kappa}^2\Psi_1\Psi_2 + \frac{3}{4}\bar{\kappa}\overline{\Omega}_{2,1}^-(1) - 3\frac{\Gamma}{\bar{\kappa}}\left(\overline{\Omega}_{1,2}^-(1) - \overline{\Omega}_{1,1}^+(1)\right) \\ &\quad + \frac{\bar{\kappa}^2(\overline{\mathcal{L}}_1 + \overline{\mathcal{L}}_1)}{4\varepsilon D e_{\kappa}^2} \\ \bar{a}_3 &= -\frac{1}{4}\frac{\bar{\kappa}^2\overline{\Omega}_{1,1}^-(1)}{\varepsilon D e_{\kappa}^2} - \frac{1}{2}\bar{\kappa}^2\left(\frac{1}{3}\overline{\Omega}_{3,1}^-(1) + 3\Psi_1\Psi_2\overline{\Omega}_{1,1}^-(1)\right) \\ &\quad + \frac{3}{2}\Gamma\left(\frac{1}{2}\overline{\Omega}_{2,2}^-(1) - \frac{1}{4}\overline{\Omega}_{2,1}^+(1)\right) - \frac{3}{2}\frac{\Gamma^2}{\bar{\kappa}^2}\left(\overline{\Omega}_{1,3}^-(1) + 2\overline{\Omega}_{1,1}^-(1) - 2\overline{\Omega}_{1,2}^+(1)\right) \\ &\quad + \frac{\bar{\kappa}^3}{4\varepsilon D e_{\kappa}^2}\left(-\overline{\mathcal{L}}_1\overline{\Omega}_1^+(-1) - \overline{\mathcal{L}}_2\overline{\Omega}(1)\right) + \frac{\bar{\kappa}^2\Gamma(-\overline{\mathcal{L}}_1 + \overline{\mathcal{L}}_2)}{4\varepsilon D e_{\kappa}^2}, \end{aligned} \quad (12.38)$$

where  $\bar{\gamma}_1 = \frac{\dot{\gamma}_1 H}{u_{sh}}$ ,  $\overline{\mathcal{L}}_1 = \mathcal{L}_1 \frac{\eta}{H}$  and  $D e_{\kappa} = \frac{\lambda u_{sh}}{\zeta} = \lambda \kappa u_{sh}$  is the Deborah number based on the EDL thickness and on the Helmholtz-Smoluchowski electro-osmotic velocity,  $u_{sh} = -\frac{\varepsilon \zeta_1 E_x}{\eta}$  (Park and Lee, 2008). For simplicity the above terms were based on the zeta potential at the bottom wall ( $\psi_{\parallel y=-H} = \zeta_1$ , and assumed negative).

By imposing a constant flow rate  $\overline{Q}$ , and performing integration of Eq. 12.35 over the channel domain, an expression relating  $\overline{Q}$  and  $\Gamma$  is obtained,

$$\begin{aligned}
\bar{Q} &= \frac{Q}{2Hu_{sh}} = \frac{\bar{u}}{u_{sh}} = \frac{1}{2} \int_{-1}^1 \frac{u}{u_{sh}} d\bar{y} = -\frac{1}{2} \bar{\mathcal{L}}_1 \left( \bar{\kappa} \bar{\Omega}_1^+(-1) + \Gamma - \bar{\dot{\gamma}}_1 \right) \\
&+ \bar{\dot{\gamma}}_1 \left( 1 + 2 \frac{\varepsilon D e_\kappa^2}{\bar{\kappa}^2} \bar{\dot{\gamma}}_1^{-2} \right) - \frac{1}{2} \Gamma \left( \frac{4}{5} \frac{\varepsilon D e_\kappa^2}{\bar{\kappa}^2} \Gamma^2 + \frac{2}{3} \left( 1 + 6 \bar{\dot{\gamma}}_1 \frac{\varepsilon D e_\kappa^2}{\bar{\kappa}^2} \right) \right) \\
&+ 2 \bar{\dot{\gamma}}_1 \frac{\varepsilon D e_\kappa^2}{\bar{\kappa}^2} \Gamma^2 - \frac{1}{2} \left( 1 + 6 \frac{\varepsilon D e_\kappa^2}{\bar{\kappa}^2} \bar{\dot{\gamma}}_1^{-2} \right) \left( \frac{\bar{\Omega}_{1,1}^+(1)}{\bar{\kappa}} - 2 \bar{\Omega}_1^-(-1) \right) \\
&+ \frac{\varepsilon D e_\kappa^2}{\bar{\kappa}} \bar{\dot{\gamma}}_1 \left( 12 \bar{\Psi}_1 \bar{\Psi}_2 \bar{\kappa} + \frac{3}{2} \left( \frac{\bar{\Omega}_{2,1}^+(1)}{2\bar{\kappa}} - 2 \bar{\Omega}_2^-(-1) \right) \right) \\
&- \varepsilon D e_\kappa^2 \left( \frac{\bar{\Omega}_{3,1}^+(1)}{9\bar{\kappa}} - \frac{2}{3} \bar{\Omega}_3^-(-1) + 3 \bar{\Psi}_1 \bar{\Psi}_2 \left( \frac{\bar{\Omega}_{1,1}^+(1)}{\bar{\kappa}} - 2 \bar{\Omega}_1^-(-1) \right) \right) \\
&- 6 \bar{\dot{\gamma}}_1 \frac{\varepsilon D e_\kappa^2}{\bar{\kappa}^4} \Gamma \left[ \bar{\Omega}_{1,2}^+(1) - 2 \bar{\Omega}_{1,1}^-(1) + 2 \bar{\kappa} \left( \bar{\kappa} \bar{\Omega}_1^-(-1) + \bar{\Omega}_1^+(-1) \right) \right] \\
&+ 3 \frac{\varepsilon D e_\kappa^2}{\bar{\kappa}^2} \Gamma \left( \frac{1}{4\bar{\kappa}} \left( \bar{\Omega}_{2,2}^+(1) - \bar{\Omega}_{2,1}^-(1) \right) - \frac{4}{3} \bar{\Psi}_1 \bar{\Psi}_2 \bar{\kappa}^2 \right) \\
&+ 3 \frac{\varepsilon D e_\kappa^2}{\bar{\kappa}^2} \Gamma \left( \bar{\kappa} \bar{\Omega}_2^-(-1) + \frac{1}{2} \bar{\Omega}_2^+(-1) \right) \\
&- 3 \frac{\varepsilon D e_\kappa^2}{\bar{\kappa}^5} \Gamma^2 \left( \bar{\Omega}_{1,3}^+(1) - 4 \bar{\Omega}_{1,2}^-(1) + 6 \bar{\Omega}_{1,1}^+(1) \right) \\
&+ 6 \frac{\varepsilon D e_\kappa^2}{\bar{\kappa}^4} \Gamma^2 \left( (\bar{\kappa}^2 + 2) \bar{\Omega}_1^-(-1) + 2 \bar{\kappa} \bar{\Omega}_1^+(-1) \right)
\end{aligned} \tag{12.39}$$

where parameter  $\Gamma = -\frac{H^2}{\varepsilon \zeta_1} \frac{p_x}{E_x}$  represents the ratio of pressure to electro-osmotic driving forces.

The explicit expressions for the dimensionless shear and normal stress components are obtained from normalization of equations (12.25) and (12.26),

$$\frac{\tau_{xy}}{3\eta u_{sh} \kappa} = \frac{1}{3} \left[ \Gamma \frac{\bar{y}}{\bar{\kappa}} + \frac{\bar{\dot{\gamma}}_1}{\bar{\kappa}} - \bar{\Omega}_1^+(\bar{y}) \right] \tag{12.40}$$

$$\frac{\tau_{xx}}{3\eta u_{sh} \kappa} = \frac{2}{3} D e_\kappa \left[ \Gamma \frac{\bar{y}}{\bar{\kappa}} + \frac{\bar{\dot{\gamma}}_1}{\bar{\kappa}} - \bar{\Omega}_1^+(\bar{y}) \right]^2. \tag{12.41}$$

The normalized shear rate is

$$\frac{\dot{\gamma}}{u_{sh} \kappa} = \left[ 1 + 2\varepsilon D e_\kappa^2 \left( \Gamma \frac{\bar{y}}{\bar{\kappa}} + \frac{\bar{\dot{\gamma}}_1}{\bar{\kappa}} - \bar{\Omega}_1^+(\bar{y}) \right)^2 \right] \left( \Gamma \frac{\bar{y}}{\bar{\kappa}} + \frac{\bar{\dot{\gamma}}_1}{\bar{\kappa}} - \bar{\Omega}_1^+(\bar{y}) \right) \tag{12.42}$$

and the viscosity profile can be obtained from

$$\mu(\dot{\gamma}) \equiv \frac{\tau_{xy}}{\dot{\gamma}} \Rightarrow \frac{\mu(\dot{\gamma})}{\eta} = \left[ 1 + 2\varepsilon D e_\kappa^2 \left( \Gamma \frac{\bar{y}}{\bar{\kappa}} + \frac{\bar{\dot{\gamma}}_1}{\bar{\kappa}} - \bar{\Omega}_1^+(\bar{y}) \right)^2 \right]^{-1}. \tag{12.43}$$

### 12.3.4 Analytical solution for the FENE-P model

The analytical solution for the FENE-P model can be easily derived from the sPTT solution, provided the following substitutions are made (Cruz et al., 2005),

$$\begin{aligned}
 f(\tau_{xx}) &\rightarrow \left(\frac{b+2}{b+5}\right) Z(\tau_{xx}) \\
 \lambda &\rightarrow \lambda \left(\frac{b+2}{b+5}\right) \\
 \varepsilon &\rightarrow \frac{1}{b+5} \\
 \eta &\rightarrow \eta
 \end{aligned} \tag{12.44}$$

## 12.4 RESULTS AND DISCUSSION

In order to understand the fluid dynamics influence of the slip velocity, we present results for the velocity profiles of an sPTT fluid under the mixed influence of electro-osmotic/pressure driving forces and asymmetric hydrophobic wall zeta potentials, and assuming different slip coefficients at the wall. The influence of the slip velocity on the coefficient of asymmetry is also studied.

### 12.4.1 Pure electro-kinetic case

For the sPTT fluid under pure electro-osmosis driving force, the solution is derived by setting  $\Gamma = 0$ , for which equation (12.35) reduces to

$$\begin{aligned}
 \frac{u}{u_{sh}} &= -\overline{\mathcal{L}}_1 \left( \overline{\kappa} \overline{\Omega}_1^+ (-1) - \overline{\gamma}_1 \right) \\
 &+ \overline{\gamma}_1 (\overline{y} + 1) \left( 1 + 2\overline{\gamma}_1 \frac{\varepsilon D e_\kappa^2}{\overline{\kappa}^2} \right) - \left( 1 + 6\overline{\gamma}_1 \frac{\varepsilon D e_\kappa^2}{\overline{\kappa}^2} \right) \overline{\Omega}_{1,1}^-(\overline{y}) \\
 &+ 2\overline{\gamma}_1 \frac{\varepsilon D e_\kappa^2}{\overline{\kappa}} \left( 6\Psi_1 \Psi_2 \overline{\kappa} (\overline{y} + 1) + \frac{3}{2} \overline{\Omega}_{2,1}^-(\overline{y}) \right) \\
 &- 2\varepsilon D e_\kappa^2 \left( \frac{1}{3} \overline{\Omega}_{3,1}^-(\overline{y}) + 3\Psi_1 \Psi_2 \overline{\Omega}_{1,1}^-(\overline{y}) \right)
 \end{aligned} \tag{12.45}$$

For symmetric boundary conditions with no slip boundary conditions ( $R_\zeta = 1$ ,  $\overline{\mathcal{L}}_1 = \overline{\mathcal{L}}_2 = 0$  and  $\overline{\gamma}_1 = 0$ ) the above equation reduces to that presented by (Afonso et al., 2011a), but for  $R_\zeta \neq 1$  and  $\overline{\mathcal{L}}_{1,2} \neq 0$  the dimensionless *shear rate asymmetry coefficient*,  $\overline{\gamma}_1$ , depends on the fluid rheological properties. As explained in the previous section,  $\overline{\gamma}_1$  depends on the ratio of zeta potentials,  $R_\zeta$ , on the relative microchannel ratio,  $\overline{\kappa}$ , on the ratio of pressure gradient to electro-osmotic driving

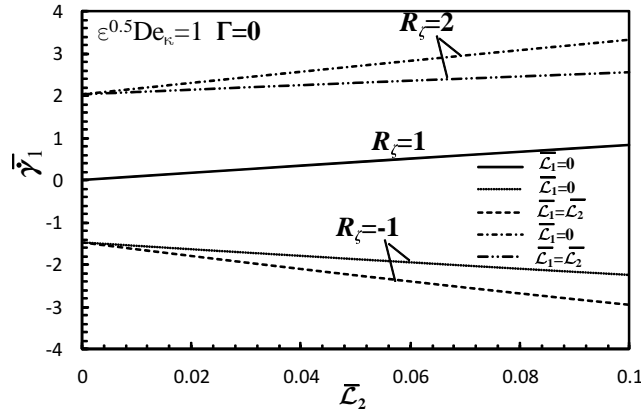


Figure 12.3: Variation of  $\bar{\gamma}_1$  with the slip coefficients,  $\bar{\mathcal{L}}_1, \bar{\mathcal{L}}_2$ , for constant values of  $R_\zeta$  and  $\sqrt{\varepsilon}De_\kappa = 1$  with a relative microchannel ratio of  $\bar{\kappa} = 20$ .

forces,  $\Gamma$ , on the slip coefficient ratio,  $R_\zeta$ , and on the fluid rheology. For a Newtonian fluid the dimensionless *shear rate asymmetry coefficient* is a linear function of  $R_\zeta$ , as expressed by  $\frac{\bar{\Omega}_{1,1}(1) + \bar{\mathcal{L}}_1 \bar{\kappa} (\bar{\Omega}_1^+(-1) + R_\zeta \bar{\Omega}_1^+(1))}{2 + \bar{\mathcal{L}}_1(1 + R_\zeta)}$ , that simplifies to  $\bar{\gamma}_1 = \frac{1}{2} \bar{\Omega}_{1,1}^-(1) = \frac{1}{2} (R_\zeta - 1)$ , when  $\bar{\mathcal{L}}_1 = 0$  as predicted by (Afonso et al., 2011a).

Assuming the no-slip boundary conditions at the walls, for a viscoelastic fluid and  $R_\zeta < 1$ ,  $\bar{\gamma}_1$  is always negative, decreasing with the increase of  $\sqrt{\varepsilon}De_\kappa$ , an indication that the shear stress is also decreasing as  $\sqrt{\varepsilon}De_\kappa$  increases. For  $R_\zeta > 1$ ,  $\bar{\gamma}_1$  is always positive and increases with  $\sqrt{\varepsilon}De_\kappa$ , due to the increasing of the shear-thinning behaviour of the fluid, leading to higher shear stress. Afonso et al. (2011a) showed that all curves asymptote to the same limiting curve when  $\sqrt{\varepsilon}De_\kappa \rightarrow \infty$ , with the absolute value of  $\bar{\gamma}_1$  increasing when  $\bar{\kappa}$  increases.

The dependence of the dimensionless *shear rate asymmetry coefficient* on the slip coefficients  $\bar{\mathcal{L}}_1, \bar{\mathcal{L}}_2$  is shown in Fig. 12.3 for the particular case of  $\sqrt{\varepsilon}De_\kappa = 1$ . We wanted to capture the influence of both slip coefficients on  $\bar{\gamma}_1$  and based on the data obtained from (Afonso et al., 2011a) we have chosen three different values of  $R_\zeta$ . With these three values,  $R_\zeta = -1, 1, 2$ , we plotted two different types of data, the variation of  $\bar{\gamma}_1$  with  $\bar{\mathcal{L}}_2$  ( $\bar{\mathcal{L}}_1 = 0$ ) and the variation of  $\bar{\gamma}_1$  with  $\bar{\mathcal{L}}_1 = \bar{\mathcal{L}}_2$ .

For the first value,  $R_\zeta = -1$ ,  $\bar{\gamma}_1$  is negative and decreases in both situations, being smaller for  $\bar{\mathcal{L}}_1 = \bar{\mathcal{L}}_2$ . The same happens with  $R_\zeta = 2$ , with the difference that  $R_\zeta$  is now positive and increases with  $\bar{\mathcal{L}}_2$  ( $\bar{\mathcal{L}}_1 = 0$ ) and  $\bar{\mathcal{L}}_1 = \bar{\mathcal{L}}_2$ . The decrease of  $\bar{\gamma}_1$  was expected, because the shear stress is reduced when slip velocity is present. We can see that the variation of  $\bar{\gamma}_1$  with the slip velocity is similar to the variation  $\bar{\gamma}_1$



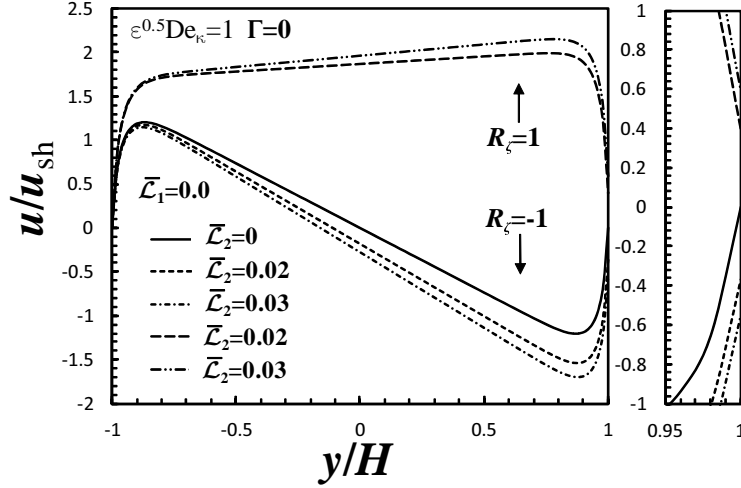


Figure 12.4: Dimensionless velocity profiles as a function of  $\overline{\mathcal{L}}_2$  for constant  $\overline{\mathcal{L}}_1 = 0$ , for the electro-osmotic flow of an sPTT fluid with  $R_\zeta = -1, 1$  and  $\sqrt{\epsilon}De_\kappa = 1$ .

with  $\sqrt{\epsilon}De_\kappa$ . It seems that the slip coefficient enhances the viscoelastic effects.

For  $R_\zeta = 1$ , only the variation of  $R_\zeta$  with  $\overline{\mathcal{L}}_2$  ( $\overline{\mathcal{L}}_1 = 0$ ) was studied because when  $\overline{\mathcal{L}}_1 = \overline{\mathcal{L}}_2$  the flow is symmetric and  $\overline{\gamma}_1 = 0$ . For this case, we found that  $\overline{\gamma}_1$  increases with  $\overline{\mathcal{L}}_2$ .

Fig. 12.4 shows the velocity profiles for asymmetric slip boundary conditions (with  $\overline{\mathcal{L}}_1 = 0$ ). Notice that for  $R_\zeta = 1$ , the velocity profile is skewed because of the asymmetry imposed by the slip velocity. We can also see, as expected, an increase in the flow rate with the slip coefficient  $\overline{\mathcal{L}}_2$ .

Because of the assumption that the slip velocity vector points in the tangent stress opposite direction, for the  $R_\zeta = -1$ , the slip velocity decreases in absolute value (increasing in magnitude).

#### 12.4.2 Mixed driving forces

For the sPTT fluid flow under the combined action of electro-osmosis, pressure gradient and slip boundary conditions we recall Eq. 12.29.

In the work of (Afonso et al., 2011a) is shown (for the asymptotic limit of  $\sqrt{\epsilon}De_\kappa \rightarrow \infty$ ) that increasing the favorable pressure gradient (decreasing  $\Gamma$ ),  $\overline{\gamma}_1$  increases, especially for  $R_\zeta < 1$ , and Increasing  $\Gamma$  for adverse pressure gradient conditions,  $\overline{\gamma}_1$  also increases, especially for  $-1 < R_\zeta < 1$ . Notice that for the asymptotic limit of  $\sqrt{\epsilon}De_\kappa \rightarrow \infty$  the cubic equation that needs to be solved is independent of the slip boundary conditions, therefore, we followed the same procedure adopted for the pure electro-osmotic case. For this case we studied the

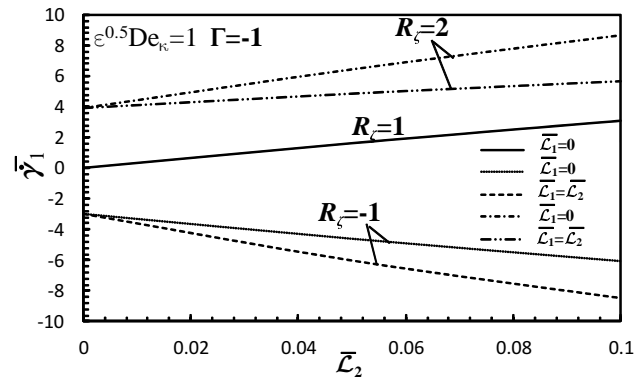


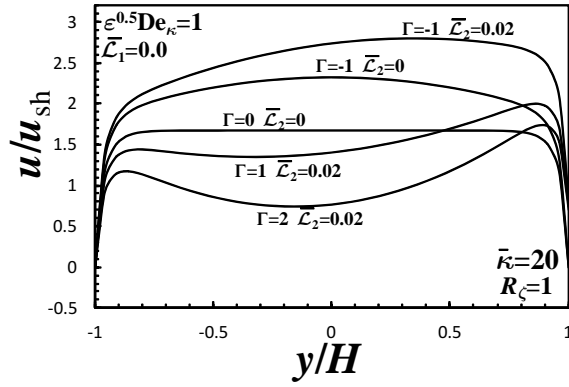
Figure 12.5: Variation of  $\bar{\gamma}_1$  with the slip coefficients,  $\bar{\mathcal{L}}_1$ ,  $\bar{\mathcal{L}}_2$ , for constant values of  $R_\zeta$  and  $\sqrt{\varepsilon}De_\kappa = 1$  with a relative microchannel ratio of  $\bar{\kappa} = 20$  and a favorable pressure gradient  $\Gamma = -1$ .

variation of  $\bar{\gamma}_1$  with the slip coefficients  $\bar{\mathcal{L}}_1$  and  $\bar{\mathcal{L}}_2$  for  $R_\zeta = -1, 1, 2$  and  $\Gamma = -2, -1, 0, 1, 2$ . The results obtained are very similar to the ones obtained for  $\Gamma = 0$  with the difference that the absolute values of  $\bar{\gamma}_1$  increased with  $\Gamma$ . (Fig. 12.5)

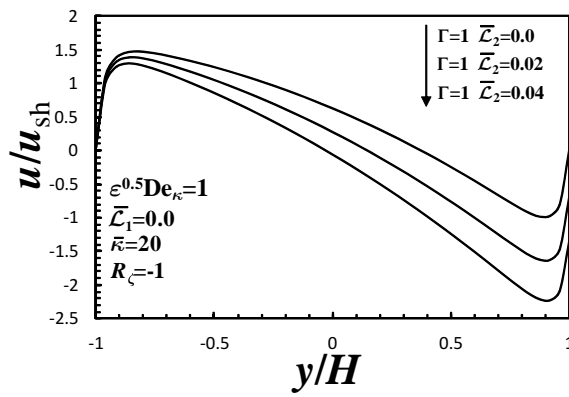
Figures 12.6 (a) and (b) present the dimensionless velocity profiles for slip flows with symmetric ( $R_\zeta = 1$ ) and anti-symmetric zeta potentials ( $R_\zeta = -1$ ), respectively, for a constant dimensionless number  $\sqrt{\varepsilon}De_\kappa$  of 1. For both, favorable ( $\Gamma < 0$ ) and adverse pressure gradients ( $\Gamma > 0$ ), Fig. 12.6 (a) shows that the velocity profile increases with  $\bar{\mathcal{L}}_2$ , this is due to the consequent reduction of the shear stress near the wall. For the case of  $R_\zeta = -1$ , Fig. 12.6 (b), shows that the slip velocity increases in the direction of the flow. For this case, the flow near the upper wall is in the adverse direction and therefore the slip velocity increases (in magnitude) in that direction.

## 12.5 CONCLUSIONS

In this work we devised analytical solutions for the fully developed channel flow of symmetric z-z electrolyte viscoelastic fluids (sPTT and FENE-P) under the mixed influence of electro-osmosis and pressure gradient forcings for the case of symmetric and asymmetric wall zeta potentials and assuming different slip coefficients at the bottom and top walls, representing the different hydrophobic characteristics of the microchannels walls. We found that an increase in the slip coefficient leads to an increase of the flow rate. This increase in the slip coefficient has also influence in the the asymmetry coefficient, with  $\bar{\gamma}_1$  decreasing for  $R_\zeta < 0$  and increasing for  $R_\zeta > 0$ . The solution for the streaming potential is also presented.



(a)



(b)

Figure 12.6: Dimensionless velocity profiles as a function of  $\overline{\mathcal{L}}_2$  for constant  $\overline{\mathcal{L}}_1 = 0$ , for the electro-osmotic flow of an sPTT fluid with  $\sqrt{\varepsilon}De_\kappa = 1$  (a)  $R_\zeta = 1$  (b)  $R_\zeta = -1$ .

## ACKNOWLEDGEMENTS

The authors acknowledge funding from FEDER and Fundação para a Ciência e a Tecnologia (FCT), Portugal, through projects PTDC/EQU-FTT/70727/2006 and PTDC/EQU-FTT/113811/2009, and FEDER, via FCT, under the PEst-C/CTM/LA0025/2011 (Strategic Project - LA 25 - 2011-2012). LLF would like to thank FCT for financial support through the scholarship SFRH/BD/37586/2007. AMA would also like to thank FCT for financial support through scholarship SFRH/BPD/75436/2010.

## APPENDIX: STREAMING POTENTIAL SOLUTION

In the solution presented before, the electrical field  $E_x$  can be applied externally or be a consequence of electric potentials created by the flow. In the absence of an externally applied electrical field, the applied pressure difference induces a flow carrying ions that generate an electrical current, called the streaming current,  $I'_s$ . The streaming current accumulates counterions at the end of the channel therefore setting up an electric field,  $E_{x,sp}$  which is associated with the so-called streaming potential,  $\phi_{sp}$  via  $E_{x,sp} = -\Delta\phi_{sp}/l$ . This induced electric field creates an opposite current,  $I'_c$ , called conduction current which induces a flow contrary to the pressure induced flow. This is established in such way that under steady state the net electrical current,  $I'$ , the sum of the streaming currents and the electrical conduction current vanishes,

$$I' = I'_s + I'_c \equiv 0. \quad (12.46)$$

The electrical streaming current (per unit of width) is of the form:

$$I'_s = \int_{-H}^H u(y)\rho_e(y)dy = \int_{-H}^H -u(y)\epsilon\kappa^2\zeta_1\Omega_1^-(y)dy, \quad (12.47)$$

which for the sPTT fluid leads to

$$\begin{aligned}
\frac{I'_s}{\epsilon\zeta_1} &= \mathcal{L}_1\eta \left( X\kappa\Omega_1^+(-H) - YH + \frac{\tau_1}{\eta} \right) \kappa\Omega_{1,1}^+(H) \\
&- \dot{\gamma}_1 \left( 1 + 2\epsilon\lambda^2\dot{\gamma}_1^2 \right) \left( 2\kappa\Omega_1^+(H) - \Omega_{1,1}^-(H) \right) + 6\epsilon\lambda^2X^2\dot{\gamma}_1\Psi_1\Psi_2 \left( 2\Omega_{1,1}^-(H) - 4\bar{\kappa}\Omega_1^+(H) \right) \\
&- \frac{1}{2}X\kappa \left( 1 + 6\dot{\gamma}_1^2\epsilon\lambda^2 \right) \left( \Omega_2^-(H) + \Omega_2^-(-H) - 2\Psi_1\Psi_2 \left( 4\bar{\kappa} + e^{-2\bar{\kappa}} - e^{2\bar{\kappa}} \right) - 2\Psi_1^2 + 2\Psi_2^2 \right) \\
&+ \epsilon\lambda^2X^2\kappa^2\dot{\gamma}_1 \left[ -\Omega_3^-(H) - 2\Omega_3^-(-H) + 3\Psi_1\Psi_2 \left( \Omega_1^-(H) - 2\Omega_1^-(-H) \right) + 3 \left( \Psi_1^3e^{-\bar{\kappa}} - \Psi_2^3e^{\bar{\kappa}} + \Psi_1^2\Psi_2e^{-3\bar{\kappa}} - \Psi_1\Psi_2^2e^{3\bar{\kappa}} \right) \right] \\
&+ \frac{1}{6}\epsilon\lambda^2X^3\kappa^3 \left[ -\Omega_4^-(H) - 3\Omega_4^-(-H) + 2\Psi_1\Psi_2 \left( \Omega_2^-(H) - 3\Omega_2^-(-H) \right) + 4 \left( \Psi_1^4e^{-2\bar{\kappa}} - \Psi_2^4e^{2\bar{\kappa}} + \Psi_1^3\Psi_2e^{-4\bar{\kappa}} - \Psi_1\Psi_2^3e^{4\bar{\kappa}} \right) \right] \\
&+ 6\epsilon\lambda^2X^3\kappa^3\Psi_1\Psi_2 \left( \Psi_1^2 - \Psi_2^2 - \frac{1}{2} \left( \Omega_2^-(H) + \Omega_2^-(-H) \right) + \Psi_1\Psi_2 \left( 4\bar{\kappa} + e^{-2\bar{\kappa}} - e^{2\bar{\kappa}} \right) \right) \\
&+ \frac{Y}{\kappa} \left( 1 + 6\epsilon\lambda^2\dot{\gamma}_1^2 \right) \left( \Omega_{1,2}^-(H) - \Omega_{1,1}^+(H) \right) + 2\frac{\epsilon\lambda^2}{\kappa^3}Y^3 \left[ \Omega_{1,4}^-(H) - 3\Omega_{1,3}^+(H) + 6\Omega_{1,2}^-(H) - 6\Omega_{1,1}^+(H) \right] \\
&- 2\frac{\dot{\gamma}_1\epsilon\lambda^2}{\kappa^2}Y^2 \left[ 2\kappa^3\Omega_1^+(H) - 3\Omega_{1,3}^+(H) + 6\Omega_{1,2}^+(H) - 6\Omega_{1,1}^-(H) \right] - 3\epsilon\lambda^2XY\dot{\gamma}_1 \left[ 2\bar{\kappa}\Omega_{2,1}^-(H) - 3\Omega_2^+(H) - \Omega_2^+(-H) \right] \\
&- 12\epsilon\lambda^2XY\dot{\gamma}_1 \left[ \Psi_1\Psi_2 \left( -2 + e^{-2\bar{\kappa}}(1 + \bar{\kappa}) + e^{2\bar{\kappa}}(1 - \bar{\kappa}) \right) + \Psi_1^2(1 + \bar{\kappa}) + \Psi_2^2(1 - \bar{\kappa}) \right] \\
&- \frac{1}{2}\frac{\epsilon\lambda^2XY^2}{\kappa} \left[ 6\bar{\kappa}\Omega_{2,2}^-(H) - 6\Omega_{2,2}^+(H) + 3\Omega_{2,1}^-(H) + 12 \left( \Psi_1\Psi_2 \left( -\frac{4}{3}\bar{\kappa}^3 - \bar{\kappa}^2e^{-2\bar{\kappa}} + \bar{\kappa}^2e^{2\bar{\kappa}} \right) + \bar{\kappa}^2\Psi_2^2 - \bar{\kappa}^2\Psi_1^2 \right) \right] \\
&- 6\frac{\epsilon\lambda^2XY^2}{\kappa} \left[ \Omega_2^-(H) + \Omega_2^-(-H) + \Psi_1\Psi_2 \left( -8\bar{\kappa} - 2e^{-2\bar{\kappa}} + 2e^{2\bar{\kappa}} \right) + 2\Psi_2^2 - 2\Psi_1^2 - \frac{1}{2} \left( 2\bar{\kappa}\Omega_{2,1}^+(H) - \Omega_{2,1}^-(H) \right) \right] \\
&+ 12\frac{\epsilon\lambda^2XY^2}{\kappa} \left[ \bar{\kappa}\Psi_1\Psi_2 \left( -2 + e^{-2\bar{\kappa}} + e^{2\bar{\kappa}} \right) + \bar{\kappa}\Psi_2^2 + \bar{\kappa}\Psi_1^2 \right] - 12\frac{\epsilon\lambda^2}{\kappa}X^2Y\Psi_1\Psi_2\kappa^2 \left( -\Omega_{1,2}^-(H) + \Omega_{1,1}^+(H) \right) \\
&- \frac{1}{6}\epsilon\lambda^2\kappa X^2Y \left[ -5\Omega_3^+(H) - 4\Omega_3^+(-H) + 6\bar{\kappa}\Omega_3^-(H) - 12\bar{\kappa}\Omega_3^-(-H) + Z \right] \\
&- \frac{3}{2}\epsilon\lambda^2\kappa X^2Y \left[ (2\bar{\kappa} + 1) \left( \Psi_1^2\Psi_2e^{-3\bar{\kappa}} + \Psi_1^3e^{-\bar{\kappa}} \right) + (1 - 2\bar{\kappa}) \left( \Psi_1\Psi_2^2e^{3\bar{\kappa}} + \Psi_2^3e^{\bar{\kappa}} \right) \right]. \tag{12.48}
\end{aligned}$$

with  $X = \frac{\epsilon E_{x,sp}\zeta_1}{\eta}$ ,  $Y = \frac{p_x}{\eta}$  and

$$Z = \Psi_1\Psi_2 \left( 27\Omega_1^+(H) - 36\Omega_1^+(-H) - 18\bar{\kappa}\Omega_1^-(H) - 36\bar{\kappa}\Omega_1^-(-H) \right)$$

In equation (12.48) the electric potential  $E_x$  has already been substituted by the corresponding streaming potential,  $E_{x,sp}$ . The electrical conduction current in the channel is defined as:

$$I'_c = 2H\sigma_t E_{x,sp}, \tag{12.49}$$

where  $\sigma_t$  is the total electric conductivity. Note that the conduction current can now flow back through both the fluid as well as the channel walls, depending on the corresponding electrical conductivities. The total electrical conductivity can be calculated as  $\sigma_t = \sigma_{fluid} + \sigma_{sur}P_{sur}/A_{chan}$ , where  $P_{sur}$  and  $A_{chan}$  are the wetting perimeter and cross section area of the channel, respectively and  $\sigma_{fluid}$  and  $\sigma_{sur}$  are the fluid bulk and wall surface conductivities, respectively. Upon substitution of equation (12.48) and (12.49) we arrive at an algebraic cubic equation in the streaming potential field as function of the imposed pressure gradient. This cubic equation has a real solution given in equation (12.33). This cubic equation in  $E_{x,sp}$  can alternatively be written in non dimensional form to give  $\Gamma_{sp}$ , where  $\Gamma_{sp} = -\frac{H^2}{\epsilon\zeta_1} \frac{p_x}{E_{x,sp}}$ . In this case, it is customary (Afonso et al., 2011a) to normalize the electric conductivity  $\sigma_t$  as  $Y_1$ , defined as  $Y_1 = \frac{H^2\eta\sigma_t}{\epsilon^2\zeta_1^2}$ .



Part VI

CONCLUSIONS AND OUTLOOK





## CONCLUSIONS

---

Because this thesis is based on articles/publications, with conclusions at the end of each article, the main conclusions will be given here as answers to the proposed objectives.

- ▶ *Derive analytical solutions for Newtonian and non-Newtonian fluids with slip boundary conditions. For the cases where an explicit formula is not possible, the existence and uniqueness of the solution must be proved;*

ANSWER: We derived analytical solutions for various Generalized Newtonian fluids and also viscoelastic fluids. These analytical solutions are helpful for the understanding of the slip phenomenon, its influence on the fluid flow and its dependence on different parameters. Some of the slip models were quite complex (nonlinear models) and an explicit solution was impossible, mainly because the resulting equations were transcendental. Because the existence and uniqueness of these simple solutions was proved, they can also be used as a “semi-analytical” solution for the problem. The full analytical solution is an equation that can be easily manipulated, the “semi-analytical” solution is represented by numerical values but gives the same information as the analytical one. The main difference is that we need to find each of these numerical values, a task that can be easily performed with any mathematics package, such as Matlab, Maple or Mathematica.

- ▶ *Derive analytical solutions for electro-osmotic flow under the influence of slip boundary conditions;*

ANSWER: It is possible to derive full analytical solutions for the electro-osmotic flow with slip boundary conditions. These analytical solutions allowed us to understand the influence of the slip velocity in the electro-osmotic flow and can also be used as a possible model for the theory of slip in the electro-osmotic flow.

- ▶ *Study the influence of the slip velocity on the development length of Newtonian and non-Newtonian fluids;*

ANSWER: We derived a correlation to predict the development length for channel flow of Newtonian fluids under the influence of slip. We concluded that the development length increased with the slip velocity, for small slip coefficients, but decreased for very

high slip coefficients. We also studied the development length for the UCM model. This development length study works for both micro and macro flows (such as extrusion process).

► *Is it possible to implement slip boundary conditions in the finite volume method framework? There are any limitations?*

ANSWER: Yes. Slip boundary conditions of different types were implemented in a Finite Volume Code, using three different approaches. For highly nonlinear slip laws convergence issues were found. These issues increased with the Hatzikiriakos slip model, a highly nonlinear model based on the sinh function. A fully implicit numerical code could give better results, but to change the intrinsic structure of the code was not possible during this thesis period. For the other nonlinear models convergence could be obtained for high values of  $De$  and  $Re$  numbers. Notice that it is not clear, in some cases, if the divergence occurs because of the implementation of the slip law, or because the combined effects of  $De$  and slip velocity that could decrease the critical  $De$ .

► *Is it possible to use slip boundary conditions as a method to improve the limits brought by the High Weissenberg Number Problem (HWNP)?*

ANSWER: Some tests were made for the case of the slip-stick flow of an Upper Convected Maxwell fluid, with and without slip velocity. We notice that convergence for the no-slip case could only be achieved up to  $De \simeq 1$ . For the case with slip velocity, we could obtain convergence for higher values of  $De$  as long as we increased the slip coefficient. The idea of using a converged solution with slip velocity, as an initial flow field for another similar simulation but now without slip velocity was not successful. In the beginning of the iterative process the residuals still decreased but rapidly they start to diverge. This happened for the UCM viscoelastic model, a model known to be very difficult to work with, in the presence of singularities. For other models no studies were made.

► *Is the presence of slip velocity always helpful during the extrusion process?*

ANSWER: On profile extrusion it is common to use external lubricants as processing aids, which improves the possibility of polymer melt to slip at the flow channel wall. Among other advantages, lubricants are known to delay the onset of flow instabilities or to contribute positively for the flow distribution, due the reduction of the differential restriction promoted by regions of different thickness (c.f. Fig. ?? and Fig. ??). The common referred as single disadvantage of lubricants is their high cost. However,

the results obtained for the sudden contraction problem, namely the increase of the vortex dimensions with the slip intensity, evidenced that the incorporation of lubricants can induce the growth of the recirculation zones and, consequently, an increase of the stagnated material extent. This information should not restrain significantly the employment of lubricants, but should be taken into account when working with the extrusion process.



## OUTLOOK

---

The modelling and numerical simulation of flows under slip is still under development and the full understanding of this subject is still an Utopia. Although most of the questions proposed in the objectives were answered, there are plenty of other works under development, or, that can be further explored.

The influence of slip velocity on the flow past a cylinder is now under development with preliminary results showing a decrease in the drag coefficient with the increase of the slip coefficient (for the Navier slip law).

The complete study of a slip-stick flow together with free-surface flow, capturing the influence on the extruded profile, of the slip-stick velocity inside the die, seems to be a difficult task, lacking a good physical model and numerical simulations. A model for this phenomenon could be based on pulsating boundary conditions, thus creating the effect of slip and stick.

The benchmark solutions of slip flows in a lid-driven cavity are still missing in the literature. The proof of existence of analytical solutions for different viscoelastic fluids and different slip models can be further developed, to allow the validation of computational codes equipped with slip models

The optimization of extrusion die design accounting for the slip velocity is already under development. Preliminary results showed that slip velocity, affect directly the flow distribution in profile extrusion dies. Additionally slip minimizes the differential restrictions promoted by regions with different thicknesses, thus contributing positively to its optimization. These results were obtained for generalized Newtonian fluids, thus lacking the relaxation times, a characteristic of viscoelastic fluids. In the near future this feature should be further investigated.

This optimization is being done without free-surface, by looking at the velocity profiles at the exit of the die. The implementation of free surface in the numerical code is another indispensable feature.

For the electro-osmotic flow, more analytical solutions can be found assuming different slip boundary conditions, but more important, is the need to find a theory connecting the slip boundary conditions with the underlying physics of the electro-osmosis.

It can be said that this journey has just begun, with a vast number of studies to be performed, so that the slip velocity phenomenon can be truly understood.



Part VII

BIBLIOGRAPHY AND REFERENCES





## BIBLIOGRAPHY

---

- Abbott, D., Kline, S., 1962. Experimental investigation of subsonic turbulent flow over single and double backward facing steps. *Journal of basic engineering* 84, 317.
- Aboubacar, M., Matallah, H., Webster, M., 2002. Highly elastic solutions for oldroyd-b and phan-thien/tanner fluids with a finite volume/element method: planar contraction flows. *Journal of non-newtonian fluid mechanics* 103 (1), 65–103.
- Aboubacar, M., Webster, M. F., 2001. A cell-vertex finite volume/element method on triangles for abrupt contraction viscoelastic flows. *J. Non-Newtonian Fluid Mech.* 98 (2-3), 83–106.
- Afonso, A., Alves, M., Pinho, F., 2011a. Electro-osmotic flow of viscoelastic fluids in microchannels under asymmetric zeta potentials. *Journal of Engineering Mathematics* 71 (1), 15–30.
- Afonso, A., Oliveira, P., Pinho, F., Alves, M., 2011b. Dynamics of high-deborah-number entry flows: a numerical study. *Journal of Fluid Mechanics* 677 (1), 272–304.
- Afonso, A., Oliveira, P. J., Pinho, F. T., Alves, M. A., 2009a. The log-conformation tensor approach in the finite volume method framework. *J. Non-Newtonian Fluid Mech.* 157, 55–65.
- Afonso, A., Pinho, F., Alves, M., 2012. Electro-osmosis of viscoelastic fluids and prediction of electro-elastic flow instabilities in a cross slot using a finite-volume method. *Journal of Non-Newtonian Fluid Mechanics*.
- Afonso, A. M., Alves, M. A., Pinho, F. T., 2009b. Analytical solution of mixed electro-osmotic pressure driven flows of viscoelastic fluids in microchannels. *J. Non-Newtonian Fluid Mech.* 159, 50–63.
- Alves, M. A., Oliveira, P. J., Pinho, F. T., 2003a. A convergent and universally bounded interpolation scheme for the treatment of advection. *International Journal for Numerical Methods in Fluids* 41 (1), 47–75.
- Alves, M. A., Oliveira, P. J., Pinho, F. T., 2003b. Benchmark solutions for the flow of Oldroyd-B and PTT fluids in planar contractions. *J. Non-Newtonian Fluid Mech.* 110 (1), 45–75.
- Alves, M. A., Pinho, F. T., Oliveira, P. J., 2000. Effect of a high-resolution differencing scheme on finite-volume predictions of viscoelastic flows. *J. Non-Newtonian Fluid Mech.* 93 (2-3), 287–314.

- Alves, M. A., Pinho, F. T., Oliveira, P. J., 2001a. Study of steady pipe and channel flows of a single-mode Phan-Thien-Tanner fluid. *J. Non-Newtonian Fluid Mech.* 101, 55–76.
- Alves, M. A., Pinho, F. T., Oliveira, P. J., 2001b. The flow of viscoelastic fluids past a cylinder: finite-volume high-resolution methods. *J. Non-Newtonian Fluid Mech.* 97 (2-3), 207–232.
- Alves, M. A., Pinho, F. T., Oliveira, P. J., 2005. Visualizations of Boger fluid flows in a 4: 1 square-square contraction. *AIChE journal* 51 (11), 2908–2922.
- Alves, M. A., Pinho, F. T., Oliveira, P. J., 2008. Viscoelastic flow in a 3D square/square contraction: Visualizations and simulations. *Journal of Rheology* 52, 1347.
- Archer, L., 2005. Wall slip: measurement and modeling issues. *Polymer Processing Instabilities*, edited by SG Hadzikiriakos, KB Migler (Marcel Dekker, New York, 2005), 73.
- Awati, K., Park, Y., Weisser, E., Mackay, M., 2000. Wall slip and shear stresses of polymer melts at high shear rates without pressure and viscous heating effects. *Journal of non-newtonian fluid mechanics* 89 (1-2), 117–131.
- Azaiez, J., Guenette, R., Aït-Kadi, A., 1996. Numerical simulation of viscoelastic flows through a planar contraction. *Journal of non-newtonian fluid mechanics* 62 (2-3), 253–277.
- Baloch, A., Townsend, P., Webster, M., 1996. On vortex development in viscoelastic expansion and contraction flows. *Journal of non-newtonian fluid mechanics* 65 (2-3), 133–149.
- Barber, R., Emerson, D., 2001. A numerical investigation of low reynolds number gaseous slip flow at the entrance of circular and parallel plate micro-channels. In: *ECCOMAS Computational Fluid Dynamics Conference*, Swansea, Wales, UK.
- Barbosa, R., 2012. Numerical study of the development length for newtonian and viscoelastic fluids flow between parallel plates. Master's thesis, FEUP.
- Barrat, J., Bocquet, L., 1999. Large slip effect at a nonwetting fluid-solid interface. *Physical Review Letters* 82 (23), 4671–4674.
- Batchelor, G., 2000. *An introduction to fluid dynamics*. Cambridge Univ Pr.
- Baudry, J., Charlaix, E., Tonck, A., Mazuyer, D., 2001. Experimental evidence for a large slip effect at a nonwetting fluid-solid interface. *Langmuir* 17 (17), 5232–5236.

- Beebe, D., Mensing, G., Walker, G., 2002. Physics and applications of microfluidics in biology. *Annual review of biomedical engineering* 4 (1), 261–286.
- Benbow, J., Lamb, P., 1963. New aspects of melt fracture. *Polymer Engineering & Science* 3 (1), 7–17.
- Berker, R., 1963. Integration des equations du mouvement d'un fluide visqueux incompressible. *Handbuch der Physik* 2, 1–384.  
URL <http://ci.nii.ac.jp/naid/10010625198/en/>
- Bernoulli, D., 1738. *Hydrodynamica*. Typs Joh. Henr. Deckeri.
- Bird, R. B., Armstrong, R. C., Hassager, O., 1987. *Dynamics of Polymeric Liquids*. Vol. 1- Fluid Mechanics, 2nd Edition. John Wiley & Sons, New York.
- Bird, R. B., Dotson, P. J., Johnson, N. L., 1980. Polymer solution rheology based on a finitely extensible bead-spring chain model. *J. Non-Newtonian Fluid Mech* 7, 213–235.
- Bird, R. B., Stewart, W. E., Lightfoot, E. N., 2002. *Transport Phenomena*, 2nd Edition. John Wiley & Sons, New York.
- Boger, D. V., 1987. Viscoelastic flows through contractions. *Annu. Rev. Fluid Mech.* 19, 157–182.
- Boger, D. V., Walters, K., 1993. *Rheological phenomena in focus*. Elsevier, Amsterdam.
- Bonaccorso, E., Kappl, M., Butt, H., 2002. Hydrodynamic force measurements: boundary slip of water on hydrophilic surfaces and electrokinetic effects. *Physical review letters* 88 (7), 76103.
- Brenner, S., Scott, L., 2008. *The mathematical theory of finite element methods*. Vol. 15. Springer Verlag.
- Bringhurst, R., 2002. *The Elements of Typographic Style*. Version 2.5. Hartley & Marks, Publishers, Point Roberts, WA, USA.
- Brochard, F., De Gennes, P., 1992. Shear-dependent slippage at a polymer/solid interface. *Langmuir* 8 (12), 3033–3037.
- Bruss, H., 2008. *Theoretical Microfluidics*, Oxford Master Series in Condensed Matter Physics. Oxford University Press, Oxford, UK.
- Carew, E., Townsend, P., Webster, M., 1993. A taylor-petrov-galerkin algorithm for viscoelastic flow. *Journal of non-newtonian fluid mechanics* 50 (2-3), 253–287.
- Chatzimina, M., Georgiou, G., Housiadas, K., Hatzikiriakos, S., 2009. Stability of the annular poiseuille flow of a newtonian liquid with slip along the walls. *Journal of Non-Newtonian Fluid Mechanics* 159 (1-3), 1–9.

- Chen, Y., Kalyon, D., Bayramli, E., 1993. Effects of surface roughness and the chemical structure of materials of construction on wall slip behavior of linear low density polyethylene in capillary flow. *Journal of applied polymer science* 50 (7), 1169–1177.
- Cherdron, W., Durst, F., Whitelaw, J., 1978. Asymmetric flows and instabilities in symmetric ducts with sudden expansions. *Journal of Fluid Mechanics* 84 (1), 13–31.
- Churaev, N., Ralston, J., Sergeeva, I., Sobolev, V., 2002. Electrokinetic properties of methylated quartz capillaries. *Advances in colloid and interface science* 96 (1-3), 265–278.
- Coates, P. J., Armstrong, R. C., Brown, R. A., 1992. Calculation of steady-state viscoelastic flow through axisymmetric contractions with the EEME formulation. *J. Non-Newtonian Fluid Mech.* 42 (1-2), 141–188.
- Cochrane, T., Walters, K., Webster, M. F., May 1981. On newtonian and non-newtonian flow in complex geometries. *Phil. Trans. R. Soc. Lond. A* 301 (1460), 163–181.
- Couette, M., 1890. Etudes sur le frottement des liquides. Ph.D. thesis.
- Coulomb, C., 1801. Experiments to determine the coherence of fluids and laws of their resistance to very slow motions. *Mem. Inst. Nat. Sci. Arts Sci. Math. Phys.*, 3, 246–307.
- Courant, R., 1994. Variational methods for the solution of problems of equilibrium and vibrations. *LECTURE NOTES IN PURE AND APPLIED MATHEMATICS*, 1–1.
- Courant, R., Friedrichs, K., Lewy, H., 1967. On the partial difference equations of mathematical physics. *IBM Journal of Research and Development* 11 (2), 215–234.
- Craig, V., Neto, C., Williams, D., 2001. Shear-dependent boundary slip in an aqueous newtonian liquid. *Physical review letters* 87 (5), 54504.
- Crocker, J., Valentine, M., Weeks, E., Gisler, T., Kaplan, P., Yodh, A., Weitz, D., 2000. Two-point microrheology of inhomogeneous soft materials. *Physical Review Letters* 85 (4), 888–891.
- Cruz, D. O. A., Pinho, F. T., Oliveira, P. J., 2005. Analytical solutions for fully developed laminar flow of some viscoelastic liquids with a newtonian solvent contribution. *J. Non-Newtonian Fluid Mech.* 132 (1-3), 28–35.
- Dales, C., Escudier, M., Poole, R., 2005. Asymmetry in the turbulent flow of a viscoelastic liquid through an axisymmetric sudden expansion. *Journal of non-newtonian fluid mechanics* 125 (1), 61–70.

- Darbandi, M., Schneider, G., 1998. Numerical study of the flow behavior in the uniform velocity entry flow problem. *Numerical Heat Transfer, Part A Applications* 34 (5), 479–494.
- Darcy, H., 1857. *Recherches experimentales relatives au mouvement de l'eau dans les tuyaux, mallet-bachelier.*
- Darwish, M., Whiteman, J., Bevis, M., 1992. Numerical modelling of viscoelastic liquids using a finite-volume method. *Journal of non-newtonian fluid mechanics* 45 (3), 311–337.
- De Gennes, P., 1979. Viscometric flows of tangled polymers. *CR Acad. Sci. Paris B* 288, 219–220.
- Dealy, J., Kim, S., 2005. Gross melt fracture in extrusion. *Polymer processing instabilities: control and understanding*, 207.
- Dean, W., Montagnon, P., 1949. On the steady motion of viscous liquid in a corner. In: *Mathematical Proceedings of the Cambridge Philosophical Society*. Vol. 45. Cambridge Univ Press, pp. 389–394.
- Debbaut, B., Crochet, M., 1988. Extensional effects in complex flows. *Journal of non-newtonian fluid mechanics* 30 (2), 169–184.
- Denn, M. M., January 2001. Extrusion instabilities and wall slip. *Annual Review of Fluid Mechanics* 33, 265–287.
- Dhinakaran, S., Afonso, A. M., Alves, M. A., Pinho, F. T., 2010. Steady viscoelastic fluid flow in microchannels under electrokinetic forces: Ptt model. *Journal of Colloid And Interface Science* 344, 513–520.
- Du Buat, P., 1786. *Principes d'hydraulique... De l'Imprimerie de Monsieur.*
- Durst, F., Melling, A., Whitelaw, J., 1974. Low reynolds number flow over symmetric sudden expansion.
- Durst, F., Ray, S., Ünsal, B., Bayoumi, O., 2005. The development lengths of laminar pipe and channel flows. *Journal of fluids engineering* 127, 1154.
- El Kissi, N., Paiu, J., 1990. The different capillary flow regimes of entangled polydimethylsiloxane polymers: macroscopic slip at the wall, hysteresis and cork flow. *Journal of Non-Newtonian Fluid Mechanics* 37 (1), 55–94.
- Ellahi, R., Hayat, T., Mahomed, F., Zeeshan, A., 2010. Exact solutions for flows of an oldroyd 8-constant fluid with nonlinear slip conditions. *Communications in Nonlinear Science and Numerical Simulation* 15 (2), 322–330.

- Escudier, M., Oliveira, P., Poole, R., 2002. Turbulent flow through a plane sudden expansion of modest aspect ratio. *Physics of Fluids* 14, 3641.
- Estellé, P., Lanos, C., 2007. Squeeze flow of bingham fluids under slip with friction boundary condition. *Rheologica acta* 46 (3), 397–404.
- Evans, J., 2010. Re-entrant corner behaviour of the ptt fluid with a solvent viscosity. *Journal of Non-Newtonian Fluid Mechanics* 165 (9–10), 527–537.
- Evans, J., Sibley, D., 2008. Re-entrant corner flows of ptt fluids in the cartesian stress basis. *Journal of Non-Newtonian Fluid Mechanics* 153 (1), 12–24.
- Evans, J., Sibley, D., 2009. Re-entrant corner flow for ptt fluids in the natural stress basis. *Journal of Non-Newtonian Fluid Mechanics* 157 (1-2), 79–91.
- Fattal, R., Kupferman, R., November 2004. Constitutive laws for the matrix-logarithm of the conformation tensor. *J. Non-Newtonian Fluid Mech.* 123 (2-3), 281–285.
- Ferrás, L., Afonso, A., Alves, M., Nóbrega, J., Olga, S., Pinho, F., 2012a. Flow of newtonian and phan-thien and tanner fluids in a 4:1 planar contraction with slip boundary conditions. submitted to *Journal of Non-Newtonian Fluid Mechanics*.
- Ferrás, L., Afonso, A., Alves, M., Nóbrega, J., Pinho, F., 2012b. Development length in planar channel flows of newtonian fluids under the influence of wall slip. accepted for publication in the *Journal of Fluids Engineering*.
- Ferrás, L., Nóbrega, J., Pinho, F., 2012c. Analytical solutions for channel flows of phan-thien–tanner and giesekus fluids under slip. *Journal of Non-Newtonian Fluid Mechanics* 171, 97–105.
- Ferrás, L., Nóbrega, J., Pinho, F., 2012d. Implementation of slip boundary conditions in the finite volume method: New techniques. accepted for publication in the *International Journal for Numerical Methods in Fluids*.
- Fordham, E., Bittleston, S., Tehrani, M., 1991. Viscoplastic flow in centered annuli, pipes, and slots. *Industrial & Engineering Chemistry Research* 30 (3), 517–524.
- Frigaard, I., Howison, S., Sobey, I., 1994. On the stability of poiseuille flow of a bingham fluid. *Journal of Fluid Mechanics* 263, 133–150.
- Fu, C., Zhou, H., Yin, H., Zhong, H., Jiang, H., 2010. Flow behavior of ucm viscoelastic fluid in sudden contraction channel. *Natural Science* 2 (7), 780–785.

- Fujita, H., 2002. A coherent analysis of stokes flows under boundary conditions of friction type. *Journal of computational and applied mathematics* 149 (1), 57–69.
- Gad-el Hak, M., 1999. The fluid mechanics of microdevices-the free-man scholar lecture. *TRANSACTIONS-AMERICAN SOCIETY OF MECHANICAL ENGINEERS JOURNAL OF FLUIDS ENGINEERING* 121, 5–33.
- Gaskell, P. H., Lau, A. K. C., 1988. Curvature-compensated convective transport: SMART, a new boundedness-preserving transport algorithm. *International Journal for Numerical Methods in Fluids* 8 (6), 617–641.
- Gevgilili, H., Kalyon, D., 2001. Step strain flow: Wall slip effects and other error sources. *Journal of Rheology* 45, 467.
- Giesekus, H., 1982. A simple constitutive equation for polymer fluids based on the concept of deformation-dependent tensorial mobility. *J. Non-Newtonian Fluid Mech.* 11 (1-2), 69–109.
- Girard, P., 1813. Motion of fluids in capillary tubes. *Mem. de l'Inst* 1816, 249–380.
- Goldstein, S., 1965. Aeronautical research council (great britain), modern developments in fluid dynamics: An account of theory and experiment relating to boundary layers, turbulent motion and wakes.
- Guermond, J., Mineev, P., Shen, J., 2006. An overview of projection methods for incompressible flows. *Computer Methods in Applied Mechanics and Engineering* 195 (44), 6011–6045.
- Guilbeau, L., 1930. The history of the solution of the cubic equation. *Mathematics News Letter*, 8–12.
- Gurtin, M., 1981. *An introduction to continuum mechanics*. Vol. 158. Academic Pr.
- Halmos, A., Boger, D., 1975. The behavior of a power-law fluid flowing through a sudden expansion. part ii. experimental verification. *AIChE Journal* 21 (3), 550–553.
- Halmos, A., Boger, D., 1976. Flow of viscoelastic polymer solutions through an abrupt 2-to-1 expansion. *Journal of Rheology* 20, 253.
- Hatzikiriakos, S., 1993. A slip model for linear polymers based on adhesive failure. *Int. Polym. Process* 8, 135–142.
- Hatzikiriakos, S., Dealy, J., 1991. Wall slip of molten high density polyethylene. i. sliding plate rheometer studies. *Journal of rheology* 35, 497.

- Hatzikiriakos, S., Dealy, J., 1992. Wall slip of molten high density polyethylenes. ii. capillary rheometer studies. *Journal of rheology* 36, 703.
- Hatzikiriakos, S., Mitsoulis, E., 2009. Slip effects in tapered dies. *Polymer Engineering & Science* 49 (10), 1960–1969.
- Hatzikiriakos, S. G., 2012. Wall slip of molten polymers. *Progress in Polymer Science* 37 (4), 624 – 643, <ce:title>Topical Issue on Polymer Physics</ce:title>.  
URL <http://www.sciencedirect.com/science/article/pii/S0079670011001109>
- Helmholtz, H., 1860. Über Reibung tropfbarer Flüssigkeiten: Von H. Helmholtz und G. v. Piotrowski. (Mit 2 Taff.)(Aus d. XL. Bd. S. 607. 1860. der Sitzgsber. der math-nat. Cl. der k. Ak. der Wiss. bes. dbg.). Hof-& Stts.-Druck.
- Herr, A., Molho, J., Santiago, J., Mungal, M., Kenny, T., Garguilo, M., 2000. Electroosmotic capillary flow with nonuniform zeta potential. *Analytical Chemistry* 72 (5), 1053–1057.
- Herschel, W., Bulkley, R., 1926. Konsistenzmessungen von gummi-benzollösungen. *Colloid & Polymer Science* 39 (4), 291–300.
- Hinch, E., 1993. The flow of an oldroyd fluid around a sharp corner. *Journal of non-newtonian fluid mechanics* 50 (2-3), 161–171.
- Horn, R., Vinogradova, O., Mackay, M., Phan-Thien, N., 2000. Hydrodynamic slippage inferred from thin film drainage measurements in a solution of nonadsorbing polymer. *The Journal of Chemical Physics* 112, 6424.
- Inn, Y., Wang, S., 1996. Hydrodynamic slip: Polymer adsorption and desorption at melt/solid interfaces. *Physical review letters* 76 (3), 467–470.
- Jamaati, J., Niazmand, H., Renksizbulut, M., 2010. Pressure-driven electrokinetic slip-flow in planar microchannels. *International Journal of Thermal Sciences* 49 (7), 1165–1174.
- John, V., 2002. Slip with friction and penetration with resistance boundary conditions for the navier-stokes equations: numerical tests and aspects of the implementation. *Journal of Computational and Applied Mathematics* 147 (2), 287–300.
- Joly, L., Ybert, C., Trizac, E., Bocquet, L., 2004. Hydrodynamics within the electric double layer on slipping surfaces. *Physical review letters* 93 (25), 257805.



- Joshi, Y., Denn, M., 2003. Planar contraction flow with a slip boundary condition. *Journal of non-newtonian fluid mechanics* 114 (2-3), 185–195.
- Joshi, Y., Lele, A., Mashelkar, R., 2000. Slipping fluids: a unified transient network model. *Journal of non-newtonian fluid mechanics* 89 (3), 303–335.
- Kalika, D., Denn, M., 1987. Wall slip and extrudate distortion in linear low-density polyethylene. *Journal of Rheology* 31, 815.
- Kawaguti, M., 1953. Numerical solution of the navier-stokes equations for the flow around a circular cylinder at reynolds number 40. *Journal of the Physical Society of Japan* 8, 747.
- Kazatchkov, I., Hatzikiriakos, S., 2010. Relaxation effects of slip in shear flow of linear molten polymers. *Rheologica Acta* 49, 267–274, 10.1007/s00397-009-0416-2.  
URL <http://dx.doi.org/10.1007/s00397-009-0416-2>
- Keiller, R., 1993. Entry-flow calculations for the oldroyd-b and fene equations. *Journal of non-newtonian fluid mechanics* 46 (2), 143–178.
- Keunings, R., Crochet, M., 1984. Numerical simulation of the flow of a viscoelastic fluid through an abrupt contraction. *Journal of non-newtonian fluid mechanics* 14, 279–299.
- Kim, S., Dealy, J., 2002. Gross melt fracture of polyethylene. i: A criterion based on tensile stress. *Polymer Engineering & Science* 42 (3), 482–494.
- Kraynik, A., Schowalter, W., 1981. Slip at the wall and extrudate roughness with aqueous solutions of polyvinyl alcohol and sodium borate. *Journal of Rheology* 25, 95.
- Kwon, Y., Han, J., 2010. Convergence limit in numerical modeling of steady contraction viscoelastic flow and time-dependent behavior near the limit. *Korea-Australia Rheology Journal* 22 (4), 237–245.
- Ladenburg, R., 1907. Über den einfluß von wänden auf die bewegung einer kugel in einer reibenden flüssigkeit. *Annalen der Physik* 328 (8), 447–458.
- Lamb, H., 1932. *Hydrodynamics*, 6th Edition. Cambridge University Press, Cambridge, UK.
- Larson, R., 1999. *The structure and rheology of complex fluids*.
- Lau, H., Schowalter, W., 1986. A model for adhesive failure of viscoelastic fluids during flow. *Journal of Rheology* 30, 193.

- Lauga, E., Brenner, M., Stone, H., 2005. Microfluidics: the no-slip boundary condition. Arxiv preprint cond-mat/0501557.
- Lee, J. S., Dylla-Spears, R., Tecler, N. P., Muller, S. J., 2007. Microfluidic four-roll mill for all flow types. *Applied Physics Letters* 90, 074103.
- Lee, S., Jang, J., Wereley, S., 2008. Effects of planar inlet plenums on the hydrodynamically developing flows in rectangular microchannels of complementary aspect ratios. *Microfluidics and Nanofluidics* 5 (1), 1–12.
- Leonard, B., 1979. A stable and accurate convective modelling procedure based on quadratic upstream interpolation. *Computer methods in applied mechanics and engineering* 19 (1), 59–98.
- Levine, S., Marriott, J. R., Neale, G., Epstein, N., 1975. Theory of electrokinetic flow in fine cylindrical capillaries at high zeta-potentials. *Journal of Colloid and Interface Science* 52 (1), 136–149.
- Liakos, A., 2001. Discretization of the navier-stokes equations with slip boundary condition. *Numerical Methods for Partial Differential Equations* 17 (1), 26–42.
- Liang, J., 1998. Determination of the entry region length of viscoelastic fluid flow in a channel. *Chemical engineering science* 53 (17), 3185–3187.
- Ligrani, P., Blanchard, D., Gale, B., 2010. Slip due to surface roughness for a newtonian liquid in a viscous microscale disk pump. *Physics of Fluids* 22, 052002.
- Luo, X., Tanner, R., 1989. A decoupled finite element streamline-upwind scheme for viscoelastic flow problems. *Journal of non-newtonian fluid mechanics* 31 (2), 143–162.
- Majda, A., Bertozzi, A., 2001. Vorticity and incompressible flow. Vol. 27. Cambridge Univ Pr.
- Marchal, J., Crochet, M., 1987. A new mixed finite element for calculating viscoelastic flow. *Journal of Non-Newtonian Fluid Mechanics* 26 (1), 77–114.
- Marchal, J. M., Crochet, M. J., 1986. Hermitian finite elements for calculating viscoelastic flow. *J. Non-Newtonian Fluid Mech.* 20, 187–207.
- Marry, V., Dufrêche, J., Jardat, M., Turq, P., 2003. Equilibrium and electrokinetic phenomena in charged porous media from microscopic and mesoscopic models: electro-osmosis in montmorillonite. *Molecular Physics* 101 (20), 3111–3119.

- Matthews, M., Hill, J., 2007. Newtonian flow with nonlinear navier boundary condition. *Acta mechanica* 191 (3), 195–217.
- Maxwell, J., 1867a. On the dynamical theory of gases. *Philosophical Transactions of the Royal Society of London* 157, 49–88.
- Maxwell, J., 1879. On stresses in rarified gases arising from inequalities of temperature. *Philosophical Transactions of the Royal Society of London* 170, 231–256.
- Maxwell, J., 1890. *The Scientific Papers of James Clerk Maxwell... Vol. 2.* University Press.
- Maxwell, J. C., 1867b. On the dynamical theory of gases. *Phil. Trans. R. Soc. Lond.* A157, 49–88.
- Meijer, H. E. H., Verbraak, C. P. J. M., 1988. Modeling of extrusion with slip boundary conditions. *Polymer Engineering & Science* 28 (11), 758–772.  
URL <http://dx.doi.org/10.1002/pen.760281108>
- Meller, M., Luciani, A., Sarioglu, A., Månson, J., 2002. Flow through a convergence. part 1: Critical conditions for unstable flow. *Polymer Engineering & Science* 42 (3), 611–633.
- Migler, K., Hervet, H., Leger, L., 1993. Slip transition of a polymer melt under shear stress. *Physical review letters* 70 (3), 287–290.
- Missirlis, K., Assimacopoulos, D., Mitsoulis, E., 1998. A finite volume approach in the simulation of viscoelastic expansion flows. *Journal of non-newtonian fluid mechanics* 78 (2-3), 91–118.
- Mitsoulis, E., Hatzikiriakos, S., 2009. Steady flow simulations of compressible ptfе paste extrusion under severe wall slip. *Journal of Non-Newtonian Fluid Mechanics* 157 (1-2), 26–33.
- Mitsoulis, E., Kazatchkov, I., Hatzikiriakos, S., 2005. The effect of slip in the flow of a branched pp melt: experiments and simulations. *Rheologica acta* 44 (4), 418–426.
- Moffatt, H. K., 1964. Viscous and resistive eddies near a sharp comer. *Journal of Fluid Mechanics* 18, 1–18.
- Mohseni, M., Rashidi, F., 2010. Viscoelastic fluid behavior in annulus using giesekus model. *Journal of Non-Newtonian Fluid Mechanics* 165 (21-22), 1550–1553.
- Mostafaiyan, M., Khodabandehlou, K., Sharif, F., 2004. Analysis of a viscoelastic fluid in an annulus using giesekus model. *Journal of non-newtonian fluid mechanics* 118 (1), 49–55.

- Münstedt, H., Schmidt, M., Wassner, E., 2000. Stick and slip phenomena during extrusion of polyethylene melts as investigated by laser-doppler velocimetry. *Journal of Rheology* 44, 413.
- Na, Y., Yoo, J., 1991. A finite volume technique to simulate the flow of a viscoelastic fluid. *Computational Mechanics* 8 (1), 43–55.
- Navier, C., 1823. Memoire sur les lois du mouvement des fluides. *Memoires de l'Academie Royale des Sciences de l'Institut de France* 6, 389–440.
- Navier, C. L. M. H., 1822. Memoire sur les lois du mouvement des fluides. *Mem. Acad. Sci. Inst. France* 6, 389–440.
- Neto, C., Evans, D., Bonaccorso, E., Butt, H., Craig, V., 2005. Boundary slip in newtonian liquids: a review of experimental studies. *Reports on Progress in Physics* 68, 2859.
- Ngoma, G., Erchiqui, F., 2007. Heat flux and slip effects on liquid flow in a microchannel. *International Journal of Thermal Sciences* 46 (11), 1076–1083.
- Nguyen, H., Boger, D. V., 1979. The kinematics and stability of die entry flows. *J. Non-Newtonian Fluid Mech.* 5, 353–368.
- Nigen, S., Walters, K., 2002. Viscoelastic contraction flows: comparison of axisymmetric and planar configurations. *J. Non-Newtonian Fluid Mech.* 102 (2), 343–359.
- Oldroyd, J., 1950. On the formulation of rheological equations of state. *Proceedings of the Royal Society of London. Series A. Mathematical and Physical Sciences* 200 (1063), 523–541.
- Oliveira, P. J., 2002. An exact solution for tube and slit flow of a fene-p fluid. *Acta Mechanica* 158 (3), 157–167.
- Oliveira, P. J., Pinho, F. T., 1999a. Analytical solution for fully developed channel and pipe flow of phan-thien-tanner fluids. *Journal of Fluid Mechanics* 387, 271–280.
- Oliveira, P. J., Pinho, F. T., 1999b. Numerical procedure for the computation of fluid flow with arbitrary stress-strain relationships. *Numer. Heat Transfer B* 35, 295–315.
- Oliveira, P. J., Pinho, F. T., 1999c. Plane contraction flows of upper convected maxwell and phan-thien-tanner fluids as predicted by a finite-volume method. *J. Non-Newtonian Fluid Mech.* 88, 63–88.
- Oliveira, P. J., Pinho, F. T., Pinto, G. A., 1998. Numerical simulation of non-linear elastic flows with a general collocated finite-volume method. *J. Non-Newtonian Fluid Mech.* 79, 1–43.

- Olsson, F., 1994. A solver for time-dependent viscoelastic fluid flows. *Journal of non-newtonian fluid mechanics* 51 (3), 309–340.
- Owens, R. G., Phillips, T. N., 2002. *Computational Rheology*. Imperial College Press, London.
- Park, H., Kim, T., 2009. Extension of the helmholtz-smoluchowski velocity to the hydrophobic microchannels with velocity slip. *Lab Chip* 9 (2), 291–296.
- Park, H. M., Lee, W. M., 2008. Helmholtz-smoluchowski velocity for viscoelastic electroosmotic flows. *Journal of colloid and interface science* 317 (2), 631–636.
- Patankar, S. V., 1980. *Numerical Heat Transfer and Fluid Flow*. Hemisphere Publishing Corporation.
- Pereira, G., 2009. Effect of variable slip boundary conditions on flows of pressure driven non-newtonian fluids. *Journal of Non-Newtonian Fluid Mechanics* 157 (3), 197–206.
- Petrie, C., Denn, M., 1976. Instabilities in polymer processing. *AIChE Journal* 22 (2), 209–236.
- Phan-Thien, N., 1978. A nonlinear network viscoelastic model. *Journal of Rheology* 22, 259.
- Phan-Thien, N., 1988. Influence of wall slip on extrudate swell: a boundary element investigation. *Journal of non-newtonian fluid mechanics* 26 (3), 327–340.
- Phan-Thien, N., 2002. *Understanding viscoelasticity: basics of rheology*. Springer Verlag.
- Phan-Thien, N., Tanner, R. I., 1977. A new constitutive equation derived from network theory. *J. Non-Newtonian Fluid Mech.* 2 (4), 353–365.
- Pit, R., Hervet, H., Leger, L., 2000. Direct experimental evidence of slip in hexadecane: solid interfaces. *Physical Review Letters* 85 (5), 980–983.
- Poiseuille, J., 1844. *Recherches expérimentales sur le mouvement des liquides dans les tubes de très-petits diamètres*. Imprimerie Royale.
- Poisson, S., 1831. Mémoire sur les mouvements simultanés d'un pendule et de l'air environnant. *L'Académie des sciences*.
- Poisson, S., 1832. 1. note sur le surface dont vaire est un minimum entre des limites données. *J. Reine Angew. Math* 8, 361–362.

- Poole, R., Alves, M., Oliveira, P., Pinho, F., 2007. Plane sudden expansion flows of viscoelastic liquids. *Journal of Non-Newtonian Fluid Mechanics* 146 (1-3), 79–91.
- Poole, R., Chhabra, R., 2010. Development length requirements for fully developed laminar pipe flow of yield stress fluids. *Journal of Fluids Engineering* 132, 034501.
- Poole, R., Escudier, M., 2003. Turbulent flow of a viscoelastic shear-thinning liquid through a plane sudden expansion of modest aspect ratio. *Journal of non-newtonian fluid mechanics* 112 (1), 1–26.
- Poole, R., Escudier, M., 2004. Turbulent flow of viscoelastic liquids through an axisymmetric sudden expansion. *Journal of non-newtonian fluid mechanics* 117 (1), 25–46.
- Poole, R., Escudier, M., Oliveira, P., 2005. Laminar flow of a viscoelastic shear-thinning liquid through a plane sudden expansion preceded by a gradual contraction. *Proceedings of the Royal Society A: Mathematical, Physical and Engineering Science* 461 (2064), 3827–3845.
- Poole, R., Pinho, F., Alves, M., Oliveira, P., 2009. The effect of expansion ratio for creeping expansion flows of ucm fluids. *Journal of Non-Newtonian Fluid Mechanics* 163 (1), 35–44.
- Poole, R., Ridley, B., 2007. Development-length requirements for fully developed laminar pipe flow of inelastic non-newtonian liquids. *Journal of Fluids Engineering* 129, 1281.
- Potente, H., Ridder, H., Cunha, R. V., 2002. Global concept for describing and investigation of wall slip effects in the extrusion process. *Macromolecular Materials and Engineering* 287 (11), 836–842.  
URL <http://dx.doi.org/10.1002/mame.200290013>
- Potente, H., Timmermann, K., Kurte-Jardin, M., 2006. Description of the pressure/throughput behavior of a single-screw plasticating unit in consideration of wall slippage effects for non-newtonian material and 1-d flow. *International Polymer Processing* 21 (3), 272–282.
- Raisi, A., Mirzazadeh, M., Dehnavi, A., Rashidi, F., 2008. An approximate solution for the couette–poiseuille flow of the giesekus model between parallel plates. *Rheologica Acta* 47 (1), 75–80.
- Ramamurthy, A., 1986. Wall slip in viscous fluids and influence of materials of construction. *Journal of Rheology* 30, 337.
- Ravanchi, M., Mirzazadeh, M., Rashidi, F., 2007. Flow of giesekus viscoelastic fluid in a concentric annulus with inner cylinder rotation. *International journal of heat and fluid flow* 28 (4), 838–845.

- Renardy, M., 1995. A matched solution for corner flow of the upper convected maxwell fluid. *Journal of non-newtonian fluid mechanics* 58 (1), 83–89.
- Rhie, C., Chow, W., 1983. Numerical study of the turbulent flow past an airfoil with trailing edge separation. *AIAA journal* 21 (11), 1525–1532.
- Richardson, L., 1910. On the approximate arithmetical solution by finite differences of physical problems involving differential equations, with an application to the stresses in a masonry dam. *Proceedings of the Royal Society of London. Series A* 83 (563), 335–336.
- Richardson, L., Gaunt, J., 1927. The deferred approach to the limit. part i. single lattice. part ii. interpenetrating lattices. *Philosophical Transactions of the Royal Society of London. Series A, containing papers of a mathematical or physical character* 226, 299–361.
- Rielly, F., Price, W., 1961. Plastic flow in injection molds. *SPE J* 17, 1097–1101.
- Roache, P. J., 1972. *Computational Fluid Dynamics*. Hermosa Publishers, Denver, Colorado.
- Robertson, R., Stiff, H., 1976. An improved mathematical model for relating shear stress to shear rate in drilling fluids and cement slurries. *Old SPE Journal* 16 (1), 31–36.
- Rocha, G., Poole, R., Oliveira, P., 2007. Bifurcation phenomena in viscoelastic flows through a symmetric 1: 4 expansion. *Journal of non-newtonian fluid mechanics* 141 (1), 1–17.
- Roux, C., Tani, A., 2007. Steady solutions of the navier–stokes equations with threshold slip boundary conditions. *Mathematical methods in the applied sciences* 30 (5), 595–624.
- Schleiniger, G., Weinacht, R. J., 1991. Steady poiseuille flows for a giesekus fluid. *J. Non-Newtonian Fluid Mech.* 40 (1), 79–102.
- Schowalter, W., 1988. The behavior of complex fluids at solid boundaries. *Journal of Non-Newtonian Fluid Mechanics* 29, 25–36.
- Sisko, A., 1958. The flow of lubricating greases. *Industrial & Engineering Chemistry* 50 (12), 1789–1792.
- Soong, C., Hwang, P., Wang, J., 2010. Analysis of pressure-driven electrokinetic flows in hydrophobic microchannels with slip-dependent zeta potential. *Microfluidics and Nanofluidics* 9 (2), 211–223.
- Sousa, J., Afonso, A., Pinho, F., Alves, M., 2011. Effect of the skimming layer on electro-osmotic poiseuille flows of viscoelastic fluids. *Microfluidics and Nanofluidics* 10 (1), 107–122.

- Stokes, G. G., 1845. On the theories of the internal friction of fluids in motion, and of the equilibrium and motion of elastic solids. *Transactions of the Cambridge Philosophical Society* 8.
- Stokes, Y., Carey, G., 2008. On penalty approaches for navier-slip and other boundary conditions in viscous flow. In: *Proceedings of the 22nd IUTAM International Congress for Theoretical and Applied Mechanics (CD-ROM)*, ISBN. pp. 978–0.
- Stone, H. A., Stroock, A. D., Ajdari, A., 2004. Engineering flows in small devices, microfluidics toward a lab-on-a-chip. *Annual Review of Fluid Mechanics* 36, 381.
- Sunarso, A., Yamamoto, T., Mori, N., 2006. Numerical simulation of polymeric flow in contraction channels: Wall slip and channel size dependent effects. In: *AIP Conference Proceedings*. Vol. 832. p. 341.
- Sunarso, A., Yamamoto, T., Mori, N., 2007. Numerical analysis of wall slip effects on flow of newtonian and non-newtonian fluids in macro and micro contraction channels. *Journal of Fluids Engineering* 129, 23.
- Tandon, V., Bhagavatula, S., Nelson, W., Kirby, B., 2008. Zeta potential and electroosmotic mobility in microfluidic devices fabricated from hydrophobic polymers: 1. the origins of charge. *Electrophoresis* 29 (5), 1092–1101.
- Thom, A., 1933. The flow past circular cylinders at low speeds. *Proceedings of the Royal Society of London. Series A, Containing Papers of a Mathematical and Physical Character* 141 (845), 651–669.
- Thompson, P., Troian, S., 1997. A general boundary condition for liquid flow at solid surfaces. *Nature* 389 (6649), 360–362.
- Townsend, P., Walters, K., 1994. Expansion flows on non-newtonian liquids. *Chemical engineering science* 49 (5), 748–763.
- Tretheway, D., Meinhart, C., 2002. Apparent fluid slip at hydrophobic microchannel walls. *Physics of Fluids* 14, L9.
- Tretheway, D., Meinhart, C., 2004. A generating mechanism for apparent fluid slip in hydrophobic microchannels. *Physics of Fluids* 16, 1509.
- Turner, M., Clough, R., Martin, H., Topp, L., 1956. Stiffness and deflection analysis of complex structures. *J. Aero. Sci* 23 (9), 805–823.
- Van Doormaal, J. P., Raithby, G. D., 1984. Enhancements of the SIMPLE method for predicting incompressible fluid flows. *Numerical Heat Transfer, Part A: Applications* 7 (2), 147–163.



- Verfürth, R., 1986. Finite element approximation on incompressible navier-stokes equations with slip boundary condition. *Numerische Mathematik* 50 (6), 697–721.
- Voronov, R., Papavassiliou, D., Lee, L., 2008. Review of fluid slip over superhydrophobic surfaces and its dependence on the contact angle. *Industrial & Engineering Chemistry Research* 47 (8), 2455–2477.
- Wahba, E., 2007. Iterative solvers and inflow boundary conditions for plane sudden expansion flows. *Applied mathematical modelling* 31 (11), 2553–2563.
- Walters, K., Webster, M. F., 1982. On dominating elasto-viscous response in some complex flows. *Phil. Trans. R. Soc. Lond. A* 308, 199–218.
- Wang, S., 1999. Molecular transitions and dynamics at polymer/wall interfaces: origins of flow instabilities and wall slip. *Polymers in Confined Environments*, 227–275.
- Wapperom, P., Webster, M., 1999. Simulation for viscoelastic flow by a finite volume/element method. *Computer methods in applied mechanics and engineering* 180 (3), 281–304.
- Watanabe, K., Mizunuma, H., et al., 1998. Slip of newtonian fluids at slid boundary. *JSME international journal. Series B, fluids and thermal engineering* 41 (3), 525–529.
- Wesseling, P., 2010. *Principles of computational fluid dynamics*. Vol. 29. Springer Verlag.
- Wesson, R., Papanastasiou, T., 1988. Flow singularity and slip velocity in plane extrudate swell computations. *Journal of non-newtonian fluid mechanics* 26 (3), 277–295.
- Whetham, W., 1890. On the alleged slipping at the boundary of a liquid in motion. *Proceedings of the Royal Society of London* 48 (292-295), 225–230.
- White, S. A., Gotsis, A. D., Baird, D. G., 1987. Review of the entry flow problem: experimental and numerical. *J. Non-Newtonian Fluid Mech.* 24 (2), 121–160.
- Wu, Y., Wiwatanapataphee, B., Hu, M., 2008. Pressure-driven transient flows of newtonian fluids through microtubes with slip boundary. *Physica A: Statistical Mechanics and its Applications* 387 (24), 5979–5990.
- Xue, S., Phan-Thien, N., Tanner, R. I., 1998a. Numerical investigations of Lagrangian unsteady extensional flows of viscoelastic fluids in 3-D rectangular ducts with sudden contractions. *Rheologica Acta* 37 (2), 158–169.

- Xue, S. C., Phan-Thien, N., Tanner, R. I., 1998b. Three dimensional numerical simulations of viscoelastic flows through planar contractions. *J. Non-Newtonian Fluid Mech.* 74 (1-3), 195–245.
- Yang, J., Kwok, D., 2002. A new method to determine zeta potential and slip coefficient simultaneously. *The Journal of Physical Chemistry B* 106 (50), 12851–12855.
- Yang, J., Kwok, D., 2004. Analytical treatment of electrokinetic microfluidics in hydrophobic microchannels. *Analytica chimica acta* 507 (1), 39–53.
- Yang, S., Zhu, K., 2006. Analytical solutions for squeeze flow of bingham fluid with navier slip condition. *Journal of non-newtonian fluid mechanics* 138 (2), 173–180.
- Yapici, K., Karasozen, B., Uludag, Y., 2012. Numerical analysis of viscoelastic fluids in steady pressure-driven channel flow. *Journal of Fluids Engineering* 134, 051206.
- Yasuda, K., Sugiura, Y., 2008. Entry flows of polymer solutions through a planar contraction in a microchannel. *Journal of Fluid Science and Technology* 3 (8), 987–998.
- Yoo, J., Choi, H., 1989. On the steady simple shear flows of the one-mode giesekus fluid. *Rheologica acta* 28 (1), 13–24.
- Yul Yoo, J., Na, Y., 1991. A numerical study of the planar contraction flow of a viscoelastic fluid using the simpler algorithm. *Journal of non-newtonian fluid mechanics* 39 (1), 89–106.
- Zhang, Y., Craster, R., Matar, O., 2003. Surfactant driven flows overlying a hydrophobic epithelium: film rupture in the presence of slip. *Journal of colloid and interface science* 264 (1), 160–175.
- Zhao, C., Yang, C., 2011. Electro-osmotic mobility of non-newtonian fluids. *Biomicrofluidics* 5, 014110.
- Zhu, Y., Granick, S., 2001. Rate-dependent slip of newtonian liquid at smooth surfaces. *Physical review letters* 87 (9), 96105.
- Zienkiewicz, O., 1991. The finite element method for fluid dynamics. Ph.D. thesis, University of Wales.

## COLOPHON

This thesis was typeset with  $\text{\LaTeX} 2_{\epsilon}$  using Hermann Zapf's *Palatino* and *Euler* type faces (Type 1 PostScript fonts *URW Palladio L* and *FPL* were used). The listings are typeset in *Bera Mono*, originally developed by Bitstream, Inc. as "Bitstream Vera". (Type 1 PostScript fonts were made available by Malte Rosenau and Ulrich Dirr.)

The typographic style was inspired by Bringhurst's genius as presented in *The Elements of Typographic Style* (Bringhurst, 2002). It is available for  $\text{\LaTeX}$  via CTAN as "classicthesis".